

Communications of the Byurakan Astrophysical Observatory

2

Erevan 2018

Editor's Introduction

H. A. Harutyunian

NAS RA V. Ambartsumian Byurakan Astrophysical Observatory (BAO), Armenia

**E-mail: hhayk@bao.sci.am*

This issue of the Communications of BAO is dedicated to the 110th anniversary of Viktor Ambartsumian – the founder of the BAO. We pointed in the first issue of the renewed ComBAO that Ambartsumian was the founder of this scientific periodical as well. More than 70 years ago, the first generation of Byurakan astrophysicists got a scientific magazine where they published many important scientific papers.

In the occasion of the jubilee, the International Conference “Instability Phenomena and Evolution of the Universe” took place at the Byurakan Astrophysical Observatory during the week 17-21 September 2018. That was a tribute to the memory of Ambartsumian, who was the first to concentrate his attention and attention of his co-workers on the decisive role of instability phenomena in the evolution of cosmic objects. Indeed, establishing the observatory in 1946 Ambartsumian also outlined its scientific priorities. Since that time the study of active or non-stationary phenomena were always among first priorities.

The point is that comparing with the long lasting evolution processes in cosmic objects activity phenomena more easily show the dominant direction of the matter evolution in the Universe. All the physical conclusions require accurate observational data, providing all necessary tools to reveal clear and unambiguous empirical regularities concerning the objects of research and the usage of physical theories well established and approved owing to their reproducible character. That was one of the cornerstones for the research methodology of studies of cosmogonic problems if one stays in the Ambartsumian's ideological frame.

Although some of the ideas stated by Ambartsumian in the field of stellar and galactic cosmogony are referred to have only historical interest, drastic changes in the comprehension of star formation or the role of active galactic nuclei, makes his research methodology rather valuable for the future studies of the relevant issues. One should mention that nowadays are common studies of the star forming regions and active galactic nuclei, any discourse about which considered to be ground less at very beginning. Speakers presented to the attention of participants of the conference many aspects of

instability in the various cosmic objects, belonging to all hierarchical levels of the Universe. Researchers considered observational data concerning the instability phenomena in separate stars, stellar groups and galaxies, which allowed comparative analyses of the types of these phenomena. In parallel, some presentations, stellar configurations consisted of various types of super-dense matter, including quark stars, are considered theoretically. These series of theoretical studies also initiated Ambartsumian in early 60s of the last century jointly with Professor Gurgen Sahakian, is under future elaboration at the Yerevan State University.

All the papers passed relevant peer-review. We are glad that in the magazine established by Ambartsumian we publish papers, which in some way are related to his scientific ideas and results.

Viktor Ambartsumian's most important scientific achievements

A. M. Mickaelian

NAS RA V. Ambartsumian Byurakan Astrophysical Observatory (BAO), Armenia

**E-mail: aregmick@yahoo.com*

Abstract

We give a review of the most important scientific achievements of one of the greatest scientists of the XX century, the founder of the modern astrophysics in Armenia, Viktor A. Ambartsumian (1908-1996). He has fundamentally contributed in various fields of astronomy and astrophysics, cosmogony, theoretical physics, mathematics, and philosophy. We list the most important scientific results, including his revolutionary works on origin and evolution of stars and activity of galactic nuclei that turned over the development of astrophysics and gave life to our before unchanged Universe. He was one of the founders of the theory of planetary nebulae, stellar dynamics, protostellar dense matter, as well as he has contributed in other important areas of the theoretical astrophysics. Ambartsumian was also a great organizer of science, important political and public figure. He was the founding Director of the Byurakan Astrophysical Observatory (BAO, 1946-1988), the President of the Armenian Academy of Sciences in 1947-1993, the President of the International Astronomical Union (IAU) in 1961-1964 and the President of the International Council of Scientific Unions (ICSU) in 1968-1972. He was the founder of the theoretical astrophysics in the Soviet Union, the founder of chairs of astrophysics in Leningrad (St. Petersburg) and Yerevan state universities, as well as the journals Communications of BAO and Astrofizika (Astrophysics).

Keywords: *Theoretical Physics – Theoretical Astrophysics – Stellar Dynamics – Stellar Evolution – Planetary Nebulae – Interstellar Medium – Radiative Transfer Theory – Stellar Associations – Active Galactic Nuclei – Superdense Matter.*

1. Introduction

Viktor Ambartsumian (1908-1996) is one of the greatest scientists of the XX century who has fundamentally contributed in various fields of astronomy and astrophysics, cosmogony, theoretical physics, mathematics, and

philosophy. His revolutionary works on origin and evolution of stars and activity of galactic nuclei turned over the development of astrophysics and gave life to our before unchanged Universe. He is one of the founders of the theory of planetary nebulae, stellar dynamics, protostellar dense matter, as well as he has contributed in other important areas of the theoretical astrophysics. Ambartsumian was also a great organizer of science, important political and public figure. He is the founder of the Astrophysics Departments at Leningrad (St. Petersburg) and Yerevan state universities, Byurakan Astrophysical Observatory (BAO), journals *Communications of BAO* and *Astrofizika (Astrophysics)*, one of the founders of the Armenian Academy of Sciences. Ambartsumian was the founding Director of BAO (1946-1988), the President of the Armenian Academy of Sciences in 1947-1993, the President of the International Astronomical Union (IAU) in 1961-1964 and the President of the International Council of Scientific Unions (ICSU) in 1968-1972.

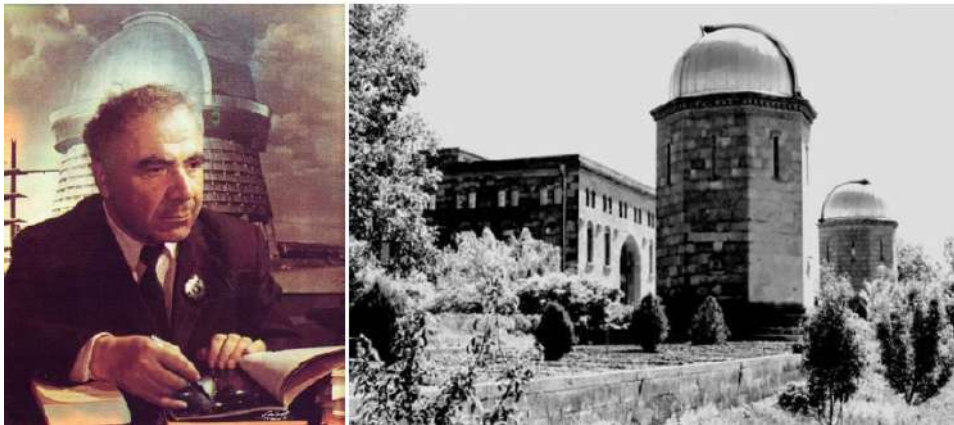


Figure 1: Viktor Ambartsumian (1908-1996) and Byurakan Astrophysical Observatory (BAO), founded by him.

Viktor Amazasp Ambartsumian was born on September 18, 1908, in Tbilisi (Georgia). After the graduation of Leningrad (Saint-Petersburg) University and post-graduate studentship in Pulkovo Observatory, he founded at the University the first Department of Astrophysics in the Soviet Union. In 1943, V.A. Ambartsumian was one of the founding members of the Armenian Academy of Sciences and its Vice-President. Soon, in 1947, he became the President of the Academy, and since 1993 he was its Honorary President. In 1946, Byurakan Astrophysical Observatory (BAO) of the Academy of Sciences of Armenia was founded. Since the first days till 1988 V.A. Ambartsumian was the Director and scientific leader of BAO. And since 1988, he was its Honorary Director. Thanks to Ambartsumian's and his colleagues' works it became one of the known observatories in the world.

Ambartsumian's research works are distinguished in perfection and al-

most every time opened new directions in astrophysics. His works on physics of gaseous nebulae and radiation transfer theory are classic. They played an important role in this field, in particular, in the theory of multiple light scattering. The invariance principle, formulated in these works for the first time, had a wide application in a number of other fields of the science. Ambartsumian's investigations on the problem of stellar evolution brought in 1947 to revealing of stellar systems of new type, stellar associations. The existence of stellar associations in the Galaxy, dynamically non-stable and disintegrating systems, was the first observational evidence in favour of continuing at present star-formation in it. Ambartsumian put forward a hypothesis about the joint origin of the diffuse matter and stars of dense matter of unknown nature, protostars. Ambartsumian's studies of early stages of evolution of stars and stellar systems are rather significant. It was shown, that in the early stages of the evolution, the instability of the state reveals itself, being the regular phase of the cosmogonic processes. Among these results the conclusions about the existence of stellar systems of positive total energy in the Galaxy, non-thermal nature of ultraviolet stellar radiation of T Tauri type and flare stars, are to be mentioned. New principle results were achieved by V.A. Ambartsumian in study of evolution of galaxies. It was shown for the first time that the central regions of galaxies, their nuclei, play a decisive role in the phenomena of instability, observed in galaxies. Besides the stars and diffuse matter, they must contain dense massive bodies of unknown nature. The activity of galactic nuclei defines their evolution. At present the active galactic nuclei (AGN) are the most intensively studied objects in extragalactic astronomy.

Ambartsumian has carried out some other investigations of great importance in astrophysics as well, such as the study of interstellar absorbing matter in the Galaxy (the idea of its clumpy structure, the theory of fluctuations of light of the Milky Way), works on stellar dynamics (establishing of the basis of new, statistical mechanics of stellar systems), statistical investigations of flare stars, and others. V.A. Ambartsumian has published about 20 books and booklets, more than 200 scientific papers, and numerous popular articles.

Ambartsumian was an outstanding organizer of science, who significantly promoted the international scientific cooperation. In 1948-1955 he was the Vice-President, and in 1961-64, the President of the International Astronomical Union (IAU), in 1968 and 1970 he was twice elected the President of the International Council of Scientific Unions (ICSU). His many-sided activity accepted high estimate. He was awarded governmental prizes, orders and medals of a number of countries (Twice Hero of Socialist Labour in 1968 and 1978, USSR State Prizes in 1946 and 1950, Russian State Prize in 1995, National Hero of Armenia in 1994), gold medals of a number of academies and scientific societies.

He was elected honorary and foreign member of 28 Academies of Sci-

ences, including USA, UK, France, Italy, Netherlands, Belgium, Denmark, Sweden, Greece, Czechoslovakia, India, Argentina, and others, honorary member of scientific societies of many countries, honorary doctor of the Universities of Canberra (Australia), La Plata (Argentina), Warsaw and Torun (Poland), Prague (Czechoslovakia), Liege (Belgium) and Sorbonne (France).

Victor A. Ambartsumian passed away on August 12, 1996 in Byurakan. He will remain forever as one of the most outstanding scientists of the XX century.

Viktor Ambartsumian's scientific achievements are well-known in the scientific community, especially among astronomers and astrophysicists. However, he has left so much legacy that one should try to thoroughly study, analyze and classify all this big material. Once, a small attempt was made by Ambartsumian himself in his memories given in the book "Life Episodes" (Shahbazyan 2001; 2003; however, this is only in Russian and Armenian and the world community still has no access). Ambartsumian recalled that some scientists especially mention some definite results by him from 1930s. Most of these concerned theoretical astrophysics, theory of planetary nebulae, stellar dynamics, etc. On the other hand, later on, many scientists considered the discovery of stellar associations (1947) and the hypothesis on the activity of galactic nuclei (1950s) as Ambartsumian's most important works. The theory of superdense matter (1960s) and the statistics of the flare stars (1968) that resulted in the major conclusion about the flare activity of all dwarf stars are also worth to mention. In 2008 we released a DVD devoted to Ambartsumian's 100th anniversary and we made an effort to sort his major achievements in science (Mickaelian 2008). These results were also published in Harutyunian Mickaelian (2008; 2011). Most detailed description of Ambartsumian's most important scientific results is given in the book "Viktor Ambartsumian: Life and Activities" (Mickaelian 2014). In this review we summarize and analyze Viktor Ambartsumian's most important achievements based on all these previous studies.

2. Most important scientific results

2.1. Astronomy, Astrophysics and Cosmogony

2.1.1. Theory of Planetary Nebulae (PN)

For the first time the **influence of the light pressure on the planetary nebulae dynamics was studied** (1932). Each quantum of light owns a definite amount of energy and linear momentum. The bigger the frequency of the quantum (or shorter the corresponding wavelength), the bigger the momentum carried by them. As there are many hot stars in the center of planetary nebulae, which emit short wavelength photons, a question arises,

how this emission may affect the circumstellar gas medium. This problem had a very important subtext. The matter was that the classical cosmogony claims that stars are being formed as a consequence of the condensation of gas and dust, and the joint existence of a star and a nebula could introduce a definite clarification in their evolutionary chain. And it was really obtained that **owing to light pressure the planetary nebulae expand and should gradually dissipate in the space**. It was also shown that **the age of the planetary nebulae could not exceed 100000 years if no continuous outflow existed from the central star**. Thus, for the first time the new evolutionary paradigm on the formation of objects from denser matter was formulated.

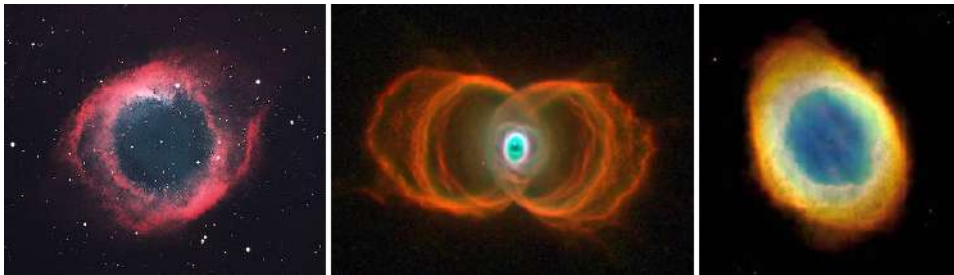


Figure 2

Zanstra's method for determination of the planetary nebulae's central star temperature was modified giving the probabilistic definition of short-wave energetic photons transformation into less energetic ones (1932). It is known that the planetary nebulae radiate due to the transformation of short-wave photons emitted by the hot stars located in their center. It means that the high energy photons emitted from the star, which are not visible to the eye due to their short wavelengths, are being absorbed in the nebula ionizing the gas atoms. Due to this, ions and electrons are being originated in the nebula. Later on, electrons couple with ions and as a result numerous different energy photons form, including those visible to the eye. If a method is being developed allowing calculate the number of the transformed and hence visible photons, the number of those short wavelength photons that originated the visible ones also may be determined. Just due to this it becomes possible to calculate the surface temperature of the star. This definition leads to the determination of radiative equilibrium.

2.1.2. Novae and Supernovae

For the first time **the amount of matter ejecting as a result of Novae and Supernovae explosions was estimated** (together with N.A. Kozyrev, 1933). The phenomena of Novae and especially Supernovae belong

to the largest stellar explosions. The first of these names has been formed historically. The matter was that in the sky from time to time people discovered stars that had never been observed before and it seemed as if they were newly born stars. Later on it was understood that they also existed before, however were not visible due to their faintness. They become visible at some moment due to a burst and increase of their brightness dozens of thousands or even million times. And in a few months they return to their previous state. The Supernova phenomenon is much more powerful compared to the ordinary Novae. If the Nova after the explosion returns to its normal state, the Supernovae after the explosion don't return to their former state anymore. For the thrown out matter as a consequence of the explosion **Ambartsumian obtained the presently known values of 0.00001 and 1 solar masses correspondingly for the Novae and Supernovae phenomena.**

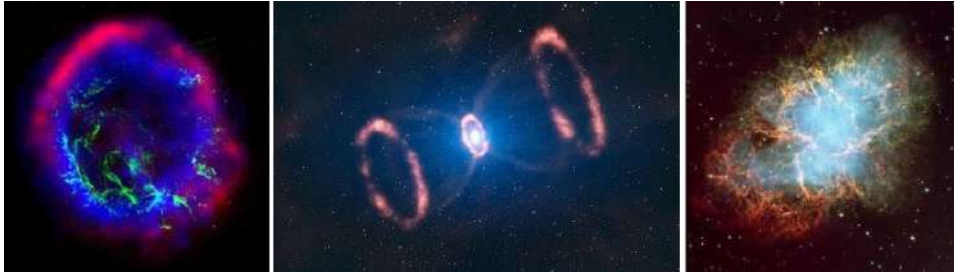


Figure 3

2.1.3. Stellar Dynamics

For the first time **the distribution of stellar spatial (3D) velocities was derived** using only the coordinates and radial velocities. By classical method, the stellar spatial velocities are being determined by their radial and tangential velocities. However, the observations at different directions lead to a variety of errors. Taking into account that the spatial velocities are being given in three components, Ambartsumian applied a completely different method using three other variables for each star; the radial velocity and celestial coordinates. As a matter of fact, a necessity originated to find the required function that depended on three variables by means of a known function also depending on three other variables. This problem was reduced to the numerical inversion of the Radon transformation. Four decades later **the same mathematical scheme was applied for the construction and exploitation of computer tomography.** *“It seems to me quite possible that Ambartsumian’s numerical methods might have made significant contributions to that part of medicine had they been applied in 1936”*, – mentioned in 1985 Allan Cormack who won the Nobel Prize in

Physiology and Medicine for creating the tomography.

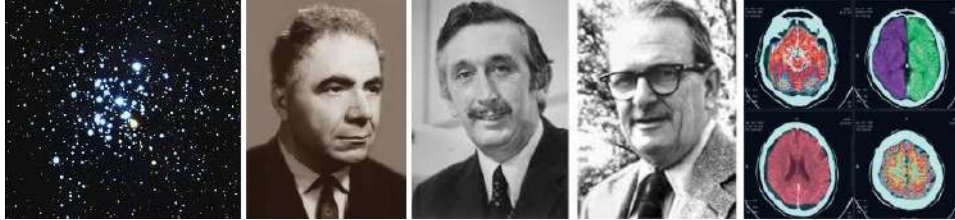


Figure 4: Viktor Ambartsumian derived the 3D distribution of the stellar velocities and 4 decades later the same mathematical scheme was applied for the construction and exploitation of computer tomography by Godfrey Hounsfield and Allan Cormack who won the Nobel Prize in Physiology and Medicine in 1979.

Using the statistical studies of, so called, wide binaries it was shown for the first time that those did not obey the dissociative equilibrium conditions (1936-1937). The matter is that during the stellar approaches as physically coupled binaries may form so as the existing binaries may disrupt. So, if three physically uncoupled stars approach each other, an energy exchange may happen between them. One of the possible consequences of such exchange is that one of the three stars obtains large energy and leaves and the remaining two, losing some part of their energy, cannot anymore move away and form a binary. The inverse phenomenon may also take place, when a third star approaches a physically coupled binary, transfers part of its energy to them and decouples them from each other and three uncoupled stars form as a consequence. A dissociative equilibrium establishes in a definite time when these two inverse processes equal each other. Ambartsumian showed that such equilibrium has not yet been established and the number of binaries is many times larger than was expected in the case of the equilibrium state. The same studies allowed arriving at a conclusion that the components of binaries had been formed jointly. Moreover, *the observed distribution put an upper limit for the Galaxy age*, which agreed with “the short scale”.



Figure 5

The mechanism of star “evaporation” from the open star clusters was revealed (1938). The use of this phenomenon allowed him for the first time find the halftime of the clusters’ decay, and was applied to anticipate the gradual decrease of the number of low mass stars in clusters. A new stellar statistical method was developed to consider this problem. For this, it was taken into account that in the stellar system of any type mutually connected by gravitational forces an ongoing energy exchange was taking place between its components. As a consequence, a so-called equilibrium Maxwell distribution of energies is being established. On the other hand, in the case of equilibrium distribution some stars gain such velocities that allow them break away from the gravitational field of the system and irreversibly leave. As a result, the energy equilibrium is being broken and the energy exchange again establishes a new equilibrium state. This process, which is by its sense the same as the water evaporation, gradually depletes the star cluster. And by the way, the low-mass stars leave the cluster the first as in the case of the same energy low-mass stars gain larger velocities. These studies provided a theoretical basis for decreasing the accepted age of the Galaxy for thousand times (the previous estimate, so-called “the long scale” was by James Jeans, 1013 years), making it equal to 10 billion years and for **introducing “the short scale” of the Galaxy age**. Note that this estimate has not changed until nowadays, though with the development of science many new methods have been applied to calculate the age of the Galaxy. It is worth stating that by modern estimates the age of the Universe is 13.8 billion years.



Figure 6: Viktor Ambartsumian and James Jeans (UK), who disputed in 1930s about the age of Our Galaxy

2.1.4. Interstellar Medium (ISM)

The patchy structure of the Milky Way’s absorbing dust component was revealed (together with Sh.G. Gordeladze, 1938). Our Galaxy has two components, one having disk-like flat form and spiral arms come out from its nucleus. The stars belonging to this component form in the sky the

nebulous strip of the Milky Way. And the whole gas-dust matter of the Galaxy belongs just to this component. Even with the naked eye one can see that the stars in the Milky Way are not distributed equally; in some parts their number is rather small compared to the neighboring regions. This is simply because of the presence of the absorbing matter. Ambartsumian was the first to show that the distribution of the absorbing matter was rather inhomogeneous and in the reality it was formed of individual clouds. The sense of the name “patchy structure” is just the fact that it is consisted of these individual clouds. For the first time, **the mean absorption of corresponding single clouds was estimated to be of the order of 0.2 magnitudes corresponding to some 1.2 times weakening of the light passing through it.**



Figure 7

The **theory of the fluctuations in brightness of the Milky Way** was formulated (1944). In the simplest form it asserts that the probability distribution of fluctuations in the brightness of the Milky Way is invariant to the location of the observer. In the interstellar space the absorbing clouds are concentrated in a rather thin strip around the plane of symmetry of the Galaxy. Definite deviations of the observed distribution of the brightness of the Milky Way have formed in the sky due to the light absorption in them. For the same reason, deviations from the equal distribution of the number of other galaxies are also formed. In other words, for example if in the case of absence of interstellar absorption, the brightness of the Milky Way in the neighboring regions of the sky would not vary much, the presence of the absorbing clouds causes abrupt variations of this brightness. The nature and size of the observed deviations are completely determined by the properties and the number of the interstellar absorbing clouds. **The investigation of the observed deviations by the theory of fluctuations allowed determine the properties of the absorbing clouds.**

2.1.5. Radiative Transfer Theory

The **Invariance principle was proposed to solve the radiative transfer problems** (1941-1942). The principle in fact has a very simple

physical sense and statement. For the first time it was established for the purpose of the formulation of the problem of the reflection of radiation from the semi-infinite medium. It is enough to imagine a radiation scattering and reflecting medium that has only one surface and fills half of the space. An example of such a medium is the ocean for the ordinary light. The radiation penetrates into the depth of the medium and may change its direction in the case of each scattering process and move in the opposite direction or continue moving in the same direction. The problem is to determine the number of the reflected radiation as a result of numerous scattering processes, which in general case depends on different variables, including the direction, wavelength, etc. Very simple physical reasoning that the reflection properties of the semi-infinite medium will not be changed if a very thin layer of the same physical properties is added to the medium boundary gave an excellent basis for creation of a new and strong research method. The mathematical equations describing the problem are much simpler and are being easily solved compared to the previously used so-called transfer equation. After many years Ambartsumian declared *the Invariance Principle* to be one of the most important tools he invented. This principle bears V. Ambartsumian's name and the corresponding function was named V. Ambartsumian's ϕ function.



Figure 8: A humorous drawing by the French astronomer Jean-Claude Pecker showing Ambartsumian's Principle of Invariance

2.1.6. Stellar Evolution

The importance of the stellar associations as dynamically unstable entities was revealed (1947-1949). The stellar associations, which

are distinguished by a rather big partial density of similar stars, attracted Ambartsumian's attention still in 1930s. A special interest caused the question how the similar stars had gathered in the same area. Investigating their structural properties, Ambartsumian showed that **they had been formed together and that they could not be older than a few dozen million years**. It meant that the stars belonging to the stellar association also could not be older than that. Taking into account that the prevailing part of the stars of the Galaxy are a few billion years old, **a conclusion was made that these were newly born stars**. Thus it was shown for the first time that **at present the star formation process also continues**. It was the first case when it was shown that in a finite space volume there exist stars of different ages. The other important conclusion was that **the star formation occurs in groups**.



Figure 9

Ambartsumian showed that **the continuous emission observed in the spectra of non-stable stars had nonthermal nature** and put forward an idea about new possible sources of stellar energy, the hypothesis of the superdense protostellar matter (1954). Moreover, later on Ambartsumian concluded that the same source might be responsible for the phenomena taking place in the centres of galaxies, galactic nuclei. Observational evidences, particularly huge amounts of energy emitted from the central parts of galaxies, insist on the existence of powerful sources of energy. At present the most popular explanation for the AGN powerhouse, the Unified Scheme, involves accretion of gas onto a Super Massive Black Hole (SMBH). Thus, Ambartsumian's suggestion that there existed a supermassive dense body in the center of galaxies is now well accepted and SMBH could be one of the possible models of such matter. Though Ambartsumian believed that the source of energy was inner, it is obvious that his idea on the activity of galaxies based on the energy sources hidden in the galactic nuclei is modified to fit known physical theories, which Ambartsumian himself did not find unambiguous.

Theoretical studies of the hypothetical superdense protostellar matter have been done in the frame of the modern knowledge of physics (to-

gether with G.S. Sahakyan, 1960-1961). The existence of stellar associations and the possibility of the formation of stellar groups in a small space volume already require the presence of matter of a new type that is by its density comparable to atomic nuclei. The activity of the galactic nuclei and the need of the presence of large masses in them even more increased the necessity of the theoretical justification of the superdense matter. **These researches allowed later increase the Chandrasekhar limit of stellar masses.** However, so far it has not been possible to theoretically prove the possibility of the existence of superdense matter concentrations having masses of galaxies or their nuclei. So far just this prevents the further dissemination of the point of view of the activity of galactic nuclei and the formation of daughter galaxies by decay and ejections from galaxies. Some researchers believe that this obstacle is in fact a consequence of the non-perfect knowledge of the laws of Nature.

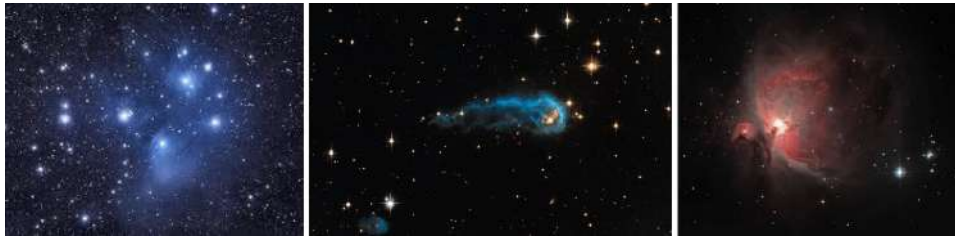


Figure 10

Statistical studies of the flare stars revealed their evolutionary status (1968). In general, on all stars one can find various evidences of activity. Even on the Sun that is considered as a quiet star, giant explosions and bursts take place, though having essentially smaller energy compared to the total energy emitted by the Sun. However, there exists a whole class of dwarf stars, which show flares having emitted energy dozens and hundreds times more than that of the star at quiet state. These stars are called flare stars and no stellar inner structure model had predicted such a phenomenon. For this reason for some time these stars were considered as “crazies” of the stellar family that do not obey the general regularities. However, their observational study and statistical investigation showed that the flare activity was a regular phase in the evolutionary path of low-mass and low-luminosity stars. It was proved that **all the stars of the mentioned category inevitably possess flare activity in the early phases of their evolution.** Later on (1978), on the basis of the chronology of discovery (first flares) and confirmation (second flares) of the flare stars, Ambartsumian by a solution of an inverse problem derived the **distribution function of average frequencies of flares in the given stellar system.**

2.1.7. Active Galactic Nuclei (AGN)

The **hypothesis on the activity of galactic nuclei** was proclaimed (1956). Previously it was believed that the nuclei of galaxies were their oldest parts that did not have any participation in the evolution of galaxies. Even there was an opinion that the nucleus was the “grave” of the dead matter. However, the observational facts showed evidence that there were ejection and outflow of matter from the nuclei of galaxies, including some cases when these processes were connected with expenditure of a rather large amount of energy. Moreover, the amount of the ejected matter sometimes can be enough to form a new smaller mass galaxy. This and other similar facts served as a basis for a formation of an unprecedented idea on the activity of galactic nuclei. The various forms of activity have been presented as different manifestations of the same phenomenon of activity. **The evolutionary significance of the activity in the galactic nuclei** was emphasized and further hypothesis was declared on the ejection of new galaxies from the active galactic nuclei.

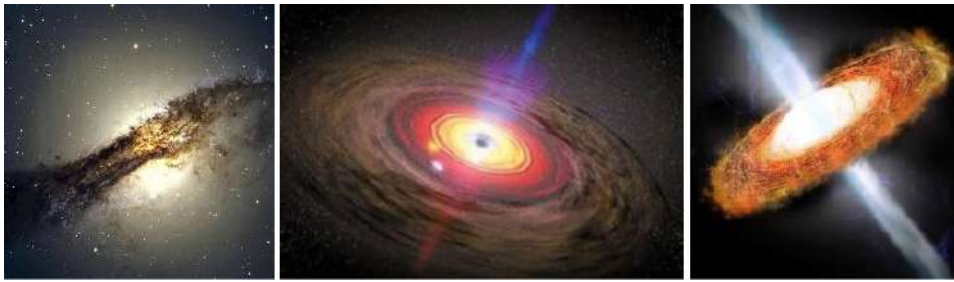


Figure 11

Since the beginning of 1950s, Ambartsumian carefully analyzed all accumulated data on emission-line galaxies, radio galaxies, blue components around giant galaxies, Haro's blue galaxies, etc. and came to a conclusion that all these different manifestations (various forms of activity) related to the same physical phenomenon, namely activity of the galactic nuclei. It was not straightforward and obvious, as the data were very few and each seemed to have independent explanation. Moreover, blue-UV emission of some nearby galaxies obviously came from their spiral arms and was explained by a large number of hot stars. Thus, a hypothesis on the activity of galactic nuclei was proclaimed by Ambartsumian (1955; 1956). The evolutionary significance of the activity in the galactic nuclei was emphasized and a further hypothesis was suggested on the ejection of new galaxies from the active galactic nuclei. The hypothesis on the superdense protostellar matter was engaged to explain the observational data. According to Ambartsumian, forms of activity could be rather different: emission of gas from the central part of the galaxy having velocities up to several hundreds of

km/sec, emission of fluxes of relativistic particles originating high-energy particles (forming radio halos around the nuclei), eruptive outbursts of gas matter, eruptive outbursts of relativistic plasma, outbursts of blue concentrations having absolute luminosity typical of dwarf galaxies, etc. A comparative analysis of all these observational data shows that independent on their apparent differences, all these phenomena have a common physical nature. Ambartsumian came to such conclusion at the very beginning of investigations, however, during many years (1960s-1980s), all types of revealed AGN were regarded as different kinds of objects, probably with different mechanisms of radiation. Moreover, all historical classifications (Seyfert 1 and 2, radio galaxy, QSO, LINER, BL Lac objects, etc.) supported an idea to explain them separately and then (if possible) try to find similarities or links between these classes.

The theoretical study of the numerous observational evidences of various sorts of physical instability in galaxies led Ambartsumian to a fundamental conclusion that in processes of origin and evolution of galaxies, the role of the central small in their sizes condensations, the nuclei of galaxies, is huge. He justified an essentially new understanding that all observational evidences of the instability of galaxies are a consequence of activity of the galactic nuclei. Further on he established that to various degrees of activity of nuclei of galaxies correspond various manifestations by the form and power in structure and radiation of galaxies.

In 1985, Antonucci and Miller published a paper "*Spectropolarimetry and the nature of NGC 1068*" (a classical Seyfert 2 type showing only narrow emission lines). The polarized flux plot revealed the presence of very highly polarized, very broad symmetric Balmer lines and also permitted Fe II closely resembling the flux spectra of Seyfert type I nuclei. This line emission indicated that both polarizations were due to scattering, probably by free electrons which must be cooler than a million K. A model was suggested in which the continuum source and broad line clouds were located inside a thick disk, with electrons above and below the disk scattering continuum and broad-line photons into the line of sight. All of the narrow lines, including the narrow Balmer lines, had similar low polarizations, unrelated to that of the continuum. Further studies strengthened such a geometrical understanding of the difference between the AGN, so that each type (the classification) depended on the observed angle.

Ambartsumian considered the existence of a supermassive dense matter in the center of stars and galaxies that was responsible for their activity and evolution. However, there in fact was no any developed model to describe this hypothesis, beside some attempts to build superdense stellar configurations. Observational evidences, particularly the huge amounts of energy emitted from the central parts of galaxies, insist on existence of a powerful source and until now this puzzle is not yet finally solved. There are in fact two opposite understanding on the phenomena of star formation, cos-

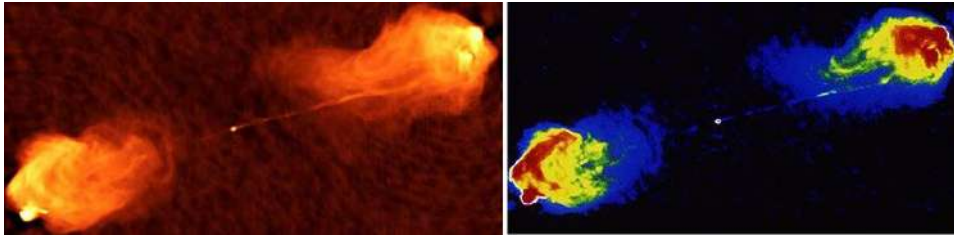


Figure 12

mogony in general, and activity of the galactic nuclei; classic approach and Ambartsumian (or Byurakan) one. It is important to anyway understand, how much these two “opposite” approaches contradict each other and how much they are related.

At present, the most popular explanation for the AGN powerhouse involves accretion of gas onto a Super-Massive, perhaps spinning Black Hole (SMBH). Different regimes of accretion have been invoked to constitute the basis of a unified picture of AGNs. The predictions of the theory are that rotationally supported thin disks would form at lower accretion rates ($M < M_{Edd}$), while supercritical ($M > M_{Edd}$) accretion flows are expected to form thick disks supported by radiation pressure. A very subcritical flow may not be able to cool and, instead of forming a thin disk, it puffs up giving rise to an ion torus supported by gas, rather than radiation, pressure. The formation of the torus is crucial to support the unified model of AGN. Further studies strengthened such an understanding of the AGN energy sources. However, there still are many difficulties and the discovery of new objects with new properties encounter challenges in their explanation in frame of the general scheme. Ambartsumian's theoretical consideration of observational data about the known forms of activity of the galactic nuclei gave serious bases to admit that activity of nuclei was caused not by stars and not by diffuse matter containing in them. They could not explain, at least, such observed forms of nuclear activity, which were connected with allocation of enormous amounts of energy and eruptions of unusually big masses of matter. Hence, it is necessary to consider that in corresponding nuclei there are bodies of at present unknown nature, which contain very big stocks of matter and have huge energy. In other words, it is necessary to consider, that in galactic nuclei physical conditions of matter are extremely unusual and strongly differ from the conditions observed in other parts of the Universe. In particular, in some bodies containing in nuclei of galaxies, the matter density should be extremely high. Only in this case the nuclei can provide the continuous outflow of matter or emissions and eruptions of the big masses from the nuclei, phenomena revealed by observations in some galaxies. These reasons also have formed a basis for working out of new important understanding that the galactic nuclei are sources of huge

amounts of matter and energy, which then give rise to formation around them galaxies or systems of galaxies and supply them with energy of the observed non-stationary motions. Ambartsumian showed that the results of studies of non-stationary systems of galaxies and various forms of display of nuclear activity of separate galaxies represent huge scientific interest not only for discovery of the laws of the origin of stars and stellar systems of various scales, but also for detection and research of while unknown states of matter, including the proto-stellar ones. And the results received by Ambartsumian in this area are in a full consent with understanding of the theory of stellar associations already mentioned earlier that matter development in the Galaxy has a certain orientation from denser states to less dense ones. One could believe that the search for such forms and states of matter in the central parts of galaxies led some astrophysicists to find the model of SMBH as such, though not completely explaining many aspects.

There are of course principle differences in the classical and Ambartsumian's approaches to the explanation of AGN energy sources. Ambartsumian believed that the source of energy was inner; it is emitted from the central engine and was directly connected to the nature of the central dense matter. The unified scheme and related accreting SMBH theory attributes the energy to the accretion on SMBH, which is in fact a physical process related to the environment of the central source. But there also are similarities between the classical and Ambartsumian's approaches. Ambartsumian's suggestion that there existed a supermassive dense body in the center of galaxies is now well accepted and SMBH could be one of the possible models of such matter. It is obvious that Ambartsumian's idea on the activity of galaxies based on the energy sources hidden in the central parts of galaxies (nuclei) is modified to fit known physical theories, which Ambartsumian himself didn't find unambiguous.

2.2. Theoretical Physics

In 1930 he published a paper with Dmitri Ivanenko where the **impossibility of the existence of free electrons in the atomic nuclei was proved**. After the formation of the first understanding on the atomic structure, the explanation of the contents of the atomic nucleus was considered as the most important problem. It was known that the nuclei were charged positively and the simplest explanation was that they consisted of protons. However, as the experiments showed, the nuclear mass was bigger than the summarizing mass of the protons corresponding to their charge. To overcome this controversy the author of the atomic structure Ernst Rutherford believed that the nuclei were formed of as many protons as was needed to reach the nuclear mass and the excessive charge was neutralized by the corresponding number of electrons located in the nucleus. Ambartsumian and Ivanenko showed that **only electrically uncharged elementary parti-**

cles of approximately proton mass could exist together with protons in the nuclei. Two years later the English physicist James Chadwick discovered the neutron. Ambartsumian and Ivanenko also put forward an idea that not only the quanta of the electromagnetic field, photons, but also other particles (including particles having nonzero rest mass) may be born and disappear as a result of their interaction with other particles (this idea lays in the basis of modern physics of the elementary particles and quantum field theory).



Figure 13: Viktor Ambartsumian, Dmitri Ivanenko and James Chadwick

2.3. Mathematics

For the first time **the problem of finding the form of the differential equation corresponding to the known family of eigenvalues was solved**. This problem is rather hard in its general statement. As an example, one can imagine such a problem. It is known that all atoms have discrete energy levels and spectral lines form due to transitions between them. A question arises; having the set of the spectral lines characterizing an atom, is it possible to find the equation with the line frequencies as its eigenvalues? The problem discussed by Ambartsumian belonged to the same family of problems but was incomparably simpler, though at that time also seemed unsolvable. It related to the frequencies of oscillations of a homogeneous string. It was shown that only the given string could have the given spectrum of frequencies. The paper devoted to the solution of this problem was published in the German Journal of Physics (*Zeitschrift für Physik*, 1929). It remained unnoticed for one and half dozen years. “*If an astronomer publishes a paper on a mathematical problem in a physical magazine, he is not to be wondered that nobody has noticed it*”, – was recalling he many years later. However, the paper was found, valued highly by mathematicians and **it initiated a wide direction in mathematics – inverse problems**.

3. Ambartsumian's most important scientific publications

Here we give the papers that contain Ambartsumian's most important scientific results listed above.

W.A. Ambarzumjan – Über eine Frage der Eigenwerttheorie (On a Problem of the Theory of Eigenvalues) // Zeitschrift für Physik, Vol. 53, Nos. 9-10, p. 690-695, 1929 (in German)

W.A. Ambarzumjan, D.D. Iwanenko – Eine quantentheoretische Bemerkung zur einheitlichen Feldtheorie (A Quantum-Theoretical Remark on the Uniform Field Theory) // Doklady USSR Acad. Sci., Ser. A, Vol. 3, p. 45-49, 1930 (in German)

W.A. Ambarzumjan, D.D. Iwanenko – Über eine Folgerung der Diracschen Theorie der Protonen und Elektronen (On a Consequence of the Dirac Theory of Protons and Electrons) // Doklady USSR Acad. Sci., Ser. A, Vol. 6, p. 153-155, 1930 (in German)

V.A. Ambartsumian, D.D. Iwanenko – Les électrons inobservables et les rayons (The Inobservable Electrons and Rays) // Comptes Rendus hebdomadaire des séances de l'Académie des sciences de Paris, Vol. 190, No. 9, p. 582-584, 1930 (in French)

V.A. Ambartsumian – The Radiative Equilibrium of a Planetary Nebula // Monthly Notices of the Royal Astronomical Society (MNRAS), Vol. 93, No. 1, p. 50-61, 1932 (in English)

V.A. Ambartsumian – On the Temperatures of the Nuclei of Planetary Nebulae // Pulkovo Observatory Circular, No. 4, p. 8-12, 1932 (in English)

W.A. Ambarzumjan, N.A. Kosyrew – Über die Massen der von den neuen Sternenausgestoßenen Gashüllen (On the Masses of Envelopes thrown out by Novae) // Zeitschrift für Astrophysik, Vol. 7, No. 4, p. 320-325, 1933 (in German)

V.A. Ambartsumian – On the Derivation of the Frequency Function of Space Velocities of the Stars from the Observed Radial Velocities // Monthly Notices of the Royal Astronomical Society (MNRAS), Vol. 96, No. 3, p. 172-179, 1936 (in English)

V.A. Ambartsumian, G.A. Shain – On the Faint White Stars in Low Galactic Latitudes // Soviet Astronomy, Vol. 13, No. 1, p. 1-7, 1936 (in English)

V.A. Ambartsumian – Double Stars and the Cosmogonic Time-Scale // Nature, Vol. 137, No. 3465, p. 537, 1936 (in English)

V.A. Ambartsumian – On the Statistics of Double Stars // Astron. Zh., Vol. 14, No. 3, p. 207-219, 1937 (in Russian)

V.A. Ambartsumian – On the Dynamics of Open Clusters // Trudy LGU; Uchenye Zapiski LGU, Ser. Math. Sciences (Astronomy). Issue 4, No. 22,

p. 19-22, 1938 (in Russian)

V.A. Ambartsumian, Sh.G. Gordeladze – Problem of Diffuse Nebulae and Cosmic Absorption // Bulletin of the Abastumani Astrophysical Observatory, No. 2, p. 37-68, 1938 (in English and Georgian)

V.A. Ambartsumian – The Scattering of Light in a Turbid Medium // Journal of Physics, Vol. 5, No. 1, p. 93, 1941 (in English)

V.A. Ambartsumian – A New Method of Calculation of the Light Scattering in Turbid Medium // Izvestiya Acad. Sci. USSR, Ser. Geograph. and Geophys. Sci., Vol. 3, p. 97-103, 1942 (in Russian)

V.A. Ambartsumian – To the Theory of Fluctuation in the Brightness of the Milky Way // Doklady USSR Acad. Sci., Vol. 44, No. 6, p. 244-247, 1944 (in Russian)

V.A. Ambartsumian – Evolution of Stars and Astrophysics // Acad. Sci. ArmSSR, 39 p., Yerevan, 1948 (in Armenian)

V.A. Ambartsumian – Preliminary Data on O-Associations in the Galaxy // Doklady USSR Acad. Sci., Vol. 68, No. 1, p. 21-22, 1949 (in Russian)

V.A. Ambartsumian – Stellar Associations // Astron. Zh., Vol. 26, No. 1, p. 3-9, 1949 (in Russian)

V.A. Ambartsumian, B.E. Markarian – Stellar Association around P Cygni // Communications of the Byurakan Observatory, No. 2, p. 3-17, 1949 (in Russian)

V.A. Ambartsumian – On the Frequency of the Orion Trapezium type Apparent Multiple Systems // Doklady Acad. Sci. ArmSSR, Vol. 13, No. 4, p. 97-103, 1951 (in Russian)

V.A. Ambartsumian – On the Statistics of Trapezium type Multiple Systems // Doklady Acad. Sci. ArmSSR, Vol. 13, No. 5, p. 129-131, 1951 (in Russian)

V.A. Ambartsumian – The Phenomenon of the Continuous Emission and Sources of Stellar Energy // Communications of Byurakan Observatory, No. 13, p. 1-36, 1954 (in Russian)

V.A. Ambartsumian – On the Nature of Radio Sources // Proc. Fifth conference on Problems of Cosmogony: “Radioastronomy”, held on 9-12 Mar 1955. Acad. Sci. USSR, p. 413-416, Moscow, 1956 (in Russian)

V.A. Ambartsumian – On Multiple Galaxies // Izvestiya Acad. Sci. ArmSSR, Ser. Phys.-Math., Nat. and Tech. Sci., Vol. 9, No. 1, p. 23-43, 1956 (in Russian)

V.A. Ambartsumian, G.S. Saakyan – The Degenerate Superdense Gas of Elementary Particles // Astron. Zh., Vol. 37, No. 2, p. 193-209, 1960 (in Russian) // English translation in: Soviet Astronomy, Vol. 4, No. 2, p. 187-201, 1960

V.A. Ambartsumian, G.S. Saakyan – On Equilibrium Configurations of Superdense Degenerate Gas Masses // Astron. Zh., Vol. 38, No. 5, p. 785-797, 1961 (in Russian) // English translation in: Soviet Astronomy, Vol. 5, No. 5, p. 601-610, 1962

V.A. Ambartsumian, G.S. Saakyan –Internal Structure of Hyperon Configurations of Stellar Masses // *Astron. Zh.*, Vol. 38, No. 6, p. 1016-1024, 1961 (in Russian) // English translation in: *Soviet Astronomy*, Vol. 5, No. 6, p. 779-784, 1962

V.A. Ambartsumian –On the Statistics of Flare Objects // Proc. symp. “Stars, Nebulae, Galaxies”, devoted to the 60th anniversary of academician V.A. Ambartsumian, held in Byurakan, 16-19 Sep 1968. *Acad. Sci. ArmSSR*, p. 283-292, Yerevan, 1969 (in Russian)

V.A. Ambartsumian –Derivation of the frequency function of stellar flares in a star cluster // *Astrofizika*, Vol. 14, No. 3, p. 367-381, 1978 (in Russian) // English translation in: *Astrophysics*, Vol. 14, No. 3, p. 209-217, 1978

4. Ambartsumian's legacy

In this paragraph we list those scientific items that relate to Viktor Ambartsumian's achievements and were named after him. They may serve as scientific commemoration of his legacy.

Ambartsumian's Hypothesis on the Activity of Galactic Nuclei.

In 1956, a hypothesis on the activity of galactic nuclei was proclaimed. The various forms of activity were presented as different manifestations of the same phenomenon of activity. The evolutionary significance of the activity in the galactic nuclei was emphasized and further hypothesis was suggested on the ejection of new galaxies from the active galactic nuclei. The hypothesis on the superdense protostellar matter was engaged to explain the observational data.

Ambartsumian (or Byurakan) School in Cosmogony. The hypotheses on superdense matter giving origin of stars and nebulae and on activity of galactic nuclei led to the establishment of a new approach in cosmogonic interpretation of the evolutionary processes in the Universe. The Ambartsumian (Byurakan) school in cosmogony appeared, describing the evolution of cosmic matter from more dense states to less dense ones. In contrary, the widely accepted classical school describes the evolution of cosmic matter from less dense states to more dense ones (origin of the stars from gas and dust).

Ambartsumian's Hypothesis on the Superdense Matter. In 1949, a theoretical prediction of the phenomenon of expansion of stellar associations was made. In 1951, Ambartsumian carried out a statistics of Trapezium Orionis type systems and proved the disintegration of young stellar systems. He showed the nonthermal nature of the continuous emission

observed in the spectra of non-stable stars and put forward an idea about new possible sources of stellar energy, the hypothesis of the superdense protostellar matter (1954). Theoretical studies of the hypothetical superdense degenerate protostellar matter led to the development of the principles of the theory of baryonic stars (1960-1961).

Ambartsumian Principle of Invariance. Development of light scattering theory in turbid medium, theory of Invariance. The principle of invariance was proposed for solving the radiative transfer problems. A very simple physical reasoning that the reflection properties of the semi-infinite plane-parallel medium do not change if a very thin layer of the same physical properties is added to its boundary gave an excellent base for creation of a new research method (1941-1942).

Ambartsumian's ϕ function. The main function defining the coefficient of reflection from semi-infinite medium by means of the principle of invariance. In the case of redistribution by frequencies it coincides with Chandrasekhar's H function.

Ambartsumian's Method for determination of the temperature of the Planetary Nebulae Nuclei. New method (modification of Zanstra's method) for determination of the planetary nebulae's central stars surface temperature giving the probabilistic definition of short-wave energetic photons transformation into less energetic ones. This definition led to the determination of the radiative equilibrium of planetary nebulae (1932).

V.A. Ambartsumian's Knot. The elliptical galaxy NGC 3561 has a jet outcoming from its central region and containing a very high luminosity condensation (this condensation is called Ambartsumian's Knot) comparable with the luminosity of such galaxies as for example the satellites of Andromeda nebula. There is no doubt that we encounter with a huge outflow from the nucleus. This outflow is actually a dwarf galaxy, which has been separated from the nucleus of the giant galaxy.

References

- Harutyunian, H. A.; Mickaelian, A. M.– Viktor Ambartsumian: Most Important Scientific Results // Yerevan, Edit Print, 2008, 20 p., 2011, 32 p. (in Armenian and English)
Mickaelian, A. M.(compiler) –Viktor Ambartsumian(DVD), Yerevan, 2008 and 2010 (in Armenian, Russian, and English)

Mickaelian, A. M.– Viktor Ambartsumian: Life and Activities, Yerevan, “Antares” Publishing House, 2014, 48 p. (in English)

Shahbazyan, K. V. (compiler) – Academician V. A. Ambartsumian. Life Episodes, Yerevan, NAS RA “Gitutyun” Publishing House, 2001, 168 p. (in Russian)

Shahbazyan, K. V. (compiler) – Academician V. A. Ambartsumian. Life Episodes, Yerevan, NAS RA “Gitutyun” Publishing House, 2003, 144 p. (in Armenian)

Toward Understanding the Origin of the B[e] phenomenon in FS CMa Type Objects

A. S. Miroshnichenko^{1,2,3*}

¹ *Department of Physics and Astronomy, University of North Carolina at Greensboro,
Greensboro, NC, USA*

² *Main (Pulkovo) Astronomical Observatory of the Russian Academy of Sciences,
Saint-Petersburg, Russia*

³ *Fesenkov Astrophysical Institute, Almaty, Kazakhstan*

**E-mail: a_mirosh@uncg.edu*

Abstract

Large amounts of circumstellar material accompany lives of most stars at different evolutionary stages. Formation mechanisms of these, often disk-like envelopes are not always clear. The B[e] phenomenon includes the presence of permitted and forbidden line emission and strong infrared (IR) excess in radiation observed from stars of the B and early-A types. It is found in several groups of mostly binary systems. The recently defined FS CMa group is thought to have their gas-and-dust disks due to an earlier strong mass-transfer between the binary system components. FS CMa objects seem to possess long-living disks, whose properties have not been studied well. I will be reviewing the group properties and results of a long-term monitoring program of some of its members with a focus on detected variations of the brightness and spectrum.

Keywords: *emission-line stars — circumstellar matter — stellar evolution — binary systems*

1. Introduction

Many stars and stellar systems go through evolutionary stages associated with strong mass loss or transfer that lead to formation of gaseous and/or dusty circumstellar envelopes/disks. The circumstellar material comes from protostellar clouds at early stages of star formation and from stellar wind at later stages in single stars as well as from mass transfer in systems with several components. As a result, the star or the entire stellar system gets partially or fully veiled and such features, as emission lines and continuum distortion are introduced. However, formation mechanisms of these, often disk-like envelopes are not always clear.

Although many phenomena concerning circumstellar matter have been successfully explained by the theory of stellar evolution, some remain puzzling even with the currently available wealth of data and sophisticated modeling methods. One of them is the B[e] phenomenon that refers to the presence of permitted and forbidden emission lines in the spectra of B-type and early A-type stars (effective temperatures, $T_{\text{eff}} = 8000\text{--}30000$ K) and strong IR excess radiation due to the presence of circumstellar dust. It is found in several groups of mostly binary systems, but was originally discovered at the dawn of IR astronomy by Allen & Swings (1976).

The presence of forbidden lines gave the name to the B[e] phenomenon (Conti 1976), although did not mention the IR excess which is also a defining factor of the phenomenon. Lamers et al. (1998) recognized 4 subgroups of B[e] objects with known evolutionary status: pre-main-sequence Herbig Ae/Be stars, symbiotic binaries (a cool giant and a white dwarf or a neutron star), compact Planetary Nebulae, and a small sample of supergiants. They confirmed the conclusion by Allen & Swings (1976) that the B[e] phenomenon is found in objects at very different evolutionary stages but with similar conditions in their circumstellar environments. However, Lamers et al. (1998) were unable to assign about half of the originally selected 65 Galactic B[e] objects to any stellar group with known evolutionary status and suggested to call them “unclassified”.

Studies of objects with the B[e] phenomenon have already made substantial contributions to the picture of stellar evolution. In particular, they led to the observational discovery of circumstellar disks around pre-main-sequence intermediate-mass Herbig Ae/Be stars (Mannings & Sargent 1997) and later to a new theoretical approach to the dusty disk modeling and planet formation (e.g., Meijer et al. 2008). Also, investigation of the Luminous Blue Variable binary η Carinae has changed our view of the post-main-sequence evolution of massive stars so much that a special Hubble Space Telescope Treasury Project was devoted to it (Davidson et al. 2003). The circumstellar matter formation and evolution mechanisms are still the least understood in the “unclassified” B[e] objects that led to defining the FS CMa group (Miroshnichenko 2007).

2. Properties of the FS CMa group

Galactic FS CMa objects named after the prototype B[e] star (Swings 2006) and defined by Miroshnichenko (2007) are characterized by a star of spectral types from early B to early A with a nearly main-sequence luminosity surrounded by large amounts of circumstellar gas, which powers low excitation forbidden lines and strong permitted lines, and circumstellar dust, which produces a strong IR excess. The main properties of FS CMa

objects include the following. 1) A very strong line emission (Fig. 1, left panel) accompanied by free-free and free-bound radiation, which may produce a strong veiling of the stellar spectra. The circumstellar contribution to the optical brightness can be up to ± 1 mag, depending on the system geometry and the tilt to the line of sight (e.g., Miroshnichenko et al. 2005). 2) A steep decrease of the IR flux at $\lambda \geq 10 \mu\text{m}$ with a typical slope of $d \log \lambda F_\lambda / d \log \lambda \leq -1.0$ that implies a compact spatial distribution of the dust, as hot stars emit enough high-energy photons to warm it even at a large distance and provide a strong far-IR flux. 3) Location not far from the main-sequence but over a wide luminosity range ($2.0 \leq \log L/L_\odot \leq 4.5$, Fig. 1, right panel) mostly determined spectroscopically. Even with the mentioned circumstellar veiling, the FS CMa objects are much less luminous than B[e] supergiants which have an average $\log L/L_\odot = 5.1$ (Miroshnichenko 2007).

The FS CMa group currently consists of 23 out of 30 original “unclassified” objects (Allen & Swings 1976) and ~ 70 others found recently (Miroshnichenko et al. 2007, 2011, 2017a), and the number of the group objects keeps growing. The nature of some “unclassified” objects has been recognized (e.g., MWC 137 was found to be a supergiant, Kraus et al. 2017; MWC 922 was classified as a planetary nebula, Zasowski et al. 2015), but a few of them still remain poorly studied (e.g., MWC 819). In addition to the above mentioned defining features, we detected the presence of absorption lines of neutral metals, which typically include the Li I 6708 Å line, in the spectra of 15 group objects (Miroshnichenko & Zharikov 2015). These lines are due to cool stellar components, and their strengths suggest these components are fainter ($\Delta V \geq 2$ mag) than the hot ones (except MWC 623, Zickgraf 2001). Orbital periods have been constrained only for several group objects. A dozen other objects show radial velocity variations possibly due to orbital motion or were detected by spectro-astrometry (Baines et al. 2006) and interferometry (Millour et al. 2009). Two FS CMa objects are known to have compact secondary components: CI Cam (a white dwarf or a neutron star, Robinson et al. 2002) and AS 386 (probably a black hole, Khokhlov et al. 2018).

3. Recent results for the FS CMa group members

Typically the brightest members of most stellar groups receive more attention, but it does not mean they are better understood. The brightest members of the FS CMa group are HD 50138 ($V \sim 6.6$ mag), FS CMa ($V \sim 6.9 - 8.8$ mag, currently ~ 7.5 mag), and HD 85567 ($V \sim 8.6$ mag). Although secondary components were detected in these three objects with the spectroastrometry technique (Baines et al. 2006), no other strong evidence for binarity has not been found for them (e.g., Khokhlov et al. 2017). This might be due to a low mass of the secondary component compared to

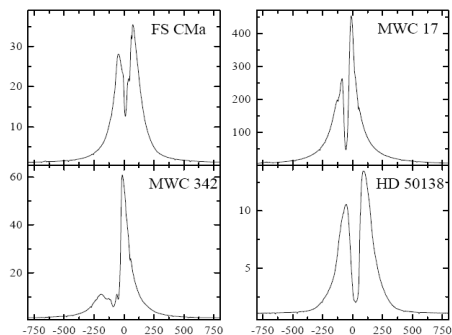


Figure 1: Left panel: Examples of $H\alpha$ profiles in FS CMa objects, whose equivalent widths reach $\sim 1500 \text{ \AA}$. Intensities are continuum normalized and radial velocities are shown in km s^{-1} . **Right panel:** Hertzsprung-Russell diagram for FS CMa objects. Solid lines: the zero-age main-sequence (ZAMS) and evolutionary tracks for single rotating stars (Ekström et al. 2012) with initial masses indicated.

that of the primary, a large orbital eccentricity along with a poor periastron epochs coverage, focus of the previous studies on mostly emission lines, a possibility of merging the secondary components, etc.

Nevertheless, we have recently managed to find orbital periods in two moderately bright FS CMa objects, MWC 728 (period 27.5 days, $V \sim 9.8$ mag, Miroshnichenko et al. 2015) and AS 386 (period 131.3 days, $V \sim 10.9$ mag, Khokhlov et al. 2018). The former object shows absorption lines of a cool star in the optical spectrum (see Fig. 3). We have measured radial velocity variations of this component but not those of the primary, B-type star. The pair can be resolved with interferometry, as the components' separation is supposed to be 20–30 mas at a distance of 1 kpc suggested by us. At the same time, the recent GAIA measurement of the parallax of MWC 728 (4.3 ± 1.0 mas, GAIA Collaboration 2018) implies a closer distance which in turn implies a lower than the main-sequence luminosity for the primary component (see Fig. 2). The distance controversy may be reconciled by interferometry, but the GAIA parallax may also be erroneous because of not taking into account the secondary component.

The second object with the measured orbital period is AS 386. It shows spectral features of a lowest-luminosity supergiant (luminosity type Ib), which also contains an unusual number of absorption lines of such species as Ne I, Si II, Al II. Along with non-detection of traces of the secondary component, the latter may be a sign of mass transfer from a more evolved and more massive component. The system mass function, $f(m) = 1.9 \pm 0.3 M_{\odot}$, along with the B-type component mass ($7 \pm 1 M_{\odot}$) leads to a mass of $\geq 7 M_{\odot}$ for the secondary component irrespective of the orbital inclination angle. No regular brightness variations have been detected in the optical

range, but only a chaotic variability with an amplitude of $\Delta V \sim 0.15$ mag. Although we have found regular variations of the object’s IR brightness with the orbital period, but it was explained by a variable illumination of the inner dusty rim by the B–type component. These results led us to a suggestion that the system contains a black hole as the undetected component. The latter does not reveal itself because of a lack of circumstellar matter in its immediate vicinity. The emission-line spectrum of AS 386 is weak, and an active mass-transfer process is not expected to be present. The GAIA parallax (0.19 ± 0.02 mas) for this system is also inconsistent with our data probably due to the same problem as for MWC 728.

Other recent results from our program include confirmation of the orbital period of the A2/3 Ib[e] object 3 Pup (in prep. for publication), a detection of very small radial velocity variations in HD 85567 (Khokhlov et al. 2017), and revealing a long-term cycle in variations of the emission-line spectrum of HD 50138. We are currently closely monitoring several other objects, whose stellar and circumstellar properties have only been vaguely constrained in the past to increase our collection of well-studied objects and tune up the observing strategy for the rest of the sample.

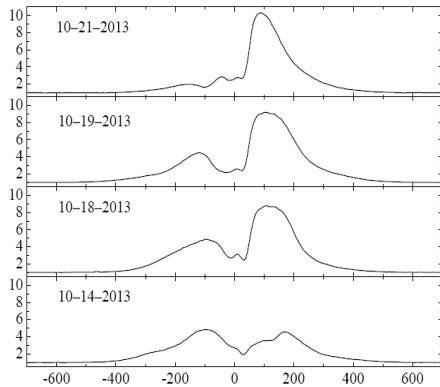


Figure 2: Left panel: $H\alpha$ line variations in the spectrum of the FS CMa object MWC 728 during a week–long period (Miroshnichenko et al. 2015). The intensity and velocity are in the same units as in Fig. 1. **Right panel:** Evolutionary tracks of $5 M_{\odot}$ (solid line) and $2 M_{\odot}$ (dotted line) components of a close binary system with non-conservative mass loss (van Rensbergen et al. 2008). The onset of mass transfer is marked with an open circle on the track of the $5 M_{\odot}$ star, while the $2 M_{\odot}$ star is still near the starting point of its evolution. The tracks are shown until the end of the mass transfer stage. The dashed lines show the zero-age and terminal-age main sequence for rotating single star models (Ekström et al. 2012). The filled circles show the fundamental parameters of the MWC 728 binary components (Miroshnichenko et al. 2015).

4. Evolutionary scenarios for explaining the group properties

We have put some constraints on the evolutionary status of the FS CMa objects. There are only two classes of hot stars surrounded by circumstellar dust in their region of the Hertzsprung-Russell diagram: pre-main-sequence Herbig Ae/Be stars and post-AGB Proto-Planetary nebulae. Pre-main-sequence stars possess larger dusty disks/envelopes, exhibit stronger far-IR excesses, and retain them longer than near-IR ones (e.g., Miroshnichenko et al. 1996a) due to dust photoevaporation (e.g., Gorti & Hollenbach 2009). In contrast, FS CMa objects are not found in star-forming regions and show much weaker far-IR excesses. Post-AGB stars with initial masses of $\geq 5 M_{\odot}$ are thought to evolve so fast that spectral changes due to increasing T_{eff} can be detected within a decade (Blöcker 1995, Miller Bertolami 2016), and their IR fluxes typically peak at $\lambda \geq 30 \mu\text{m}$. Low-mass ($\sim 1 M_{\odot}$) post-AGB stars evolve very slowly and exhibit very weak emission-line spectra. Neither of these properties of post-AGB stars is observed in FS CMa objects (Miroshnichenko 2007). Nevertheless, a thorough comparison of properties of known binary post-AGB objects (Van Winckel 2018) needs to be done to rule out a possibility that the lowest mass FS CMa objects are not currently undergoing this final stage of evolution.

The above results strongly suggest that FS CMa objects are binary systems that have undergone a phase of a strong and non-conservative mass transfer. This hypothesis is supported by our early modeling results that mass loss rates of $\dot{M} \sim 10^{-6} - 10^{-7} M_{\odot} \text{yr}^{-1}$ are required to explain the Balmer line strengths in most FS CMa objects (Miroshnichenko 2008, Carciofi, Miroshnichenko, & Bjorkman 2010). Such high rates are predicted only for single supergiants with $L \geq 10^5 L_{\odot}$ (Vink et al. 2001), while for single main-sequence early B-type stars they do not exceed $\sim 10^{-9} M_{\odot} \text{yr}^{-1}$ (Krtićka 2014).

We found that neither component of the detected binary systems currently fills its Roche lobes, at least no signs of strong mass transfer have been detected in the spectral line profiles. The circumstellar disks were probably created during the mass transfer phase from the formerly more massive and currently cool or compact component. The observed line profile variations (Fig. 2, left panel) can be qualitatively explained by interaction of the disk material with the wind of the hot component that could result in creation of unusual density distributions.

Matter may also accumulate in the circumbinary area, where its density may be sufficient for dust formation. Theoretical studies of intermediate-mass binaries (e.g., Van Rensbergen et al. 2008) predict periods of strong mass transfer (up to $\sim 10^{-3} M_{\odot} \text{yr}^{-1}$ due to a Roche lobe overflow), when

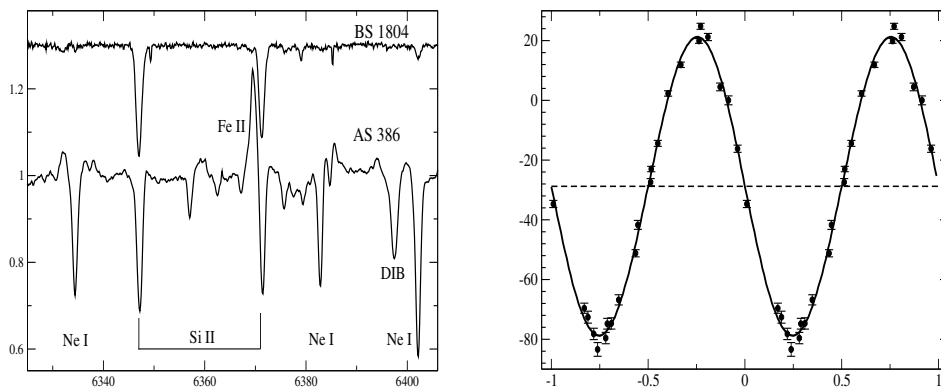


Figure 3: Left panel: Comparison of the spectrum of AS 386 with that of BS 1804 (B9 Ib). The spectra are continuum normalized and shifted with respect to each other along the vertical axis, and the wavelength scale is heliocentric and shown in Angströms. The spectrum of BS 1804 was taken at the 2.1 m telescope of the Observatorio Astronomico Nacional San Pedro Martir (OAN SPM). The shown spectrum of AS 386 is an average from several spectra that were shifted to the same (zero) heliocentric radial velocity. **Right panel:** A radial velocity curve derived from the spectra of AS 386 and folded with the orbital period. The dashed line shows the systemic radial velocity, the solid line represents the best fit to the data. The velocity is shown in km s^{-1} along the Y-axis, and the orbital phase is shown along the X-axis.

the gainer cannot accept all the mass. If this scenario is indeed working in FS CMa type objects, then there is an unaccounted channel for dust production in galaxies. Such objects have not been ever considered as dust producers (e.g., Gehrz 1989).

5. Conclusions and future work

We have defined the FS CMa group of objects with the B[e] phenomenon which most likely different from other four groups showing this phenomenon, found ~ 70 new members and candidates, revealed 15 binary systems among the group members, suggested a hypothesis for the group nature and evolutionary status, published studies of 11 group members (e.g., Miroshnichenko et al. 2000, 2002, 2003, 2015, Khokhlov et al. 2017, 2018) and intermediate results of our observing program in the proceedings of the third international conference on studies of objects with the B[e] phenomenon held in 2016 in Prague (Miroshnichenko et al. 2017b), obtained a large collection of observational data, and prepared a set of tools to prove our hypothesis. This hypothesis suggests that the group represents an evolutionary stage of close,

mostly intermediate-mass binary systems which have undergone a phase of a strong, non-conservative mass transfer. Part of the mass transferred from the originally more massive star was captured by the originally less massive one, but a noticeable part of this mass settled down in the circumprimary and circumbinary region. This process has most likely spun up the star which accepted the mass and is currently the hot one. The donor star is currently either a cool giant or a stellar remnant, such as a neutron star or a black hole. Evidence for the latter case is currently emerging. It is already clear that the FS CMa group is a new source of interstellar dust. A number of FS CMa objects with cool secondary components show the presence of neutral lithium, a feature that is rare and still awaiting explanation.

Since the beginning of the century, we have been collecting multicolor photometric and high-resolution (spectral resolving power $R = 12000 - 80000$) spectroscopic data for the group members and candidates. To date 50–250 spectra have been taken for the brightest group objects of FS CMa, HD 50138, MWC 342, MWC 728, MWC 623, IRAS17449+2320, and 3 Pup (which has always been classified a B[e] supergiant but may actually be closer to FS CMa objects by both mass and luminosity). Most spectra are being taken at the 2.1 m telescope of OAN SPM (Mexico), 3.6 m CFHT (Hawaii), and 0.81 m telescope of the Three College Observatory (North Carolina, USA). Various samples of the group members are also observed at the 9 m South African Large Telescope (SALT), 3.5 m telescope of the Apache Point Observatory (New Mexico, USA), the 2 m telescope of the Ondřejov Observatory (Czech Republic), 1.5 m telescope of CTIO (Chile), and 2 m Himalayan Chandra Telescope (India). Long-term data sets have also been obtained for such fainter group objects as AS 78, AS 116, AS 160, AS 174, MWC 657, MWC 1055, Hen 3–140, IRAS 07080+0605, IRAS 06341+0159, and a few more ($V = 10 - 12$ mag). The faintest objects ($V \geq 13$ mag) are being observed at a lower spectral resolution at several telescopes including the 2.6 m telescope of the Byurakan Astrophysical Observatory (Armenia), 2.1 m telescope of OAN SPM (Mexico), 1.82 m telescope of the Asiago Observatory (Italy), and the 1.5 m telescope of the Bologna Observatory (Italy).

Photometric observations in the optical spectral range are being taken at a 1 m telescope of the Tien-Shan Astronomical Observatory (near Almaty, Kazakhstan) and a set of robotic telescopes (e.g., PROMPT, Moran & Reichart 2005), while near-IR observations are being taken at 1 m telescope at Campo Imperatore (Italy) and 0.84 m telescope of OAN SPM. Since the objects are complicated, data modeling has only been done for a handful of them (e.g., Carciofi, Miroshnichenko, & Bjorkman 2010). With a better understanding of the group properties, which comes as a result of our observing program, the modeling process will become easier.

Acknowledgements

I am grateful to the conference organizing committee for inviting me to the place where my astronomy career has begun. I acknowledge support from the American Astronomical Society International Travel Grant that allowed me to come to the conference. This contribution would not be possible without collaborations with S.V. Zharikov, N. Manset, S. Danford, D. Korčáková, S.A. Khokhlov, S.N. Shore, C. Rossi, V.F. Polcaro, A.C. Carciofi, K.S. Bjorkman, J.E. Bjorkman, A.A. Arkharov, R. Mennickent, M. Cabezas, V.G. Klochkova, E.L. Chentsov, V.E. Panchuk, R.J. Rudy, D.E. Reichart, D.B. Caton, A.V. Kusakina, R.I. Kokumbaeva, I. Reva, M.A. Krugov, K.S. Kuratov, A.K. Kuratova, A.Zh. Naurzbayeva, N.Sh. Alimgazinova, A.B. Manapbayeva, H. Levato, M. Grosso, I. Usenko, A.V. Knyazev, N.A. Drake, K.N. Grankin, S.D. Chojnowski, and A. Raj.

References

- Allen, D.A.; Swings, J.-P. 1976, *A&A*, 47, 293
 Baines, D.; Oudmaijer, R.D.; Porter, J.M.; et al. 2006, *MNRAS*, 367, 737
 Blöcker, T. 1995, *A&A*, 299, 755
 Carciofi, A.C.; Miroshnichenko, A.S.; Bjorkman, J.E. 2010, *ApJ*, 721, 1079
 Conti, P. 1976, *Proc. IAU Symposium* 70, 447
 Davidson, K.; Ishibashi, K.; Gull, T.R.; et al. 2003, *American Astronomical Society Meeting* 203, 58.05
 Ekström, S.; Georgy, C.; Eggenberger, P.; et al. 2012, *A&A*, 537, A146
 GAIA Collaboration 2018, *A&A*, 616, A1
 Gehrz, R.D. 1989, *Proc. IAU Symp.* 135, 445
 Gorti, U.; Hollenbach, D. 2009, *ApJ*, 690, 1539
 Jeřábková, T., Korčáková, D., Miroshnichenko, A.S.; et al. 2016, *A&A*, 586, A116
 Khokhlov, S.A.; Miroshnichenko, A.S.; Mennickent, R.; et al. 2017, *ApJ*, 835, 53
 Khokhlov, S.A.; Miroshnichenko, A.S.; Zharikov, S.V.; et al. 2018, *ApJ*, 856, 158
 Kraus, M.; Liimets, T.; Cappa, C.E.; et al. 2017, *AJ*, 154, 186
 Krtićka, J. 2014, *A&A*, 564, A70
 Lamers, H.J.G.L.M.; Zickgraf, F.-J.; de Winter, D.; et al. 1998, *A&A*, 340, 117
 Mannings, V.; Sargent, A.I. 1997, *ApJ*, 490, 792
 Meijer, J.; Dominik, C.; de Koter, A.; et al. 2008, *A&A*, 492, 451
 Miller Bertolami, M.M. 2016, *A&A*, 588, A25
 Millour, F.; Chesneau, O.; Borges Fernandes, M.; et al. 2009, *A&A*, 507, 317
 Miroshnichenko, A.S. 2007, *ApJ*, 667, 497
 Miroshnichenko, A.S. 2008, *ASP Conf. Ser.*, 388, 205
 Miroshnichenko, A.S. 2017, *ASP Conf. Ser.*, 508, 285
 Miroshnichenko, A.S.; Bergner, Yu.K.; Kuratov, K.S.; et al. 1996, *Astron. Reports*, 40, 509
 Miroshnichenko, A.S.; Chentsov, E.L.; Klochkova, V.G.; et al. 2000, *A&AS*, 147, 5
 Miroshnichenko, A.S.; Bjorkman, K.S.; Klochkova, V.G. 2002, *A&A*, 390, 627
 Miroshnichenko, A.S.; Klochkova, V.G.; Bjorkman, K.S. 2003, *Astronomy Letters*, 29, 336
 Miroshnichenko, A.S.; Bjorkman, K.S.; Grosso, M.; et al. 2005, *MNRAS*, 364, 335
 Miroshnichenko, A.S.; Manset, N.; Kusakina, A.V.; et al. 2007, *ApJ*, 671, 828
 Miroshnichenko, A.S.; Manset, N.; Polcaro, V.F.; et al. 2011, *Proc. IAU Symp.* 272, 260
 Miroshnichenko, A.S.; Zharikov, S.V.; Danford, S.; et al. 2015, *ApJ*, 809, 129
 Miroshnichenko, A.S.; Zharikov, S.V. 2015, *EAS Publication Series*, v.71/72, 181
 Miroshnichenko, A.S.; Polcaro, V.-F.; Rossi, C.; et al. 2017a, *ASP Conf. Ser.*, 508, 387
 Miroshnichenko, A.S.; Korčáková, D., Zharikov, S.V.; Wolf, M. 2017b, *ASP Conf. Ser.*, 508
 Moran, J.A.; Reichart, D.E. 2005, *ApJ*, 632, 438
 Robinson, E.L.; Ivans, I.I.; Welsh, W.F. 2002, *ApJ*, 565, 1169
 Swings, J.-P. 2006, *ASP Conf. Ser.*, 355, 3
 van Rensbergen, W.; De Greve, J.P.; De Loore, C.; et al. 2008, *A&A*, 487, 1129
 Van Winckel, H. 2018, *arXiv:1809.00871*
 Vink, J.S.; de Koter, A.; Lamers, H.J.G.L.M. 2001, *A&A*, 369, 574
 Zasowski, G.; Chojnowski, S.D.; Whelan, D.G., et al. 2015, *ApJ*, 811, 119
 Zickgraf, F.-J. 2001, *A&A*, 375, 122

Blue straggler populations beyond the Milky Way

Richard de Grijs^{1,2*}, Weijia Sun^{3,4}, Chengyuan Li,¹ Licai Deng⁴

¹*Department of Physics and Astronomy, Macquarie University, Balaclava Road, Sydney, NSW 2109, Australia*

**E-mail: richard.de-grijs@mq.edu.au*

²*International Space Science Institute-Beijing, 1 Nanertiao, Zhonguancun, Hai Dian District, Beijing 100190, China*

³*Kavli Institute for Astronomy and Astrophysics, Peking University, Yi He Yuan Lu 5, Hai Dian District, Beijing 100871, China*

⁴*Key Laboratory for Optical Astronomy, National Astronomical Observatories, Chinese Academy of Sciences, 20A Datun Road, Chaoyang District, Beijing 100012, China*

Abstract

Although the formation of blue straggler stars (BSSs) is routinely attributed to stellar interactions in binary systems, the relative importance of the direct collision and slow(er) stellar coalescence formation channels is still poorly understood. We selected a sample of 24 Magellanic Cloud star clusters for which multi-passband *Hubble Space Telescope* images are available to address this outstanding question. We compiled a BSS database, containing both traditional and evolved BSSs. We found a robust correlation between the number of BSSs in a cluster's core and its core mass, $N_{\text{BSS,core}} \propto M_{\text{core}}^{0.51 \pm 0.07}$, which supports the notion that BSS formation is linked to a population's binary fraction. At low stellar collision rates, the mass-normalised number of BSSs does not appear to depend on the collision rate, which implies that the coalescence-driven BSS formation channel dominates. Comparison with simulations suggests that stellar collisions contribute less than 20% to the total number of BSSs formed.

Keywords: *blue stragglers — galaxies: star clusters - Hertzsprung-Russell and C-M diagrams - Magellanic Clouds.*

1. Blue straggler stars

Blue straggler stars (BSSs) are among the most visible deviations from the once generally accepted ‘simple stellar population’ model of star clus-

ters. In essence, this model assumes that star clusters were formed almost instantaneously from the same progenitor molecular cloud, so that the nascent stars have almost identical ages and the same chemical composition. Translated into colour–magnitude space, the Hertzsprung–Russell diagrams of single-aged, single-metallicity star clusters would exhibit narrow stellar evolutionary features, including a tight main sequence and a well-defined, sharp main-sequence turn-off, in turn leading to narrow subgiant and red giant branches. BSSs, which are predominantly found at brighter magnitudes and bluer colours than the main-sequence turn-offs of their host clusters, do not fit well into this picture.

First discovered by Sandage (1953) in the outer regions of the old Galactic globular cluster (GC) M3, many decades of research effort has led to the realisation that BSS formation is intimately linked to the evolution of stellar binary systems. In essence, the primary and secondary components of the binary system evolve into a single object with the combined mass of its progenitor components to gain a new lease of life as an apparently rejuvenated BSS. The current consensus is that BSSs can form in one of two ways, that is, through direct collisions between two stars and through a slower process leading to stellar coalescence. In the former scenario, when two low-mass stars collide, they will form a gravitationally bound system that is subject to rotation to satisfy the conservation of angular momentum. As both stars merge, they release some of the collision products in the form of debris, which eventually disperses.

The resulting object is a more massive, rapidly rotating star that appears blue because the stellar atmospheres of the progenitor stars have been stirred up violently, allowing core materials to float up to the surface layers. The merged collision product gradually heats up under the effects of gravitational contraction and it eventually expands to become a red giant-like star. Magnetic braking causes a reduction in the star’s rotation rate, allowing the star to shrink, heat up again, and eventually settle as a slowly rotating BSS. In the coalescence model, the resulting merger into a more massive star occurs on a much longer timescale. The merger product is a rapidly rotating BSS.

Observational evidence in apparent support of these two BSS formation channels was first provided by Ferraro et al. (2009), who showed that the colour–magnitude diagram of the core-collapse Galactic GC M30 exhibited two clearly separated ‘sequences’ of stars in the area of parameter space usually occupied by BSSs. The fainter, blue sequence appeared to be an extension of the cluster’s single-star main sequence to brighter magnitudes (that is, including younger ages but offset by $\Delta V \sim -0.4$ mag with respect to the younger extension of the isochrone describing the GC’s bulk stellar population), while the bottom envelope of the brighter, red swarm of data points coincided with the locus of the equal-mass binary sequence if extended to higher masses than those defining the main-sequence turn-

off. The natural interpretation of these observations was that the blue BSS sequence had resulted from stellar collisions triggered by the cluster's core collapse, while the red main sequence and the stellar sample at brighter magnitudes may have formed through stellar coalescence (but see below). Note that this latter sample in Ferraro et al. (2009) observations did not occupy a single, well-defined red sequence, presumably because a fraction of the coalescence products had already undergone further evolution, and thus they would have started to move away from their birth environment in colour–magnitude space. Alternatively, some of those objects could simply be unresolved interacting binary systems involving non-main-sequence components that have yet to merge.

Further evidence provided by Ferraro et al. (2009) suggested that the collision products were mostly found in the GC's core environment, while the coalescence products occupied larger clustercentric radii. Similar results were reported by Li et al. (2013) for the Large Magellanic Cloud (LMC) GC Hodge 11, although their results were less clear-cut. At the larger distance of the LMC, of order 50 kpc, the effects of (back- or foreground) field contamination and stellar crowding could significantly affect the quality and reliability of photometric observations of dense star clusters in their outer and core regions, respectively.

2. Star clusters in the Magellanic Clouds

Nevertheless, the Magellanic Clouds are better environments to study the evolution of dense, massive star clusters than the Milk Way, for a number of important reasons: (i) star clusters in the Magellanic Clouds cover a large range in ages (by contrast, Milky Way GCs are almost uniformly older than 10 Gyr); (ii) given their far southern location in the sky, the Clouds are located far from the Galactic plane, and hence they are negligibly affected by foreground extinction (although a relatively small level of internal extinction still needs to be dealt with); and (iii) the set of massive star clusters in the Magellanic Clouds are less dense than their Galactic GC counterparts, thus counteracting the distance effects (i.e., stellar crowding) to some extent.

Despite these clear advantages of exploring the physical properties of Magellanic Cloud clusters, their large distances still require us to avail ourselves of high-resolution imaging observations with the *Hubble Space Telescope* (*HST*), particularly using the Advanced Camera for Surveys (ACS)/Wide-Field Channel (WFC) or the Ultraviolet–Visible (UVIS) channel/Wide-Field Camera-3 (WFC3), to resolve the bulk of their stellar populations. The resolution of ~ 80 milli-arcsec at optical wavelength attainable with these instruments translates to ~ 0.02 pc at the distance of the LMC. For our analysis we selected all intermediate-age (1–3 Gyr-old) and old (~ 10 Gyr-old) clusters in the Magellanic Clouds for which suitable *HST* observations

were available. Young massive clusters were excluded, because the latter do not exhibit clear main-sequence turn-offs, which thus complicates the selection of BSSs. Application of these considerations resulted in a sample of 24 massive clusters (for details, see Sun et al. 2018).

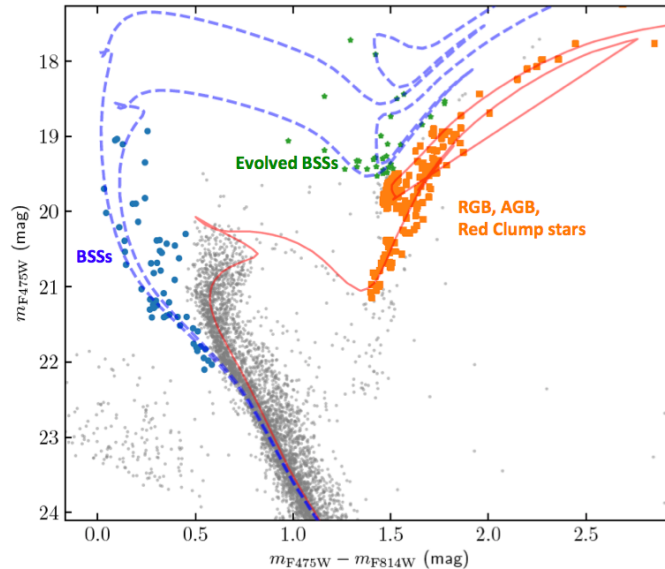


Figure 1: Colour–magnitude diagram of the LMC star cluster NGC 2173. BSSs, evolved BSSs, as well as red giant branch (RGB)/asymptotic giant branch (AGB)/red clump stars are marked with blue circles, green pentagons, and orange squares, respectively. The best-fitting PARSEC isochrones (Bressan et al. 2012) for the bulk stellar population (red solid line) and the BSS population (blue dashed line) are also shown. (Adapted from Sun et al. 2018.)

In a series of recent articles (Li et al. 2018; Sun et al. 2018), we realised that while the best-fitting isochrones representing the bulk stellar populations in our sample of Magellanic Cloud star clusters also matched the ridgelines of their red giant branches very well, many clusters exhibited significant numbers of stars blueward of the blue envelopes defined by the red giant branch ridgelines and well beyond the prevailing 3σ observational uncertainties. In fact, isochrone fits to the cluster’s BSS sequences appeared to adequately match those bluer red giant branch-like stars, which led us to suggest that the latter objects might be evolved BSSs: see Fig. 1. We carefully validated this idea on the basis of Monte Carlo simulations including the prevailing uncertainties, the number distributions, as well as their spatial distributions (Li et al. 2018; Sun et al. 2018). Henceforth, in relation to each of our sample clusters, we will therefore refer to (i) our core BSS sample and (ii) our evolved BSS sample. BSSs are found in all of our clusters, with BSS numbers in their cores ranging from five to 70. Evolved

BSSs can be resolved in the intermediate-age clusters using optical filters, but they cannot be disentangled easily from the red clump in old clusters.

Following Knigge et al. (2009) and Leigh et al. (2013), we explored whether our Magellanic Cloud BSS numbers, N_{BSS} , also correlated with the core mass, M_{core} , of their host clusters. Knigge et al. (2009) and Leigh et al. (2013) reported a relationship of the form

$$N_{\text{BSS,core}} \propto M_{\text{core}}^{\alpha}; \alpha \sim 0.5 \quad (1)$$

for samples of 57 and 30 additional Galactic GCs, respectively. Our 24 LMC clusters, on the other hand, yielded a significantly steeper proportionality,

$$N_{\text{BSS,core}} \propto M_{\text{core}}^{\alpha_c}; \alpha_c = 0.66 \pm 0.07, \quad (2)$$

and a Spearman coefficient of $\rho_S = 0.84$ (Sun et al. 2018). If we include the ‘evolved BSSs,’ however, the power-law index of this latter proportionality becomes $\alpha_{c+e} = 0.51 \pm 0.07$ (and $\rho_S = 0.80$), which implies a robust correlation that is indeed very close to the previously published Galactic GC results.

Knigge et al. (2009) suggested that the ‘sublinear’ relation between the number of BSS stars in a cluster and its core mass could be explained as the result of binary interactions if the binary fraction, f_{bin} , also depends on the core mass (Milone et al. 2012),

$$f_{\text{bin}} \propto M_{\text{core}}^{-0.5}. \quad (3)$$

However, Leigh et al. (2013) found that including the numbers of binary stars in the cores of their sample of 30 additional Galactic GCs did not strengthen the correlation, either because of the empirical uncertainties affecting the derived binary fractions or owing to the correlation’s intrinsic dispersion; the resulting degradation of the correlation further complicated efforts to understand the BSSs’ origins.

Therefore, we explored whether the numbers of BSSs, both in the cluster cores and including the evolved counterparts, might be correlated with the clusters’ representative (annual) stellar collision rates: see Fig. 2. We normalised both quantities by the clusters’ core masses to reduce any effects owing to a dependence of the collision rates on the core masses of our clusters. It is clear that in low collision-rate clusters, the collision rates do not depend on core mass. At high collision rates, on the other hand, BSS formation appears to be suppressed. We suspected that this could be evidence of the importance of binary-mediated BSS formation.

Figure 2 also includes the results of the numerical simulations performed by Chatterjee et al. (2013). The simulation results shown in, respectively, the left- and right-hand panels highlight BSSs formed through coalescence of binary systems and direct collisions, for different initial binary fractions. The

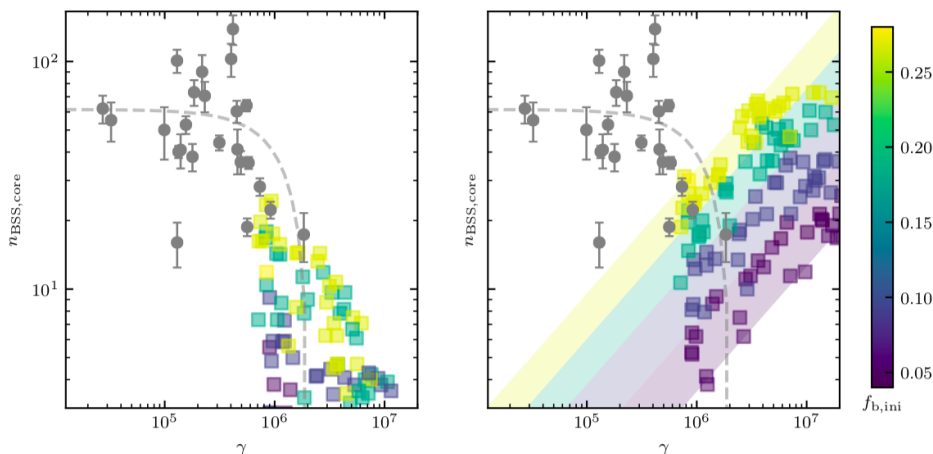


Figure 2: Mass-normalised number of BSSs in the core ($n_{\text{BSS,core}}$) as a function of the mass-normalised collision parameter, γ (single star collisions only). Magellanic Cloud clusters are shown as the grey data points. The grey dashed line represents the best-fitting model of the form $n = C + a\gamma^b$. The simulation of Chatterjee et al. (2013) is overplotted. BSSs formed through the binary and collision channels in the simulation are shown in, respectively, the left- and right-hand panels as coloured squares, for different initial binary fractions ($f_{\text{b,ini}}$). The shaded regions encompass the possible contributions from collisions in lower collision-rate environments. (Source: Sun et al. 2018.)

left-hand panel shows that the mass-normalised number of BSSs generated from primordial binaries in the Chatterjee et al. (2013) simulations declines toward higher collision rates, as observed in our Magellanic Cloud cluster sample, while the collision model predicts the opposite. This suggests that binary disruption may be at work. Extrapolating, we estimate that the share contributed by collisions in lower collision-rate environments is less than 20%, thus demonstrating a more significant contribution from binary coalescence.

Although our results for 24 Magellanic Cloud clusters appear very similar to those published previously for Galactic GCs, we emphasise that the Magellanic Cloud clusters represent a special environment for the study of BSS formation in star clusters. The underlying formation channels might be different in the Magellanic Clouds compared with the Milky Way. Indeed, the low stellar densities and low collision rates in the Magellanic Clouds provides a great opportunity to resolve the tension between observations and simulations in the interpretation of the observed correlation between BSS number and core mass in Galactic GCs.

Acknowledgements

RdG would like to thank the organisers of the conference ‘Instability Phenomena and Evolution of the Universe’ (September 2018), held in honour of Viktor Ambartsumian’s 110th birthday, for their invitation to deliver this talk as well as for their partial financial support. This work was supported by the National Key Research and Development Program of China through grant 2017YFA0402702 (RdG). We also acknowledge research support from the National Natural Science Foundation of China (grants U1631102, 11373010, and 11633005). CL is supported by the Macquarie Research Fellowship Scheme.

References

- Bressan, A., Marigo, P., Girardi, L., et al. 2012, *MNRAS*, 427, 12
Chatterjee, S., Rasio, F. A., Sills, A., & Glebbeek, E. 2013, *ApJ*, 777, 106
Ferraro, F. R., Beccari, G., Dalessandro, E., et al. 2009, *Nat.*, 462, 1028
Knigge, C., Leigh, N., & Sills, A. 2009, *Nat.*, 457, 288
Leigh, N., Knigge, C., Sills, A., et al. 2013, *MNRAS*, 428, 897
Li, C., de Grijs, R., & Deng, L. 2013, *MNRAS*, 436, 1497
Li, C., Deng, L., Bekki, K., et al. 2018, *AJ*, 156, 110
Milone, A. P., Piotto, G., Bedin, L. R., et al. 2012, *A&A*, 540, A1
Sandage, A. R. 1953, *AJ*, 58, 61
Sun, W., Li, C., de Grijs, R., & Deng, L. 2018, *ApJ*, 862, 133

Stellar kinematics in the IC 348 cluster

E.H. Nikoghosyan^{1*}, H.A. Harutyunian¹, N.M. Azatyan¹,
A.M. Grigoryan¹

¹NAS RA V. Ambartsumian Byurakan Astrophysical Observatory (BAO), Armenia

*E-mail: elena@bao.sci.am

Abstract

In 30 - 40s of the last century Viktor Ambartsumian has published several studies on the kinematics and dynamics of stellar systems. The scientific issues of these papers not only remain relevant up to nowadays, but also are of key importance for the construction of the generalized theory of star formation. The launch of the Gaia spacecraft on December 19, 2013, opens up new horizons in the study of young stellar systems origin and evolution. The accuracy of astrometric measurements (the typical uncertainty is about 0.04 - 0.7 mas for the positions and parallaxes, and about 0.05 - 1.2 $mas\ yr^{-1}$ for the proper motions), undoubtedly, will allow lifting the possibilities of study the kinematics and dynamics of star-forming regions to a new level. We focus our present research on the young ($\sim 2 - 3Myr$) stellar cluster IC 348. It has a complex structure, which includes the older compact core and the younger subgroup in the vicinity of HH 211 outflow. Based on the Gaia DR2 data, we considered the kinematic properties of both the cluster as a whole and its subgroups. We found that special velocity dispersion significantly exceeds the virial velocity dispersion and, therefore, the IC 348 stellar cluster is a supervirial or gravitationally unbound system.

1. Introduction

In 1936 academician Ambartsumyan published a work "*On the Deviation of the Frequency Function of Space velocities*" of the Stars from the Observed Radial Velocities, in which he provided an elegant mathematical solution to the problem posed earlier by Eddington (Eddington, 1915) of determining the distribution of the spatial velocities of stars from the distribution of their radial velocities, obtained for various regions of the sky. The equations, provided in Ambarzumian (1936) were of fundamental importance for study the kinematics and dynamics of stellar systems. Moreover, this work was the second one among Ambartsumian's series of papers on the solution of

the inverse problems. It had an essential significance also for another series of papers devoted to the problems of cosmogony and formed part of the discussions of the 1930s between advocates of the *long* (10^{13} years) and *short* (10^{10} years) scales for galactic evolution (Ambartsumyan 1937a, 1937b, 1938). The scientific arguments presented in these papers put the final point in the debate about the ages of our galaxy in favour to the *short* scale. Furthermore, because of their profundity, Ambartsumyans papers had more than a momentary significance and have had an influence on research in stellar kinematics and dynamics that is perceptible even now. In particular, the Eq. (1) in Ambarzumian (1936) made the possibility to determine the spatial velocities of stars for a given set of coordinates and radial velocities of these stars, but without invoking their proper motions.

$$f(V, \alpha)dV = n(\alpha) \int_{(S)} \phi(\xi, \eta)d\eta, \quad (1)$$

where $f(V, \alpha)dV$ is the number of the observed stars with azimuths between α and $\alpha + d\alpha$ and with radial velocities between V and $V + dV$. The graph, which is explaining the notation in the Eq. (1), is borrowed from Ambarzumian (1936) and represented on Fig. 1.

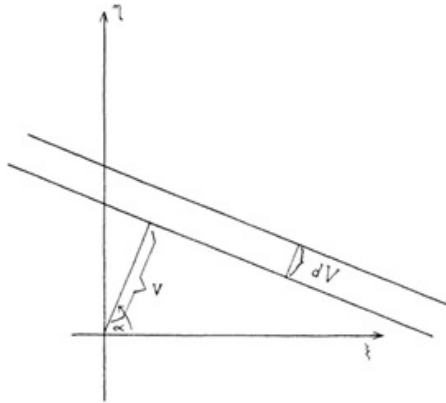


Figure 1. The graph explaining the notation in the Eq. (1).

Further, this mathematical solution was the subject of active research. (Ossipkov 2012 and ref. therein). It should be emphasized that the solution of Eq. (1) is of great importance not only for solving problems related to the kinematics of stellar systems, but also goes far beyond astronomy, in particular, computerized tomography (Cormack 1985). Looking back, it can be said that mentioned above Ambartsumian's several papers contributed significantly to the formation and development of such a fundamental direction of modern astrophysics as the study of kinematics and dynamics of stellar systems.

2. New era. Gaia satellite

The launch of Gaia satellite in 2013 opened a new era for a number of fields of modern astrophysical research. In particular, the phenomenal astrometric resolution, has opened up new possibilities for the study of stellar systems structure. Currently, Gaia Data Release 2 (Gaia DR2) contains results for 1693 million sources in the magnitude range 3 to 21. The median uncertainty in parallax are 0.04 mas for bright ($G < 14$ mag) sources, 0.1 mas at $G = 17$ mag, and 0.7 mas at $G = 20$ mag. The median uncertainties in proper motion are 0.05, 0.2, and 1.2 mas yr⁻¹, respectively (Lindegren et al. 2018). Observational data with such parameters provide great opportunities for more detailed studies of a number of issues.

Among these issues, it should be noted the identification of new stellar clusters and checking of the membership of already known, including brown dwarfs that is very important for construction the luminosity or mass function for stellar formation at different stages of evolution. Among the most interesting results obtained in this area can be mentioned the several papers. Beccari et al. (2018) using Gaia DR2 data on positions, proper motions, and parallax in Vela OB2 region six new clusters or associations have discovered. Analysis of the colour-magnitude diagram for these clusters shows that four of them formed coevally in the same molecular clouds 10 Myr ago, while NGC 2547 formed together with a newly discovered cluster 30 Myr ago. In the nearest (100 pc) 27 associations 898 new high-likelihood candidate members with spectral types from B9 to L2 were discovered (Gagné & Faherty 2018). Wilkinson et al (2018), using Gaia DR1 data, identified 167 member candidates of Upper Scorpius, of which 78 are new. The newly discovered stellar objects are distributed within a 10 arcmin radius from core of star-forming region. These member candidates have a mean distance of 145.6 ± 7.5 pc and a mean proper motion of $\text{pm(RA)} = -11.4 \pm 0.7$ mas yr⁻¹ and $\text{pm(Dec)} = -23.5 \pm 0.4$ mas yr⁻¹. These values are consistent with measured distances and proper motions of previously identified *bona fide* members of the Upper Scorpius association. Earlier, in the same star-forming region Cook et al. (2017) identified about 100 brown dwarfs with masses $M < 0.05M_{\odot}$. They showed that the mass function of stellar objects with $0.01 < M < 0.1M_{\odot}$ masses is consistent with the Kroupa Initial Mass Function and proposed that some proper motion outliers among the brown dwarfs have undergone a dynamical ejection early in their evolution.

The Gaia DR2 data provide great opportunities for studying the structural, as well as kinematic and dynamical properties of the stellar formation on a different evolutionary stages. For instance, the study of proper motions in Upper Scorpius association showed that the morphology of the association defined by brightest and faintest members are different (Galli et al 2018). The brightest (and most massive) stellar objects are distributed in a prolate ellipsoid with dimensions of $74 \times 38 \times 32$ pc³, while the faintest cluster

members define a more elongated structure with dimensions of $98 \times 24 \times 18 \text{ pc}^3$.

The examination of the proper motions of star in the several young stellar cluster showed that they are gravitationally unbound systems and have non-isotropic velocity dispersions that undoubtedly requires the revision of some of the main tenets of the general theory of star formation. Among these works, we note the following papers. On the basis of the value of the virial velocity dispersion σ_{vir} in Bravi et al. (2018) it was found that four open stellar clusters IC 2602, IC 2391, IC 4665, and NGC 2547 are supervirial. It was shown that three subgroups of Scorpius-Centaurus OB association are gravitationally unbound and have non-isotropic velocity dispersions (Wright Mamajek 2018). The authors find the evidence that the subgroups were not formed by the disruption of individual star clusters. They conclude that Sco-Cen was likely to have been born highly substructured, with multiple small-scale star formation events contributing to the overall OB association, and not as single, monolithic burst of clustered star formation. A dynamical analysis shows that the stellar surface population of L1688 has a velocity dispersion $\sigma \sim 1.14 \pm 0.35 \text{ km s}^{-1}$ that is consistent with being in virial equilibrium only with a $\sim 80\%$ probability (Rigliaco et al., 2016). The study the dynamical ages of the Young Local Associations showed that in these star-forming region there were two episodes of star formation: one $\sim 40 \text{ Myr}$ (Chamaeleontis, TW Hydrae, and β Pictoris) and another 5 – 15 Myr ago (Tucana-Horologium, Columba, and Carina) (Miret-Roig et al. 2018).

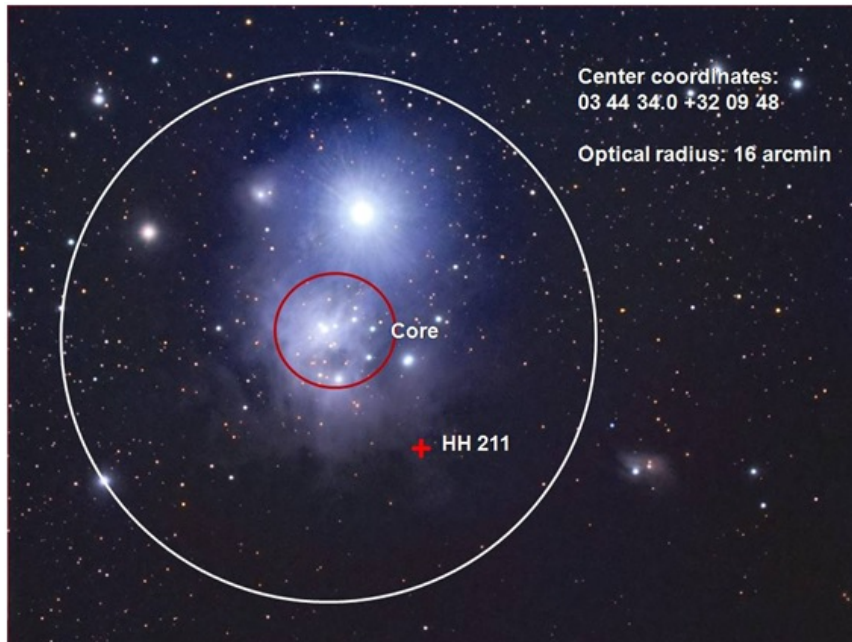


Figure 2. DSS2 R image of the IC 348 cluster and its structural features

3. Kinematics in the IC 348 cluster

3.1. IC 348 stellar cluster.

For our study we have chosen a relatively well-studied compact young star cluster IC 348 ($\sim 2 - 3$ Myr, Stelzer et al. 2012) which is associated with the Perseus molecular cloud complex and is located at distance ~ 300 pc from the Sun. The pioneering studies of Herbig (1954, 1988) discovered about 100 stars with H_α emission in this cluster. Later, the number of known H_α emitters was doubled (Luhman et al. 2003). In Nikoghosyan et al. (2015), it was shown that among the cluster members with $13.0 < R \text{ mag} < 19.0$ the percentage of emission stellar objects reaches 80%. IC 348 was also extensively studied in near- and mid-infrared wavelengths (Lada et al. 2006, Muench et al. 2007, Currie Kenyon 2009). Using measurements of infrared excess between 3.6 and 8.0 μm , Lada et al. (2006) find that the total frequency of disk bearing stars in the cluster is $\sim 50\%$ and only $\sim 30\%$ of the cluster members are surrounded by optically thick, primordial disks. IC 348 is also well studied in the X-ray regime. It was detected about 200 X-ray sources, which are associated with known cluster members (Preibisch Zinnecker 2002, Stelzer et al. 2012, and ref. herein). As it was concluded in Stelzer et al. (2012), the evolutionary stage of IC 348 cluster corresponds to the time where the structure of the disks of most young stellar objects changes from primordial, rather massive accretion disks to transitional and debris disks. Therefore, the cluster population represents the outcome of a recent star-formation event. However, on the southwestern direction on a distance about 1 pc molecular hydrogen jet HH 211 is located. The dynamical age of this jet is about 1000 yr, that suggesting that this is the region of a later wave of star formation. On the other hand, in the central region of the cluster more massive stellar objects with low H_α activity and a small infrared excess, i.e. the members of the cluster at a later stage of evolution, are concentrated. The age of these objects is about $7 \cdot 10^6$ years, which exceeds the average age of the cluster's members (Nikoghosyan et al. 2015). These objects form a core with surveys stellar density, which is almost 20 times higher than the average one in the cluster. Figure 2 shows an image of the IC 348 cluster and its structural features.

3.2. Cluster's membership

In previous works, according to the data of spectral and photometric observations, 377 star objects were identified as the members of the IC 348 cluster. The most complete list is given in Flaherty et al. (2013). The optical radius of the cluster is ~ 16 arcmin from the centre with coordinates RA (2000) $03^h 44^m 34.0^s$ and Dec (2000) $+32^\circ 09' 48''$ (Wu et al. 2006).

A histogram of parallaxes on the left panel, clearly defines a maximum in the range of 2.5 to 3.5 mas, which corresponds to the cluster distance.

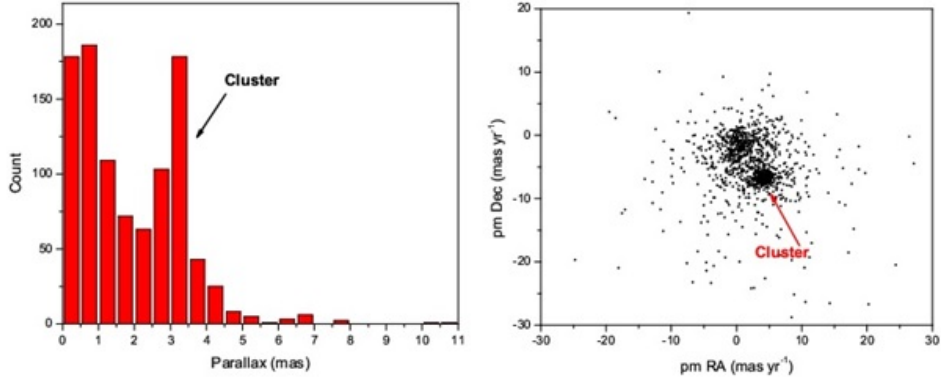


Figure 3. Distribution of the parallaxes (left panel) and proper motions (right panel) of the objects located in the region of the IC 348 cluster.

The distribution of proper motions also reflects the existence of a cluster. On right panel of Fig. 3 besides the concentration around zero values, which corresponds to the field objects, one more concentration of objects around the $\text{pm(RA)} \approx 4.5 \text{ mas yr}^{-1}$ and $\text{pm(Dec)} \approx -7 \text{ mas yr}^{-1}$ is clearly distinguished.

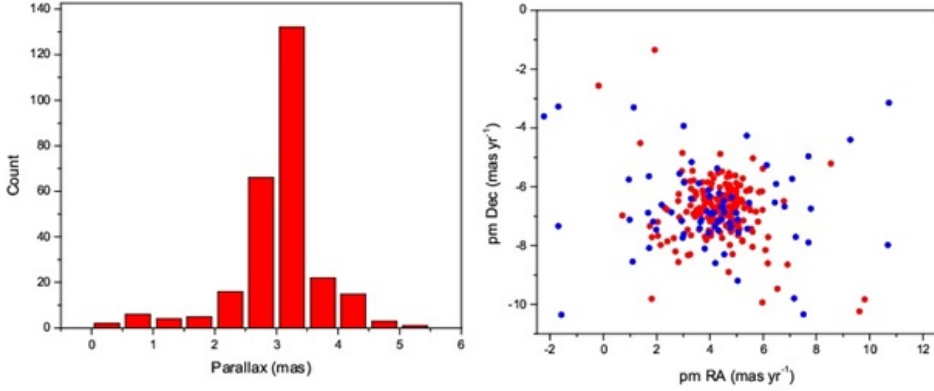


Figure 4. Distribution of the parallaxes (left panel) and proper motions (right panel) of the objects identified as cluster members. On the right panel the objects with parallaxes in the range from 2.5 to 3.5 mas are marked by red and other objects by blue.

In the Gaia DR2 database we were able to identify only 300 objects among the 377 members of the cluster. Among them the parallaxes and proper motions were determined only for 272 stellar objects. The distributions of these parameters are shown in Fig. 4. By the histogram on the left panel it is clearly seen that the parallaxes of a vast majority of objects,

namely 199, are in the range from 2.5 to 3.5 mas. If we assume that the cluster has a spherical shape, then at a radius of 16 arcmin and a distance of approximately 300 pc, within the errors (~ 0.37 mas), the parallaxes of the cluster's members should fall precisely into this range. The median value of the parallaxes of these 199 stellar objects is 3.069 ± 0.23 mas, which corresponds to a distance of 326 pc. This value of a distance is in good agreement with the results of previous studies. The parallaxes of the remaining 73 star objects, which were previously identified as members of the cluster, have a significant shift from the median value and do not fall within the range from 2.5 to 3.5 mas. The right panel of Fig. 4 shows the distribution of the proper motions of all cluster's members identified in the Gaia DR2 database. Notice that the stellar objects with parallaxes in the range from 2.5 to 3.5 mas are marked by red circles, the other stars are marked by blue ones. According to the graph, it is noticeable that in the first case, the values of the proper motions, especially in the direction of a right ascension, have a smaller variation relative to the average values, which are $\text{pm}(\text{RA}) = 4.31 \pm 1.26 \text{ mas yr}^{-1}$ and $\text{pm}(\text{Dec}) = -6.78 \pm 1.02 \text{ mas yr}^{-1}$. The standard deviations in this case are 1.23 and 1.03 mas for $\text{pm}(\text{RA})$ and $\text{pm}(\text{Dec})$, respectively. For other objects the standard deviations are higher: 3.21 and 1.66 mas for pm RA and pm Dec , respectively. Taking into account the fact that parallax is a reliable parameter for determining the distance, we used only 199 stellar objects with parallaxes in the range from 2.5 to 3.5 mas to study the kinematics of the cluster.

3.3. Stellar kinematics

To study the kinematics of the star population of the cluster, we transformed the proper motions into tangential velocities in the directions of right ascension and declination and determined their average values and standard deviations, which are equal to $3.07\text{E-}6 \pm 1.88 \text{ km s}^{-1}$ and $5.39\text{E-}6 \pm 1.51 \text{ km s}^{-1}$, respectively. The histograms of the distribution of these velocities are shown in Figure 5. The distribution has a wide spread, which is also indicated by the values of the standard deviation.

In Cottaar et al. (2015) it was determined that the value of the virial equilibrium velocity dispersion for IC 348 should be of $0.44 \pm 0.06 \text{ km s}^{-1}$. Moreover, the authors of this paper, on the basis of the values of the radial velocities of 157 cluster members, obtained the value of velocity dispersion ($0.72 \pm 0.07 \text{ km s}^{-1}$ or $0.64 \pm 0.08 \text{ km s}^{-1}$, if two Gaussians are fitted), which is almost $\sqrt{2}$ times more than the virial one and came to the conclusion that the cluster is in a superviral state. In our case, the dispersion value is significant greater, which also, suggests that in general the cluster is not in equilibrium state and gravitationally unbound. The authors of the mentioned above paper also did not found the evidence for a dependence of velocity dispersion on a distance from the cluster centre or stellar mass.

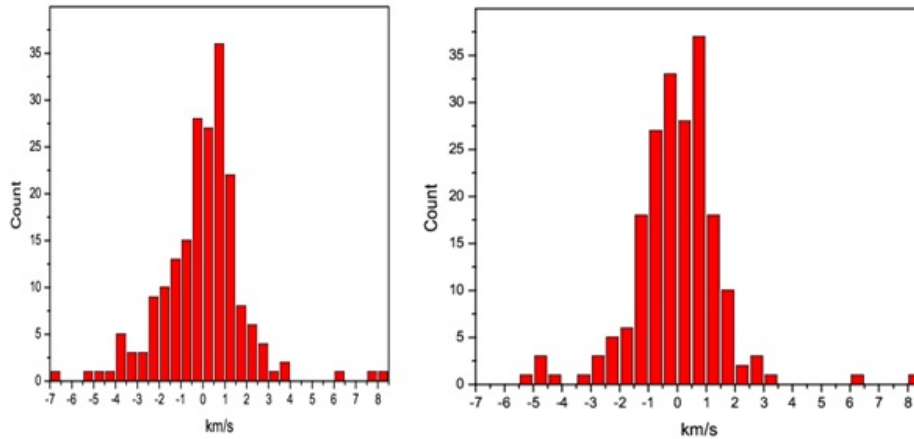


Figure 5. Distribution of the tangential velocities of the IC 348 cluster members in the direction of right ascension (left panel) and declination (right panel).

Moreover, they concluded that the stars in IC 348 are converging along the line of sight.

We also considered the averaged values of tangential velocities and standard deviations in different samples: in the quadrants and along the radius of the cluster. Fig. 6 shows the result obtained for quadrants. On this figure the red arrows represent the direction of motion of the stars in each quadrant. In general, we can say that modules of average velocities do not differ by quadrants. The direction of motion in both northern and south-eastern quadrants to some extent confirms the conclusion of Cottaar et al. (2015) that the stars in IC 348 are converging along the line of sight. The exception is the south-western quadrant, for which, in addition, the highest values of standard deviations for both directions are obtained. It should be recalled that the region of a later wave of star formation associated with HH 211 object is located in this quadrant.

The distribution of the averaged values of tangential velocities and standard deviations along cluster radius in the rings with a width of 2 arcmin is presented in Table 1. From these data, we can conclude that in the central region of the cluster, the dispersion of velocities in the direction of right ascension significantly exceeds the values of the same parameter in more external areas of the cluster. As mentioned above, in the central region of the cluster massive stellar objects at a later stage of evolution, are concentrated. As in the previous case, it can be assumed that the presence of this substructure is the cause of the greater value of the velocity dispersion.

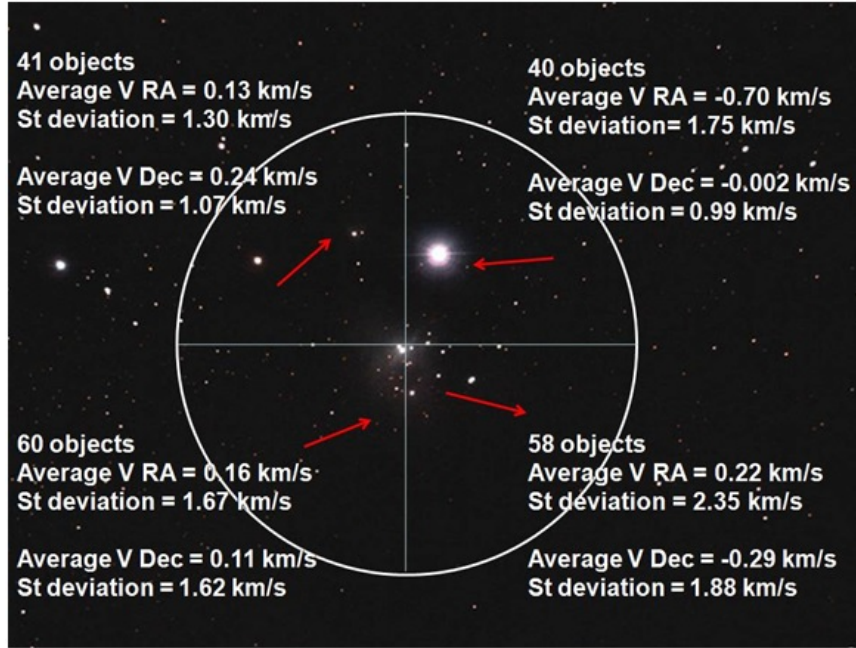


Figure 6. Average velocities and standard deviations in the quadrants. The red arrows show the direction of motion of the stars in each quadrant.

Table 1. The kinematic parameters along the radius of cluster

Region (arcmin)	Number	Velocity in RA direction (km s^{-1})		Velocity in Dec direction (km s^{-1})	
		Average	Sd. dev.	Average	Sd. dev.
0 - 2	14	0.11	2.15	-0.57	1.14
2 - 4	31	0.31	2.87	0.10	1.72
4 - 6	27	0.21	1.15	0.01	1.16
6 - 8	14	0.16	1.39	-0.25	1.41
8 - 10	18	-0.16	1.09	1.46	1.08

4. Discussion and conclusion

The early (i.e., few Myr) dynamical evolution of star clusters is still poorly constrained. The majority of stars form in clusters and associations inside giant molecular clouds. However, most clusters dissipate within 10 – 100 Myr, leaving more than 90% of the stellar population dispersed in the Galactic field (e.g., Ambartsumyan 1947, 1949, Lada & Lada 2003). The scientific debate on the origin of bound and unbound clusters, along with the processes leading to their dissolution, is still open. Several authors suggest that all stars form in dense clusters (density $\geq 10^3 - 10^4$ stars pc³), which rapidly dissipate after feedback from massive stars (i.e., supernova explosions, stellar winds, and radiation pressure) sweeps out the gas that was keeping the cluster bound (e.g., Goodwin & Bastian 2006, Baumgardt & Kroupa 2007). These models predict that clusters – after gas dispersion – should be found in a supervirial state. Recent observations and simulations question this scenario suggesting that clusters have origin in a hierarchically structured environment covering a large range of densities and that the stellar feedback and gas expulsion are irrelevant for the cluster dispersion, which is, instead, driven by two-body interactions (e.g., Parker & Dale 2013; Parker & Wright 2016).

From this perspective, the possible scenarios for explanation of observed supervirial state in IC 348 cluster include: a) the cluster is fluctuating around a new virial equilibrium after a recent disruption due to gas expulsion or a merger event, or b) the stellar population in IC 348 a is forming the subgroups which, moreover, may be the result of successive two or more star formation waves.

Undoubtedly, the presented results are only the initial stage of the study of the kinematics and dynamics of the young stellar cluster IC 348. For the study of the above issues, it is planned to conduct a more detailed study of various samples of cluster members, relation to both masses and evolutionary stages. As noted above, in previous works it was shown that in the cluster there is a stellar population with different infrared excess and activity, i.e. stellar objects at II and III evolutionary classes (Herbig 1988, Lada 2006, Falaherty et al. 2013, Nikoghosyan et al. 2015). Moreover, stellar objects with different degrees of activity form substructures, which, as already shown, can affect the kinematics. The presence of a rich database of observational data, including radial velocities, will allow us to construct 3D model of the cluster as a whole.

Acknowledgements

These data have been obtained from the Gaia-ESO Survey Data Archive, prepared and hosted by the Wide Field Astronomy Unit, Institute for Astronomy, University of Edinburgh, which is funded by the UK Science and Technology Facilities Council.

References

- Ambarzumian, V. A. 1936, MNRAS. Soc. 96, 172
Ambartsumyan V. A. 1937a, Astron. zh. 14, 207
Ambartsumyan, V. A. 1937b, Uchen. zap. Leningradsk. un-ta., No. 17, 96
Ambartsumyan V. A. 1938, Uchen. zap. Leningradsk. un-ta., No. 22
Ambartsumyan, V. A. 1947, Stellar Evolution and Astrophysics [in Russian], Izd. AN ArmSSR, Erevan
Ambartsumyan V. A. 1949, Astron. zh. 26, 3
Baumgardt, H.; Kroupa, P. 2007, MNRAS, 380, 1589
Beccari, G.; Boffin, H. M. J.; Jerabkova, T. et al. 2018, MNRAS, 481, L11
Bravi, L.; Zari, E.; Sacco, G. G. et al. 2018, A&A, 615, 37
Cook, N. J.; Scholz, A.; Jayawardhana, R. 2017, AJ, 154, 256
Cormack, A. 1985, Computed Tomography, Some History and Recent Developments, Proc. Symp. in Applied Mathematics, vol. 29, p. 35
Cottaar, M.; Covey, K. R.; Foster, J. B. 2015, ApJ, 807, 27
Currie, T.; Kenyon, S. J. 2009, AJ, 138, 703
Eddington, A. S. 1915, MNRAS, 72, 368
Flaherty, K. M.; Muzerolle, J.; Rieke, G. 2013, AJ, 145, 66
Gagné, G.; Faherty, J. K. 2018, ApJ, 862, 138
Galli, P. A. B.; Joncour, I.; Moraux, E. 2018, MNRAS, 477, 50
Goodwin, S. P.; Bastian, N. 2006, MNRAS, 373, 752
Herbig, G. H. 1954, PASP, 66, 19
Herbig, G. H. 1998, ApJ, 497, 736
Lada, C. J.; Lada, E. A. 2003, ARAA, 41, 57
Lada, C. J.; Muench, A. A.; Luhman, K. L. et al. 2006, AJ, 131, 1574
Lindgren, L.; Hernández, J.; Bombrun, A. et al. 2018, AA, 616, 2L
Luhman, K. L.; Stauffer, J. R.; Muench, A. A. et al. 2003, ApJ, 593, 1093
Miret-Roig N.; Antoja T.; Romero-Gómez M.; Figueras, F. et al. 2018, AA, 615, 51
Muench, A. A.; Lada, C. J.; Luhman, K. L.; Muzerolle, J.; Young, E. 2007, AJ, 134, 411
Nikoghosyan, E. H.; Vardanyan, A. V.; Khachatryan, K. G. 2015, Astrophysics, 58, 490
Ossipkov L. P., 2012, in " Ambartsumian's Legacy and Active Universe", Eds. Harutyunian, H.; Sedrakian, D.; Kaloghlian, A.; Nikoghossian, A. p. 21
Preibisch, T.; Zinnecker, H. 2002, AJ, 123, 1613
Rigliaco, E.; Wilking, B.; Meyer, M. R. 2016, AA, 588, 123
Parker, R. J.; Dale, J. E. 2013, MNRAS, 432, 986
Parker, R. J.; Wright, N. J. 2016, MNRAS, 457, 3430
Stelzer, B.; Preibisch, T.; Alexander, F. et al. 2012, AA, 537, A135
Wilkinson, S.; Merín, B.; Riviere-Marichalar, P. 2018, AA, 618, 12
Wu, Z.-Y.; Zhou, X.; Ma, J.; Du C.-H. 2006, MNRAS, 299, 2146

Identifying birth places of high-velocity stars

V. Hambaryan^{1,2*}, R. Neuhäuser¹

¹*Astrophysical Institut and University Observatory Jena, Germany*

²*NAS RA V. Ambartsumian Byurakan Astrophysical Observatory (BAO), Armenia*

**E-mail: Valeri.Hambaryan@uni-jena.de*

Abstract

We searched for the high-velocity and isolated neutron stars that encountered in the past with a stellar cluster/association closer than 20 pc. We took about 830000 stars with the high-quality astrometry and radial velocities from the Gaia DR2 catalogue and empirically selected about 560 high-velocity stars.

We used a full gravitational potential of the Galaxy to calculate the motion of a stellar cluster/association and a candidate of high-velocity star from their current positions to the proximity epoch. For this calculations we used a numerical integration in rectangular, Galactocentric coordinates. We used a covariance matrices of the astrometric data for each star to estimate the accuracy of the obtained proximity distance and epoch. For this aim we used a Monte Carlo method, replaced each star with 10 000 of its simulations and studied the distribution of their individual close passages near a stellar cluster/association. In addition we investigated a neutron star/runaway star pairs very likely both ejected from binary system during supernova event.

Keywords: *high-velocity stars – runaway stars – hyper-velocity stars – neutron stars – stellar associations – stellar clusters – Gaia astrometry.*

1. Introduction

What are high-velocity stars? Depending on the definition, a high-velocity star is a star moving faster than 60-100 km/s relative to the average motion of the stars in its ($V_{Sun}=18.0-20.0$ km/s) neighbourhood. Obviously, this definition is somewhat arbitrary and it depends on the many factors (for example, star mass, age, origin, galactic potential, velocity distribution model, etc.). Therefore, empirical determination of them might be more robust given the huge number of stars with reliable astrometric parameters and radial velocities provided by *Gaia* mission.

In general, there are three subclasses for high-velocity stars and they have different origin.

- Runaway stars: First of all, so called, “Runaway stars” are subclass of high velocity stars and were first introduced as O and B type stars by Blaauw [5]. Runaway stars are thought to have formed in the stellar associations[2] and ejected into the general Galactic field. The proper motion of a runaway star often points exactly away from a stellar association, of which the star was formerly a member. The majority of runaway stars in the literature are high-mass O and B type stars with ejection velocities less than 200 km s^{-1} [23]. Recent results show it is possible for low-mass G/K type stars with ejection velocities up to $\sim 1300 \text{ km s}^{-1}$ [26].
- Hypervelocity stars (HVSs): are another subclass of high velocity stars, the fastest stars in our Galaxy, which have extreme velocities above the escape speed of the Milky Way. HVSs can obtain their large velocity from a number of different processes. Hills [16] first theoretically predicted the formation of HVSs via three-body interactions between a binary star system and the massive nucleus in the Galactic Center (GC). Hypervelocity stars are stars with velocities that are substantially different from that expected for a star belonging to the normal distribution of stars in a galaxy. Such stars may have velocities on the order of 1000 km/s.
- Pulsars: Some neutron stars are inferred to be traveling with similar speeds as HVSs. This could be related to runaway-stars and their ejection mechanism. Neutron stars are the remnants of supernova explosions, and their extreme speeds are very likely the result of an asymmetric supernova explosion or the loss of their near partner during the supernova explosions that forms them.

Origin mechanisms

The Binary Ejection Mechanism (BEM): this was first proposed by Blaauw (1961) to explain the ejection of runaway O and B stars out of galactic plane. In this scenario the secondary star of a close binary receives its ejection velocity when the primary explodes as a supernova.

The Dynamical Ejection Mechanism (DEM): this was first proposed by Ambartsumian [1] in a Trapezium type young multiple systems and by Poveda, Ruiz & Allen [24] as an alternative to BEM to produce runaway stars. Dynamical interactions between stars inside young, open clusters and associations can give large kicks to one or both stars in a collision.

2. Selection of candidates of high-velocity stars

The recent release of the *Gaia* DR2 catalog [9] has renewed interest in the high-velocity stars in the Galaxy. In addition to contributing new samples of candidates [e.g., 19, 25, 12, 14], *Gaia* proper motions and radial velocities allow more robust assessments of the distances and space velocities of previously identified high velocity stars.

The positions and velocities available for over 7 million sources in the *Gaia* DR2 archive also enable new tests of theoretical models for the highest velocity stars.

Here, we use the *Gaia* DR2 proper motion and radial velocity data for the brightest and nearby (up to 3kpc from the Sun) stars to select high-velocity candidates and identify possible birth place and counterparts.

Identifying true high-velocity outliers in the *Gaia DR2* archive is challenging. Among the roughly 7 million stars with measured parallax, proper motion, and radial velocity, no more than a few hundred candidates emerge with Galactic rest-frame velocity close to or exceeding the local escape velocity [e.g., 20, 12]. Based on the quoted errors of the measured quantities, first we have followed the recommendations in the basic source parameter descriptions [9, 7, 17] by requiring for high-quality astrometry and quality of the reported radial velocity.

Next, we have selected *Gaia* DR2 sources for which astrometric parameters (positions, parallax and proper motions) and radial velocity have relative errors not exceeding 10%. Further, these sources converted into Galacto-centric cartesian coordinates (X,Y,Z,U,V,W) and analysed empirical distribution of total velocities in a spherical rings of 5 pc width around center of the Galaxy. The estimates of distribution parameters (the median, most probable value, the highest posterior density intervals¹) of total

¹The highest posterior density interval (HPD) determined as a probabilistic region

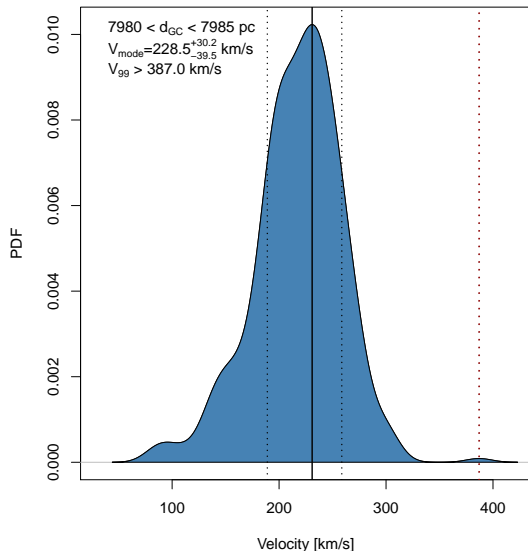


Figure 1: Selection procedure of high-velocity candidates in the spherical ring of $7980 < d_{GC} < 7985$ pc around center of the Galaxy. By vertical dashed (darkred, $V_{99} = 387.0$ km/s) line indicated the selection criteria of high-velocity candidate stars

velocity in a spherical ring, having at least 100 sources, performed with kernel-density estimates obtained with the function density in R (an example is illustrated in Figure 1). From this distribution as a high-velocity candidates were selected outliers which have a value $V_{total} > V_{HPD_{hi}}(99\%)$ (c.f., vertical darkred-dashed line in the Figure 1 for the spherical ring at the distance of $7980 < d_{GC} < 7985$ pc from GC, containing 2955 stars, 68% of which in the interval of $[189.0 - 258.7]$ km/s and only 6 stars exceeding $V_{HPD_{hi}}(99\%) = 387.0$ km/s). Note, that this is a conservative criteria with higher confidence for the selection of a high-velocity candidate star and by an application of a different methods (e.g., the Mahalanobis distance distance or $3-\sigma$ clipping algorithm) lead to the similar results. With above-mentioned procedure, we have selected 557 high-velocity (see, Fig. 2) candidate stars (367 within 3 kpc distance from the Sun) not included also in the list of so-called potentially contaminated radial velocity stars [6].

3. Motion of stars in the Galaxy

To study the Galactocentric motion of a high-velocity star we use a numerical integration of its equations of motion (Eq. 1) in the gravitational field of the Galaxy:

around a posterior mode, and is similar to a confidence interval in a classical statistics [see e.g. 11].

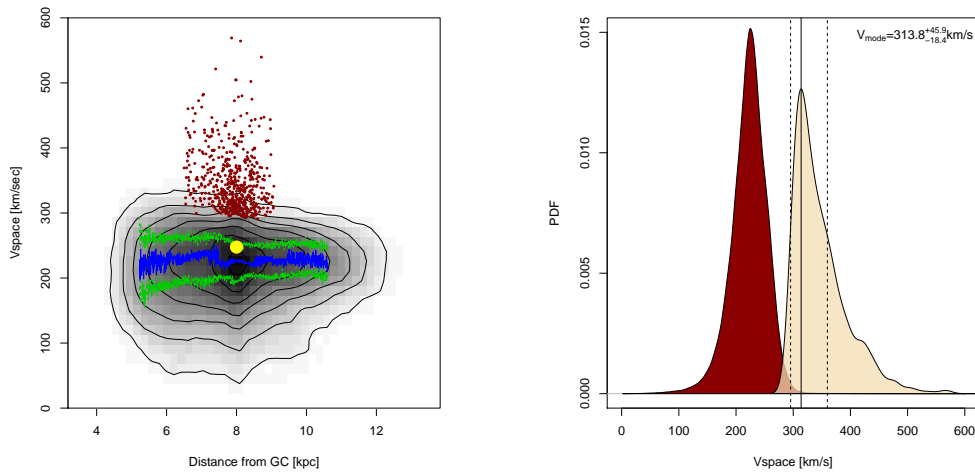


Figure 2: Selected high-velocity candidate stars based on the empirical distribution function of space velocities of *Gaia* DR2 catalog. *Left panel* : Total velocity in the Galactic rest-frame as a function of Galactocentric distance for all selected the 828098 stars in *Gaia* DR2 with high quality astrometric and $10\text{-}\sigma$ data (see details in the text). Grey colour level is proportional to the logarithmic number density of stars. The blue and green solid lines are the most probable value and HPD(68%) interval of total velocity of stars derived from empirical probability distribution function using kernel-density estimator. The dark red points are selected candidates of 557 high-velocity stars also derived from the same probability density function with $Prob(V_{total}) > 99\%$. The yellow filled dot presents the Sun position in the diagram. *Right panel* : A normalized probability density function of distributions of velocities of all (dark red) and selected as high-velocity candidate stars.

$$\begin{aligned}
 \ddot{x} &= -\frac{\partial}{\partial x}\Phi(x, y, z), \\
 \ddot{y} &= -\frac{\partial}{\partial y}\Phi(x, y, z), \\
 \ddot{z} &= -\frac{\partial}{\partial z}\Phi(x, y, z),
 \end{aligned} \tag{1}$$

where gravitational potential $\Phi(x, y, z)$ is expressed in rectangular coordinates. Here, we considered widely used the Milky-Way gravitational potential model. This model of gravitational potential $\Phi(x, y, z)$ is the sum of a central bulge component $\Phi_b(x, y, z)$ (spherically symmetric), an axisymmetric disk $\Phi_d(x, y, z)$ and a massive spherical Galactic halo $\Phi_h(x, y, z)$ (dark matter included):

$$\Phi(x, y, z) = \Phi_b(x, y, z) + \Phi_d(x, y, z) + \Phi_h(x, y, z), \tag{2}$$

where (x, y, z) are Galactocentric cartesian coordinates.

For the Galactic bulge and disk components we use formulae ($\Phi_b(r)$, Hernquist bulge, [15] and $\Phi_d(R, z)$, Miyamoto-Nagai disk, [21]):

$$\Phi_b(r) = -\frac{GM_b}{\sqrt{r^2 + b_b^2}}, \tag{3}$$

$$\Phi_d(R, z) = -\frac{GM_d}{\sqrt{R^2 + \left(a_d + \sqrt{z^2 + b_d^2}\right)^2}}, \tag{4}$$

and for a massive spherical Galactic halo ($\Phi_h(r)$, Navarro-Frenk-White halo, [22]):

$$\Phi_h(r) = -\frac{GM_h}{r} \ln\left(1 + \frac{r}{a_h}\right), \tag{5}$$

where $r^2 = x^2 + y^2 + z^2$ and $R^2 = x^2 + y^2$, with parameters of $M_b = (0.103 \pm 0.006) \times 10^{11} M_\odot$, $M_d = (0.650 \pm 0.020) \times 10^{11} M_\odot$, $M_h = (2.900 \pm 0.765) \times 10^{11} M_\odot$, $b_b = (0.267 \pm 0.009)$, $a_d = (4.40 \pm 0.73)$, $b_d = (0.308 \pm 0.005)$, and $a_h = (7.7 \pm 2.1)$ in kpc (Model III from Bajkova & Bobylev [4]), derived by fitting of modern data on circular velocities of Galactic objects located at distances up to 200 kpc from the Galactic center.

For numerical integration we utilise the fast and accurate Gauss-Everhart orbit integrator provided by Avdyushev [3].

3.1. Simulation of astrometric parameters

In order to estimate the uncertainty of the close stellar passage parameters we replace each considered star with a large number (typically 10 000) of its simulations, drawn from a multivariate normal distribution. This is

possible because in Gaia DR2 catalogue included full information on the covariance matrix of astrometric parameters. Such a procedure possesses an evident superiority over the individual, independent random drawing of each parameter what ignores their obvious mutual dependence. To generate random vectors \mathbf{x} , i.e. of proper motions, parallax, and radial velocity, from a multivariate normal distribution $\mathcal{N}_n(\mathbf{m}, \Sigma)$ with a given vector of means \mathbf{m} and a given covariance matrix Σ , we used `mvtnorm`: a Multivariate Normal and t Distributions R package with Cholesky method, developed by Genz et al. [10]:

$$\mathbf{m} = [\mu_{\alpha*}, \mu_{\delta}, \varpi, v_{\text{rad}}] \quad (6)$$

$$\Sigma = \begin{pmatrix} \sigma_{\mu_{\alpha*}}^2 & \sigma_{\mu_{\alpha*}} \sigma_{\mu_{\delta}} \rho(\mu_{\alpha*}, \mu_{\delta}) & \sigma_{\mu_{\alpha*}} \sigma_{\varpi} \rho(\mu_{\alpha*}, \varpi) & 0.0 \\ \sigma_{\mu_{\alpha*}} \sigma_{\mu_{\delta}} \rho(\mu_{\alpha*}, \mu_{\delta}) & \sigma_{\mu_{\delta}}^2 & \sigma_{\mu_{\delta}} \sigma_{\varpi} \rho(\mu_{\delta}, \varpi) & 0.0 \\ \sigma_{\mu_{\alpha*}} \sigma_{\varpi} \rho(\mu_{\alpha*}, \varpi) & \sigma_{\mu_{\delta}} \sigma_{\varpi} \rho(\mu_{\delta}, \mu_{\varpi}) & \sigma_{\varpi}^2 & 0.0 \\ 0.0 & 0.0 & 0.0 & \sigma_{v_{\text{rad}}}^2 \end{pmatrix}, \quad (7)$$

where ρ denotes the correlation coefficient between the astrometric parameters, and it is provided in the Gaia DR2 catalogue. Radial velocities are uncorrelated to the astrometric parameters, and we assume them to follow a Gaussian distribution centered on v_{rad} , and with standard deviation $\sigma_{v_{\text{rad}}}$.

In order to determine most likely backward in time stellar trajectories of candidates of a high-velocity stars and their potential birth places (stellar cluster/association or hypothetical supernova), we used as a measure a multivariate Gaussian likelihood in four dimensional space (time and position):

$$L(\mu, \Sigma | Z) = \prod_{i=1}^n L_i(\mu_i, \Sigma_i | z_i) = \prod_{i=1}^n (2\pi)^{-\frac{1}{2}p_i} |\Sigma_i|^{-\frac{1}{2}} e^{-(z_i - \mu_i) \Sigma_i^{-1} (z_i - \mu_i)^T} \quad (8)$$

3.2. Runaway stars AE aur, μ Col and 53 Eri and star forming region Orion

AE Aur, μ Col, and 53 Ari are runaway stars traced to the Trapezium cluster in the Orion Nebula two million years ago. These stars might have been ejected during a collision of two binary star groups Hoogerwerf et al. [13]. For the testing purpose, we have applied our approach to these stars and young clusters in Orion star forming region (see Table 1,2 and Figure 3).

4. Preliminary results

In order to identify the most probable parent stellar association/cluster of a high-velocity candidate stars we used updated catalogue of optically

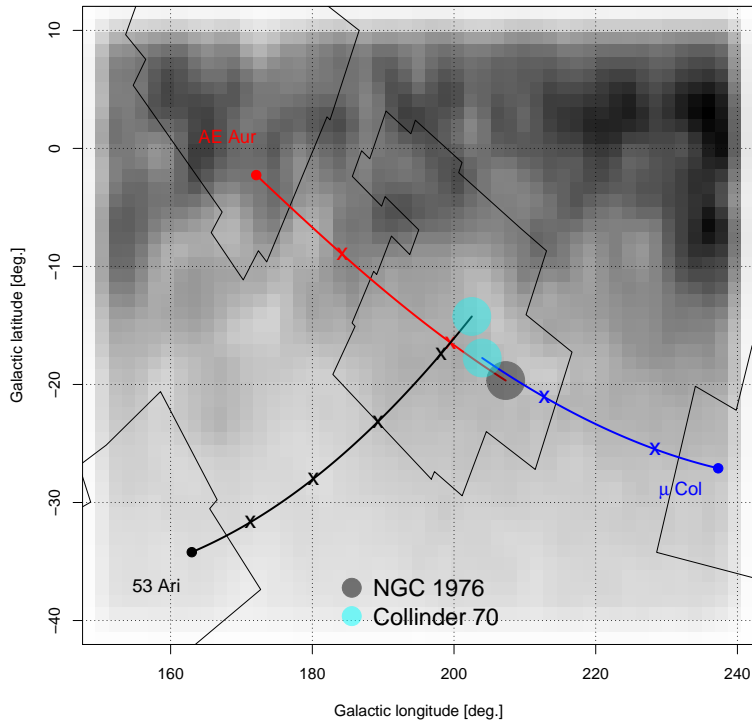


Figure 3: Simulated closest approach of stellar trajectories of runaway stars AE Aur, μ Col, 53 Ari and young stellar groups (NGC 1976, 1977, 1980, 1981 and Collinder 70) in Orion complex star forming region. The most probable traceback stellar trajectories, birth places and ejection times (highest likelihoods) of these runaway stars are presented in the bottom right panel (see also Table 2).

Name	RA [$^{\circ}$]	DEC [$^{\circ}$]	$\mu_{\alpha} \cos \delta$ [mas/yr]	μ_{δ} [mas/yr]	RV [km/s]	d [pc]	lg(Age) [year]
NGC 1976	83.82	-5.39	1.96	-0.77	27.80	400.0	7.71
NGC 1977	83.85	-4.82	2.42	-1.90	24.20	500.0	7.08
NGC 1980	83.85	-5.91	0.83	-0.36	23.00	550.0	6.67
NGC 1981	83.79	-4.40	1.01	1.14	27.90	400.0	7.50
Collinder 70	83.88	-1.10	0.36	-0.68	31.70	390.0	6.71
HIP24575(AE Aur)	79.076	34.313	-4.440	43.368	56.7	405.81	
HIP27204(μ Col)	86.500	-32.307	2.988	-22.030	109.0	465.64	
HIP14514(53 Ari)	46.857	17.880	-23.268	7.973	21.7	315.77	

Table 1: Input parameters for simulation of young clusters in Orion star forming region and runaway stars AE Aur, μ Col, and 53 Ari.

Cluster name	Runaway name	Relative number [%]	Most probable time [Myr]	Time range [Myr]
NGC 1976	AE Aur(HIP24575)	22.30	-2.48	-2.66 -2.26
NGC 1981	AE Aur(HIP24575)	16.70	-2.52	-2.71 -2.31
Collinder 70	AE Aur(HIP24575)	10.70	-2.25	-2.38 -2.12
Collinder 70	μ Col(HIP27204)	4.26	-2.46	-2.69 -2.23
Collinder 70	53 Ari(HIP14514)	2.36	-4.59	-5.09 -4.21
NGC 1981	μ Col(HIP27204)	1.30	-2.29	-2.47 -2.15
NGC 1976	μ Col(HIP27204)	0.93	-2.36	-2.49 -2.20
NGC 1977	AE Aur(HIP24575)	0.77	-2.48	-2.57 -2.35

Table 2: Results of simulation of young clusters in Orion star forming region and runaway stars AE Aur, μ Col, and 53 Ari.

visible open clusters and candidates [8] consisting of 710 objects with astrometric parameters and radial velocity of the stellar system and traced back in time up to 30 Myrs with the step of 1000 yrs.

The similar procedure was applied also for pulsars [18] having good astrometric parameters, i.e. the distance and proper motions have relative errors not exceeding 10%. In this case radial velocity of a pulsar was simulated from a uniform distribution in the range of -1000 to 1000 km/s.

5. Summary

We searched for the high-velocity stars from the Gaia DR2 catalogue and selected about 560 candidates.

We developed a new software to trace back the motion of stars through the Galactic potential, tested it successfully with the original case runaway stars AE Aur, μ Col, and 53 Ari and then applied it to above mentioned

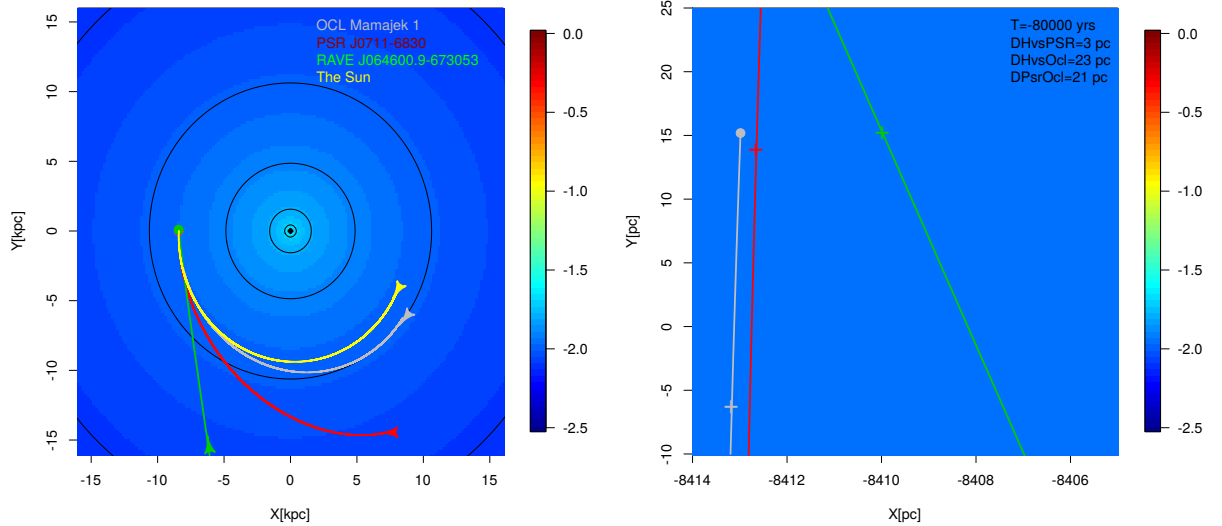


Figure 4: Possible triple associated with each other: star RAVE J064600.9-673053=CD-67 470=Gaia2 5280169713520753536, OCL Mamajek 1 and PSR J0711-6830

high-velocity stars and optically visible open clusters.

It turned out that for $\sim 15\%$ of high-velocity stars can be identified parent stellar cluster/association.

In some case we found also a plausible pulsar born in a possible supernova event (see Table 4 and Fig. 4).

References

- [1] Ambartsumian, V. A. 1954, Communications of BAO, 1954, 15, 3.
- [2] Ambartsumian, V. A. 1955, The Observatory, 75, 72.
- [3] Avdyushev, V. A. Vychisl. Tekhnol. Journal Profile 15, No. 4, 31-46, 2010
- [4] Bajkova and Bobilev, Open Astronomy, 26, 72, 2017, arXiv:1801.08875
- [5] Blaauw, A. 1961, BAN, 15, 265
- [6] Boubert, D., Strader, J., Aguado, D., et al. 2019, MNRAS, 280.
- [7] Bromley, B.C., Kenyon, S.J., Brown, W.R., Geller, M. J. ,2018, 868, 25
- [8] Dias, W. S., Alessi, B. S., Moitinho, A. & Lépine, J. R. D., 2002, A&A, 389,871

Cluster name	Gaia DR2 name	D_{min} number [pc]	Most probable time [Myr]
FSR0237	26381685304316212480	0.22	-4.22
Dolidze52	25229899212967139200	0.67	-6.10
Trumpler	2262053757371463808	0.87	-0.75
Turner 9	2940306024863622400	0.96	-2.75
Kronberger 13	2480690918702319104	1.30	-5.12
Dolidze 44	26544977963748689920	1.44	-5.02
Berkeley 87	25973898809770425344	1.73	-2.35

Table 3: Most probable parent open cluster of some high-velocity candidate stars.

Cluster name	Gaia DR2 name	Rave name	PSR	D_{min} (HP) [pc]	Most probable time [Myr]
Mamajek 1	5280169713520753536	J064600.9-673053	J0711-6830	-0.08	3.0
Collinder 132	5605471258084062464	J072858.5-301147	J0630-2834	-0.60	3.5

Table 4: Most probable parent open cluster, high-velocity candidate stars and pulsars.

- [9] Gaia Collaboration, (Brown, A. G. A., et al.) 2018, A&A, arXiv:1804.09365
- [10] Alan Genz, Frank Bretz, Tetsuhisa Miwa, Xuefei Mi, Friedrich Leisch, Fabian Scheipl, Torsten Hothorn (2018). mvtnorm: Multivariate Normal and t Distributions. R package version 1.0-8.
- [11] Gregory P. C., Loredano T. J., 1992, ApJ, 398, 146
- [12] Hattori, K., Valluri, M., Bell, E. F., & Roederer, I. U. 2018, ArXiv e-prints, arXiv:1805.03194
- [13] Hoogerwerf, R.; De Bruijne, J. H. J.; De Zeeuw, P. T. 2001 A & A, 365 49.
- [14] Irrgang, A., Kreuzer, S., & Heber, U. 2018, Astronomy and Astrophysics, 620, A48.
- [15] Hernquist L., 1990, ApJ, 356, 359
- [16] Hills, J.G., 1988, Nature, 331, 687
- [17] Lindegren, L., Hernández, J., Bombrun, A., et al. 2018, AJ, 616, A2
- [18] Manchester, R. N., Hobbs, G.B., Teoh, A. & Hobbs, M., AJ, 2005, 129, 1993-2006

- [19] Marchetti, T., Rossi, E.M. and Brown, A.G.A. 2018, 1804, arXiv:1804.10607v1
- [20] Marchetti, T., Rossi, E. M., & Brown, A. G. A. 2018, ArXiv e-prints, arXiv:1804.10607
- [21] Miyamoto & Nagai, 1975, PASJ, 27, 533
- [22] Navarro, Frenk & White, 1996, ApJ, 462, 563
- [23] Perets, H. B., & Šubr, L., 2012, ApJ, 751, 133
- [24] Poveda A., Ruiz J., Allen C., 1967, BOTT, 4, 86
- [25] Shen, K. J., Boubert, D., Gänsicke, B. T., et al. 2018, ArXiv e-prints, arXiv:1804.11163
- [26] Tauris, T.M., 2015, MNRAS Lett., 448, L6

Statistical analysis of the new catalogue of CP stars

S. Ghazaryan^{1*}, G. Alecian², A. A. Hakobyan¹

¹NAS RA V. Ambartsumian Byurakan Astrophysical Observatory (BAO), Armenia

²LUTH, CNRS, Observatoire de Paris, PSL University, Université Paris Diderot, 5 Place Jules Janssen, 92190 Meudon, France

*E-mail: satenikghazarjan@yahoo.de

Abstract

This talk is devoted to the statistical analysis of the new catalogue of Chemically Peculiar stars compiled from papers, where chemical abundances of those stars were given. The catalogue contains chemical abundances and physical parameters of 428 stars based on high-resolution spectroscopy data. Spearman's rank correlation test was applied for 416 CP (108 HgMn, 188 ApBp and 120 AmFm) stars and the correlation between chemical abundances and different physical parameters (effective temperature, surface gravity and rotational velocity) was checked. From dozens interesting cases we secluded four cases: the Mn peculiarities in HgMn stars, the Ca correlation with respect to effective temperature in AmFm stars, the case of helium and iron in ApBp stars. We applied also Anderson-Darling (AD) test on ApBp stars to check if multiplicity is a determinant parameter for abundance peculiarities.

Keywords: *Chemically Peculiar stars - abundances - catalogues - individual stars: HgMn, ApBp and AmFm.*

1. Introduction

Historically, main sequence Chemically Peculiar (CP) stars were divided in 4 groups by Preston (1974) – AmFm, ApBp, HgMn and λ Boo stars. Later, two groups of CP stars were added to the known ones - He-weak and He-rich stars. All CP stars have different physical properties. The effective temperatures of all CP stars are in the range of 7000-30000K, some of them are non-magnetic, some- magnetic. More than 50 percent of CP stars are binaries or belongs to the multiple systems. But all those stars have one generality – in the atmospheres of those stars we see peculiarities of different chemical element' abundances. AmFm stars are non-magnetic and they are characterized by underabundances of calcium and scandium, and high overabundances of iron and nickel (see Kunzli & North 1998; Gebran,

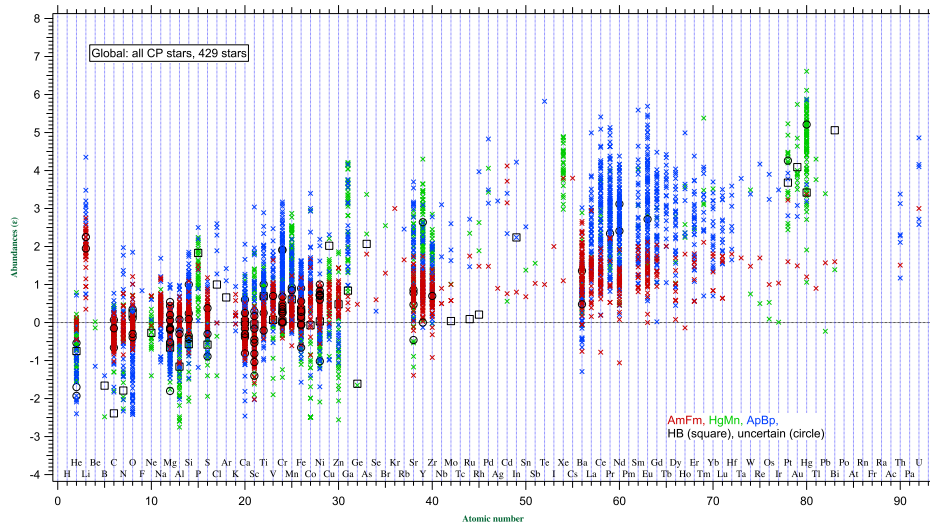


Figure 1. Abundances for the three CP Types in the present compilation versus atomic number. Abundances are the logarithm of the abundances divided by the solar Asplund et al. (2009) ones, the zero line corresponds to solar abundances. In the HgMn panel, the squares are abundances of the horizontal-branch star Feige 86.

Monier & Richard 2008, for example). HgMn stars are non-magnetic as well; they are characterized by strong overabundances of mercury and manganese (Hg overabundance reaches up to 107) (see Catanzaro, Leone & Leto 2003; Dolk, Wahlgren & Hubrig 2003, Alecian et al. 2009, etc.). In contrary, ApBp stars are magnetic and characterized by silicon, chromium, europium and strontium overabundances (see Leckrone 1981; Ryabchikova et al. 1999; Kochukhov et al. 2006, etc.). In this research we studied 3 groups of CP stars – AmFm, ApBp and HgMn stars.

2. The new catalogue of CP stars

Our new catalogue of CP stars consists in 428 stars, for which all chemical abundances were determined through high resolution spectroscopy techniques. 108 stars are identified as HgMn stars (see Ghazaryan & Alecian 2016), 128 stars as AmFm and 188 as ApBp stars. The types of 11 stars are uncertain and one star is a known horizontal-branch star (Feige 86). The catalogue contains physical parameters such as effective temperature, gravity, rotational velocity, and chemical abundances with their error measurements. If for a given element the abundances of different ions were given, we took the mean of them for the abundance value, and the error bars were recalculated by the mean square of the errors as in Ghazaryan & Alecian (2016). Compiled abundances with their errors are shown in Fig. 1. The

detailed information on our catalogue is given in Ghazaryan et al. (2018).

Table 1. Spearman’s rank test results for HgMn stars. Statistically significant correlations are shown in boldface (p -value ≤ 0.05), marginal ones are underlined ($0.05 < p$ -value < 0.06).

<i>Elements</i>	$\epsilon(T_{\text{eff}})$			$\epsilon(\log g)$			$\epsilon(v \sin i)$		
	ρ	p	N	ρ	p	N	ρ	p	N
He	-0.40	0.001	65	-0.10	0.450	65	0.12	0.355	64
C	-0.23	0.105	51	0.00	0.982	51	0.03	0.841	50
O	0.23	0.156	38	-0.28	0.091	38	0.15	0.391	37
Mg	-0.39	0.001	69	-0.07	0.580	69	0.09	0.489	68
Al	-0.42	0.005	44	0.24	0.112	44	0.32	0.037	44
Si	0.01	0.929	74	-0.15	0.192	74	-0.01	0.913	73
S	-0.61	0.000	52	0.05	0.743	52	-0.03	0.813	51
Ti	0.24	0.064	62	0.11	0.403	62	0.10	0.448	61
Cr	-0.28	0.010	86	-0.02	0.828	86	0.22	0.041	85
Mn	0.48	0.000	70	0.06	0.650	70	0.26	0.032	69
Fe	0.07	0.488	90	0.06	0.561	90	-0.11	0.313	89
Ni	-0.05	0.730	48	-0.01	0.945	48	0.11	0.473	47
Cu	0.32	0.106	26	<u>-0.38</u>	<u>0.053</u>	<u>26</u>	0.22	0.289	26
Zn	-0.18	0.339	29	<u>0.00</u>	<u>0.999</u>	<u>29</u>	0.12	0.533	29
Ga	0.30	0.083	34	0.23	0.184	34	0.00	0.997	33
Sr	-0.49	0.001	45	0.33	0.027	45	0.11	0.492	44
Y	-0.17	0.220	55	0.20	0.134	55	0.19	0.161	54
Zr	0.25	0.133	37	0.25	0.136	37	0.38	0.021	36
Xe	0.41	0.032	28	-0.04	0.823	28	0.11	0.568	28
Hg	-0.22	0.045	86	0.27	0.011	86	-0.01	0.944	85

3. Statistical analysis

The abundance anomalies may be explained by theoretical models, including atomic diffusion, and for that reason it is interesting to know the correlation between abundances and physical parameters, such as effective temperature, surface gravity and rotational velocity. To check that correlation we applied Spearman’s rank test (see Spearman 1904) between abundances and mentioned physical parameters. The statistical analysis was done for each element measured in more than 11 stars. In Table 1 as an example we show statistical results for HgMn stars. As you see, we found significant correlation with respect to effective temperature for Mg, Al, S, Cr, Mn, Sr, Xe, Hg. Possible correlations suggested by Ghazaryan & Alecian (2016) for Ni, Ti, and Si are not confirmed in this study. We found also significant correlation with respect to gravity for strontium and confirmed

it for mercury suggested in our previous paper. Considering rotation velocity as parameter, correlations have been found for aluminum, chromium, manganese, and zirconium.

Such types of tables were created for ApBp and AmFm stars as well. Dozens correlations between abundances and fundamental parameters were found for those type of stars too. Four noteworthy cases are secluded and explained in detail in our paper (see Ghazaryan et al. 2018).

We have applied AD test on single CP stars and those being in binary systems and do not find any relation between abundance anomalies and multiplicity in all three CP type stars, possibly because of the lack of data.

4. Conclusions

We present a unique catalogue of 428 Chemically Peculiar stars observed by spectroscopy during the last decades. Our new compilation of the main physical parameters and the abundances of elements from helium to uranium for 108 HgMn, 188 ApBp, 120 AmFm stars, plus 12 other peculiar stars (including 1 horizontal-branch star) confirms the increase of overabundances for heavy elements with atomic number (see Smith 1996) and the large scatter of the abundances anomalies. This scatter is not only due to the heterogeneity of the data, or abundance determination errors, but it is real. The applied statistical tests proofs that there is no any correlation between abundance anomalies and multiplicity of HgMn, ApBp and AmFm stars. We have found a significant number of correlations with the effective temperatures, but also some (fewer) with gravity and rotational velocity. We discuss also four noteworthy cases, but this does not mean that there are only four cases that deserve discussion. We are convinced that considering as a whole, the abundance measurements in CP stars will lead to interesting understanding of the physical processes in play in the atmospheres of those stars. In the near future we plan to extend our database to other categories of CP stars (such as stars with helium anomalies), and we have no doubt that a major extension of such a database will be achieved from the final GAIA catalogue.

Acknowledgements

This work was supported by the RA MES State Committee of Science, in the frames of the research project N^o 16YR-1C034.

References

- Alecian G., Gebran M., Auvergne M., et al. 2009, *A&A*, 506, 69
- Asplund M., Grevesse N., Sauval A. J., Scott P. 2009, *ARA&A*, 47, 481
- Catanzaro G., Leone F., Leto P. 2003, *A&A*, 407, 669
- Dolk L., Wahlgren G. M., Hubrig S. 2003, *A&A*, 402, 299

- Gebran M., Monier R., Richard O. 2008, *A&A*, 479, 189
Ghazaryan S., Alecian G. 2016, *MNRAS*, 460, 1912
Ghazaryan S., Alecian G., Hakobyan A. A. 2018, *MNRAS*, 480, 2953
Kochukhov O., Tsymbal V., Ryabchikova T., et al. 2006, *A&A*, 460, 831
Kunzli M., North P. 1998, *A&A*, 330, 651
Leckrone D. S. 1981, *ApJ*, 250, 687
Preston G. W. 1974, *ARA&A*, 12, 257
Ryabchikova T., Piskunov N., Savanov I., et al. 1999, *A&A*, 343, 229
Smith K. C. 1996, *Ap&SS*, 237, 77
Spearman C. 1904, *Am. J. Psychol.*, 15, 72

Study of stellar population in the new extended star formation region associated with five IRAS sources

N.M.Azatyán* and E.H. Nikoghosyan

NAS RA V. Ambartsumian Byurakan Astrophysical Observatory (BAO), Armenia

** E-mail: nayazatyan@bao.sci.am*

Abstract

We present the investigation results of structure and stellar content of a molecular cloud surrounding the five IRAS sources: 05168+3634, 05184+3635, 05177+3636, 05162+3639, and IRAS 05156+3643. Using multi-color criteria, we identified a rich population of embedded YSO candidates with infrared excess (Class 0/I and Class II) and their characteristics in a quite large molecular cloud which is located in the region of 24 arcmin radius. The molecular cloud includes 240 candidates of YSOs within the radii of sub-regions around 5 IRAS sources. The color-magnitude diagrams of the sub-regions suggest a very young stellar population. We construct the K luminosity function (KLF) of the sub-regions and according to the values of the slopes of KLFs, the age of the sub-regions can be estimated between 0.1-3 Myr. The SEDs are constructed for 45 Class I and 75 Class II evolutionary stages YSOs and the received parameters of those YSOs are well correlated with the results obtained by other methods.

Keywords: *stars: pre-main sequence – stars: luminosity function – infrared: stars – radiative transfer – individual objects: IRAS 05168+3634, IRAS 05184+3635, IRAS 05177+3636, IRAS 05162+3639, IRAS 05156+3643*

1. Introduction

In this paper, we present a detailed study of a extended star formation region surrounding IRAS 05168+3634 source. IRAS 05168+3634 is also known as Mol 9 from the catalogue of Molinari et al. (1996). Within 2 arcmin radius from IRAS 05168+3634 source, it has been detected three objects with magnitudes of MSX survey (Egan et al. 2003), one of which is associated with IRAS 05168+3634 source.

IRAS 05168+3634 is a luminous YSO with estimated $L=24 \times 10^3 L_{\odot}$ (Varricatt et al. 2010) and it is located in a high-mass star-forming region

in the pre-UCHII phase (Wang et al. 2009). This star-forming region associated with H₂O, NH₃, 44 GHz CH₃OH, as well as 1665 MHz and 1667 MHz OH maser emission (Zhang et al. 2005, Molinari et al. 1996, Fontani et al. 2010, Ruiz-Velasco et al. 2016), the SiO (J = 2–1) line (Harju et al. 1998), and four ¹³CO cores (Guan et al. 2008b). Molinari et al. (1998) have detected 6-cm radio emission 102 arcsec away from the IRAS 05168+3634 source.

The embedded stellar cluster in this region was detected in the NIR and MIR by various authors (Kumar et al. 2006; Faustini et al. 2009; Azatyan et al. 2016). In (Azatyan et al. 2016) it was showed that this is a bimodal cluster with 1.5 arcmin radius from geometric center of the cluster which does not coincide with the IRAS 05168+3634 source. One of the subgroups is concentrated around the IRAS 05168+3634 source and one must notice, it does not contain a rich population compared to other concentration.

The distance estimations of this region are different. A kinematic distance was estimated 6.08 kpc (Molinari et al. 1996) based on systemic LSR velocity $V_{LSR} = -15.5 \pm 1.9$ km/s. The trigonometric parallax of IRAS 05168+3634 with VERA is 0.532 ± 0.053 mas, which is corresponding to a distance of $1.88^{+0.21}_{-0.17}$ kpc placing the region in the Perseus arm, rather than the Outer arm (Sakai et al. 2012). This large difference of estimated distances causes some significant differences of physical parameters for individual members.

The observational data used to make the subsequent analysis are discussed in Section 2. The results and discussion are given in Section 3 and Section 4 concludes the results of this work.

2. Archival data

For our study, we have used the data covering a wide infrared range from NIR to FIR wavelength. At first, it is the NIR photometric data and images of UKIRT Infrared Deep Sky Survey (UKIDSS) Galactic Plane Survey DR6 (GPS, Lucas et al. 2008) in J, H, and K bands.

MIR observations of this region have obtained using the *Spitzer* Space Telescope under the Galactic Legacy Infrared Midplane Survey Extraordinaire 360 (GLIMPSE 360) program (Churchwell et al. 2009) in the 3.6, 4.5 μ m bands with the resolution of 0.6''/px. We have also used the data of Wide-field Infrared Survey Explorer (WISE, Wright et al. 2010) (3.4 μ m, 4.6 μ m, 12 μ m and 22 μ m) and the MSX survey (8.28 μ m, 12.13 μ m, 14.65 μ m and 21.3 μ m).

We obtained FIR data using the instruments Photodetector Array Camera and Spectrometer (PACS, Poglitsch et al. 2010) and Spectral and Photometric Imaging Receiver (SPIRE, Griffin et al. 2010) on the 3.5 m Herschel Space Observatory (Pilbratt et al. 2010). For our analyses, we used the

PACS 70, 160 μm and the SPIRE 250,350 and 50 μm photometric data and images with resolutions varying $\sim 5.5''$ - $36''$. We also used photometric data of IRAS mission (12 and 25 μm).

3. Results and discussion

3.1. Structure of the molecular cloud

Comparison of images taken in different spectral ranges showed that IRAS 05168+3634 star-forming region has more complicated structure in the FIR wavelengths than in the NIR and MIR. Figure 1 shows the region in different wavelengths. Moving toward longer wavelengths, the cloud filaments surrounding IRAS 05168+3634 source become more expressive and it is obvious that the IRAS 05168+3634 star-forming region is not limited in 1.5 arcmin radius from geometric center (Azatyan et al. 2016) but is more extended and is located within a 24 arcmin radius molecular cloud where the center of molecular cloud is conditionally selected IRAS 05168+3634 source. Studying common star-forming region in the molecular cloud, it turns out that apart from IRAS 05168+3634, there are four IRAS sources: IRAS 05184+3635, IRAS 05177+3636, IRAS 05162+3639, and IRAS 05156+3643, which are embedded in the same molecular cloud. There is very few information about these IRAS sources. IRAS 05184+3635 and IRAS 05177+3636 are associated with dark clouds DOBASHI 4334 and 4326, respectively (Dobashi 2011). In Casoli et al. (1986), the distances of IRAS 05184+3635 and IRAS 05177+3636 were assessed based on the ^{13}CO velocities: -17 km/s and -15 km/s respectively, as a result of which both IRAS 05184+3635 and IRAS 05177+3636 were evaluated at the same 1.4 kpc distance. The latter value coincides with the distance of IRAS 05168+3634 based on trigonometric parallax. This fact also indicates that these IRAS sources are most likely to be found in the same molecular cloud. There are 2 objects near to IRAS 05177+3636 source detected in submillimeter wavelength (Di Francesco et al. 2008). IRAS 05162+3639 associated with H_2O maser (Sunada et al. 2007). It has been detected a high proper-motion star in LSPM-NORTH catalog by 0.35 arcmin far away from the IRAS 05156+3643 (Lépine & Shara 2005), which is probably compatible with IRAS 05156+3643 source within error bar.

We have constructed map of the distribution of stellar surface density within a $48' \times 48'$ region to investigate the structure of each concentration in the molecular cloud, using photometric data of Herschel PACS Point Source Catalog: 160 μm and Extended Source List (red band). The density was determined simply by dividing the number of stellar objects in $200'' \times 200''$ area with step size $100''$. Figure 2 shows the map of the distribution of stellar surface density based on Herschel PACS 160 μm photometry.

It is known that in the case of homogeneous distribution of stars in the

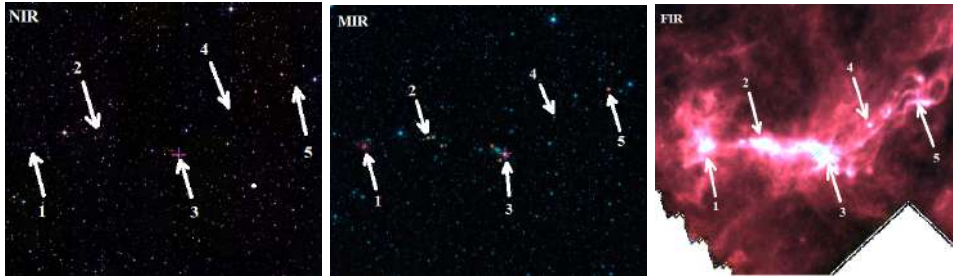


Figure 1: Investigated region in different wavelengths from NIR to FIR. The positions of 5 IRAS sources are marked by arrows and the IRASs are numbered as follows 1-IRAS 05184+3635, 2-IRAS 05177+3636, 3-IRAS 05168+3634, 4-IRAS 05162+3639 and 5-IRAS 05156+3643.

field, the number of stars is comparable to the surface area occupied by those stars. Let us figure out how much the distribution of stars in this field differs from the homogeneous distribution. We can clearly distinguish five subgroups, the distribution of which can not be accidental. From this, one can conclude that all 5 IRAS star-forming regions with high probability belong to the same molecular cloud and, therefore, are at the same distance. As the distances for whole region, we used the distance estimations of IRAS 05168+3634 star-forming region: 6.08 kpc (kinematic estimation) and $1.88_{-0.17}^{+0.21}$ kpc distance (based on the trigonometric parallax).

3.2. Selection of Objects

For the selection of objects in the molecular cloud, we have used the data of NIR, MIR and FIR catalogs (see Section 2) within the radius of 24 arcmin concerning to conditionally selected IRAS 05168+3634 source. As the main catalog, we have chosen GPS UKIDSS-DR6. We have selected objects with a probability of being noise $< 50\%$ and taking into account the completeness limit of UKIDSS survey in K band, the objects that have a measured magnitude of $K \geq 18.02$ have been removed from the list. This yielded approximately 48000 objects. The MIR and FIR photometric catalogs were cross-matched with GPS UKIDSS-DR6 catalog within 3σ of combined error matching radius and then was obtained a combined photometric catalog. Thereafter, the following set of steps were followed for the identification of the young stellar objects (YSOs).

3.3. C-C diagrams

One of the most powerful tools for identifying YSO candidates via reddening and excess is their location on color-color diagrams. The choice of colors depends on the available data. We have constructed 4 color-color (hereafter C-C) diagrams. As YSOs we have chosen those ones which are

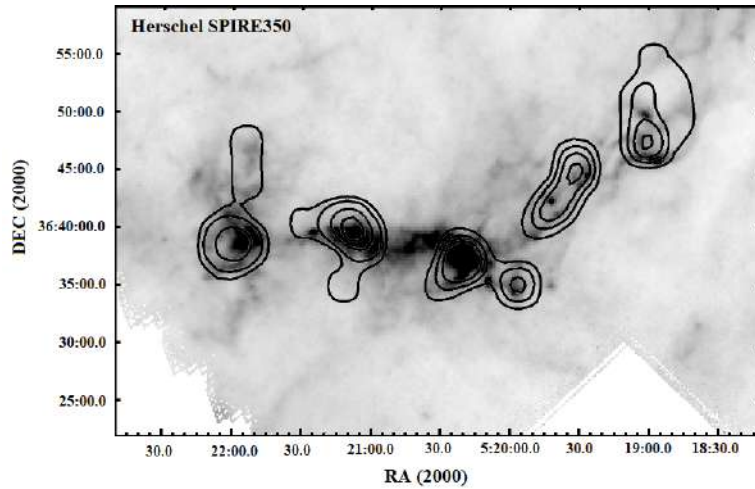


Figure 2: Stellar surface density distribution based on Herschel PACS 160 μm photometry. Stellar surface density distribution map is overplotted on Herschel SPIRE 350 μm image. The surface density of the last isodences exceeds the average value of the field surface density on 1σ

classified as objects with infrared excess in at least 2 C-C diagrams to minimize the likelihood of the wrong choices.

The first infrared excess objects identification was carried out with (J-H) vs. (H-K) C-C diagram. Figure 3 top left panel shows the (J-H) vs. (H-K) C-C diagram where the solid and dashed curves represent the locus of the intrinsic colors of dwarf and giant stars, taken from Bessell & Brett (1988) after being converted to the CIT system using the relations given by Carpenter (2001). The parallel solid lines drawn from the base and tip of the dwarf and giant loci, are the interstellar reddening vectors (Rieke & Lebofsky 1985). The locus of unreddened classical T Tauri stars (CTTSs) is taken from Meyer et al. (1997). The region bounded by the dashed lines where the PMS stars with intermediate mass, i.e., Herbig Ae/Be stars are usually found (Hernández et al. 2005). The objects with different evolutionary stages have certain places in this diagram (Lada & Adams 1992). We have selected those stars as YSOs, which have the considerable, accurately expressed IR excess i.e objects located to the right of reddening vectors.

We have used the data of GLIMPSE 360 catalog to construct C-C diagram combining NIR and MIR photometry. Figure 2 top right panel shows the K-[3.6] vs. [3.6]-[4.5] C-C diagram where the diagonal lines outline the region of location of YSOs with both Class I and Class II evolutionary stages. The de-reddened colors are separated into Class I and II domains by the dashed line. Arrow shows extinction vector (Flaherty et al. 2007). All the lines in the K- [3.6] vs. [3.6]-[4.5] diagram are taken from the (Allen et al. 2007).

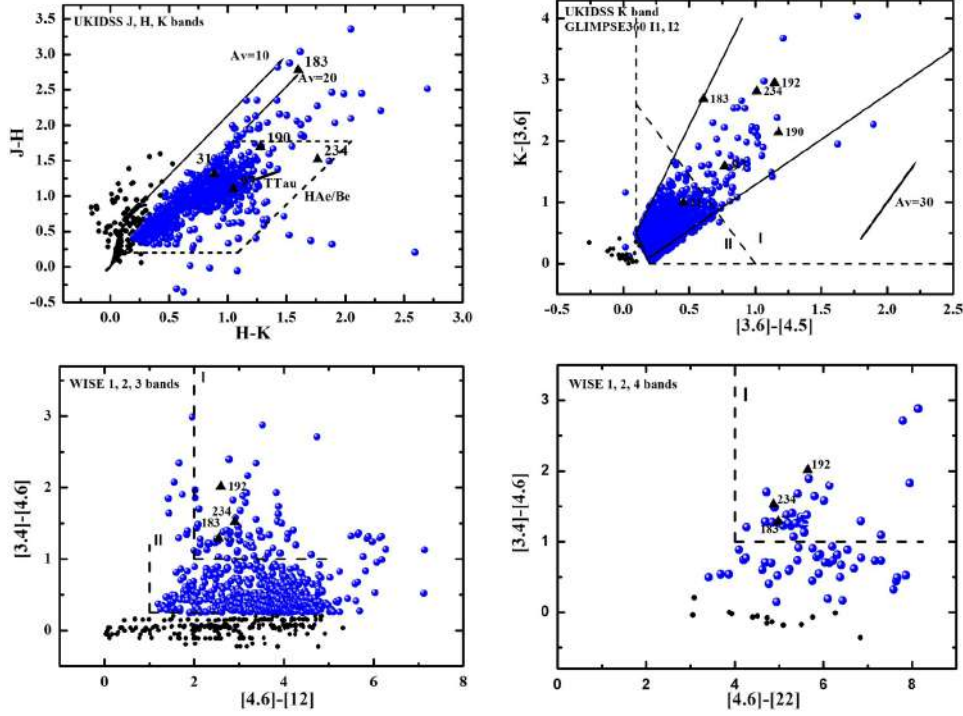


Figure 3: The C-C diagrams of the region. The blue circles are selected YSOs and black circles are unclassified ones. Not all unclassified objects are presented in these diagrams. IRAS sources are marked by triangles and they are labelled.

We have also constructed 2 other C-C diagrams using the list of objects with good WISE detection, i.e., those possessing photometric uncertainty < 0.2 mag in WISE bands. Figure 3 below left panel shows the $[3.4]-[4.6]$ vs. $[4.6]-[12]$ C-C diagram and below right panel shows $[3.4]-[4.6]$ vs. $[4.6]-[22]$ C-C diagram. As it was mentioned for previous C-C diagrams, the objects with different evolutionary stages are located in certain places in this diagram too (Koenig et al. 2012).

Totally, we have selected 1224 YSOs within 24 arcmin radius and they are marked with blue circles. IRAS sources are marked by triangles and they are labelled in diagrams. Unfortunately, this kind of selection of YSOs cannot give a possibility to find the exact number of YSOs.

The distribution of classified YSOs in the field, shown on Figure 4, clearly shows that Class II objects are distributed more homogeneous on the field than Class I objects which are located in certain areas and show clear concentrations. Since the region is quite large, then the probability of being fore/background objects within the selected Class II objects is very high, and in case of Class I objects, that possibility is small, as they are not detected outside of the molecular cloud filaments. In order to minimize the number of incorrect Class II objects, further investigations will only be per-

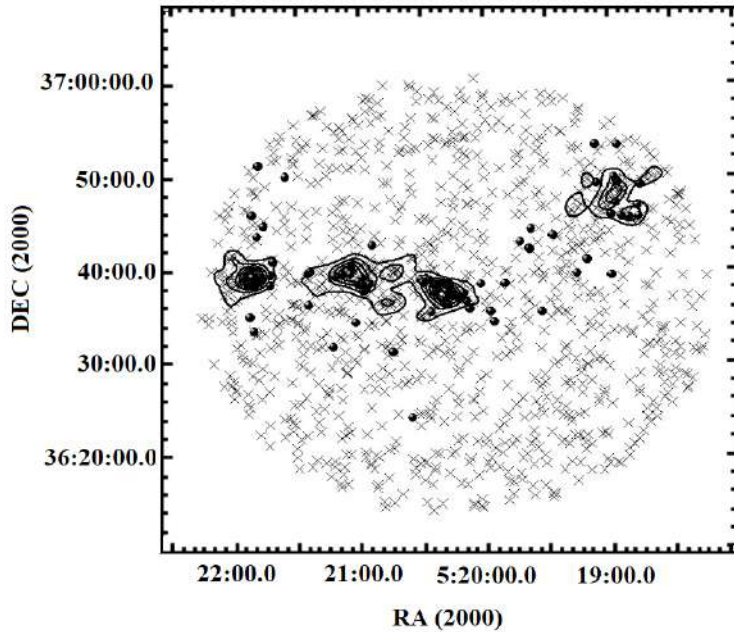


Figure 4: Stellar surface density distribution based on color-color diagrams. Class I and Class II evolutionary stage objects are marked by filled circles and crosses, respectively.

formed on concentration areas. For that purpose, we have constructed map of the distribution of stellar surface density within a $48' \times 48'$ region to investigate the structure and the size of each concentration in the molecular cloud, using the coordinates of selected YSOs. We have refined the radius of each sub-region relative to the geometric centers of them based on the density distribution of selected YSOs. Table 1 presents the coordinates of IRAS sources in (2)-(3) columns, in (4)-(5) columns are the coordinates of geometric centers and in last column are shown the radii based on stellar density distribution. Two objects from GPS UKIDSS-DR6 catalog were identified with IRAS 05162+3639 source as a result of cross-match, i.e. probably IRAS 05162+3639 source is binary object and three more Class I objects are located very close to it, but they do not show any real concentration. Therefore, the 0.25 arcmin value of radius given in the Table 1 is conditional and includes those three Class I objects and the binary associated with IRAS 05162+3639 source. Further studies will be conducted for the 240 YSOs of 1224 selected from C-C diagrams and it is a total number of objects falling within the already-defined radii of five sub-regions.

IRAS	C-C		C-M-1.88 kpc		C-M-6.1 kpc		Class I	A_v (mag)	α slope
	Mem.	Class I	Mem.	Class I	Mem.	Class I			
	(%)		(%)		(%)				
(1)	(2)	(3)	(4)	(5)	(6)	(7)	(8)	(9)	(10)
05184+3635	52	21	48	23	52	21	11	1.4	0.12 ± 0.04
05177+3636	79	28	65	34	79	28	22	1.34	0.2 ± 0.02
05168+3634	57	43	45	54	56	45	24	4.3 (4.5)	0.21 ± 0.05
05162+3639	5	–	5	–	5	–	5	1.23	–
05156+3643	47	20	40	23	47	20	9	1.03	0.15 ± 0.04

Table 2: Characterizes of sub-regions. (1)-Name of sub-regions, (2)-(3)-number of YSOs and the fraction of Class I objects (in percent) according to the C-C diagrams, (4)-(7)-number of YSOs and the fraction of Class I objects (in percent) according to the C-M diagrams in different distances, (8)-number of Class I evolutionary stage objects, (9)-Interstellar extinction, (10)-The α slope of KLF of each sub-region

According to the results of C-C and C-M diagrams, one can note that within the selected radius of each sub-region the youngest is IRAS 05168+3634 star-forming region, since Class I objects represent a fairly large percentage.

3.5. K Luminosity function

The luminosity function in the K-band (KLF) is frequently used in studies of young clusters and star-forming regions as a diagnostic tool of the initial mass function (IMF) and the star formation history of their stellar populations (Zinnecker et al. 1993; Lada & Lada 1995). It is possible to construct the KLF to constrain the age of the embedded stellar population in each star-forming region independently. As pointed out by Lada et al. (1996), the age of a sub-region can be estimated by comparing its KLF to the observed KLFs of other young clusters. In the case of IRAS 05162+3639 sub-region, the number of YSOs is not enough to construct KLF and so it is impossible to estimate the value of α slope. The KLFs corresponding fitted slopes are provided in Column (10) of Table 2. According to the calculation of Massi et al. (2000), α values between 0.2-0.28 are consistent with the ages of 0.1 - 3 Myr. The α values of the observable sub-regions are close to this range of values, therefore, the age of all four sub-regions can be estimated between 0.1-3 Myr, which also well reflects the location of stellar objects relatively to the isochrones.

3.6. SED analysis

We have constructed the spectral energy distributions (SEDs) for 45 Class I and 75 Class II evolutionary stage YSOs and fitted them with the radiative transfer models of Robitaille et al. (2007). This procedure has

been done using wavelengths ranging from $1.1 \mu\text{m}$ to $160 \mu\text{m}$ in particular J, H, K (UKIDSS), 3.6 and $4.5 \mu\text{m}$ (*Spitzer* IRAC), 3.4 , 4.6 , 12 and $22 \mu\text{m}$ (WISE), 8.28 , 12.13 , 14.65 and $21.3 \mu\text{m}$ (MSX), 12 and $25 \mu\text{m}$ (IRAS) and 70 , $160 \mu\text{m}$ (*Herschel* PACS). The SED fitting was carried out using both distance estimations: 1.88 and 6.1 kpc. We used the ranges of the interstellar extinction (A_v) and the distances of $1 - 40$ mag and $5.5-6.5$ kpc and $1.6-2$ kpc, respectively.

The results of the SED fitting tool in general confirm the age estimations obtained by the KLF slope for each sub-region and the results obtained in the C-C and C-M diagrams for individual objects.

4. Conclusion

Our investigation shows that the IRAS 05168+3634 star-forming region has more complicated structure in the FIR wavelengths and is located in a quite large molecular cloud within the region of ~ 24 arcmin radius (the center of the molecular cloud is conditionally selected IRAS 05168+3634 source), which, in turn, consists of another four star-forming regions. From the statistical analysis follows that all IRAS star-forming regions are at the same distance: 6.1 kpc (Molinari et al. 1996) or 1.88 kpc (Sakai et al. 2012). In addition, these regions repeat the shape of the molecular cloud. And also the distances of IRAS 05184+3635 and IRAS 05177+3636 assessed based on the ^{13}CO velocities were evaluated at the same 1.4 kpc value, which coincides with the distance of IRAS 05168+3634 based on trigonometric parallax.

In this paper, we analyzed the stellar content of the molecular cloud and separately for each star-forming region associated with IRAS sources using the NIR and MIR photometric data. We obtained the census of the young stellar population and their characteristics within 24 arcmin radius region surrounding the molecular cloud, which includes 1224 candidate YSOs, and 240 of them are concentrated around five IRAS sources. We have classified 71 YSOs as objects with evolutionary stage Class I and $132-169$ YSOs (depending on the distance) with evolutionary stage Class II stars within radii of sub-regions. It should be noted that, unlike the Class II objects, the Class I objects are located mainly in the filaments of the molecular cloud, i.e. the distribution of Class I objects reflects the initial state of the parent molecular cloud. The estimated distances and the interstellar extinctions of each sub-region were taken into account in corrections of J and K magnitudes for C-M diagrams which generates such a difference in the number of Class II objects.

We have also calculated the slope the KLFs for four sub-regions, namely IRAS 05184+3635, IRAS 05177+3636, IRAS 05168+3634 and IRAS 05156+3643. According to the values of the slopes of KLFs, the age of all four sub-

regions can be estimated between 0.1-3 Myr. There are not enough YSOs in IRAS 05162+3639 sub-region, so KLF for this sub-region were not constructed.

The SEDs are constructed for 45 Class I and 75 Class II YSOs. This procedure has been done using wavelengths ranging from 1.1 μm to 160 μm . The results of the SED fitting tool, in general, are well correlated with the age estimations obtained by the KLF slope for each sub-region and also, at the distance of 1.88 and 6.1 kpc, IRAS sources can be classified as middle-mass YSOs which confirm the results obtained in the C-C and C-M diagrams.

Acknowledgements

This research has made use the data obtained at UKIRT, which is supported by NASA and operated under an agreement among the University of Hawaii, the University of Arizona and Lockheed Martin Advanced Technology Center. We gratefully acknowledge the use of data from the NASA/IPAC Infrared Science Archive, which is operated by the Jet Propulsion Laboratory, California Institute of Technology. This work was made by a research grant from the Armenian National Science and Education Fund (ANSEF) based in New York, USA.

References

- Allen, L., Megeath, S. T., Gutermuth, R., et al. 2007, *Protostars and Planets V*, 361
 Azatyan, N. M., Nikoghosyan, E. H., & Khachatryan, K. G. 2016, *Astrophysics*, 59, 339
 Bessell, M. S., & Brett, J. M. 1988, *PASP*, 100, 1134
 Carpenter, J. M. 2001, *AJ*, 121, 2851
 Casoli, F., Dupraz, C., Gerin, M., Combes, F., & Boulanger, F. 1986, *A&A*, 169, 281
 Churchwell, E., Babler, B. L., Meade, M. R., et al. 2009, *PASP*, 121, 213
 Di Francesco, J., Johnstone, D., et al. 2008, *ApJS*, 175, 277
 Dobashi, K. 2011, *PASJ*, 63, S1
 Egan, M. P., Price, S. D., Kraemer, K. E., et al. 2003, *VizieR Online Data Catalog*, 5114
 Faustini, F., Molinari, S., Testi, L., & Brand, J. 2009, *A&A*, 503, 801
 Flaherty, K. M., Pipher, J. L., Megeath, S. T., et al. 2007, *ApJ*, 663, 1069
 Fontani, F., Cesaroni, R., & Furuya, R. S. 2010, *A&A*, 517, A56
 Griffin, M. J., Abergel, A., Abreu, A., et al. 2010, *A&A*, 518, L3
 Guan, X., Wu, Y., & Ju, B. 2008, *MNRAS*, 391, 869
 Harju, J., Lehtinen, K., Booth, R. S., & Zinchenko, I. 1998, *A&AS*, 132, 211
 Hernández, J., Calvet, N., Hartmann, L., et al. 2005, *AJ*, 129, 856
 Koenig, X. P., Leisawitz, D. T., Benford, D. J., et al. 2012, *ApJ*, 744, 130
 Kumar, M. S. N., Keto, E., & Clerkin, E. 2006, *A&A*, 449, 1033
 Lada, C. J., Alves, J., & Lada, E. A. 1996, *AJ*, 111, 1964
 Lada, C. J., & Adams, F. C. 1992, *ApJ*, 393, 278
 Lada, E. A., & Lada, C. J. 1995, *AJ*, 109, 1682
 Lépine, S., & Shara, M. M. 2005, *AJ*, 129, 1483
 Lucas, P. W., Hoare, M. G., Longmore, A., et al. 2008, *MNRAS*, 391, 136
 Massi, F., Lorenzetti, D., Giannini, T., & Vitali, F. 2000, *A&A*, 353, 598
 Meyer, M. R., Calvet, N., & Hillenbrand, L. A. 1997, *AJ*, 114, 288
 Molinari, S., Brand, J., Cesaroni, R., & Palla, F. 1996, *A&A*, 308, 573
 Molinari, S., Brand, J., Cesaroni, R., Palla, F., & Palumbo, G. G. C. 1998, *A&A*, 336, 339
 Pilbratt, G. L., Riedinger, J. R., Passvogel, T., et al. 2010, *A&A*, 518, L1
 Poglitsch, A., Waelkens, C., Geis, N., et al. 2010, *A&A*, 518, L2
 Rieke, G. H., & Lebofsky, M. J. 1985, *ApJ*, 288, 618
 Robitaille, T. P., Whitney, B. A., Indebetouw, R., & Wood, K. 2007, *ApJS*, 169, 328
 Ruiz-Velasco, A. E., Felli, D., Migenes, V., & Wiggins, B. K. 2016, *ApJ*, 822, 101
 Sakai, N., Honma, M., Nakanishi, H., et al. 2012, *PASJ*, 64, 108
 Siess, L., Dufour, E., & Forestini, M. 2000, *A&A*, 358, 593

- Sunada, K., Nakazato, T., Ikeda, N., et al. 2007, PASJ, 59, 1185
Varricatt, W. P., Davis, C. J., Ramsay, S., & Todd, S. P. 2010, MNRAS, 404, 661
Wang, K., Wu, Y. F., Ran, L., Yu, W. T., & Miller, M. 2009, A&A, 507, 369
Wright, E. L., Eisenhardt, P. R. M., Mainzer, A. K., et al. 2010, AJ, 140, 1868
Zhang, Q., Hunter, T. R., Brand, J., et al. 2005, Apj, 625, 864
Zinnecker, H., McCaughrean, M. J., & Wilking, B. A. 1993, Protostars and Planets III, 429

Long-term Photometric Monitoring of FUor and FUor-like Objects

E. Semkov^{1*}, S. Ibryamov², S. Peneva¹, A. Mutafov¹

¹*Institute of Astronomy and National Astronomical Observatory, Bulgarian Academy of Sciences, Sofia, Bulgaria,*

²*Department of Theoretical and Applied Physics, Faculty of Natural Sciences, University of Shumen, Shumen, Bulgaria*

**E – mail : esemkov@astro.bas.bg*

Abstract

A phenomenon with a significant role in stellar evolution is the FU Orionis (FUor) type of outburst. The first three (classical) FUors (FU Ori, V1515 Cyg and V1057 Cyg) are well-studied and their light curves are published in the literature. But recently, over a dozen new objects of this type were discovered, whose photometric history we do not know well. Using recent data from photometric monitoring and data from the photographic plate archives we aim to study, the long-term photometric behavior of FUor and FUor-like objects. The construction of the historical light curves of FUors could be very important for determining the beginning of the outburst, the time to reach the maximum light, the rate of increase and decrease in brightness, the pre-outburst variability of the star. So far we have published our results for the light curves of V2493 Cyg, V582 Aur, Parsamian 21 and V1647 Ori. In this paper we present new data that describe more accurately the photometric behavior of these objects. In comparing our results with light curves of the well-studied FUors (FU Ori, V1515 Cyg and V1057 Cyg), we conclude that every object shows different photometric behavior. Each known FUor has a different rate of increase and decrease in brightness and a different light curve shape.

Keywords: *stars: pre-main sequence – stars: variables: T Tauri, Herbig Ae/Be – stars: individual: V2493 Cyg, V582 Aur, V1647 Ori, Parsamian 21*

1 Introduction

During the pre-main sequence (PMS) stage of evolution, young stellar objects exhibit different types of photometric variability (Herbst et al. 1994). One of the most dramatic of these events, with very high amplitude

variations, is the FU Orionis outburst. First Ambartsumyan (1971) draws attention to this object by linking it to the evolution of the PMS stars and proposes the abbreviation FUor. Herbig (1977) defined FUors as a class of young stellar objects after the discovery of two new FUor stars: V1057 Cyg and V1515 Cyg. The main characteristics of FUors are a significant increase in optical brightness of about 4-5 magnitudes, a F-G supergiant spectrum with broad blue-shifted Balmer lines, strong infrared excess, location in star-forming regions, and connection with reflection nebulae (Reipurth & Aspin 2010, Audard et al. 2014, Connelley & Reipurth 2018). Typical spectroscopic properties of FUor objects include a gradual change in the spectrum from earlier to later spectral type from the blue to the infrared, a strong Li I 6707 line, P Cygni profiles of H α and Na I 5890/5896 lines, and the presence of CO bands in the near infrared spectra (Herbig 1977, Connelley & Reipurth 2018). The prototypes of FUors seem to be low-mass PMS objects (T Tauri stars) with massive circumstellar disks.

According to a commonly accepted view, the FUor outburst is produced by a sizable increase in accretion from the circumstellar disk to the stellar surface (Hartmann & Kenyon 1996). The cause of this increase in accretion from $\sim 10^{-7} M_{\odot}/\text{yr}$ to $\sim 10^{-4} M_{\odot}/\text{yr}$ appears to be thermal or gravitational instability in the circumstellar disk. This accretion disk model can account for most of the main properties of FUors.

Among all objects associated with the group of FUors, only three (FU Ori, V1057 Cyg, and V1515 Cyg) have detailed photometric observations taken during the outburst and during the fading period (Clarke et al. 2005). For a few objects, V1735 Cyg (Elias 1978, Peneva et al. 2009), V733 Cep (Reipurth et al. 2007, Peneva et al. 2010), V2493 Cyg (Semkov et al. 2010, 2012), V582 Aur (Semkov et al. 2013) the presence of an optical outburst is also documented and they are labeled classical FUors. About a dozen objects have spectroscopic properties similar to the classical FUors, but there is no evidence of an outburst at optical wavelengths. These objects are termed FUor-like (Reipurth et al. 2002, Greene et al. 2008) and only partial photometric observations have been published for them.

2 Observations

The photometric observations of FUor and FUor-like objects were performed with the 2 m RCC, the 50/70 cm Schmidt and the 60-cm Cassegrain telescopes of the National Astronomical Observatory Rozhen (Bulgaria) and with the 1.3 m RC telescope of the Skinakas Observatory¹ of the Institute of Astronomy, University of Crete (Greece). The observations were per-

¹Skinakas Observatory is a collaborative project of the University of Crete, the Foundation for Research and Technology - Hellas, and the Max-Planck-Institut für Extraterrestrische Physik.

formed with eight different types of CCD cameras Photometrics AT200 and VersArray 1300B at the 2-m RCC telescope; Photometrics CH360 and ANDOR DZ436-BV at the 1.3-m RC telescope; SBIG ST-8, SBIG STL-11000M and FLI PL16803 at the 50/70-cm Schmidt telescope; FLI PL09000 at the 60-cm Cassegrain telescope. The technical parameters and specifications of the used CCD are summarized in Ibryamov et al. (2015). All frames were exposed through a set of standard Johnson-Cousins filters. All the data for each object were analyzed using the same apertures and the same background annulus. In this way, we have reached the maximum correspondence of data obtained from different telescopes.

In order to facilitate transformation from instrumental measurement to the standard Johnson-Cousins system for each of the studied objects we are calibrated a sequence of photometric standards. Calibration in *BVRI* bands was made during several completely clear nights with the 1.3-m RC telescope in Crete, where the conditions for precise photometric observations are very good.

3 Archival photographic observations

The construction of the historical light curves of FUors could be very important for determining the exact moment of the beginning of the outburst and the time to reach the maximum light. Another important option is to study the pre-outburst variability of the star. The only possibility for such a study is a search in the photographic plate archives at the astronomical observatories around the world. Most suitable for this type of research are the plate archives of the big Schmidt telescopes that have a large field of view. Photographic observations from BAO could also be used for these purposes after the implementation of the Byurakan Astrophysical Observatory Plate Archive Project (Mickaelian et al. 2017).

In this paper, we present some of our result using the photographic plate archives of the 105/150 cm Schmidt telescope at Kiso Observatory (Japan), the 67/92 cm Schmidt telescope at Asiago Observatory (Italy) and the 2-m RCC and the 50/70 cm Schmidt telescopes at NAO Rozhen (Bulgaria). We also used the digitized plates from the Palomar Schmidt telescope, available via the website of the Space Telescope Science Institute.

The plates from Asiago Schmidt telescope are inspected visually through a high-quality Carl Zeiss microscope offering a variety of magnifications. The magnitude is then derived by comparing the stars in the photometric sequence with the variable, identifying those that are more closely bracketing the variable. The plates from Kiso Schmidt telescope were scanned with Canon CanoScan LiDE 600F portable scanner, which has 1200 dpi resolution. The plates from NAO Rozhen were scanned with Epson Expression 1640 XL/10000XL scanners, which have 1600-2400 dpi resolution and a cor-

responding pixel size from $16 \times 16 \mu\text{m}$ to $10 \times 10 \mu\text{m}$. Aperture photometry of the digitized plates was performed with DAOPHOT routines using the same aperture radius and the background annulus as for CCD photometry.

4 Results and discussion

4.1 V2493 Cyg

The large amplitude outburst of V2493 Cyg was discovered during the summer of 2010 (Semkov & Peneva 2010, Miller et al. 2011, Semkov et al. 2012). The new FUor candidate is located in the dark clouds (so-called "Gulf of Mexico") between NGC 7000 and IC 5070 a region of active star formation. Simultaneously with the optical outburst appearance of a reflection nebula around V2493 Cyg typical of all classical FUor objects was observed. Follow-up photometric observations recorded an ongoing light increase in both the optical and infrared (Kóspál et al. 2016, Semkov et al. 2017). The high and low resolution spectroscopic observations by Miller et al. (2011), Lee et al. (2015), Semkov et al. (2017) showed significant variability in both the profiles and intensity of the spectral lines. On the basis of our photometric monitoring and the spectral properties at the maximal light (a G3I supergiant spectrum with strong P Cyg profiles of $\text{H}\alpha$ and Na I D lines), we have confirmed that the observed outburst of V2493 Cyg is of FUor type (Semkov et al. 2012).

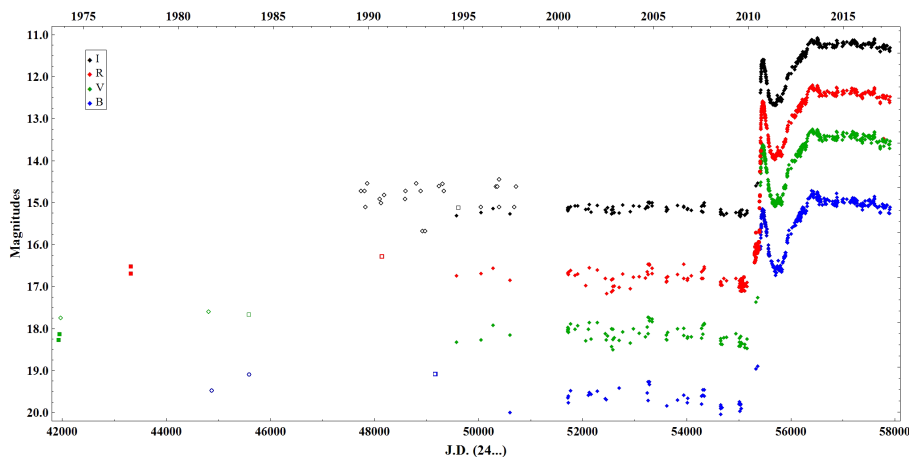


Figure 1: Long term *BVRI* light curves of V2493 Cyg.

The *BVRI* light-curves of V2493 Cyg during the period September 1973 – May 2017 are plotted in Fig. 1. The filled diamonds represent our CCD observations, the filled circles CCD observations from the Palomar Schmidt telescope, the open diamonds photographic data from the Asiago Schmidt telescopes, the open squares photographic data from the Palomar Schmidt

telescope, the filled squares photographic data from the Byurakan Schmidt telescope and the open circles photographic data from the Rozhen 2-m RCC telescope. The photometric observation obtained before the outburst displayed only small amplitude variations in all pass-bands typical of T Tauri stars. The observational data indicate that the outburst started sometime before May 2010, and reached the first maximum in September/October 2010. Since October 2010, a slow fading was observed and up to May 2011 the star brightness decreased by 1.4 mag. (V). Since the autumn of 2011, another light increase occurred and the star became brighter by 1.8 mag. (V) until April 2013. During the period April 2013 - May 2017 the star continues to keep its maximum brightness showing a little bit fluctuations around it. V2493 Cyg was the first FUor object observed in all spectral ranges during the rise of the brightness as well as during the first year after reaching the maximum brightness.

4.2 V582 Aur

An object with a very strong increase in brightness is discovered by Anton Khruslov (Samus 2009) in the region of active star formation near Auriga OB2 association. The star was cataloged as USNO A2.0 1200-03303169 and according to the General Catalog of Variable Stars as V582 Aur. Munari et al. (2009) obtained the first low-resolution spectrum of V582 Aur and registered the presence of absorption lines of the Balmer series, Na I D and Ba II (λ 6496) and the absence of the Li I (λ 6707) line in the spectrum. Our results from detailed photometric and spectral observations of the star were reported in Semkov et al. (2013). In the paper we come to the conclusion that V582 Aur has all observational characteristics of FUor objects.

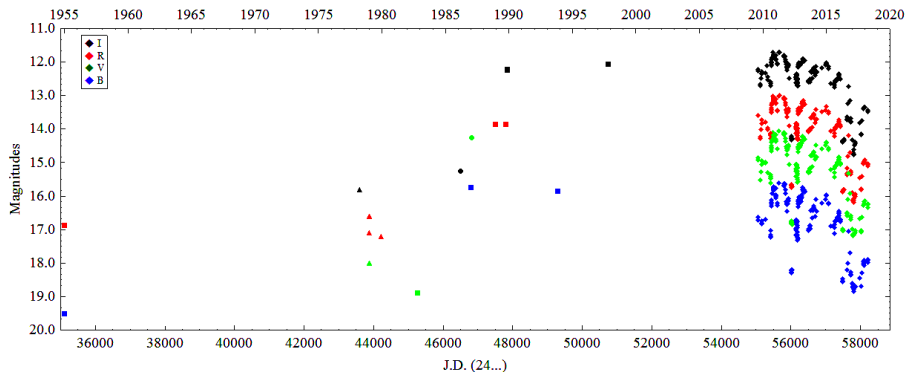


Figure 2: Long term $BVRI$ light curves of V582 Aur.

The historical $BVRI$ light curves of V582 Aur from all available photometric observations are plotted in Fig. 2. On the figure, the filled diamonds represent our CCD observations, the filled circles photographic data from

the 67/92 cm Asiago Schmidt telescope, the filled triangles photographic data from the 105/150 cm Kiso Schmidt telescope, and the filled squares photographic data from the Oschin Schmidt Telescope on Palomar. Typical for this FUor object is a very strong variability with a large amplitudes. During the large drop in brightness on 2012, the spectrum of V582 Aur change from a typical FUor to typical T Tauri star spectrum. And also during this period the star indicate the typical for UX Orionis objects effect of color reversal due to the appearance of dust particles in the circumstellar environment (Semkov et al. 2013).

4.3 V1547 Ori

The outburst of PMS star V1647 Ori was discovered by amateur astronomer Jay McNeil in January 2004 (McNeil 2004). The star showed an increase in optical brightness by around 5 mag. beginning from November 2003 till February-March 2004 (Briceño et al. 2004). V1647 Ori remains in a state of maximal light about two years, then its brightness declined to the pre-outburst level. During the outburst V1647 Ori exhibited a strong emission spectrum in the optical and near-IR, typical for eruptive PMS stars from EXor type (Herbig 2008). A second outburst of the star was registered in 2008, when its brightness increased again to the level of the first eruption (Kun 2008). The optical and infrared follow-up observations show that the star and the surrounding nebula appear photometrically and morphologically similar to the first outburst.

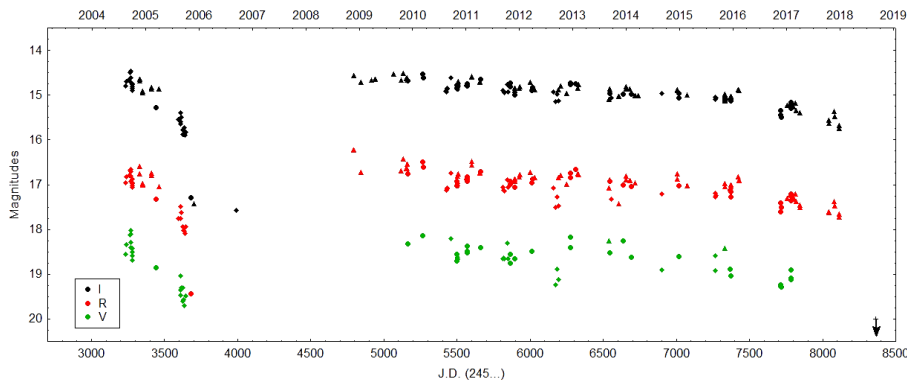


Figure 3: *VRI* light curves of V1547 Ori during the first and second outburst. Only data from our photometric monitor are plotted. The observation limit of the 2-m RCC telescope (September 1 and 2, 2018) is indicated by an arrow.

Our observations suggest that the second outburst of V1647 Ori continued for approximately ten years. At the beginning of September 2018, we recorded a new drop in the brightness of the object, which is below the

2-m RCC telescope I-band limit. The photometric data show a continuous slight decrease in brightness during the period from the end of 2008 to the beginning of 2018. In the meantime the star becomes redder with decreasing of brightness. According to Aspin et al. (2009) the decrease in brightness of V1647 Ori over the period 2006-2008 was caused by reduction in accretion rate and reformation of dust in the circumstellar environment of the star. Such interpretation of the observational results leads Aspin et al. (2009) to the hypothesis that V1647 Ori is a FUor object.

4.4 Parsamian 21

Parsamian 21 is a young stellar object surrounded by an extended reflection nebula, located in a small dark cloud in Aquila. The object was discovered on the plates from the Palomar Observatory Sky Survey and included in the catalog of cometary nebulae (Parsamian 1965). On the basis of optical spectroscopic and far-infrared properties Staude & Neckel (1992) suggest affiliation of Parsamian 21 to the group of FUor objects. Results supporting the FUor nature of Parsamian 21 were published in Kóspál et al. (2008). Parsamian 21 was a subject of many studies, but very few optical photometric data have been published to the present. Since no outburst was observed at optical wavelengths in most of the studies Parsamian 21 is classified as FUor-like object (Greene et al., 2008).

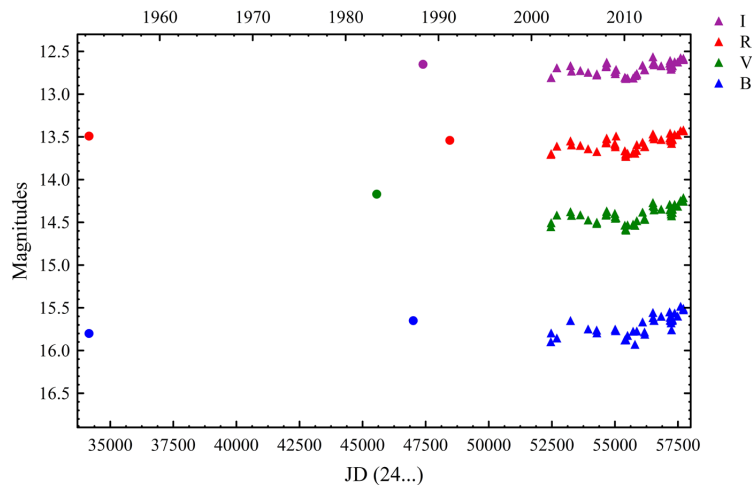


Figure 4: Long term *BVRI* light curves of Parsamian 21. The filled triangles represent our CCD observations, and the filled circles photographic data from the Palomar Schmidt telescope.

Our CCD photometric observations of Parsamian 21 in the period 2003 - 2017 show that the brightness of the star is almost steady. We observed only low amplitude fluctuations around the middle values. Comparing our

CCD photometric observations with the data from Palomar plates showed no significant change in the brightness of the star for a very long period (65 years). We conclude that Parsamian 21 is probably a member of the group of long-lived FUors and that the time-scale of the FUor phenomenon in some cases is much longer than that predicted in previous studies.

5 Summary

Photometric results presented in this paper show the usefulness of systematic photometric monitoring of the regions of star formation. These data can be used to detect new FUor or EXor events and to determine the type of the registered outbursts. Therefore, the collection of new photometric data (from photographic plate archives and ongoing photometric monitoring) will be of great importance for study of PMS variability. At the same time, according to existing observations the light curves of FUor objects, confirming the hypothesis that each known FUor has a different rate of increase and decrease in brightness and a different light curve shape.

Acknowledgements

The authors thank the Director of Skinakas Observatory Prof. I. Papamastorakis and Prof. I. Papadakis for the award of telescope time. This work was partly supported by the Bulgarian Scientific Research Fund of the Ministry of Education and Science under the grants DM 08-2/2016, DN 08-1/2016, DN 08-20/2016 and DN 18-13/2017 as well as by the project RD-08-112/2018 of the University of Shumen. This research has made use of the NASA's Astrophysics Data System Abstract Service, the SIMBAD database and the VizieR catalogue access tool, operated at CDS, Strasbourg, France. Some of the data presented in this paper were obtained from the Mikulski Archive for Space Telescopes (MAST). STScI is operated by the Association of Universities for Research in Astronomy, Inc., under NASA contract NAS5-26555.

References

- Ambartsumyan, V. A. 1971, *Astrophysics*, 7, 331
Aspin, C.; Reipurth, B. 2009, *AJ*, 138, 1137
Aspin, C.; Reipurth, B.; Beck, T. L. et al. 2009, *ApJ*, 692, L67
Audard, M., Ábrahám, P., Dunham, M. M., et al. 2014, in *Protostars and Planets VI*, ed. H. Beuther et al. (Tucson, AZ: Univ. Arizona Press), p. 387
Briceño, C., Vivas, A. K., Hernandez, J. et al. 2004, *ApJ*, 606, L123
Clarke, C.; Lodato, G.; Melnikov, S. Y.; Ibrahimov, M. A. 2005, *MNRAS*, 361, 942
Connelley, M. S.; Reipurth, B. 2018, *ApJ*, 861, 145
Elias, J. H. 1978, *ApJ*, 223, 859
Greene, T. P.; Aspin, C.; Reipurth, B. 2008, *AJ*, 135, 1421
Hartmann, L.; Kenyon, S. J. 1996, *ARA&A*, 34, 207
Herbig, G. H. 1977, *ApJ*, 217, 693
Herbig, G. H. 2008, *AJ*, 135, 637
Herbst, W.; Herbst, D. K.; Grossman, E. J.; Weinstein, D. 1994, *ApJ*, 108, 1906
Ibrayamov, S. I.; Semkov, E. H.; Peneva, S. P. 2015, *PASA*, 32, id. e021
Kóspál, Á.; Ábrahám, P.; Apai, D. et al. 2008, *MNRAS*, 383, 1015
Kóspál, Á.; Ábrahám, P.; Acosta-Pulido, J. A. et al., 2016, *A&A*, 596, A52
Kun, M. 2008, *IBVS*, 5850, 1
Lee, J.-E., Kang, W., Lee, S.-G. et al. 2011, *JKAS*, 44, 39
McNeil, J. W. 2004, *IAU Circ.*, 8284

- Mickaelian, A. M.; Gigoyan, K. S.; Gyulzadyan, M. V. et al. 2017, *ComBAO*, 64, 102
Miller, A. A.; Hillenbrand, L. A.; Covey, K. R. et al., 2011, *ApJ*, 730, 80
Munari, U.; Siviero, A.; Ochner, P.; Fiorucci, M.; Dallaporta, S. 2009, *CBET*, 1898, 1
Parsamian E. S. 1965, *Izv. Akad. Nauk Armyan. SSR., Ser. Fiz.-Math.*, 18, 146
Peneva, S. P.; Semkov, E. H.; Munari, U.; Birkle, K. 2010, *A&A*, 515, A24
Peneva, S. P.; Semkov, E. H.; Stavrev, K. Y. 2009, *Ap&SS*, 323, 329
Reipurth, B.; Hartmann, L.; Kenyon, S. J.; Smette, A.; Bouchet, P. 2002, *AJ*, 124, 2194
Reipurth, B.; Aspin, C., 2010, in *Evolution of Cosmic Objects through their Physical Activity*, eds. H. A. Harutyunian, A. M. Mickaelian, Y. Terzian (Yerevan: Gitutyun), p. 19
Reipurth, B.; Aspin, C.; Beck, T. et al. 2007, *AJ*, 133, 1000
Samus, N. 2009, *CBET*, 1896, 1
Semkov, E. H.; Peneva, S. P.; Munari, U.; Milani, A.; Valisa, P. 2010, *A&A*, 523, L3
Semkov, E. H.; Peneva, S. P.; Munari, U. et al. 2012, *A&A*, 542, A43
Semkov, E. H.; Peneva, S. P.; Munari, U. et al. 2013, *A&A*, 556, A60
Semkov, E. H.; Peneva, S. P.; Ibryamov, S. I. 2017, *Bulg. Ast. J.*, 26, 57
Staude, H. J.; Neckel, Th., 1992, *ApJ*, 400, 556

Simultaneous photometric and spectral analysis of new outburst of V1686 Cyg

H. R. Andriasyan^{1*}, T. Yu. Magakian¹, T. A. Movsessian¹,
M. H. Gevorgyan¹

¹NAS RA V. Ambartsumian Byurakan Astrophysical Observatory (BAO), Armenia

*E-mail: hasmik.andriasyan@gmail.com

Abstract

We present an analysis of the optical observations of Herbig AeBe star V1686 Cyg, which is demonstrating photometric variability up to 3 to 4 magnitudes. We observed this star as a part of our project of young eruptive stars investigation. Observations were performed on 2.6m telescope of Byurakan Observatory. In the course of observations we noticed that this star underwent a new outburst. After data reduction we found that full rise and decline of V1686 Cyg brightness for almost 3 magnitudes lasted about 2 months. We were able to trace the changes of the stellar spectrum during the outburst. They are discussed and compared with other young eruptive variables.

Keywords: *stars – variables – T Tauri – Herbig Ae/Be – photometry – spectroscopy.*

1 Introduction

LkH α 224 is Herbig AeBe star with characteristic H α emission. It is located in the vicinity of bright BD+404124 star, which is showing very strong H α line in emission. For the first time this star was mentioned by Herbig (1960), when he studied AeBe stars connected with bright nebulosities. There are other emission line stars near this object, e.g. V1318 Cyg, so they create a small cluster of young stars. Optically brightest member of this cluster is BD+404124, which itself is Herbig Be star. Shevchenko et al (1991) estimate a distance to this group as 980 pc. In general this region is embedded in the dense molecular cloud. The most complete information about photometric behavior of LkH α 224=V1686 Cyg so far is collected in the work of Shevchenko et al. (1991). Based on their observations, the star demonstrates irregular variability: 2 mag outbursts of four-five days duration, with about 2 months of minimum brightness between. Beside

these short-term variations, this star shows also long-term variations: it decreased in brightness by more than 4.5 mag in 7.5 yr, and then raised its brightness by 4 mag in 4 yr. In the survey of Herbst & Shevchenko (1999) of UBV_R photometry of Herbig AeBe stars, carried out since 1983, they estimate $V=14.07$ for V1686 Cyg mean brightness, while Hillenbrand et al. (1995) found out $V=16.13$. Concerning the spectrum of this star, it should be noted that no final agreement on its spectral type exists. The prominent variations of absorption features make classification process very problematic. Hillenbrand et al. (1995) suggest spectral type B5Ve, while Mora et al. (2001) estimated the spectral type to be A4, but with more than 5 subclasses error. Hernandez et al. (2004) obtained spectra of all Herbig AeBe stars from the Herbig-Bell Catalog (Herbig & Bell 1988) and noticed that spectrum of V1686 Cyg looks very different compared to the previous observations, and classified it as F9. In the work of Magakian et al. (1997) the spectrum of V1686 Cyg was studied in details. They confirmed that this star is an early-type star, where only the broad H α emission with an asymmetric profile is visible in the optical range. There are no detailed studies of this star during its brightening phase, so this work will for the first time show the differences in the spectrum of V1686 Cyg in two phases.

2 Observations

In 2015 we started our project on investigation of eruptive stars. Observations were carried out on 2.6 m telescope in Byurakan Observatory. We used SCORPIO spectral camera, and obtained direct images, as well as long-slit spectra. As an object of our previous interests we started our observations for V1318 Cyg young variable star, and at the same time obtained data for the neighbor V1686 Cyg star. Observations were implemented from September 2015 to July 2017. Data reduction was done in the usual way, using IRAF and ESO-MIDAS programs. Photometric estimations were done by aperture photometry. For calibration we used several stars in the field, measured by Hillenbrand et al. (1995) and Shevchenko et al. (1991). The typical errors for our data are about $0^m.02 - 0^m.03$. We also obtained spectra for this star from Sept. 2015 to Dec. 2016, with different spectral resolutions: 0.50, 0.80, 1.50 and 2.65 Å/pix.

3 The new outburst of V1686 Cyg

In the period of Sept. 2015 – Aug. 2016 V1686 Cyg did not show any significant variability. But in Aug. 2016, during our regular observation we noticed that V1686 Cyg raised its brightness. In Fig. 1 we see the appearance of the star before the outburst, while in Fig. 2 it is already raised its brightness. For the comparison we found out the images of IPHAS

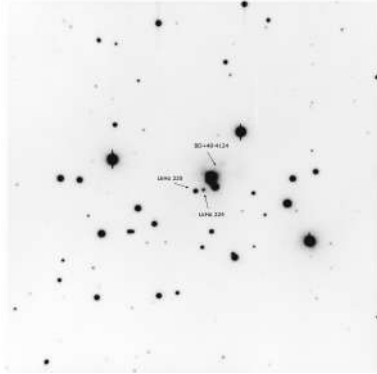


Figure 1: Before the outburst

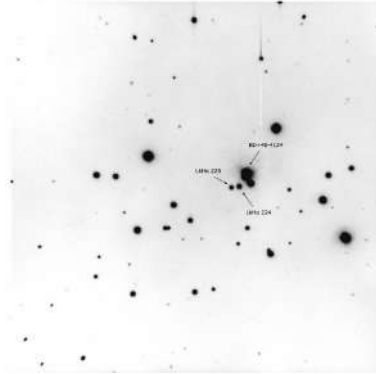


Figure 2: During the outburst

survey in R, I bands, and estimated the brightness of the star in 2003-2006. The continuation of our observations demonstrated that V1686 Cyg star raised its brightness for almost 3 magnitudes for 2-3 months, and then again gradually came to its typical appearance in minimum. In the Table 1 and Table 2 we present the results of our photometry of 2.6 m telescope images and IPHAS survey images correspondingly. Such type of brightness fluctuations is usual for this star and is in a good agreement with the previous works, described above.

Date	B	V	R	I
22.09.2015	17.22	15.88	14.68	13.27
18.11.2015	17.18	15.96	14.87	13.56
31.03.2016	17.03	15.61	14.48	13.07
10.06.2016	17.42	16.05	14.76	13.00
23.08.2016	14.82	13.50	12.48	11.58
20.12.2016	16.34	14.98	13.62	12.49
17.07.2017	16.99	15.66	14.63	13.53

Table 1: V1686 Cyg photometry

Year	R	I
2003	13.29	13.37
2004	15.00	13.90
2006	14.98	13.79

Table 2: Photometry of IPHAS images of V1686 Cyg star

4 Spectrum of V1686 Cyg in minimum

As was pointed out above, we obtained the spectra of V1686 Cyg during the whole period of its outburst. First spectra, taken before the outburst, are quite typical for this star, and very similar to description of Magakian & Movsessian (1997). One can see broad $H\alpha$ in emission, and [OI] and [SII] forbidden lines, which belong to background nebulosity around the star. After the ending of outburst, in Nov. 2016, spectrum looks the same way, without any significant differences.

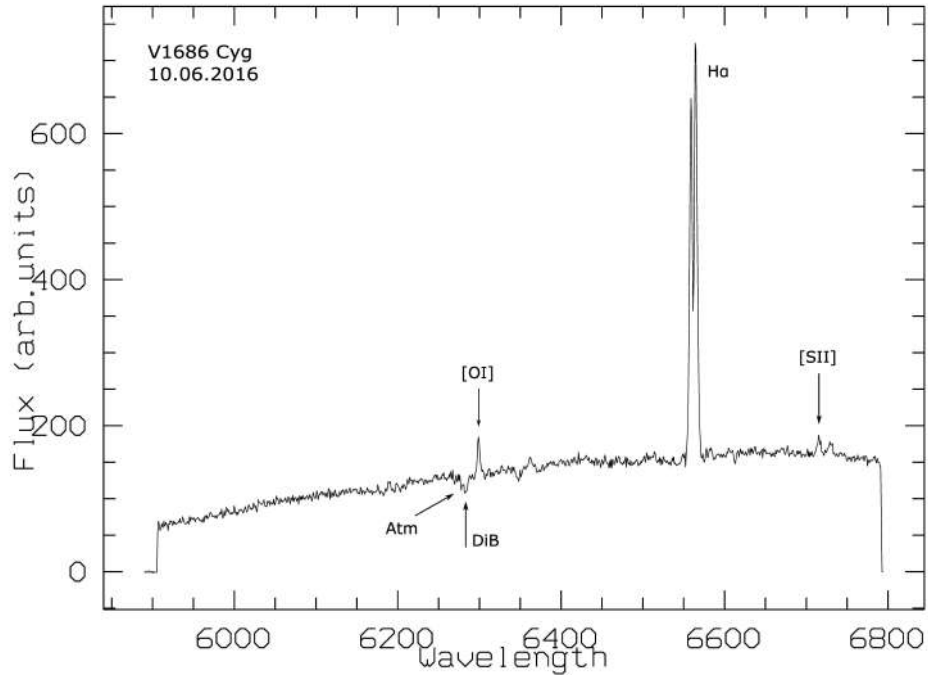


Figure 3: Spectrum of LkH α 224 in minimum

5 Spectrum of V1686 Cyg in maximum

Spectrum of Aug. 24 of 2016 corresponds to the outburst of V1686 Cyg. It keeps its appearance at least until Aug. 30 of 2016. We do not know exactly when the star started lowering its brightness. The next spectrum we obtained in Nov. 6, when this star returned to its mean brightness, and it does not differ from the spectra before the outburst. One can see that during the outburst V1686 Cyg spectrum is quite different and has remarkable changes especially in the profile of $H\alpha$ line: it has narrow, but very deep, lowering down the continuum absorption component, superposed on the bright emission. Besides, in maximum one can notice a variety of

low-excitation FeI and FeII emission lines.

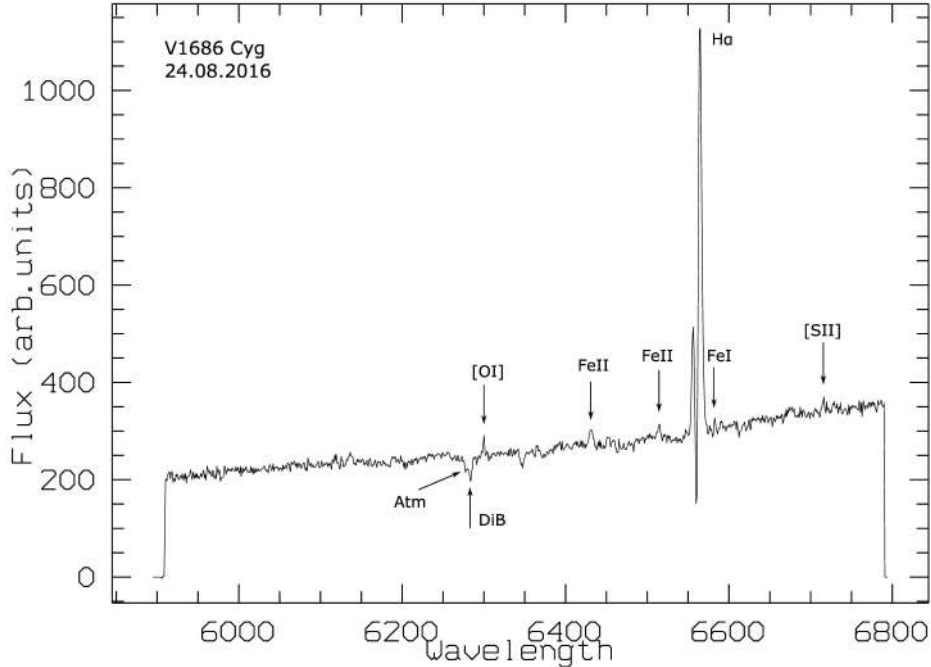


Figure 4: Spectrum of LkH α 224 during the outburst

Besides, it is ought to mention that in both minimum and maximum spectra we detected diffuse interstellar band (DIB) 6284 Å, which is distinguished from the nearby atmospheric absorption line 6278 Å. This DIB is among the strongest ones (Herbig 1995).

6 Summary

The new photometric and spectroscopic data confirm, that V1686 Cyg is HAeBe type star, which constantly vary its brightness for 2-3 magnitudes, with maxima about 1-2 months duration. Spectral type of this star could be early A.

The prominent changes in its spectrum in maximal and quiescent states, observed in detail for the first time, unambiguously show that such outbursts are accompanied with significant increase of mass loss from the star. From the H α line profile changes and appearance of iron emission lines we can conclude that during the outburst the star became surrounded by an enlarging envelope which afterwards dissipates into space.

We should also note, that this star is immersed in dense molecular core, so λ 6284 Å DIB line which is detected in both minimum and maximum spectra of V1688 Cyg, is probably related with this cloud.

References

- Herbig, G. H. 1960, *ApJ* 4, 337
Herbig, G. H. 1995, *A&A*, 33, 19
Herbig, G. H., & Bell, K. R. 1988, Third catalog of emission-line stars of the Orion population., *cels.book*, 90p.
Herbst, W., & Shevchenko, V. S., 1999, *AJ* 118, 1043
Hernández, J., Calvet, N., Briceño, C., Hartmann, L., & Berlind, P. 2004, *A&A*, 127, 1682
Hillenbrand, L. A.; Meyer, M. R.; Strom, S. E.; Skrutskie, M. F. 1995, *AJ* 109, 280
Shevchenko, V. S. 1991, *SvA* 35, 229
Magakyan, T. Y., & Movsesyan, T. A. 1997, *AstL*, 23, 666
Mora, A.; Merín, B.; Solano, E.; et al. 2001, *A&A* 378, 116

Old and New Observational Data of P Cygni

S. Beradze^{1,2*}, N. Kochiashvili¹, R. Natsvlishvili¹, I. Kochiashvili¹,
M. Vardosanidze^{1,2}

¹*E. Kharadze Abastumani Astrophysical Observatory, Ilia State University*

²*Samtskhe-Javakheti State University*

**E-mail: sopia.beradze.1@iliauni.edu.ge*

Abstract

Luminous Blue Variables (LBV) are extremely rare and enigmatic stars on the short-lived evolutionary phase with different variation scales of brightness and spectrum. Some of them are confirmed binary systems and even secondary components have found by direct imaging. The blue supergiant P Cygni is one of the prototypes of LBVs, showing photometric and spectroscopic variability on various timescales. We are going to present results of the old and new photometric observations of P Cygni. Old 1951-1983 years photometric observations were made by E. Kharadze and N. Magalashvili in the Abastumani Astrophysical Observatory, Georgia, during which they found, recalculated and made conclusion that the star should undergone the next great eruption in some 100 years. New observations were obtained in 2014, using the 48 cm Cassegrain telescope of the Abastumani Observatory. Some interesting behaviors of the light curves were revealed.

Keywords: *UBVRI photometry - Luminous Blue Variable Stars - P Cygni.*

1. Introduction

P Cygni is one of the most luminous stars of the Galaxy. It has been classified as an Luminous Blue Variable (LBV) after two major outbursts in 1600 and 1655. The term Luminous Blue Variable was imported by P. Conti in 1984 and combined the P Cygni type stars, S Dor variable and Hubble-Sandage variable (Conti 1984). LBVs are descendants of massive O stars, which are nearly to the end of the core hydrogen burning. They undergo episodic mass-loss and probably represent a transition between the most massive O star and the red supergiant and/or W-R stage (Massey 2006). They are characterized by large variability of amplitudes and violent mass ejections. They have unusually high mass loss rates ranging from 10^{-6} up to $10^{-3}M_{sun}/yr$.

LBVs are extraordinary, because they can show different type of photometric and spectroscopic variations. Three types of variability of Luminous Blue Variables are known:

1. Micro-variations with 0.1 mag. amplitude and comparatively small time-scale variations from days to weeks or months;
2. S Dor type variations or outbursts with amplitudes of 0.5 mag.;
3. Large sporadic outbursts with amplitude > 2 mag. on a time-scale of 100 years.

In 1600 Dutch chart-maker, mathematician and geographer W. J. Blaeu recorded P Cygni (34 Cyg) as a nova. Giant eruption occurred in 1600, followed by four, compared with the first one, less capacity eruptions, which began in 1655 and ended in 1684. Analysis of historical observations of P Cygni has shown that between 1700 and 1988 its overall brightness slowly increased by 0.15 ± 0.02 mag/century and reached its current value of $V=4.82$ (Israelian & de Groot, 1999).

P Cygni is an early B(B1Ia) spectral type hypergiant star. The first spectra of P Cygni, obtained as early as 1897, already shown the famous P Cygni-type spectral lines - an undisplaced emission accompanied by a short-ward displaced absorption core. Initially this was interpreted as a blend of two different lines. McCrea (1929) and Beals (1930) were the first to interpret P Cygni-type profiles in novae, Wolf-Rayet stars and P Cygni itself as due to a radially expanding stellar envelope.

Early serious, detailed analysis of P Cygni spectrum has been carried out by Beals (1950), Hutchings (1969), and de Groot (1969). Later, Stahl et al. (1993) have published spectral atlases with identifications of many weak lines in the visual spectral range. Skinner et al (1996) presented radio observation of the P Cyg, which revealed the nature and speed of its variability at radio wavelengths and the size and structure of the radio nebula. P Cyg's nebula is harder to observe than the Homunculus of η Car because contrast with the central star is very faint at all wavelengths. Study the near IR spectrum of P Cygni Smith Hartigan (2006) show that the total mass of P Cygni nebula is about $0.1 M_{sun}$.

P Cygni is located on the upper part of the Hertzsprung-Russell (HR) diagram populated by different types of emission-line stars, including Of supergiants, B[e], LBVs, and Wolf-Rayet stars (Israelian & de Groot 1999). It was found that P Cyg has three different type variations: 1. Short, 17 days variation; 2. 100 days variation, which is also observed in LBVs; and 3. Long-period variation of several years period.

P Cygni is the nearest LBV, at a distance of 1.7 kpc. At present estimated that its mass is $30 M_{sun}$, however initially it might have been $50 M_{sun}$, but portion of the mass was lost during evolution. The effective temperature is $T_{eff} = 18200$ K, radius - $R=75 R_{sun}$ and Luminosity of $L= 5.6 \times 10^5 L_{sun}$. A. Kashi (2010) suggested that P Cyg has a companion star with approximately 3-6 solar masses and with orbital period of 7 years. Using

photometric observations taken from AAVSO databases and photometric data from Abastumani Observatory obtained during 1951-1983 Michaelis et al (2018) found that the P Cyg companion orbital period should be 4.7 years.

2. Observations of P Cygni in Abastumani

Observations of P Cygni were held in the Abastumani Astrophysical Observatory from its very establishment. Two articles are published (Nikonov, 1937 and Kharadze, 1937). Photoelectric observations of P Cyg were made using 33 cm reflector. The telescope was equipped with electro-photometer with maximum of spectral sensitivity at 4350 Angstrom of wavelength. The photometric system was similar with Johnson's B band (color).

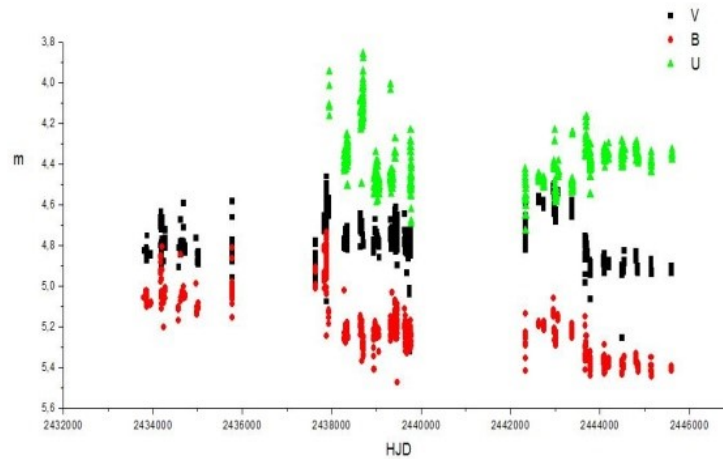


Figure 1: UBV observations of P Cygni made by E. Kharadze and N. Magalashvili during 1951-1983. 36 Cygni = HD 193369 used as a comparison star.

From 1951 N. Magalashvili and E. Kharadze were regularly observing P Cyg, using 33 cm reflector with electro-photometer. B and V filters were used during 1951-1960 and then, after 1961, U, B and V filters instead. On the basis of these above-mentioned observations, Magalashvili and Kharadze made conclusion that the behavior of the star was similar to W UMa variability, with the period of 0.500565 d and 0.10-0.08 mag. (Magalashvili & Kharadze, 1967). The article gained great attention from the investigators of variable stars, but W UMa variability was not confirmed. Kharadze and Magalashvili continued observing the star until 1983. After 1968 they used the same filters and the same photometer with the 48 cm Cassegrain telescope of the Abastumani Observatory. We had the opportunity to re-process

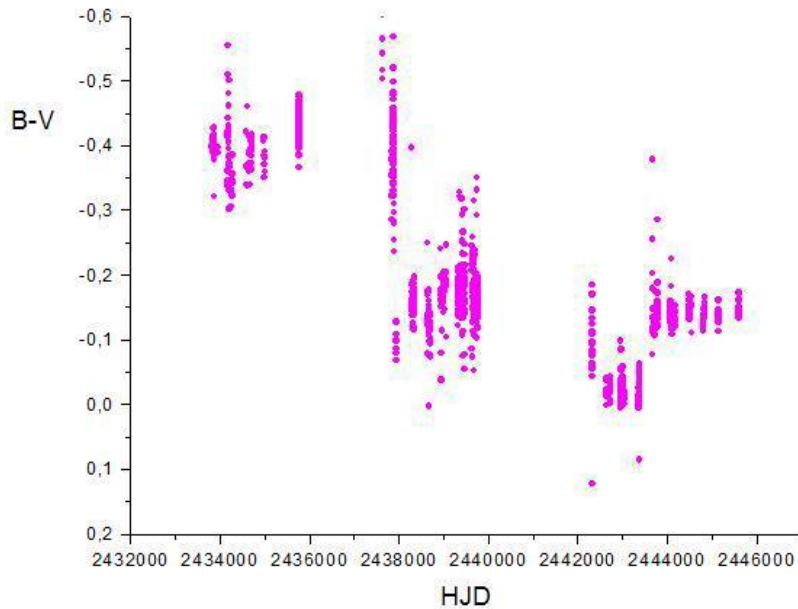


Figure 2: Color behavior of P Cygni during 1951-1983. The star became redder by at least 0.4: B-V changed from -0.5 to -0.1 during 1951-1983.

the observations and calculate difference of brightness between the variable and 36 Cyg, which gave us a real light variation of P Cyg and we are giving these UBIV data on Fig. 2.

At the first glance we can see that during 1974-1983 years the star was dimmed in U band while brightened in B and V bands (the last third part of the Fig. 1). The middle part of the figure represents time interval of 1961-1967 and here the color behavior of the star is different: during brightening in V band the star is fainter in B and U.

3. Quasi-periods of P Cygni

According to the above mentioned photometric data by Magalashvili and Kharadze, it seems that the star has different longer and shorter quasi-periodic flux variability:

1. (1480 ± 31) days; (736 ± 27) days (29 Cyg (HD 192640) used as a comparison star).
2. (1123 ± 36) days; ~ 579 days and ≈ 128.7 days 36 Cyg (HD 193369) used as a comparison star). Short quasi-period was also revealed $\sim 15-18$ days. Long-period variability maybe due to the binarity of the star.

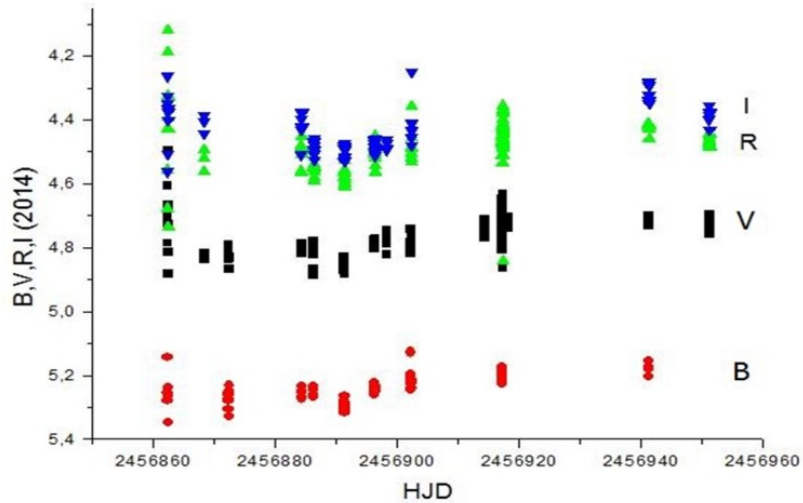


Figure 3: BVR,I photometric Observations of P Cygni during 2014.

4. Colour behavior of P Cygni

Long-term photometric observations of P Cygni gives us possibility to trace B-V color variability of the star. Accepted, that P Cygni gradually reddens. This reddening is very impressive in the observations by Kharadze and Magalashvili, because (after correcting for the reddening by 0.5 B-V value) it varies from -0.5 to -0.1 from 1951 up to 1983 (left part of Fig.2). The star's color corresponds to the early B-spectral type.

5. Photometric observations of P Cygni in 2014

We observed P Cygni during July 23 - October 20, 2014 using the 48 cm Cassegrain telescope and standard B,V,R,I filters. HD 228793 ($V = 9.9$, $B = 10.16$) has been used as a comparison star (see Fig. 3). We revealed that during our observations the star underwent light variations with the mean amplitude of approximately 0.1 magnitudes in all pass-bands and the period of this change was approximately 68 days.

6. Conclusion

So, we revised observational data of P Cyg obtained during 1951 - 1983 and in 2014 in the Abastumani Astrophysical Observatory. Observations of P Cygni obtained by Kharadze and Magalashvili at the Abastumani Obser-

vatory are very significant due to the following reasons:

1. they represent homogenous data of more than 30 years;
2. There are UBV observations and we can trace colour behavior of the star;
3. The observations by Kharadze and Magalashvili are unique because they are the only existing data of P Cygni observed with UBV filters between 1951 and 1983.

We need more observational data and detailed analysis because we still have some unanswered questions like, for example, the binarity of P Cyg. The mechanism of great eruptions is still not established. Also the connection between stellar rotation, pulsation and magnetic fields of P Cyg are not very clear so far.

References

- Abott, R. I; Tse, S.F.; 1984, in Proceedings of the Conference, Lake Placid, NY, August 22-25, 1983. Part 1 (A84-30526 13-13). San Diego, CA, Univelt, Inc., p. 543
- Barlow, M.J; Cohen, M., 1977, ApJ, 213, 737
- Beals, C.S. 1984, Journal of the Royal Astronomical Society of Canada, 24, 277
- Conti P. S 1984, in Proceeding of International Astronomical Union Symposium No. 105, p. 233
- de Jager, C.; Israelian, G. 2003, New Astronomy, 8, Is. 5, 475
- de Groot, M.; Stercken, C. 2001, P Cygni 2000: 400 Years of Progress. The Publications of the Astronomical Society of the Pacific, Vol. 113, Is. 780, 258
- de Groot, M. 1969, Communications of the Konkoly Observatory, No. 65, 203
- de Groot, M; Sterken, C; van Genderen, A.M. P 2001, P Cygni 2000: 400 Years of progress, ASP Conference Proceeding Vol. 233, 15
- El Eid, M. F; Hartmann, D. H. 1993, ApJ, 404, 271
- Israelian, G.;de Groot, M.1999, Space Science Reviews, 90, 493
- Kashi, A. 2010, MNRAS. 405, 1924
- Kashi, A., Soker, N. 2010, ApJ, 723, 602
- Kochiashvili et al. 2015, in Proceedings of an International Workshop held in Potsdam, Germany, 1-5 June 2015. Edited by Wolf-Rainer Hamann, Andreas Sander, Helge Todt. Universitätsverlag Potsdam, 360
- Kochiashvili et al. 2018, Astrophysics, 61, 22
- Kochiashvili et al. 2018, Astronomy Astrophysics (CAUCASUS), 3, id. 36
- Kharadze E.K., 1937, Bull. Of AbAO, No 1, 45
- Magalashvili N; Kharadze E: 1967, Information Bulletin on Variable

- Stars, 210, 1 Magalashvili, N.L. and Kharadze, E.K.1967, Observatory 87, 295 Massey, P. 2006,ApJ, 238, L93
Michaelis, A. M.; Kashi, A.; Kochiashvili, N. 2018, New Astronomy, 65, 29
McCrea, W.H. 1929,The Observatory, 52, 267
Najarro, F.; Hillier, D. J.; Stahl, O. 1997, AA, 326, 1117
Najarro, F.; Kudritzki, R.; Hillier, D. J.; Lamers, H. J. G. L. M.; Voors, R. H. M.; Morris, P. W.; Waters, L. B. F. M. 1997, "Luminous Blue Variable: Massive stars in Transition". ASP Conference Series, Vol. 120. 105
Percy, J. R. ; Evans, T. D. K.; Henry, G. W.; Mattei, J. A. 2001, P Cygni 2000: 400 Years of Progress, ASP Conference Proceeding, Vol. 233, Edited by M. de Groot and C. Sterken, San Francisco: Astronomical Society of the Pacific. 31
Smith, N.; Hartigan, P. 2006, ApJ, 638, 1045
Stahl, O. 1993, SFB No. 328 'Evolution of Galaxies', Heidelberg, Germany, June 15-17, 1992, p. 263
van Genderen A.M., Sterken C., de Groot M.J.H., 1977, AA, 318, 81
van Genderen A.M., Sterken C., de Groot M.J.H. 1997, AA Suppl, 124, 517
van Genderen A.M. 2001,AA, 366, 508
Waters, L.B.F.M; Wesselius, P.R. 1986, AA, 155. 104

Revised and Updated Catalogue of the First Byurakan Survey Late-Type Stars. 2nd Edition

K. S. Gigoyan^{1*}, A. M. Mickaelian¹, G. R. Kostandyan¹

¹*NAS RA V. Ambartsumian Byurakan Astrophysical Observatory (BAO), Armenia*

**E-mail: kgigoyan@bao.sci.am*

Abstract

Eighteen lists of late-type stars (LTSs) have been published between 1990 and 2016. These LTSs have been found in the low-dispersion spectroscopic plates of the First Byurakan Survey (FBS). The systematic search and selection was carried out on a surface $\sim 16000 \text{ deg}^2$ on almost the whole area of the FBS. As a result, “Revised And Updated Catalogue Of The First Byurakan Survey Of Late-Type Stars” was generated (LTSs, first version). Since 2007, all FBS low-resolution spectral plates are digitized, and Digitized First Byurakan Survey (DFBS) database and second catalog of objects has been assembled. All DFBS spectral plates are analysed with the help of standard image analysis softwares (FITSView and SAO Image ds9) and numerous of comparatively faint LTSs were discovered. We present the 2nd version of the FBS catalogue of LTSs with new data. We have made cross-correlation with the Digitized First Byurakan Survey (DFBS), the United State Naval Observatory-B1.0 Catalogue, the Two Micron All-Sky Survey (2MASS), the Wide-Field Infrared Survey Explorer (new version-ALLWISE) catalogue, the Infrared Astronomical Satellite Point Source Catalogue/Faint Source Catalogue, the AKARI catalogue, the ROSAT Bright Source Catalogue/Faint Source Catalogue, the General Catalogue of Variable Stars, Sloan Digital Sky Survey (SDSS) photometric catalogue. We have added updated SIMBAD data for the objects. For numerous of the new detected objects we present accurate Digitized Sky Survey 2 positions, approximate spectral subtypes refined from the DFBS low-dispersion spectra, luminosity classes estimated from 2MASS colours, and available proper motions for 1471 FBS LTSs. 2nd Version of the Revised and Updated Catalogue lists a large number of completely new objects, which promise to extend very significantly the census of M giants, faint N-type Asymptotic Giant Branch (AGB) carbon stars, CH-type carbon giants at high Galactic latitudes, also M dwarfs in the vicinity of the Sun up to 16.0-17.0 mag. in visual. We present also some important data from the Gaia DR2 data base for FBS LTSs. Some supplementary spectra obtained with

the Byurakan Observatory 2.6 m telescope and LAMOST telescope are shown.

Keywords: *astronomical data bases: miscellaneous - catalogues - surveys - stars: carbon - stars: late-type.*

1. Introduction

The First Byurakan Survey (FBS), known also as the Markarian Survey, was the first systematic objective-prism survey of the extragalactic sky. This survey was conducted by B. E. Markarian, V. A. Lipovetski and J. A. Stepanian from 1965 to 1980. The Photographic plates were obtained using the 1m Schmidt telescope at the Byurakan Astrophysical Observatory (BAO), which was equipped with a 1.5° prism giving a reciprocal dispersion of 1800 Å/mm near H_γ throughout a useful field of $4^\circ \times 4^\circ$. The FBS is the largest area low-resolution spectral survey and covers a total of 17 000 deg², segmented in 28 parallel zones of all the Northern sky and part of the Southern sky at high Galactic latitudes by $\delta > -15^\circ$ and $|b| > 15^\circ$. Later, several other projects based on the FBS were conducted, which resulted in the discovery of various important objects, such as FBS blue stellar objects (BSOs) and late-type stars (LTSs) and in the identification of Infrared Astronomical Satellite (IRAS) sources.

We present in this paper the 2nd updated version of the FBS LTSs Catalogue at high Galactic latitudes, which is a comprehensive list of 1471 objects.

2. The Second Part of the FBS and Late-Type Stars

The second part of the FBS (which started in 1980s) was devoted to the discovery and study of BSOs (Abrahamian & Mickaelian, 1996, and reference therein). The main goal of the second part of the FBS was the discovery of new bright quasi-stellar objects (QSOs), Seyferts, white dwarfs (WDs), subdwarfs (sds), planetary nebula nucleus (PNNs), cataclysmic variables (CVs), and other interesting objects. The results of the investigations of the new FBS of BSOs are summarized and presented by Mickaelian (2008) in the “Revised and Updated Catalogue of the First Byurakan Survey of Blue Stellar Objects”, which contains data for 1103 objects.

The second part of the FBS includes also selection, listing and investigation of faint LTSs at high Galactic latitudes. The large spectral range of the FBS is also suited to identify cool M-type or carbon (C)-type stars. The visual inspection (with help of the eye-piece, with magnification of $15\times$) was used for selecting slitless spectra showing pronounced absorption bands. C stars can be identified through the presence of the Swan bands of

the C_2 molecule at 4737, 5165, and 5636 Å (N-type C stars). Several objects showing the bandhead at 4382Å are early-type C stars (R or CH-type stars). M-type spectra can easily be distinguished because of the titanium oxide (TiO) molecule absorption bands at 4584, 4762, 4954, 5167, 5500, 6200 and 6700Å (the same criteries of selection that used to select the LTSs on objective-prism plates taken with the Burrell Schmidt telescope at Kitt Peak (Stephenson 1986; Sanduleak & Pesch 1988). In practice, the limiting magnitude of the FBS for LTSs is estimated to be 16.0-17.0 in the V-band (Gigoyan et al 2001).

3. Optical Spectroscopy and Classification of FBS LTSs

For FBS LTSs a medium-resolution spectrum was obtained on different epochs with the Byurakan Observatory 2.6-m telescope (UAGS, ByuFOSC2 and SCORPIO spectrographs; Abrahamyan & Gigoyan 1993, Abrahamyan, Hambaryan & Gigoyan 1994; Gigoyan, Mickaelian & Mauron 2006). Medium and high-resolution CCD spectra for FBS C stars were also obtained with the Observatory de Haute-Provence (OHP, France) 1.93-m telescope (CARELEC spectrograph; Gigoyan et al., 2001, Mauron 2008). Moderate-resolution CCD spectra for FBS C stars also were obtained at the 1.83-m Cima-Ekar telescope of the Padova Astronomical Observatory (Italy) equipped with the Asiago faint Objects Spectrometer and Camera (AFOSC) and with the 1.52-m Cassini telescope of the Bologna Astronomical Observatory at Loiano (Italy) equipped with the Bologna Faint Objects Spectrometer and Camera (BFOSC; Gigoyan et al., 2008). All CCD observations, confirms reliability of our preliminary low-resolution spectral class determinations on the FBS plates.

Figure 1 presents 2.6 m Byurakan Astrophysical Observatory telescope moderate-resolution CCD spectra for some objects.

4. LAMOST Spectra

For 179 FBS LTSs moderate-resolution spectra is available in LAMOST (Large Sky Area Multi-Objects Fiber Spectroscopic Telescope) DR2 data base (Luo et al, 2016, CDS VizieR catalog V/149dr2, wavelength coverage 4000-9100Å).

5. Summary

All Digitized First Byurakan Survey (DFBS) spectral plates are analysed with the help of standard image analysis softwares (FITSView and SAO Image ds9) on the base of present of the absorption bands of C₂ and TiO molecule in the low-resolution spectrum of the objects. We revised, updated and generated the new version of the FBS LTSs catalogue. The second version of the catalogue contains main available data for 1471 objects. In revised catalogue we present DSS1/DSS2 accurate positions, USNO-B1.0 catalogue optical photometry and proper motions, WISE IR photometry, et al. for 1471 objects. Among 1471 objects, 127 are carbon stars of the early and late classes. Remaining objects are M giants and dwarfs. Large number of the FBS LTSs are completely new objects, which promise to expand the census of M giants and M dwarfs in the vicinity of the Sun. In combination with new Gaia DR2 data with the existing photometric and spectroscopic data, further studies is needed to clarify the nature of the FBS LTSs, particularly the origin of the high radial velocity M-giants, N-type AGB C stars, and CH-type faint C stars at high Galactic latitudes and in Galactic Halo.

References

- Abrahamyan H. V., Gigoyan K. S., 1989, *Astrofiz.*, 31, 601 (List I)
- Drake A. J., Graham M. J., Gjorgovski S. D., et al., 2014, *ApJS*, 213, 9
- Erastova L. K., Shapovalova A. I., 1989, *Commun. Special Astrophys. Obs.*, 62, 5
- Gigoyan K. S., Abrahamyan H. V. et al., Maunon N., 2003b, *Astrophys.*, 46 475 (List XIV)
- Gigoyan K. S., Maunon N., Azzopardi M. et al. Abrahamian H., 2001, *A&A*, 371, 560
- Gigoyan K. S., Mickaelian A. M., *Mon. Not. Roy Astron. Soc.*, 2012, 419, 3346
- Gigoyan K. S., Russeil D., Mickaelian A. M., A. Sarkissian, M. G., 2012a, *A&A*, 544, A95
- Markarian B. E., Lipovetski V. A., Stepanian J. A., Massaro E., Mickaelian A., Nesci R. et al., 2008, *The DFBS*, Arance Editrice S. r. l., Roma, Italy
- Wei Ji., Wenyuan C., Chao L., et al., 2016, *ApJS*, 226, 1

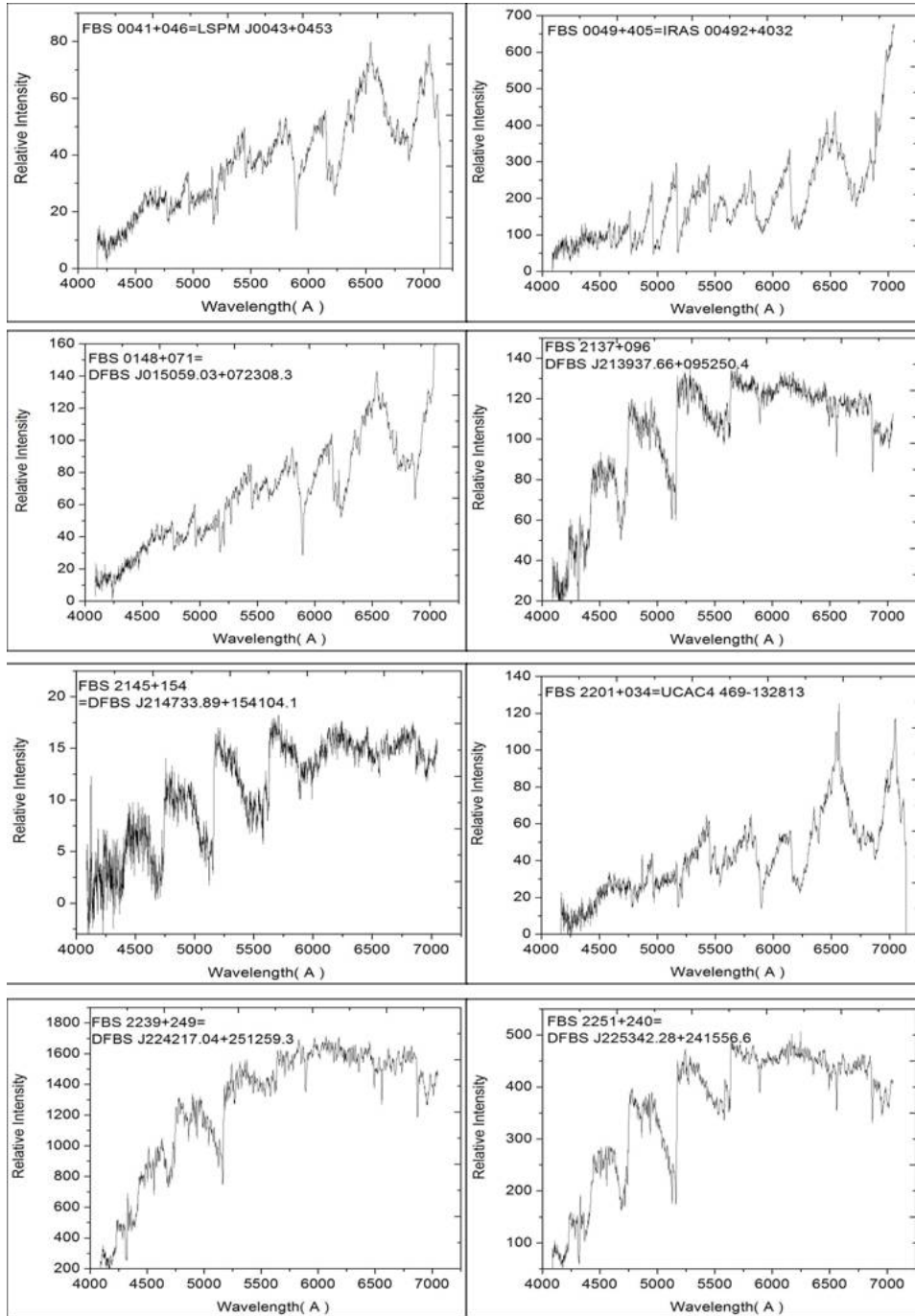


Figure 1: 2.6 m BAO telescope moderate-resolution CCD spectra for some objects.

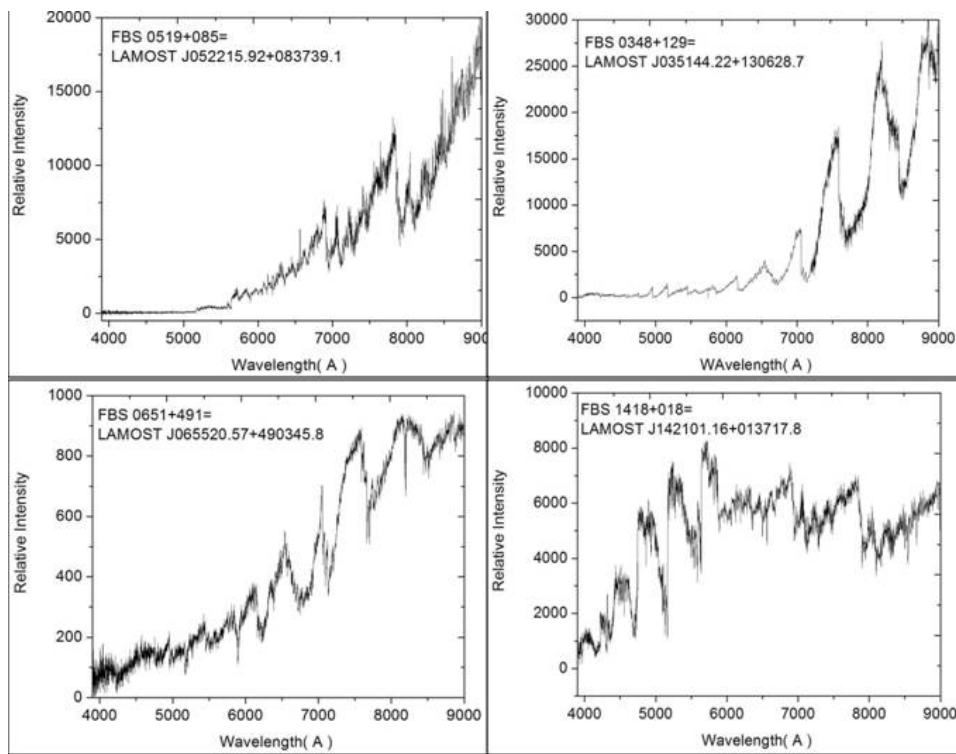


Figure 2: LAMOST moderate-resolution spectra for some sample of FBS LTSs.

The Growing Astronomical Unit and the Dark Energy Influence on the Baryonic Matter Evolution

H. Harutyunian^{1*}, A. Grigoryan¹

¹*NAS RA V. Ambartsumian Byurakan Astrophysical Observatory (BAO), Armenia*

**E-mail: hhayk@bao.sci.am*

Abstract

The effect of the Earths removal from the Sun is considered. This effect is difficult to interpret within the traditional paradigm of cosmic objects formation and evolution. Currently tidal mechanism is used as the most appropriate tool for explaining the Earth removal although no any quantitative data exist concerning the deceleration of Suns spin. We argue in favor of the dark energy influence, which, on the other hand, leads to the gradual increase of the Sun mass. Applying self-consistently all the known consequences of the interaction between the dark energy carrier and the baryonic matter, one arrives at a conclusion that the energy of the baryonic objects should grow up which, in its turn, increases their total mass. The mass growth of the Sun is estimated using the relevant observational data.

Keywords: *Dark energy – expansion at short scales – second law of thermodynamics – energy-mass transformation – mass growth – Astronomical unit – Sun mass.*

1. Introduction

When the linear relation between the galaxies distance and redshift was discovered in 20s of the last century (Lemaître 1927; Hubble 1929) it was interpreted as a ponderable proof of correctness of the solutions obtained for the Einstein gravitational equation (Friedman 1922; Lemaître 1927). No attention was paid to the fact that the equation has been solved for the homogeneous and isotropic distribution of the matter in the Universe, while these conditions are more or less satisfied only for the large scales. Although, the inhomogeneity scale was not a common knowledge then. Moreover, at the end of last century the observational base of cosmology changed drastically owing to the discovery of the accelerated expansion of the Universe (Riess et al 1998; Perlmutter et al 1999). Actually, the revealed new behavior of the

Universe expansion should change scientific views on the Universe structure and evolution. However, the predominant paradigm remained unchanged in its main axioms. The Universe origination due to the unique grand explosion followed by countless local, so called, Kantian condensations of matter in various scales was updated with several fitting parameters, but otherwise it continued serving as the only adoptable and comprehensive doctrine, describing the birth and evolution of everything. On the other hand, observational data constantly provided by ground based and orbital observatories grows with an accelerating rate, and the existing theories continuously need inventive updates of fitting parameters for explaining the variety of phenomena and regularities. Researchers use this kind of tricks for reconciling the dominant paradigm with empirical data if necessary long enough. One can recall a number of such situations in the history of science dictated due to a desperate need of overcoming any deadlock appeared because of discrepancy between new empirical data and established theories. As a striking example of such a situation, one can remind of the inconsistency revealed between very high dispersion of galaxy velocities and the total mass of the clusters. The idea on the existence of dark matter (Zwicky 1933; 1937) was invented then as a fitting tool, to overcome the ideological difficulty. Now, after more than eighty years, one can state that this fitting trick remained a thing in itself, despite the fact that it is used everywhere, where any system of cosmic objects is suspected to have positive total energy. Even worse, such an assumption is now considered a sign of a good scientific manner. According to the predominant concept on the cosmic objects formation, now we have a strange physical picture, where the universe is expanding with an accelerating rate to the infinity, while at the shorter scales everything shrinks, making material objects of bigger and more massive clumps. It does mean that a violation of continuity occurs due to these mutually exclusive processes. Therefore, for the self-consistency of the physical picture one should point out the scales where discontinuity expected or the turning point. This issue is extremely important to consider in detail. Actually, we hold a different point of view. Keeping in mind that the expansion of the Universe in fact is the reflection of processes occurring in the micro world, we try to reveal, wherever possible, all the physical consequences of this physical mechanism, staying at the same time in the frame of the modern physical knowledge. For this approach the analysis of the lunar retreat served as a bench mark (Harutyunian 1995), which showed that one can interpret correctly the Moon removal if the Universe expansion rate is taken into account for the smaller space scales. Some other physical consequences show up when this approach is used, provided, that all the physical laws and regularities are taken into account keeping always in mind the self-consistency of all the physical picture (Harutyunian 2017a; 2017b). In this report we consider the observed change of the Astronomical Unit (AU) again using the hypothesis concerning the universality of the Universe expansion.

2. Removal of Earth from Sun

On the base of analysis of radiometric measurements in the inner Solar System suggested that the secular increase in the unit distance on 154 meters per century (Krasinsky and Brumberg 2004). Calculations show that this increase is much larger than can be accounted for any known mechanism. The trivial one, taking into account the mass loss gives very small effect. Indeed, owing to radiation, it loses about $7 \times 10^{-14} M_{\odot}$ per year. Besides, it due to the mass ejection Sun loses in addition $1.5 \div 2 \times 10^{-14} M_{\odot}$ per year. Thus, our Sun loses yearly less, than about $9 \times 10^{-14} M_{\odot}$. One can calculate easily the upper limit of the AU growth, taking place due to the mass loss of Sun. One needs to write the Earth angular momentum conservation law with the dynamical equilibrium of the Earth keeping the planet in the orbit:

$$\frac{M_{\oplus} v^2}{R} = G \frac{M_{\odot} M_{\oplus}}{R^2} \quad (1)$$

$$M_{\oplus} v R = \text{const} \quad (2)$$

where R is the Astronomical Unit, M_{\oplus} is the Earth mass and v is the orbital velocity of Earth. From (1) and (2) one can find the following relation:

$$M_{\odot} R = \text{const} \quad (3)$$

provided that the Earth mass does not change. One finds using (3) that the growth of the Astronomical Unit is not more than 1.35 meter per century, which is on one order of magnitude smaller than the observed value. Hence, the most natural, from the viewpoint of the traditional physics, mechanism cannot explain the observed value of the AU growth. Researchers made several attempts to explain this possible secular increase of AU, including e.g., the effects of the cosmic expansion (Krasinsky and Brumberg 2004; Mashhoon et al. 2007; Arakida 2009), mass loss of the Sun (Krasinsky and Brumberg 2004, Noerdlinger 2008), the time variation of gravitational constant G (Krasinsky and Brumberg 2004), the influence of dark matter (Arakida 2009). Another interpretation, which uses the old idea proposed for the tidal acceleration in the Earth-Moon system, based on the conservation of the total angular momentum appeared about a decade ago (Miura et al 2009). However, if there are methods for estimating the Earths spin decreasing rate for the Earth-Moon system, there is no any applicable method for Sun's spin change. Moreover, one cannot solve the paradox of the very rapid retreat of Moon even in the case of the Earth-Moon system, if one stays in the frame of the mentioned traditional approach (Harutyunian 1995). Indeed, according to analysis of the chronography of eclipses observed during last two thousand years, for the deceleration of the Earths diurnal rotation period amounted about 1.8ms per century (Stephenson Morrison 1995;

Morrison Stephenson 2002). It is not difficult then finding the lunar retreat rate if one considers that the portion of angular momentum lost by Earth completely transfers to the Moon. Evidently, for finding the removal rate one should take into account the angular momentum conservation law with the Kepler third law. Then one finds the following relation:

$$k_E \frac{4\pi}{5} \frac{M_{\oplus} R_{\oplus}^2}{T} + 2\pi \frac{ma^2}{p} + k_M \frac{4\pi}{5} \frac{mr^2}{p} = const, \quad (4)$$

where the coefficients k_E and k_M depend on radial density distribution in the Earth and Moon, correspondingly, T is the period of the Earth diurnal rotation, m is the mass of Moon, a - the average radius of lunar orbit, r - the radius of Moon, p - the period of lunar rotation. In the given relation, the third term is much smaller compared with the first two and therefore can be neglected. Then from the (4) one easily can derive the following formula:

$$\frac{\Delta a}{a} = 0.664 \frac{M_{\oplus}}{m} \frac{R_{\oplus}^2}{a} \frac{p}{T} \frac{\Delta T}{T}, \quad (5)$$

or after putting the constants into the relation

$$\frac{\Delta a}{a} = 0.406 \frac{\Delta T}{T}. \quad (6)$$

For the Earths deceleration rate equal to 1.8 ms per century, one obtains 3.26 cm for the lunar annual retreat, which is sufficiently below of the observed value 3.82 ± 0.07 cm (Dickey et al, 1994). It does mean that the angular momentum lost by the Earth is not enough to explain the lunar retreat rate. The situation sufficiently changes, if one takes into account the possibility of the Hubble-like expansion at the smaller scales. If one applies the Hubble constant value equal to 70 km/s per Mpc, one finds the value of 2.74cm per year provided by cosmological expansion solely. This part of lunar retreat does not depend on the angular momentum transfer from the Earth to the Moon. In this framework, the Earth radius also should grow up. Simple calculations made for finding this growth amounts to about 0.455mm per year. This increase of the Earth radius decelerates the Earths diurnal rotation by 1.23ms per century. Therefore, only a portion of deceleration equal to 0.57ms per century remains, which can be caused by tidal effects. The remained portion of angular momentum provides additional rate of lunar removal, which amounts to 1.03cm per year. These two effects together result 3.77cm growth of the lunar orbit radius per year, which is in the error box of the observed value. This mechanism allows using of some physically valid suggestions as well, which makes it much more flexible for usage. On the other hand, it separates the role of two physical mechanisms and shows that only about 25 percent of the lunar retreat rate can be stipulated for tidal effects.

3. Hubble expansion influence on the Astronomical Unit

Let us stay in the frame of the universality of the Hubble expansion. Then one can calculate the value of its growth solely due to the universal expansion. It is easy to find that for the Hubble constant equal to 70 km/s per Mpc the relative growth of the length unit amounts 7.14×10^{-11} per year. If the Astronomical Unit obey the same law of expansion, it should increase by 10.7m per year, which exceeds the observable value by two orders of magnitude. Therefore, it seems at first glance that one cannot hope for any natural solution of the problem in this frame of thinking. However, the wonderful result obtained for the Earth-Moon system suggests that the main idea likely is plausible, and one needs to find how to use it more correctly. First idea coming to mind about this is the one, which requires finding a physical mechanism preventing the Earth from moving away from the Sun. No doubt, the mass growth of the Sun could prevent the Earths moving away. One of the authors (Harutyunian) has mentioned that the idea of dark energy and its possible influence on the baryonic matter are not considered with proper attention. One can do it from the viewpoint of general physical ideas. First, one should take into attention that dark energy has been discovered thanks to the galaxies acceleration. Then one inevitably arrives at a conclusion that dark energy (or something carrying dark energy) interacts with the ordinary baryonic matter and transfers to the later some energy to accelerate all the baryonic matter. Hence, a regular energy exchange should occur there between the ordinary baryonic matter and the carrier of dark energy, whatever it is. Second, the second law of thermodynamics states, that in the process of interaction between systems of different energies, the system possessing of higher energy loses some part of it, which goes to another one of lower energy. Modern physics considers this law as a monotonic growth of entropy isolated systems. One should bear in mind that the second law of thermodynamics belongs to the class of physical laws, which possess of high priority. According to Eddington the law that entropy always increases holds, I think, the supreme position among the laws of Nature (Eddington 1927). Third, all the objects composed of baryonic matter exist as such exceptionally thanks to negative energy balance (or lack of energy). Gravitationally bound objects possess of negative potential energy, and one can find in any textbook on the general physics the formula describing the energy depending on its mass and size. The atomic nuclei are the natural tools of transforming mass into energy and vice versa. One needs a definite quantity of energy to destroy any atomic nucleus and divide into separate nucleons, increasing by this their combined mass. Moreover, the contemporary physics of elementary particles states that much more energy is needed for destroying the elementary particles and obtaining free

quarks. Therefore, combining all three statements one arrives at inevitable conclusion that all the objects of the Universe composed of baryonic matter should grow in their mass during the evolution. This conclusion is very important from, at least, two points of view. First, using its mechanism of expansion the Nature uses the expansion energy also for increasing the mass of the baryonic Universe, preventing thus excessive decrease of its density. It seems that the Nature acts according self-consistent scenario programmed in a way to keep the average density unchanged. Second, this mechanism of energy-mass transformation explains the paradox once introduced by the big bang paradigm, which states that the baryonic matter of the Universe was appeared during one act of creation. If one applies physical knowledge in a self-consistent way, one should expect immediate collapse of the newborn universe but not its expansion as one observes at present time. Indeed, it is obvious, that the Universe could not exist if it was born in the same mass it has at present. The baby baryonic Universe, which had many times smaller radius, was within the Schwarzschild radius for long time and should collapse but not expand. It does mean that its mass was many times smaller not to fall into the conditions obeying the requirement of the gravitational collapse. If we agree that the Universe is expanding and it was expanding during all the time, we inevitably should agree that its mass was increasing in course of its expansion.

4. The rate of solar mass growth

One can use the relation (3) for estimating the mass growth necessary for compensating the universal expansion rate. Then one should take into attention both effects, namely, the expected growth of the AU without mass change and the shortening of the AU growth with the mass increase:

$$M_{\odot}R(1 + \delta) = M_{\odot}(1 + \Delta_M)R(1 + \Delta_R), \quad (7)$$

where $\delta = 7.14 \times 10^{-11}$ is the growth of the unit length per year for the Hubble constant amounting 70 km/sec per Mpc, $R\Delta_R=15\text{cm}$ is the observed growth of the AU. It is easy to find that the rate of mass growth for the Sun is equal to

$$\Delta_M = \frac{\delta - \Delta_R}{1 + \Delta_R} = 7.04 \times 10^{-11} \quad (8)$$

Obtained mass growth amounts about 4.5×10^{15} g/s, which is equivalent to the energetic power of 4.5×10^{36} erg/s or about 1000 times of the solar luminosity. This is a huge amount, which can explain the discrepancy between the measured and predicted values of the AU growth. Nevertheless, the growth of the mass of Sun, if it occurs, should have a natural physical explanation, and we will dwell on this in a little more detail. To do this, we turn again to the structural features of the baryonic matter. The basis of all

baryonic objects is the atomic structure, as well as the structural features of the elementary particles, the carriers of mass, charge, and spin of the baryonic substance. It is also obvious that almost all the mass of the substance we observe in the Universe is accumulated in atomic nuclei. Moreover, only atomic nuclei and elementary particles possess of remarkable property responsible for existence of all the objects. That is their self-consistent change of individual masses, depending on their binding degree and other physical conditions, in which they are located. Although it is considered, for example, that all baryons of the same name are indistinguishable and in no way differ from each other, they may have different masses in different atomic nuclei, that is, in different nuclei they transform different parts of their mass into the binding energy. This is a very important empirical fact. Figuratively speaking, this natural fitting mechanism makes baryonic configurations of nuclei energetically balanced with the surrounding physical conditions. Indeed, nuclear binding energy calculated per nucleon changes in a wide range. For the nucleus 2H it amounts about 1.112Mev, and increases for 3H up to 2.827Mev, though the replacing one neutron by a proton decreases the binding energy for 2He down to 2.573Mev, while for the alpha particle 4He it increases up to 7.074Mev. The largest values of the nuclear binding energy have the iron group nuclei, namely, ${}^{56}Fe$, ${}^{58}Fe$, ${}^{60}Ni$ and ${}^{62}Ni$, which possess of binding energies 8.791Mev, 8.793Mev, 8.781Mev and 8.795Mev, accordingly. One can find many other values of nuclear binding energy showing that the binding energy can take on a variety of values, showing thus the variability of the nucleus mass in a nucleus depending on physical conditions. Taking into account these facts and empirical regularities one arrives at a conclusion that it is not very heretical if one will consider the possibility of changing of the binding energy of the given atomic nuclei over the time due to evolution effects. This conclusion follows from the indisputable facts that baryons in different nuclei can exist with different amounts of mass defect, and that baryonic matter interacts with dark energy carrier. Interaction of various systems of energy carriers obey the thermodynamic laws, including the second law of thermodynamics. If the premises is correct, then one should look more precisely for the physical consequences of such physical effects. Let us emphasize for the later consideration that dark energy evidently has positive sign, since it implements a huge physical work accelerating the Universe expansion. In contrast with it, internal energy of baryonic objects is negative. According to the second law of thermodynamics, the interaction between the baryonic objects and the carrier of dark energy, baryonic objects should gain energy and therefore their internal energy will increase, which does mean decreasing the absolute value of the energy. Gravitationally bound spherical object of mass M and

radius R_U possesses of energy equal to

$$U = -k_U G \frac{M^2}{R_U}, \quad (9)$$

where the coefficient k_U depends on the radial distribution of density in the given object. The gravitational energy increase for such objects should mean decrease of the ratio at the right hand side of the formula (9). It can happen if the radius R_U increases more rapidly than M^2 . On the other hand, the baryonic mass of an object grows if the total mass of atoms increases. It can happen due to the interaction between the carrier of dark energy and atomic nuclei, resulting decrease of binding energy and mass defect. This is the plausible way of the mass growth effect for all the objects of the Universe. The suggested mechanism is perfectly new. It assumes that in the course of the Universe evolution all the objects, starting with elementary particles and atomic nuclei and up to gravitationally bound ones undergo a type of secular variation, which is resulted by their interaction with the carrier of dark energy. Thanks to this variation, they gradually change their intrinsic features to be always in the balanced physical interrelation. All the secular variations are caused by the energy interchange or rather energy injection processes, when dark energy carrier gradually exerts influence upon the baryonic objects giving them definite portions of energy. Depending on their intrinsic features, the objects of various hierarchical levels react in completely different ways. Non the less, the general trend for all these objects are several they all increase their gravitational mass, they all can decay in various ways when the internal energy excides some boundary threshold and they transform the portions of dark energy into familiar forms of energy to release it in the form of radiation, mass ejection or other. Within the given context, the change of atomic nuclei can be represented on the base of a phenomenological analysis. If one adopts the law of conservation of baryons in the Universe, then one should arrive at a conclusion, that at the very beginning of our Universe, as we imagine it, baryons possessed only the negligible portion of their masses. Figuratively speaking, there were embryos of baryons packaged into atomic nuclei characterized by enormous mass defect. Nowadays the atomic nuclei continue to gain mass, if the scenario described above is realistic and makes sense. Simply extrapolating this process back to the past, one inevitably concludes, the farther into the past, the fainter baryonic embryos were. Another important conclusion concerns the radioactive nuclei we observe today. The most massive stable nucleus existing today is ^{206}Pb with its 206 baryons. All other nuclei, which consist of more baryons, are instable. Even ^{209}Bi traditionally regarded as the heaviest nuclei appeared to be alpha radioactive, although its half-life is billion times longer than the estimated age of the Universe. If the secular change of nuclear properties is something real and the nuclear binding energy was bigger in the past, one should consent that there were stable nuclei composed of much

more baryons in the past.

5. Concluding remarks

The contemporary physics provides the only toolkit for interpretation and description of the world consisted of matter. It does mean that one should operate by approved and valid concepts when trying to explain results of experiments or astronomical observations. However, approved by time does not yet guarantee the applied concept is certainly right for all the similar conditions or it was right everywhere it was suggested to be right a priori. We consider here a scenario according which the Hubble expansion is not the prerogative of cosmologic scale only but it is a particular manifestation of the universal expansion taking place at all scales. In other words, we consider the Universe where dark energy implements physical work and interact with the baryonic objects at all scales. Interaction between the dark energy carrier and baryonic objects causes and predetermines the evolutionary path for all baryonic objects in our world. This approach seems to be an extremely heretical one if considered from the conventional viewpoint. One can easily find the roots of such prejudice in relation to any concept speaking in favor of expansion effects at smaller scales. It is hidden in the predominant hypothesis on the formation of cosmic objects - the kantian events at all scales which suggest condensation of matter for reaching the balanced dynamical conditions. Actually the original idea concerning the origin of cosmic objects due to the expansion, decay and fragmentation processes belongs to Viktor Ambartsumian who was insisting for long time on the existence of pre-stellar super-dense matter, which gradually transforms into ordinary matter giving born cosmic objects at different hierarchical levels. The idea could not gain many supporters because the physical laws we apply do not allow existence of such masses in small volumes. Therefore, the idea has been consigned to oblivion. However, the situation drastically changes if one takes into account the physical consequences of the interaction between baryonic matter and dark energy. Any piece of baryonic matter regardless of its size and number of baryons in it accumulates energy and mass growth due to the mentioned interaction, which leads ultimately to the processes of energy release through all the possible mechanisms including the mass ejection and decay of the initial piece. It is evident, that the substance located on or closer to the surface of the decay fragment is more committed to the influence of the external factors and more easily subject to change due to such influences that those parts that are dipper inside. If so, one should expect a negative gradient of the matter evolution or "aging" degree to the center of cosmic objects. The bigger the object, the larger the "age" difference between surface and the center of the object. Therefore, in the depths of massive cosmic objects, baryonic matter must be preserved

with physical properties it had in the early phases of the Universe evolution. Using the new paradigm on the spatial universality of dark energy, which leads to the expansion effects in the non-quantum world, one can solve the problem appearing in connection with the extremely big masses in small volumes. It follows from the self-consistent application of our knowledge of modern physics. Acting this way one arrives at a conclusion that the self-consistency of the baryonic world is of a very high level. Interaction with dark energy leads to the growth of spatial sizes of the baryonic world, but also increases its total mass as the injected into the baryonic objects energy transforms into the mass. It does mean, that the matter ejected due to Ambartsumian events could initially have possessed of much less mass and be increased during the ejection process due to the physical conditions change and decrease of the mass defect. In our opinion, this paradigm removes limitations imposed on the Ambartsumian concept on the cosmic objects formation. The fact that the mass of these objects grows in the course of evolution, and a large stock of mass increase is stored in the deep depths of massive space objects in the form of baryon embryos, allows us to solve this problem as well as the paradox already mentioned - why the Universe did not slam immediately after its birth within scenario based on the big bang hypotheses.

References

- Anderson, J.D., Nieto, M.M., 2009, American Astronomical Society, 261, 189, arXiv:0907.2469
- Arakida, H., New Astron., 2009, 14, 275
- Dickey, J.O., Bender, P.L., Faller, J.E., Newhall, X.X., Ricklefs, R.L., et al, 1994, Science, 265, 482
- Eddington, A.S., 1927, The Nature of the Physical World: Gifford Lectures, Cambridge University Press
- Friedman, A., 1922, Zeitschrift für Physik, 10 (1), 377. English translation in: Friedman, A. (1999), General Relativity and Gravitation, 31 (12), 1991 – 2000.
- Harutyunian, H.A., 1995, Astrophysics, 38, 374
- Harutyunian, H.A., 2017a, in "Non-Stable Universe: Energetic Resources, Activity Phenomena, and Evolutionary Processes" ASP Conference Series, v.511, 207
- Harutyunian, H.A., 2017b, Astrophysics, 60, 627
- Hubble, E. P., 1929, Proc. Nat. Acad. Sci. USA ,15, 168
- Lemaître, G., 1927, Ann. Soc. Sci. Brux. A 47, 49
- Krasinsky, G.A. and Brumberg, V.A., 2004, Celestial Mechanics and Dynamical Astronomy, 90, 267
- Mashhoon, B., Mobed, N., Singh, D. 2007, Class. Quant.Grav., 24, 5031.

- Miura, T., Arakida, H., Kasai, M., Kuramata, S., 2009, Publ. Astr. Soc. of Japan, 61, 1247
- Morrison, L.V. Stephenson, F.R., 2002, in "Highlights of Astronomy", ed. H.Rickman, 12, 338
- Noerdlinger, P. D. 2008, arXiv:0801.3807
- Perlmutter, S., Aldering, G., Goldhaber, G., Knop, R.A., Nugent, P., et al, 1999, Ap.J, 517, 565.
- Riess, A.G., Filippenko, A.V., Challis, P., Clocchiatti, A., Diercks, P., et al, 1998, AJ, 116, 1009
- Stephenson, F.R., Morrison, L.V., 1995, Phil. Trans. R. Soc. London, Ser.A, 351, 165
- Zwicky, F., 1933, Helvetica Physica Acta, 6, 110
- Zwicky, F., 1937, ApJ, 86, 217

Some Problems of Solar Quiescent Prominences in the Light of Ambartsumian's Ideas

A.Nikoghossian

*NAS RA V. Ambartsumian Byurakan Astrophysical Observatory (BAO), Armenia
E-mail: nikoghoss@yahoo.com*

Abstract

The report is a brief overview of our results in the theory of spectral line formation in atmospheres with complex fine structure. The research motivation was due to interpretation of the EUV spectrum of solar quiescent prominences observed with the SUMER spectrograph as a part of the SOHO space program. We describe the methods proposed for solving the line-radiation transfer problems in multicomponent atmospheres which use Ambartsumian's ideas proposed in the theory of radiation transfer and its applications. It is demonstrated that even the simplest static model radiating medium composed of physically different types of elements shows line profiles differing from those formed in the medium with preliminarily averaged properties. The more realistic and complicated case of a multicomponent atmosphere with randomly varying properties is considered with special attention paid to the effect of the velocity field. An important role of the relative mean square deviation of observed line intensities in the diagnostics of physical features of spatial and temporal variations of prominences is shown.

1. Introduction

The need to create a theory of radiation transfer in the media with complicated fine structure subject to random variations has long been felt in the theory of the solar atmosphere. As early as in the 1970's Cram showed that the observed profiles of chromospheric lines of ionized calcium cannot be explained in terms of the theory developed for homogeneous stationary media. Similar problems arise also in interpreting nonstationary phenomena in spicules, coronal streams, and polar plums. Problems involving the propagation of radiation in randomly varying inhomogeneous media appear also in other branches of astrophysics. Examples include the scattering of light on molecular clouds in the interstellar medium (Juvela 1997, Juvela

& Padovan 2001) and the stochastic attenuation of galactic radiation as it travels over cosmologic distances (Madau 1995).

The procedure for calculating the statistical properties of the radiation emerging from a multicomponent LTE-atmosphere was presented by Lindsey and Jefferies (1987) and Lindsey (1988) for the interpretation of total solar eclipse observations in the far infrared. These authors derived relations describing the evolution behavior of the mean value of the intensity and its variance along the radiation path.

The theory we developed for interpreting the observable emergence of complex structural pattern of media in the line spectrum may be regarded as a further generalization of the Ambartsumian layers adding method (Ambartsumian 1944, 1960).

The theory is especially simple for the atmosphere in LTE: because of the absence of scattering, and hence reflection from structural elements, the mean value of intensity emerging from any part of the multicomponent atmosphere remains unaltered when new components are added. This fact is essential in the sense that it simplifies the problem and allows one to establish immediately the recurrence relationship for both the mean intensity and variance so that the problem admits a simple closed-form solution. These results for the LTE atmospheres were generalized by Nikoghossian and co-authors (Nikoghossian, Pojoga & Mouradian 1997, 1999), which allows to reveal quantitative as well as qualitative discrepancies with respect to those formed in a homogeneous atmosphere with preliminarily averaged random characteristics. The further development of the theory given in (Nikoghossian & Mouradian 2000) allows to formulate and solve the problem of the spectral line-radiation also in the NLTE composite atmospheres.

On the other hand, one should take into account the fact that the plasma in the prominences is known to participate in various kinds of motions which, of course, affect the observed spectral line profiles. Random thermal and turbulent motions in prominences with velocities on the order of 5-10 km/s are superimposed on ascending (eruption) or descending (mass loss owing to its return to the chromosphere and photosphere) flows and large-scale hydrodynamic motions (Tandberg-Hanssen 1995). The radiation transfer in a line through a dynamically active medium of this sort leads to a great variety of line shapes which are distorted by the Doppler effect. Furthermore, the line profiles depend on a number of other parameters characterizing the emitting volume, so that a quantitative interpretation of the observed spectra is a rather complicated problem in general. This more realistic problem making allowance for the dynamics of a radiating multicomponent medium was considered by the author in (Nikoghossian 2002). An important place in all the mentioned model problems occupies the frequency-dependent relative mean square deviations (RelMSD) of the observed line intensities due to spatial or/and temporal variation of the number or physical properties and non-thermal motions of the fine structural elements. The idea to use

the variance of fluctuations in the observed superficial brightness as an additional tool in investigating astrophysical objects goes back to Ambartsumian's work (1944), where the brightness fluctuations of the Milky Way were used in estimating the value of interstellar absorption. Generalizing this approach, we showed that there is a well pronounced relationship between functional form of the RelMSD within a spectral line and the sources of the observed line intensity spatial/temporal fluctuations. The direct motivation of the theory we developed was the rich observational material gained in frameworks of the Skylab and SOHO space missions for the EUV spectrum of prominences. The theory we developed in the aforementioned papers is applied to find out some physical and geometrical features of solar quiescent prominences characterized by composite threadlike structure.

2. Lines profiles in stochastic multicomponent media

We start with treating the simplest model of the static LTE multicomponent medium composed of a certain number of structural elements of two sorts each of which is characterized by its optical thickness τ_i , the power of the contained energy sources B_i and the probability p_i of appearance ($i=1,2$). The dependence on frequency within the spectral line is described by the Dopplerian profile of the absorption coefficient $\alpha(x) = \exp(-x^2)$, where the dimensionless frequency x is measured from the center of the line in Doppler widths. We are interested with the statistical mean value of the observed intensity $\langle I(x) \rangle$ and the RelMSD $\delta_N(x)$ in the line, where N denotes the number of structural elements. The closed form analytical expressions for the mentioned quantities were obtained in (Nikoghossian, Pojoga & Mouradian 1997, 1999)

$$\langle I_N(x) \rangle = L_N(x) \langle I_1(x) \rangle, \quad (1)$$

$$\delta_N(x) = \frac{M_N(x)}{L_N(x)} [1 + \delta_1(x)] + 2 \frac{K(x) A_N(x)}{\langle I_1(x) \rangle L_N^2(x)} - 1, \quad (2)$$

where the following notations are introduced

$$L_N(x) = \frac{1 - q^N(x)}{1 - q(x)}, \quad M_N(x) = \frac{1 - \beta^N(x)}{1 - \beta(x)}, \quad A_N(x) = \frac{L_N(x) - M_N(x)}{q(x) - \beta(x)},$$

$$K(x) = \langle J_i(x) e^{-\alpha(x)\tau_i} \rangle, \quad q(x) = \langle e^{-\alpha(x)\tau_i} \rangle, \quad \beta(x) = \langle e^{-2\alpha(x)\tau_i} \rangle,$$

$$J_i(x) = B_i \alpha(x) [1 - e^{-\alpha(x)\tau_i}],$$

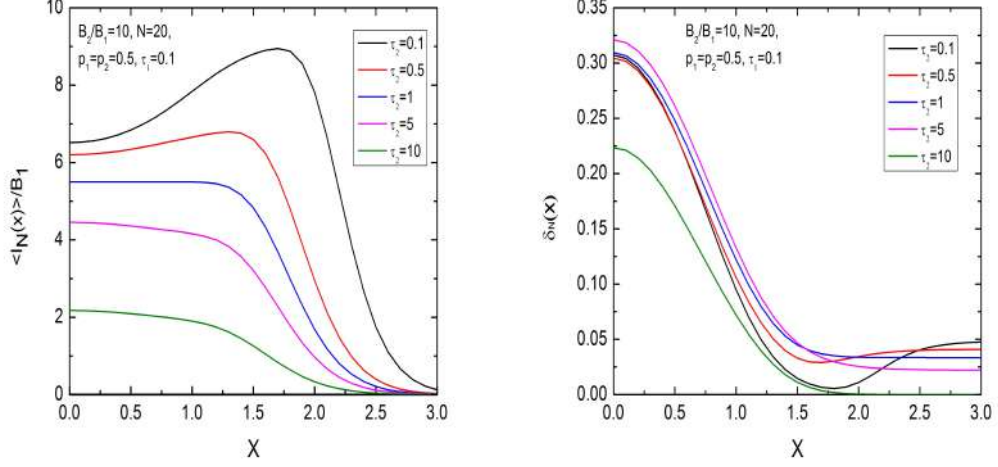


Figure 1: The statistical mean of the emitting intensities (left panel) and RelMSD (right panel) for different values of parameters. Special attention is paid to different combinations of optical thicknesses of structural elements

According to definition, we have

$$\langle I_1(x) \rangle = \sum_{i=1}^2 p_i J_i(x), \quad \delta_1(x) = \frac{1}{2\langle I_1(x) \rangle^2} \sum_{k=1}^2 p_k \sum_{i=1}^2 p_i [J_i(x) - J_k(x)]^2,$$

We see that the degree of fluctuations for any number of components N is determined by four parameters q , β , δ_1 and $K/\langle I_1 \rangle$ (or by three parameters for $p_1 = p_2$), which are statistical characteristics of the emission and absorption of a single element of the multicomponent medium.

Fig.1 illustrates profiles of spectral lines and proper RelMSD when the number structural elements is 20. In this model case the elements differ with each other in the power of the internal energy sources. The opacities are chosen on the ground that the hotter components must mainly be more opaque. The first effect that attract attention is the double-peaked profile formed preferably in cases when difference between components are due predominately to the value of the sources of internal energy. Remind that such profiles are usually associated with the lines formed in a NLTE atmosphere as a result of the frequency redistribution. We see now that multicomponent media may generate double-peaked profiles even in the absence of the radiation scattering. Another result concerns the frequency behaviour of the RelMSD in the wings of the line. It is also seen that its value can either decrease or increase dependent on values of other parameters.

Further progress of the theory allowed to handle more general and complex models with greater sorts of components and greater number of possible

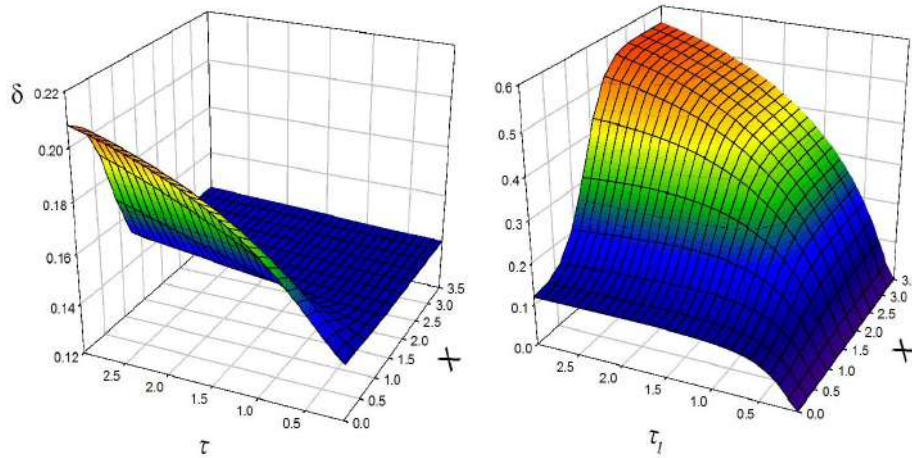


Figure 2: The RelMSD of intensity fluctuations in two models of the NLTE atmosphere. Calculations are performed for $\lambda = 0.99$, where λ is the photon re-radiation coefficient in the multiple scattering process. For simplicity's sake, the number of components are taken $N = 4$ and $p_1 = p_2$. The values of other parameters are $S = B_2/B_1 = 7$, $\tau_1 = \tau_2 = \tau$ (left panel) and $S = 1$, $\tau = 0.1$ (right panel)

realizations. More realistic models consider the correlations between realizations of different parameters in two adjacent components. The theory becomes much more complicated in the case of NLTE atmospheres (see the above cited papers of the author). The most important conclusion is that the aforementioned features of RelMSD remain qualitatively valid in the NLTE media. Fig.2 shows the frequency-dependent RelMSD of observed intensities in two mutually opposite situations of equal opacities $\tau_1 = \tau_2$ and $B_1 \neq B_2$ and the opposite case of differing opacities and equal B_i .

We see the quite distinct variation of the RelMSD over the entire frequency range within a line. This effect can obviously be regarded as a diagnostic tool in revealing the physical properties of various regions of prominences. It is evident that the real state of the prominence is generally more complex and depends on variations of both the mentioned parameters. In this more realistic situation when the optical thickness in the line and the power of the energy sources take arbitrary non-equal values, the variation of the RelMSD towards the wings of a line becomes more complex (Nikoghossian 2002, Nikoghossian, Aboudarham & Mouradian 2005). The resulting center-to-wings variation of the RelMSD obviously depends on that which of considered causes of fluctuations predominates (see Fig,3). The situation becomes simpler if we suppose that the opaque lines are formed in the hotter radiating volumes, which is often the case. It must be noted that

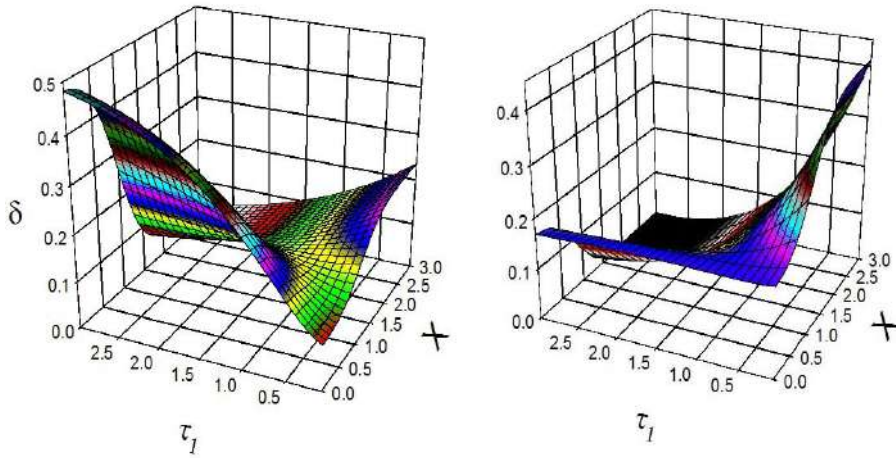


Figure 3: The RelMSD of intensity fluctuations in two model atmospheres for $N = 4$ and $p_1 = p_2$. $S = B_2/B_1 = 7$, $\tau_2 = 1$: $\lambda = 0$ (LTE, left panel) and $\lambda = 0.99$ (Non-LTE, right panel)

these effects quantitatively depend on the number of structural elements. Fig.4 illustrates the variation of averaged values of dimensionless intensities and proper RelMSD in frequency within a line. As might be expected, with growing the number of components, the values of RelMSD decrease towards to wings. As above, the behavior of the RelMSD in the far wings of the line in these two model cases is diametrically different. It is not worthy that these considerations are important from the point of view of interpretation of the nature of the surface brightness fluctuations of any extended astronomical object with a randomly varying fine structure.

3. Lines profiles in dynamically active multicomponent media

As it was mentioned, in the real stochastic atmospheres of astrophysical interest the velocity field is subject to random variations together with physical and geometrical characteristics of the medium. It is evident that such kind of velocity variations may affect the observed line profiles generally in a great degree. Radiative transfer in a line through a dynamically active medium leads to a great variety of line shapes which are distorted by the Doppler effect. Furthermore, the line profiles depend on a number of other parameters characterizing the emitting volume, so that a quantitative interpretation of the observed spectra is a rather complicated problem, in general. The problem of the spectral line formation in a stochastic multicomponent atmosphere in LTE was treated by the author in (Nikoghossian,

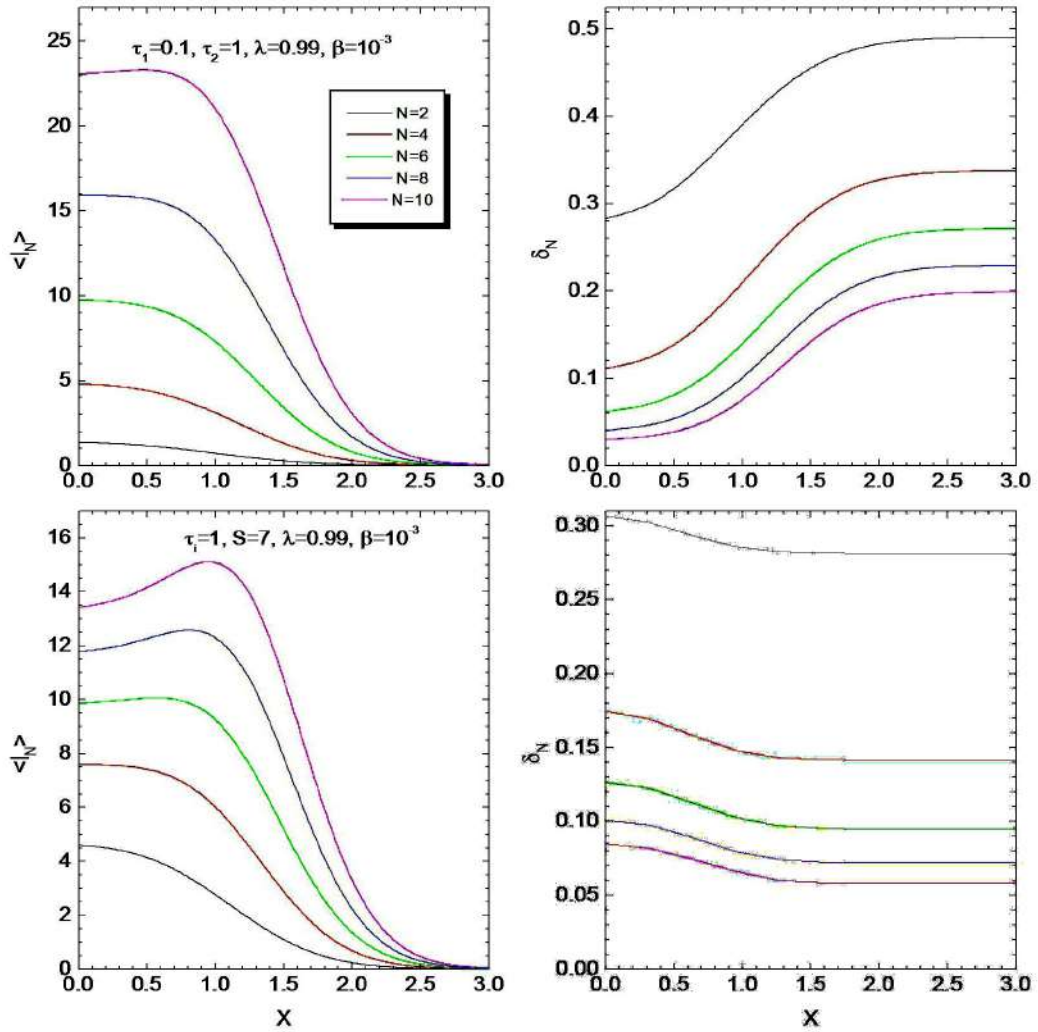


Figure 4: Dependence of averaged intensities radiating in a line and the proper RelMSD on the number of structural elements for indicated values of realized opacities, the power of internal energy sources and other parameters describing the elementary event of scattering (β is the ratio of the absorption coefficient in continuum to that in the centre of the line)

2007). Motions considered in this paper imitate the large scale hydrodynamic motions usually observed in solar prominences. The effect of the radiation on the velocity field is neglected which is reasonable for the lines with low optical thickness. We set ourselves the problem of determining the radiation emerging from a dynamically active atmosphere consisting of N structural elements whose physical characteristics undergo random variations. It is assumed that the spatial process of realization of components of a given type is Markovian, i.e., the realization of physical properties of a given component depends only on the realized properties of the preceding component. Particular attention we paid to RelMSD of the intensity of the observed radiation. The important feature of the developed method is that, for determining the mean intensity of the emerged line radiation, $\langle I_N(x) \rangle$, one preliminarily finds the auxiliary quantities $\langle I_N^i(x_i) \rangle$ characterizing the mean mathematical expectation of the intensity of the observed radiation under the condition that the N -th element belongs to the i -th type, so that

$$\langle I_N(x) \rangle = \frac{1}{n} \sum_{i=1}^n \langle I_N^i(x) \rangle \quad (3)$$

In the case of Markov process $\langle I_N^i(x) \rangle$ are determined by recurrence relations

$$\langle I_N^i(x) \rangle = \sum_{k=1}^n q_{ik} [\langle I_N^k(x) \rangle \exp(-z^i \tau_i) + P_{N-1}^k J_i(x)], \quad (4)$$

where the following notations are introduced: the coefficients q_{ik} are elements of the Markov transition matrix, $z^i = \alpha(x - u') + \beta$ and $J_i(x) = B_i [1 - \exp(-z^i \tau_i)]$, the P_N^i represents the probability of an event in which an element of i -th type will appear at the N -th position. Further, $u^i = V_{hyd}^i / V_{th}$, where V_{th} is the mean thermal velocity and V_{hyd} - the line-of-sight component of the hydrodynamic velocity.

Fig.5 shows typical examples of profiles and RelMSD calculated for the purely stochastic case, when the atmosphere consists of only two types of structural elements. Along with the profile of the average radiation intensity, $\langle I \rangle$, emerging from the medium, we present two other profiles $\langle I_1 \rangle$ and $\langle I_2 \rangle$ calculated under the condition that the N -th element belongs, respectively, to the first and second types. To make the changes in the RelMSD clearer, N has been chosen to be relatively small. In order to clarify the effect of the Markovian interaction between the components on observed profiles and the RelMSD, we considered the case of the so-called doubly stochastic atmosphere.

The profiles depicted in the right panel demonstrate essential distortion of the line profiles caused by hydrodynamic motions. Another important result is the distinctive feature of the RelMSD of the radiation in a line formed in a dynamically active stochastic atmosphere is local spikes (maxima) in

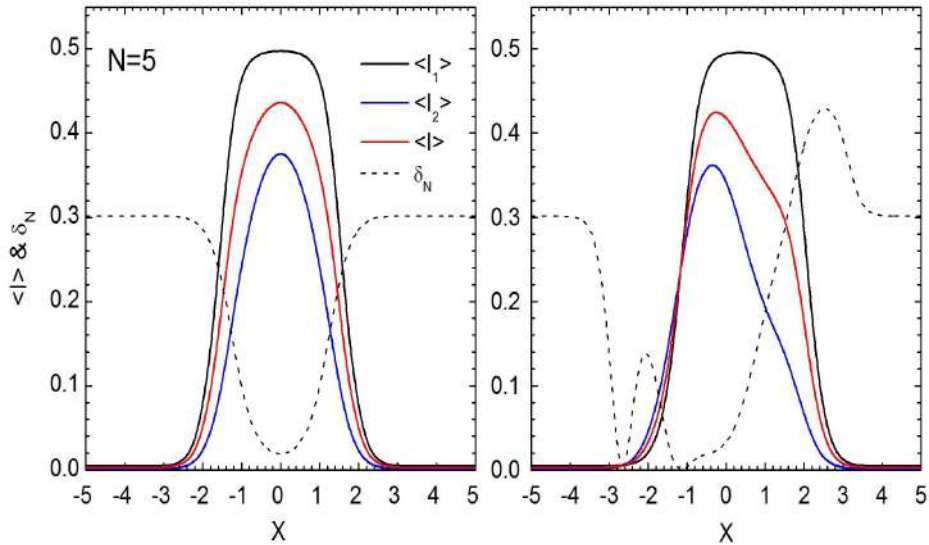


Figure 5: Theoretical profiles of a spectral line and the RelMSD for double stochastic static (left) and dynamically active (right) atmospheres. It is assumed that the latter consists of two types of structural elements with the following parameters: $B_1 = B_2 = 1, p_1 = p_2 = 0.5, \tau_1 = 2, \tau_2 = 0.2, \beta = 10^{-3}, u^1 = 0.5, u^2 = 0.5,$ and $q_{11} = q_{22} = 0.9, q_{12} = q_{21} = 0.1$

the wings of the line. The obtained theoretical results were compared with spectral observations of quiescent solar prominences obtained in framework of the SOHO space mission.

4. Observation data

In order to verify the theoretical results, we have used some observational data on spectral lines of solar quiescent prominences in the EUV domain of the spectrum obtained on August 10, 1999 using the SUMER spectrometer in frameworks of the SOHO space mission. We were interested in the fluctuations in the surface brightness of the prominences in several of strongest lines. With each observation, the spectrometer slit with its field of $1''120''$ yields 120 line profiles so that their variation along the slit could be traced. These data are usually sufficient for determining the statistical averages of the radiation intensity and the corresponding RelMSD as functions of frequency within a line.

Fig.6 shows data on the relative mean intensity and RelMSD (broken curves) for several relatively strong EUV lines. We pointed out above that the RelMSD increases on going to the line wings. According to the theoret-

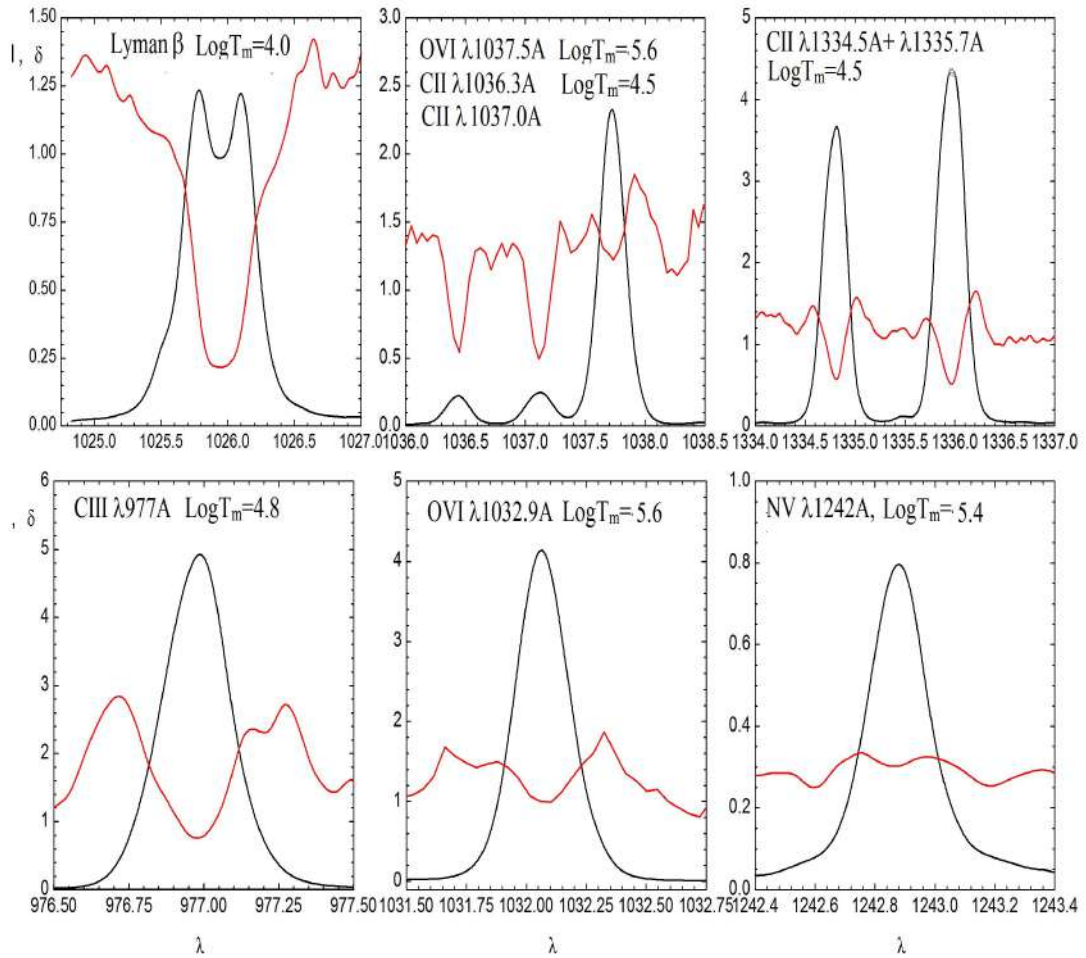


Figure 6: Statistical mean profiles (smooth curves) and the corresponding RelMSD (dotted curves) for a series of relatively strong EUV lines of a solar prominence observed on August 10, 1999, in frameworks of the SOHO space mission

ical discussion, this was an indication of the fact that the fluctuations in the surface brightness of the prominence are caused mainly by changes in optical thicknesses. We see that the central depression in the frequency profile of the RelMSD is different for different lines and is correlated with the effective temperature at which they are formed. The spikes (local maxima) in the wings of the lines predicted by the above theory for non-thermal (hydrodynamic) motions can be distinctly seen. One can also see that for lines with a high effective formation temperature (i.e., the lines formed primarily in the surrounding corona), such as OVI $\lambda 1032 \text{ \AA}$, $\lambda 1037 \text{ \AA}$, and NV $\lambda 1242 \text{ \AA}$, the magnitude of these spikes appears to be smaller than for the lines formed entirely within the prominence. The appearance of isolated single spikes is an indication that the velocities of the non-thermal motions are only slightly greater than the thermal speed, if they exceed it at all.

5. Discussion

The idea of invoking fluctuations in the surface brightness of prominences as an additional source of information on the radiating volume described above shows that important information can be extracted by studying the RelMSD of these changes as a function of frequency within a line. Theoretical studies have been compared with the data on changes in the profiles of EUV lines along the slit of the SUMER spectrograph obtained as part of the SOHO space program. Thus, it has been shown that, with some exceptions, fluctuations in the surface brightness of prominences in different lines are caused by changes in the optical thickness and that the changes are smaller when the lines are formed at higher effective temperatures. The study of these fluctuations is especially informative when large scale or hydrodynamic motions are present in the medium. If the radiating volume participates in rising and falling motions, then the frequency dependence of the RelMSD is characterized by unique spikes (local maxima) in the wings of the lines. The magnitude of the latter depends on the velocity of the large scale motion

References

- Ambartsumian, V.A. 1944, *Izv. AN ArmSSR*, N1-2
- Ambartsumian, V.A. 1944, *Dokl. Acad. Sci. USSR*, 44, 244
- Ambartsumian, V.A. 1960, *Scientific Works*, v.1, Izd. AN ArmSSR, Yerevan
- Cram, L.E. 1972, *Sol. Phys.*, 22, 375
- Jefferies, J.T.; Lindsey, C. 1988, *Astrophys. J.*, 335, 372
- Juvela, M. 1997, *A&A*, 1997, 322, 943
- Juvela, M.; Padovan, P. 2001, *A&A*, 397, 201
- Lindsey, C. 1987, *ApJ.*, 320, 893

- Madau, P. 1995, ApJ. 441, 18
Nikoghossian, A.G. 2002, Astrophysics, 45, 223
Nikoghossian, A.G. 2007, Astrophysics., 50, 94
Nikoghossian, A.G.; Abouharham, J., Mouradian, Z. 2005, Astrophysics. 48, 253
Nikoghossian, A.G.; Mouradian Z. 2000, A&A, 360, 2000
Nikoghossian, A.G.; Pojoga, S.; Mouradian, Z. 1997, A&A, 325, 813
Nikoghossian, A.G.; Pojoga, S.; Mouradian, Z. 1999, A&A, 342, 785
Tandberg-Hanssen, E. 1995, The Nature of Solar Prominences, Kluver, Dordrecht

Qualitative Analysis of Cosmological Models in $f(R)$ -Gravity

R. M. Avagyan, E. V. Chubaryan, G. H. Harutyunyan,
A. A. Saharian*

*Department of Physics, Yerevan State University, 1 Alex Manoogian Street, 0025 Yerevan,
Armenia*

**E-mail: saharian@ysu.am*

Abstract

The spatially flat cosmological models are investigated within the framework of $f(R)$ -gravity. An equivalent representation in the form of a scalar-tensor theory is discussed. For the general case of the $f(R)$ function, the corresponding cosmological equations are presented in the form of a third order autonomous dynamical system. The qualitative analysis of the latter is given in the absence of nongravitational matter. Various special cases of the function $F(R)$ are considered and the corresponding phase portraits are depicted. The possibility for the realization of a phase with accelerated expansion of the Universe is discussed.

Keywords: $f(R)$ -gravity – scalar-tensor theories – cosmological models.

1. Introduction

It is known that suitable modifications of General Relativity can result in an accelerating expansion of the Universe at present epoch. These modifications fall into two general groups. The first one consists of scalar-tensor theories that are most widely considered extensions of General Relativity (Will 2018). In addition to the metric tensor, these theories contain scalar fields in their gravitational sector and typically arise in the context of models with extra dimensions (Kaluza-Klein-type models, braneworld scenario) and within the framework of the low-energy string effective gravity. In the second group of models, the Ricci scalar R in the Einstein-Hilbert action is replaced by a general function $f(R)$ (for recent reviews see Nojiri & Odintso (2007) and Clifton et al. (2012)). One of the first models for inflation with quadratic in the Ricci scalar Lagrangian, proposed by Starobinsky (1980),

falls into this class of theories. An additional motivation for the $f(R)$ theories comes from quantum field theory in classical curved backgrounds (Birrell & Davies (1982), Buchbinder et al. (1992) and from string theories. The recent investigations of cosmological models in the $f(R)$ theories of gravity have shown a possibility for a unified description of the inflation and the late-time acceleration.

$f(R)$ -gravities can be recast as scalar tensor theories of a special type with a potential determined by the form of the function $f(R)$. Various special forms of this function have been discussed in the literature. In particular, the functions were considered that realize the cosmological dynamics with radiation dominated, matter dominated and accelerated epoch. Unified models of inflation and dark energy have been studied as well (Nojiri & Odintsov 2011). In the present paper we consider the qualitative evolution of the cosmological model for a general $f(R)$ function. The general analysis is specified for various examples, including the original Starobinsky model.

2. $f(R)$ -gravity as a scalar-tensor theory

The action in $(D + 1)$ -dimensional $f(R)$ theory of gravity has the form

$$S = \int d^{D+1}x \sqrt{|g|} [f(R) + L_m(g_{ik}, \psi)], \quad (1)$$

where $L_m(g_{ik}, \psi)$ is the Lagrangian density for non-gravitational matter collectively denoted by ψ . It is well known (see Nojiri & Odintsov (2011) and Clifton et al. (2012)) that (1) can be presented in the form of the action for scalar-tensor gravity. In order to show that we consider the action

$$S = \int d^{D+1}x \sqrt{|g|} [f'(\eta)(R - \eta) + f(\eta) + L_m(g_{ik}, \psi)], \quad (2)$$

with a scalar field η . The equation for the latter is reduced to $f''(\eta)(R - \eta) = 0$. Assuming that $f''(\eta) \neq 0$, from the field equation we get $\eta = R$. With this solution, the action (2) is reduced to the original action (1).

Introducing a new scalar field $\varphi = -f'(\eta)$, the action (2) is written in the form

$$S = \int d^{D+1}x \sqrt{|g|} [-\varphi R - V(\varphi) + L_m(g_{ik}, \psi)], \quad (3)$$

with the scalar potential

$$V(\varphi) = -f(\eta(\varphi)) - \varphi\eta(\varphi). \quad (4)$$

Here, we have assumed that the function $\varphi(\eta)$ is invertible. The action (3) describes a scalar-tensor theory. In the representation (3) the Lagrangian density of the non-gravitational matter does not depend on the scalar field φ . Hence, the representation corresponds to the Jordan frame.

By the conformal transformation

$$g_{ik} = \Omega^2(\varphi)g_{(E)ik}, \quad \Omega(\varphi) = m_P\varphi^{1/(1-D)}, \quad (5)$$

where $m_P = 1/(16\pi G_{D+1})^{1/(D-1)}$ is the Planck mass in $(D+1)$ -dimensions and G_{D+1} is the corresponding gravitational constant, the action is presented as

$$S = \int d^Dx \sqrt{|g_{(E)}|} \left[-m_P^{D-1} R_{(E)} + \frac{1}{2} g_{(E)}^{ik} \partial_i \phi \partial_k \phi - V_E(\phi) + L_m^E(\phi, g_{(E)ik}, \psi) \right]. \quad (6)$$

Here we have introduced a scalar field

$$\phi = \phi_0 \ln \left(\varphi / m_P^{D-1} \right), \quad \phi_0 = m_P^{(D-1)/2} \sqrt{2D/(D-1)}, \quad (7)$$

with a canonical kinetic term and with the potential

$$V_E(\phi) = -\exp \left(-\frac{D+1}{D-1} \frac{\phi}{\phi_0} \right) [f(\eta(\varphi)) + \varphi \eta(\varphi)], \quad \varphi = m_P^{D-1} e^{\phi/\phi_0}. \quad (8)$$

The non-gravitational Lagrangian density is expressed as

$$L_m^E(\phi, g_{(E)ik}, \psi) = \Omega^{D+1} L_m(\Omega^2 g_{(E)ik}, \psi), \quad \Omega = \exp \left[-\frac{\phi}{(D-1)\phi_0} \right]. \quad (9)$$

In the new conformal frame, referred as the Einstein frame, the gravitational part of the action takes the form of that for $(D+1)$ -dimensional General Relativity. In this frame there is a direct interaction between the non-gravitational matter and the scalar field. Several examples of the function $f(R)$ with the corresponding potentials will be discussed below.

3. Cosmological model and the dynamical system

Consider a homogeneous and isotropic cosmological model described by the Einstein frame action (6). The corresponding line element has the form

$$ds_E^2 = dt^2 - a^2(t) dl^2 \quad (10)$$

where dl is the line element of a D -dimensional space of constant curvature, $a(t)$ is the scale factor. From the homogeneity of the model it follows that the scalar field should also depend on time only, $\phi = \phi(t)$. The energy-momentum tensor corresponding to the metric (10) is diagonal and can be presented in the perfect fluid form $T_i^k = \text{diag}(\varepsilon, \dots, -p, \dots)$, where ε is the energy density and p is the effective pressure.

Introducing dimensionless quantities $x = \phi/\phi_0$, $\tau = t/t_0$, with t_0 being a positive constant with the dimension of time, for expanding models with

a flat space the set of cosmological equations is written in terms of the third order autonomous dynamical system

$$\begin{aligned}\frac{dx}{d\tau} &= y, \quad \frac{dy}{d\tau} = -by[2\epsilon + y^2 + 2V(x)]^{1/2} + \phi_0\alpha\epsilon - V'(x), \\ \frac{d\epsilon}{d\tau} &= -\{b(1+w)[2\epsilon + y^2 + 2V(x)]^{1/2} + \phi_0\alpha y\}\epsilon,\end{aligned}\quad (11)$$

where $w = p/\epsilon$, $\epsilon = (t_0/\phi_0)^2\epsilon$, $b = D/(D-1)$, and

$$V(x) = (t_0/\phi_0)^2 V_E(\phi_0 x), \quad \alpha = \frac{1}{\epsilon\sqrt{|g_{(E)}|}} \frac{\delta L_m^E \sqrt{|g_{(E)}|}}{\delta \phi}.\quad (12)$$

The Einstein frame Hubble function $H = a^{-1}da/dt$ is expressed in terms of the variables of the dynamical system (11) as

$$H^2 = \frac{2\epsilon + y^2 + 2V(x)}{(D-1)^2 t_0^2}.\quad (13)$$

The set of equations (11) describes the cosmological dynamics in the Einstein frame (for qualitative analysis of cosmological models of string effective gravity in the Einstein frame see Saharian (1999, 2000a)). The corresponding dynamics in the Jordan frame is obtained by using the conformal transformation (5). For the line element in the Jordan frame one has $ds_J^2 = dt_J^2 - a_J^2(t_J)dl^2$, where the comoving time coordinate and the scale factor are related to the corresponding Einstein frame quantities by $dt_J = m_P\varphi^{1/(1-D)}dt$ and $a_J(t_J) = m_P\varphi^{1/(1-D)}a(t)$. For the Hubble function in the Jordan frame we get

$$H_J = \frac{e^{\phi/(\phi_0(D-1))}}{(D-1)\phi_0} \left[\pm\sqrt{2\epsilon + (d\phi/dt)^2 + 2V_E(\phi)} - \frac{d\phi}{dt} \right],\quad (14)$$

where the upper/lower sign corresponds to expanding/contracting models in the Einstein frame. From the relation (14) it follows that for $V_E(\phi) + \epsilon > 0$ the expansion/contraction in the Einstein frame corresponds to the expansion/contraction in the Jordan frame (H and H_J have the same sign).

4. Qualitative analysis of gravi-scalar models

The dynamical system (11) has an invariant phase plane $\epsilon = 0$ which corresponds to the pure gravi-scalar models. For those models, the system (11) is reduced to the second order dynamical system

$$\frac{dx}{d\tau} = y, \quad \frac{dy}{d\tau} = -by[y^2 + 2V(x)]^{1/2} - V'(x).\quad (15)$$

For Einstein frame expanding models, the Hubble function is expressed in terms of the solution of (15) by (13) with $\epsilon = 0$. The critical points for (15) are the points of the phase plane (x, y) with the coordinates $(x_c, 0)$ where $V'(x_c) = 0$, $V(x_c) \geq 0$. For the corresponding solution the Hubble function is a constant, $H = H_c$, with $H_c^2 = V_E(\phi_c)/[D(D-1)m_P^{D-1}]$. This solution describes the Minkowski spacetime for $V_E(\phi_c) = 0$ and the de Sitter spacetime for $V_E(\phi_c) > 0$. In the latter case for the cosmological constant one has $\Lambda = V_E(\phi_c)/(2m_P^{D-1})$.

The character of the critical points is determined by the eigenvalues

$$\lambda_{1,2} = -b\sqrt{V_c/2} \pm \sqrt{b^2V_c/2 - V_c''}, \quad (16)$$

where $V_c = V(x_c)$, $V_c'' = V''(x_c)$. For $V_c'' < 0$ (x_c is a maximum of the potential $V(x)$) the critical point is a saddle. The directions of the corresponding separatrices are determined by the unit vectors $\mathbf{n}^{(i)} = (1, \lambda_i)/\sqrt{1 + \lambda_i^2}$, $i = 1, 2$. For $V_c'' > 0$ (x_c is a minimum of the potential $V(x)$) two cases should be considered separately. When $0 < V_c'' < b^2V_c/2$, the critical point is a stable node. For $0 < b^2V_c/2 < V_c''$ the critical point is a stable sink. In the case $V_c > 0$, $V_c^{(i)} \equiv (d^iV/dx^i)_{x=x_c} = 0$ for $i = 1, \dots, n-1$, and $V_c^{(n)} \neq 0$, the critical point is (i) a saddle for even n and $V_c^{(n)} < 0$, (ii) a stable node for even n and $V_c^{(n)} > 0$, (iii) a degenerate critical point with one stable node sector and with two saddle sectors for odd n . Another degenerate case corresponds to $V_c = 0$ and $V_c'' > 0$. In this case the critical point is a stable sink.

If the value of the potential at the minimum is negative, then there is a classically forbidden region in the phase plane (x, y) . This region is determined by the inequality $y^2 + 2V(x) < 0$. At the boundary of the forbidden region, given by $y^2 + 2V(x) = 0$, one has $H = 0$ and $dH/dt = m_P^{1-D}V_E(\phi)/(D-1) < 0$. Hence, at the boundary the expansion stops at a finite value of the cosmological time t and then the model enters the stage of the contraction ($H < 0$). The corresponding dynamics is described by the dynamical system (15) with the opposite sign of the first term in the right-hand side of the second equation. For nonnegative potentials the expansion-contraction transition in models with flat space is not classically allowed.

We should also consider the behavior of the phase trajectories at the infinity of the phase plane. With this aim, it is convenient to introduce polar coordinates (ρ, θ) defined as $x = \rho \cos \theta / (1 - \rho)$ and $y = \rho \sin \theta / (1 - \rho)$, with $0 \leq \rho \leq 1$, $0 \leq \theta \leq 2\pi$. Now the phase space is mapped onto a unite circle. The points at infinity correspond to $\rho = 1$. For the potentials having the asymptotic behavior $V(x) \sim B|x|^m$, $m < 4$, in the limit $x \rightarrow \infty$ one has the following critical points on the circle $\rho = 1$. The points $\theta = 0$ and $\theta = \pi$ are stable nodes for $m < 0$ and saddles with two sectors for $m > 0$. In the

latter case the sectors are separated by a special solution described by the trajectory

$$y(x) \approx -\frac{V'(x)}{b\sqrt{2V(x)}} \sim \frac{m}{b}\sqrt{B/2}|x|^{m/2-1}, \quad (17)$$

for $|x| \rightarrow \infty$. In the vicinity of the points $\theta = \pi/2$ and $\theta = 3\pi/2$ the potential terms can be neglected and these points are unstable degenerate nodes. For $m = 4$ the nature of the critical points at $\theta = \pi/2$ and $\theta = 3\pi/2$ remains the same. In this case the other critical points correspond to $\theta = -\arctan(\sqrt{8B}/b)$ and $\theta = \pi - \arctan(\sqrt{8B}/b)$. The phase portrait near these points have two saddle sectors which are separated by the trajectory corresponding to the special solution (17). For $m > 4$ there are two critical points on the circle $\rho = 1$ corresponding to $\theta = \pi/2$ and $\theta = 3\pi/2$. These points are degenerate and have an unstable node sector and a saddle sector separated by the special solution (17). Similar behavior of the phase trajectories at the infinity takes place for the potentials with the asymptotic behavior $V(x) \sim Be^{\sigma|x|}$, $\sigma > 0$, for $x \rightarrow \infty$ and for the values of the parameter $0 < \sigma < 2b$. The separatrix between the saddle and node sectors is described by the special solution $y \approx -\text{sgn}(x)\sigma\sqrt{2B}e^{\sigma|x|/2}/\sqrt{4b^2 - \sigma^2}$ for $x \rightarrow \infty$. The general solution behaves as $y \approx -\text{sgn}(x)Ce^{b|x|}$, with a positive constant C . This behavior coincides with that in the absence of the potential. For $\sigma \geq 2b$ the dynamical system (15) has no critical points at infinity (on the circle $\rho = 1$).

5. Special cases

A number of specific choices for the function $f(R)$ have been discussed in the literature. In the models with quantum corrections to the Einstein-Hilbert Lagrangian the function $f(R)$ is of the polynomial form. A similar structure is obtained in the string-inspired models with the effective action expanded in powers of the string tension. However, it should be noted that in both these types of models coming from high-energy physics, the Lagrangian density in addition to the scalar curvature contains other scalars constructed from the Riemann tensor. In this context, the $f(R)$ theories can be considered as models simple enough to be easy to handle from which we gain some insight in modifications of gravity. In some models proposed for dark energy the function $f(R)$ contains terms with the inverse power of the Ricci scalar. For one of the first models of this type $f(R) = m_P^{D-1}(-R + \gamma/R^m)$ with γ and $m > 0$ being constants (Capozziell 2002). However, there is a matter instability problem in these models. The model with an additional term βR^2 in the brackets has been discussed in Brookfield et al. (2006). Models containing in $f(R)$ exponential functions of the form $e^{\gamma R}$ and providing the accelerating cosmological solutions without a future singularity are considered in Cognola et al. (2008). Examples of the $f(R)$

functions, containing combinations of the powers and exponentials of R , that allow to construct models with a late-time accelerated expansion consistent with local gravity constraints, are studied in references Hu & Sawicki (2007) (see also Nojiri & Odintsov (2011) and Clifton et al. (2012)). For example, in the Tsujikawa model $f(R) = m_P^{D-1}[-R + \gamma \tanh(R/R_0)]$, whereas in the Hu % Sawicki model $f(R) = m_P^{D-1}[-R + \gamma(1 + (R/R_0)^{-m})]$ with constants γ and R_0 .

As an application of general analysis given above, first let us consider a $(D + 1)$ -dimensional generalization of the Starobinsky model (see [?] for the discussion of inflation in this type of models). The corresponding lagrangian density is taken as

$$f(R) = m_P^{D-1} (-R + \beta R^2), \quad (18)$$

where β is a constant. The potential in terms of the canonical scalar field is written in the form

$$V(x) = V_0 \exp\left(\frac{D-3}{D-1}x\right) (1 - e^{-x})^2, \quad (19)$$

where $V_0 = (t_0/\phi_0)^2 m_P^{D-1}/(4\beta)$. For $\beta > 0$ and $x \neq 0$ the potential (19) is positive. It has a minimum at $x = 0$ with $V(0) = 0$. In figure 1 we have plotted the potential (19) as a function of ϕ/ϕ_0 for $D = 3, 4, 5$ (numbers near the curves). As is seen from the graphs, in the case $D = 3$ an inflationary plateau appears for large values of ϕ/ϕ_0 which corresponds to the Starobinsky inflation. Hence, from the point of view of the Starobinsky inflation, the spatial dimension $D = 3$ is special.

In the limit $x \rightarrow -\infty$ the potential behaves as $\exp[-(D + 1)x/(D - 1)]$. From here it follows that the point $\rho = 1$, $\theta = \pi/2$ is degenerate having an unstable node sector and a saddle sector (see figure 2). In the limit $x \rightarrow +\infty$ one has $V(x) \propto \exp[(D - 3)x/(D - 1)]$ and for $D > 3$ the behavior of the phase trajectories near the point $\rho = 1$, $\theta = 3\pi/2$ is similar to that for the point $\rho = 1$, $\theta = \pi/2$. In the special case $D = 3$ the dynamical system has a critical point at $\rho = 1$, $\theta = 0$. This point is a node (see the left panel in figure 2) and the corresponding unstable separatrix describes an inflationary expansion. This special solution is an attractor for the general solution. For $D = 3$ the point $\rho = 1$, $\theta = 3\pi/2$ at the infinity of the phase plane is an unstable node. The only critical point in the finite region of the phase plane, $(x, y) = (0, 0)$, corresponds to the minimum of the potential. This point is a stable sink and the corresponding geometry is the Minkowski spacetime. The phase portrait, mapped on the unit circle, is presented in the left panel of figure 2 for $D = 3$ and in the right panel for $D > 3$.

For the model

$$f(R) = m_P^{D-1} (-R + \beta_n R^n), \quad (20)$$

with even n and $\beta_n > 0$, the potential is nonnegative and is given by the

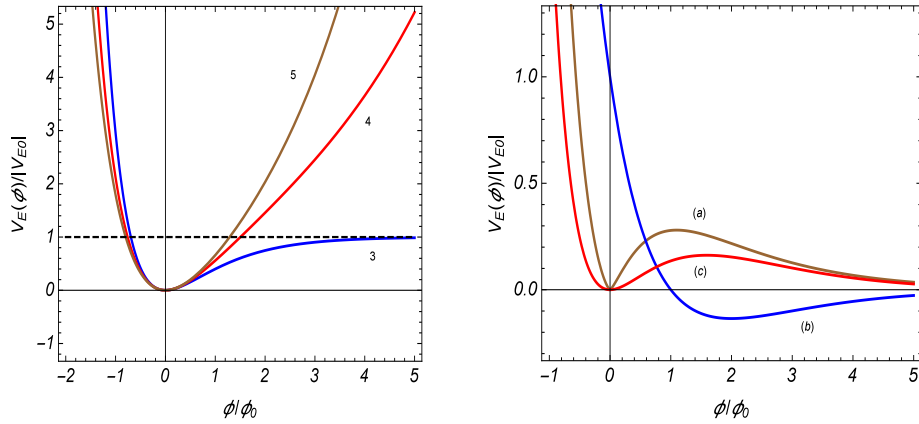


Figure 1: The left panel presents the Einstein frame potentials in the Starobinsky model for different values of the spatial dimension (numbers near the curves). On the right panel the potentials corresponding to the $f(R)$ functions (20) (for $n = 4$, curve (a)), (22) (curve (b)) and (25) (curve (c)) are plotted.

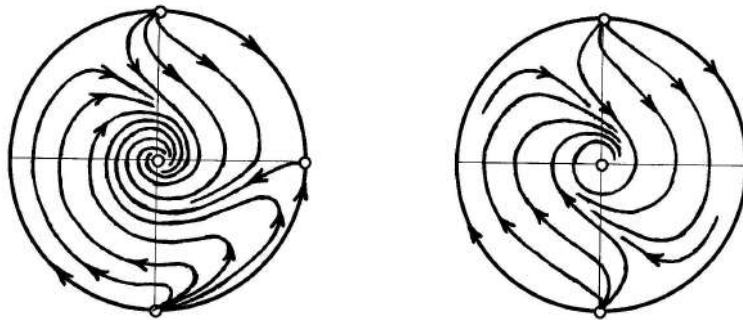


Figure 2: Phase portraits of the dynamical system for a $(D+1)$ -dimensional generalization of the Starobinsky model in the cases $D = 3$ (left panel) and $D > 3$ (right panel).

expression:

$$V(\phi) = V_0 \exp\left(-\frac{D+1}{D-1}x\right) [(1-e^x)^n]^{1/(n-1)}, \quad (21)$$

where $V_0 = (n-1)(t_0/\phi_0)^2 n^{n/(1-n)} \beta_n^{1/(1-n)} m_P^{D-1}$. For $n = 2$ the potential is reduced to the one for the Starobinsky model. In the limit $x \gg 1$ one has $V(x) \rightarrow +\infty$ for $n < (D+1)/2$ and $V(x) \rightarrow 0$ for $n > (D+1)/2$. For $n = (D+1)/2$, in the limit $x \rightarrow +\infty$ the potential has a nonzero plateau: $V(\phi) \rightarrow V_0$. The potential (21) for $n = 4$ and $D = 3$ is depicted in the right panel of figure 1 (graph (a)). For $n > (D+1)/2$ (see graph (a) in the right panel of figure 1) we have two critical points in the finite region of the phase plane. The first one, $(x, y) = (0, 0)$, corresponds to the minimum of the potential and is a stable sink. The second one, $(x, y) = (x_c, 0)$, corresponds to the maximum of the potential and is a saddle. The phase portrait is depicted in the left panel of figure 3. At infinity of the phase plane, the nature of the point $\rho = 1, \theta = \pi/2$ remains the same as in the previous example, whereas the point $\rho = 1, \theta = 3\pi/2$ becomes an unstable node. In the region $x \gg 1$ and for $n > (D+1)/2$ the special solution is an attractor for a general solution in the limit $t \rightarrow +\infty$.

For the next example we take the function

$$f(R) = f_0 e^{\gamma R}. \quad (22)$$

The corresponding potential takes the form

$$V(x) = V_0 \exp\left(-\frac{2}{D-1}x\right) \left[x + \ln(-M_{D+1}^{D-1}/\gamma f_0) - 1\right], \quad (23)$$

with $V_0 = -(t_0/\phi_0)^2 m_P^{D-1}/\gamma$. For $|\gamma R| \ll 1$ one has $f(R) = f_0 + f_0 \gamma R$. Taking $f_0 \gamma = -m_P^{D-1}$, the linear in R term coincides with the Hilbert-Einstein lagrangian density. With this choice the potential simplifies to

$$V(x) = V_0 \exp\left(-\frac{2x}{D-1}\right) (x-1). \quad (24)$$

The graph of this potential for $\gamma > 0$ is plotted in the right panel of figure 1 (curve (b)). The value of the potential at the minimum is negative. Note that in this case for $|\gamma R| \ll 1$ the model reduces to General Relativity with a negative cosmological constant.

In the case of the function

$$f(R) = f_0 (e^{\gamma R} - 1), \quad (25)$$

with $f_0 \gamma = -m_P^{D-1}$ and for small curvatures, corresponding to $|\gamma R| \ll 1$, the model is reduced to General Relativity with zero cosmological constant. The corresponding potential is given by the expression

$$V(x) = V_0 \exp\left(-\frac{D+1}{D-1}x\right) [1 + e^x (x-1)], \quad (26)$$

with the same notation V_0 as in (24). This potential for $\gamma < 0$ ($V_0 > 0$) is plotted in figure 1 (curve (c)).

In the case of the function (22) with $f_0\gamma = -m_P^{D-1}$ and $\gamma > 0$ a characteristic feature of the potential is the presence of the region in the field space where it is negative. For this type of potentials there is a classically forbidden region determined by $y^2 + 2V(x) < 0$. As it has been noted above, at the boundary of this region the expansion stops at a finite value of the cosmological time t and then the model enters the stage of the contraction. For the potential (24), the only critical points of the dynamical system (15) are at the infinity of the phase plane. The corresponding phase portrait is depicted in the right panel of figure 3. The classically forbidden region of the phase space is shaded. The full/dashed trajectories correspond to the expansion/contraction phases. As it follows from (15), the trajectories for the contraction stage are obtained from those describing an expansion by the transformation $\tau \rightarrow -\tau$, $y \rightarrow -y$. For expanding models, near the point $\rho = 1$, $\theta = \pi/2$ the phase portrait has two sectors: an unstable node sector and a saddle sector. The point $\rho = 1$, $\theta = 3\pi/2$ is an unstable node. Depending on the initial conditions, the expanding models start their evolution at finite cosmic time $t = t_i$ from the point $\rho = 1$, $\theta = \pi/2$ or from the point $\rho = 1$, $\theta = 3\pi/2$. During a finite time interval the trajectories reach the boundary of the forbidden region at $t = t_c > t_i$. At this moment the expansion stops ($H(t_c) = 0$) and the model enters the contraction stage (dashed trajectories on the phase portrait). The corresponding trajectories enter the critical points $\rho = 1$, $\theta = 3\pi/2$ and $\rho = 1$, $\theta = \pi/2$ at finite time $t_f > t_c$. Hence, all the models have a finite lifetime $t_f - t_i$.

For the function (25) with $f_0\gamma = -m_P^{D-1}$ the potential is given by the expression (26). In the case $\gamma < 0$ the qualitative behavior of this potential is similar to that for the function (20) with $n > (D + 1)/2$ and the corresponding phase portrait is qualitatively equivalent to the one presented in the left panel of figure 3. However, note that the asymptotic behavior of the potential in the limit $\phi \rightarrow +\infty$ is not purely exponential. For the corresponding potential in (15) from (26) one has $V(x) \approx V_2 x e^{-2x/(D-1)}$ in the limit $x \gg 1$. Here, V_2 is expressed in terms of the coefficient V_0 in (26). It can be seen that the dynamical system has a special solution with the asymptotic behavior $y^2 \approx 2V(x)/(D^2 - 1)$ in the region $x \gg 1$. This special solution is an attractor for the general solution near the critical point $(\rho, \theta) = (1, 0)$. The corresponding time dependence of the scalar field is determined from the relation $2V(x) \approx (D - 1)^2 (D^2 - 1)/\tau^2$, which is obtained by the integration of the first equation in (15). With the help of this relation, the asymptotic behavior of the Einstein frame scale factor is found: $a(t) \approx a_0(t/t_0)^D$, $t \rightarrow +\infty$. The asymptotic behavior of x near the critical point $(\rho, \theta) = (1, 0)$, as a function of the time coordinate is simpler in the Jordan frame. By using the expression for the function $y(x)$ and the relation $dt_J = e^{-x/(D-1)} dt$, in the region $x \gg 1$ we can see that

$x \approx V_2 \tau_J^2 / [2(D^2 - 1)]$, where $\tau_J = t_J / t_0$. For the scale factor in the Jordan frame one gets $a_J(t_J) \approx \text{const } e^x$.

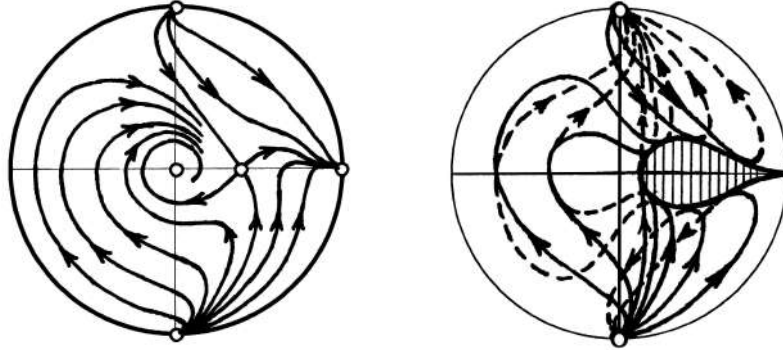


Figure 3: Phase portraits of the dynamical system for the potential (21), with $n = 4$, and for the potential (24).

6. Conclusion

We have considered the qualitative evolution of cosmological models in $(D + 1)$ -dimensional $f(R)$ gravity. In order to do that the model is transformed to an equivalent model described by a scalar-tensor theory. From the point of view of the description of the cosmological dynamics, the most convenient representation corresponds to the Einstein frame, in which the gravitational part of the action coincides with that for General Relativity. In this frame there is a direct interaction of the scalar field with a non-gravitational matter.

For homogeneous and isotropic cosmological models with flat space the equations can be presented in the form of a third order autonomous dynamical system (11). The corresponding phase space has an invariant subspace describing the gravi-scalar models in the absence of a non-gravitational matter. For a general case of the function $f(R)$, we have found the critical points of the system and their nature, including the points at the infinity of the phase plane. As applications of general analysis, various special cases of the function $f(R)$ are considered.

Acknowledgments

R. M. A. and G. H. H. were supported by the Committee of Science Ministry of Education and Science RA, within the frame of the Project No. 18T-1C355.

References

- Birrell, N.D.; Davies, P.C.W. *Quantum Fields in Curved Space*, Cambridge University Press, Cambridge, 1982
- Brookfield, A. W.; van de Bruck, C.; Hall, L.M.H. 2006, Phys. Rev. D, 74, 064028
- Buchbinder, I.L., Odintsov, S.D., Shapiro, I.L. *Effective Action in Quantum Gravity*, IOP, Bristol, 1992
- Capozziello, S. 2002, Int. J. Mod. Phys. D, 11, 483
- Capozziello, S.; De Laurentis, M., 2011, Phys. Rept., 509, 167
- Capozziello, S.; Francaviglia, M., 2008, Gen. Rel. Grav., 357
- Clifton, T.; Ferreira, P.G.; Padilla, A.; Skordis, . 2012, Phys. Rept., 513, 1
- Cognola, G.; Elizalde, E.; Nojiri, S.; Odintsov, S.D., Sebastiani, L.; Zerbini, S. 2008, Phys. Rev. D, 77, 046009
- De Felice, A.; Tsujikawa, S. 2010, Living Rev. Rel., 13, 3
- Hu, W.; Sawicki, I. 2007, Phys. Rev. D, 76, 064004
- Maeda, K. 1988, Phys. Rev. D, 37, 858
- Nojiri, S.; Odintsov, S. D. 2007, Int. J. Geom. Meth. Mod. Phys., 4, 115
- Nojiri, S.; Odintsov, S. D. 2011, Phys. Rept. 59
- Saharian, A.A. 1999, Class. Quantum Grav., 16, 2057
- Saharian, A.A. 2000a, Astrophysics, 43, 92
- Sotiriou, T.P.; Faraoni, V. 2010, Rev. Mod. Phys., 451
- Starobinsky, A.A. 1980, Phys. Lett. B, 91, 99
- Will C.M., *Theory and Experiment in Gravitational Physics*, Cambridge University Press, Cambridge, 2018

WR galaxies and PAH: observations and modeling

A. Yeghikyan^{1*}, J. Martirosyan²

¹*NAS RA V. Ambartsumian Byurakan Astrophysical Observatory (BAO), Armenia*

²*Yerevan State University, Armenia*

**E-mail: ayarayeg@gmail.com*

Abstract

This report analyzes the archival data of the Spitzer observatory for 9 WR galaxies showing PAH emission lines at 6.2 and 7.7 μ . For these galaxies, the effective radii of the emitting regions and the total number of hydrogen ionizing quanta were calculated on the base of the fluxes corrected for interstellar extinction. Using the observed values (which are obtained using SDSS data), and taking as an example stars of the WNh type ($T_s = 50000$ K, $R = 20 R_\odot$), the number of massive WR stars in the cluster and the distance to the nearest neighbor are determined. With these data, the theoretical Cloudy models, in particular, the distribution of H and He, C, O, Ne atoms and ions along the radius are calculated. The theoretical intensities of the characteristic PAH bands at 6.2 and 7.7 μ were obtained for two types of PAH (containing 15 and 120 carbon atoms, respectively). The corpuscular radiation doses accumulated in PAH molecules due to hard irradiation by MeV protons were calculated and it was shown that such molecules had to decay for a time less than the lifetime of the cluster. A conclusion is drawn about the permanent source of PAH, most likely, the remnants of supernova explosions.

Keywords: *WR galaxies – PAH – observations – Cloudy modeling – energetic particles – PAH survivability.*

1. Introduction

The activity of galaxies with a high star formation rate is characterized by the birth of a large number of stars of large mass in one cluster (Crowther et al. 2005). If the mass of the O class star exceeds $25 M_\odot$ (with the solar abundance of chemical elements), the star evolves into a WR phase of no more than 0.5 Myr lifetime, characterized by a very high mass loss rate (of the order of $10^{-5} M_\odot/\text{year}$) and speeds of 500-5000 km/s, but mostly, 1500-2000 km/s (Meynet and Maeder 2005). In this case, the lifetime of

massive O stars stage does not exceed 5 million years (at a mass loss rate of about $10^{-6} M_{\odot}/\text{yr}$). If the number of very massive stars in one cluster is sufficiently large, then many stars can also be caught in the WR phase at the same time, since the number of stars in the WR phase is comparable to the number O of stars (Crowther et al. 2005). This circumstance is confirmed in the spectra of many active galaxies with characteristic features of WR stars. First of all, it is a characteristic emission component in the spectrum with a width of about 40-50 Å at a center at 4650 Å (for WN stars) which is a superposition of 3 lines, He II 4686 Å, NeIII 4640 Å and CIII/IV 4650 Å. A feature of 5808 Å (for WC stars) related to CIV 5808 Å is also possible. With these features, such galaxies are called WR galaxies (Conti 1991), and they are good indicators of the star formation rate, since the lifetime of massive O stars does not exceed 5 million years (Meynet and Maeder 2005). Upon completion of evolution, they explode in the form of supernovae Ib, c. Perhaps they are also associated with the predecessors of GRB (Vink1 et al. 2011). The active regions of these galaxies, and the WR galaxies themselves, include a morphologically diverse range of objects with an increased star formation rate (SB), for example, giant HII regions in spiral arms, irregular galaxies, blue compact dwarf galaxies, bright galaxies in the process of merging, galaxies with active nuclei, etc. (Brinchmann et al. 2008). The number of massive stars in one (active) cluster is estimated as 100-100000 (Crowther et al. 2005). It is interesting to note that the intensity of the emission "bump" in the spectra of WR galaxies depends on the degree of "metallicity": the lower the metal content, the less intense wind can generate a WR star, since it is the radiation pressure in the resonance lines of the C, N, O ions that accelerates the wind to the observed speeds. However, the "bump" is also observed in objects with a very low "metallicity", for example, in Izw18 (Crowther et al. 2005, Brinchmann et al. 2008), although it requires the presence of very massive stars with a mass more than $80 M_{\odot}$ (with a metallicity of 0.05).

In the spectra of many galaxies, including active ones, characteristic bands of many molecules are observed, for example, water, carbon monoxide, polycyclic aromatic hydrocarbons (PAHs), etc. In particular, PAHs are also observed in the spectra of WR galaxies (Martirosyan, Sargsyan 2012), in this case, the emission is provided by PAH molecules with a relative concentration to hydrogen (in all forms) of the order of $2 \cdot 10^{-7} - 2 \cdot 10^{-8}$ and a carbon to hydrogen ratio of about $3 \cdot 10^{-4}$ (Ferland et al. 2017). In the theoretical interpretation of the spectra of PAHs, the number of carbon atoms is usually in the range from 15 to 120 (Ferland et al. 2017). PAHs are very sensitive to the intense radiation fields, which makes it possible to use the equivalent widths of PAH emission lines as an indicator, allowing to distinguish galaxies with active nuclei (PAH lines are very weak or absent) from galaxies with intense star formation (lines are relatively strong) (Martirosyan, Sargsyan 2012). From an evolutionary point of view, the question

of PAHs sources in active galaxies in general, and in WR galaxies in particular, is very interesting and directly related to the conditions of their survival in the presence of hard electromagnetic and corpuscular radiation. The exact estimation of the UV radiation field depends on many parameters, e.g. on the amount of neutral gas in the cluster, the theoretical value of which is strongly model-dependent, and there is no observational data for WR galaxies (Risaliti et al. 1999). This article is devoted to the calculation of PAH radiation doses by corpuscular radiation from massive stars in a WR galaxy, the problem of the survival of PAH molecules under these conditions, and a discussion on the issue of PAH sources in the such galaxy .

2. Observational data

There are 570 WR galaxies, 422 of which are SB (Brinchmann et al. 2008). In (Martirosyan, Sargsyan 2012), 22 WR galaxies were selected from this list, for which Spitzer observations in the region of 5.2-14.5 μ and 14-38 μ are known, including emission lines of PAHs at 6.2 and 7.7 μ . For these galaxies, also known are the SDSS data (sdss.org 2018) on the main emission lines in the visible region, which allowed us to carry out standard diagnostics of the HII regions associated with the WR regions of galaxies. In particular, the electron concentrations and temperatures were determined, as well as the interstellar extinction values for 9 galaxies according to the formulas (Crowther 2007):

$$\frac{F(H_\alpha)}{F(H_\beta)} = \frac{I(H_\alpha)}{I(H_\beta)} \cdot 10^{-c(H_\beta)[x(H_\alpha)-x(H_\beta)]} \quad (1)$$

$$E(B - V) = 0.77 \cdot c(H_\beta), [x(H_\alpha) - x(H_\beta)] = 0.346, R_V = 3.1 \quad (2)$$

$$\frac{I(H_\alpha)}{I(H_\beta)} = 2.86, m = m_{obs} - A_V, A_V \approx 3 \cdot E(B - V) \quad (3)$$

$$F(H_\beta) = 3 \cdot 10^{-9} \cdot W(H_\beta) \cdot 10^{-0.4m} \text{ (erg/cm}^2\text{/s)} \quad (4)$$

$$L(H_\beta) = 4\pi d^2 F(H_\beta), (d - \text{distance to the galaxy}). \quad (5)$$

All initial values of 9 galaxies (from 22 galaxies) are shown in Table 1.

Further, since the data on interstellar extinction are known only for 9 galaxies then we will carry out all calculations only for these objects. So, according to the luminosities in the H_β line corrected for the interstellar extinction and the calculated values of the emission coefficient in the same line (in the unit volume of the HII region) we have well known relation (with the value of $b_4(T_e)$ defined in (Ferland et al. 2017)):

$$E(H_\beta) = 22.4 \cdot 10^{-20} \frac{(n_e)^2 b_4(T_e)}{(T_e)^{3/2}} e^{9814/T_e} \text{ (erg/cm}^2\text{/s)}. \quad (6)$$

WR number	ra	dec	z	EW, PAH 6.2 μ , \AA
31	12 53 05.96	-03 12 58.94	0.02276	0.01
40	17 35 01.24	+57 03 08.55	0.04722	0.01
48	00 55 27.46	-00 21 48.76	0.16741	0.09
108	09 38 13.49	+54 28 25.03	0.10213	0.21
190	10 34 10.15	+58 03 49.06	0.00749	0.15
277	11 05 08.11	+44 44 47.24	0.02154	0.3
288	13 28 44.05	+43 55 50.51	0.02795	0.37
292	15 22 38.09	+33 31 35.81	0.12529	0.26
296	10 16 24.51	+37 54 45.96	0.00394	0.02

Table 1: Observational values of WR galaxies with PAH data

Then one can determine the effective volume of radiation as a ratio

$$V_{eff} = \frac{L(H_\beta)}{E(H_\beta)}, \quad (7)$$

and the effective radius

$$R_{eff} = \sqrt[3]{V_{eff}}. \quad (8)$$

Now we can determine the number of ionizing hydrogen quanta by the known formula

$$\Sigma N(L_c) = q \cdot N(H_\beta), \quad (9)$$

where $q=10.97$ at $T_e=10000$ K and $N(H_\beta) = L(H_\beta)/h\nu(H_\beta) s^{-1}$ – number of quanta in the H_β line, with the energy of a single quantum equal to $h\nu(H_\beta) = 4.09 \cdot 10^{12}$ erg. To estimate the hardness of photon radiation, the parameter U is usually used (Ferland et al. 2017):

$$U = \frac{\Sigma N(L_c)}{4\pi c \cdot n_e \cdot (R_{eff})^2}. \quad (10)$$

The values of $N(L_c)$ and U are given in Tables 2.

WR number	n_e, cm^{-3}	T_e, K	$\Sigma N(L_c), s^{-1}$	N_s	R, pc	lg(U)
31	390.7	19830	2.310+57	2.310+7	2.199+21	0.5113
40	254.7	9581	1.942+54	19420	3.408+20	-0.7588
48	302.7	9077	1.623+54	16230	2.564+20	-0.6647
108	60.59	15300	9.508+53	9508	6.331+20	-0.9835
190	62.59	12490	5.812+51	58	1.384+20	-1.8905
277	80.19	15750	2.321+53	2321	3.268+20	-0.1432
288	94.53	8708	3.034+53	3034	3.237+20	-1.0899
292	204.3	24970	5.054+54	50541	4.884+20	-0.5604
296	15.07	10360	3.248+51	32	3.136+20	-2.2354

Table 2: Observed and calculated data for WR galaxies

3. Young stellar clusters in WR galaxies

The number of stars in the cluster can be estimated by the ratio $N_s = \Sigma N(L_c)/N(L_c)$, where $\Sigma N(L_c)$ is the total number of quanta ionizing hydrogen in the nebula, and $N(L_c)$ is the number of such photons emitting from one star per unit time. Taking, as an example, WN type stars with the presence of hydrogen ($T_s = 50000$ K, $R_s = 20 R_\odot$, but the presence of hydrogen is not important in this case), we have the amount of such quanta by the relation

$$N(L_c) = 4\pi R_s^2 \cdot \frac{2\pi}{c^2} \left(\frac{kT_s}{h} \right)^3 \cdot \delta = 1.8 \cdot 10^{50} \text{ s}^{-1} \quad (11)$$

where

$$\delta = \int_{x_0}^{\infty} \frac{x^2 dx}{e^x - 1}, x_0 = \frac{k_e T_e}{13.6}, k_e = 8.6 \cdot 10^{-5} \frac{\text{eV}}{\text{K}}, \quad (12)$$

while according to calculations based on stellar atmospheric models, $N(L_c) = 1.0 \cdot 10^{-50} \text{ s}^{-1}$ (Crowther 2007; Hamann et al. 2006). So, we get an estimate of the number of massive stars in the cluster, for 9 WR galaxies, for which interstellar extinction data are known. The results are shown in Table 2. With three exceptions, the number of massive stars in the cluster was several thousand or tens of thousands. As cluster sizes from Table 2 are about 100 parsec, these clusters are close to the super-associations according to (Ambartsumian 1964). Being less (in the sense of the classical definition) in size, absolute luminosity and age, and not quite coinciding in the type of host galaxies, these systems with a large number of massive hot and young stars, mostly coincide with the definition of V. Ambartsumyan and are one of the most important star formation activity indicators. So this term also will be used below - superassociation, as a young cluster of a very large number of very massive stars. At present, they are also called Super Star Clusters (Crowther et al. 2005).

Further, Table 3 shows the distances to the nearest neighbor star, calculated for a sphere uniformly filled with similar stars, using the obvious formula

$$d = \frac{R_{eff}}{\sqrt[3]{N_s}}. \quad (13)$$

Then, models of the ionization structures of nebulae associated with WR clusters were calculated. The parameters of the model have already taken the distances to the nearest neighbor as the characteristic thickness of the nebula, $n_H \approx n_e$ as the characteristic concentration of hydrogen, the ionization parameter U , the blackbody temperature $T_s = 50000$ K, the effective radius R_{eff} as the characteristic radius of the incident radiation, chemical composition was assumed to be equal to solar, and the value of the turbulent velocity in the medium about 10 km/s. It is easy to show on the

base of calculations of ionizational structures that at a distance of more than 1 pc, the medium at such a density becomes neutral and then molecular, protecting the PAH molecules from destruction by UV photons. The same is true for other galaxies from the list. Let us get started, therefore, to estimate of the degree of impact of corpuscular irradiation on PAH molecules, since for energies of the order of 1 MeV and higher, nebulae in WR clusters are transparent for such radiation.

4. Corpuscular radiation fluxes, radiation doses and survivability of PAH

There are a large number of analytical and numerical models describing intensities of energetic particles accelerated at the shock that is formed during the interaction of a fast stellar wind with a given nebula (in this case, with a super-association nebula) (Drury 1983; Decourchelle 2008). Detailed calculations take into account the many features of the process, such as the formation of a spectrum of particles, the orientation of the magnetic field vector with respect to the normal to the front, the presence of sources of super-thermal particles experiencing acceleration by the Fermi 1 diffusion mechanism. These theories predict reasonable values of particle intensities, in particular, galactic cosmic rays, and are now generally accepted. For example, in the case of the heliosphere, that is, the shock wave front at the interface of the solar wind interaction with the surrounding interstellar gas, the intensities of the accelerated particles are in good agreement with direct observations of the Voyager 1 and 2 probes (Yeghikyan 2018 and references therein).

According to Yeghikyan (2018), in a time shorter than the dynamic time of the WR nebulae (about 10^5 years), the part of the particles energetic spectrum in the energy range 1-100 MeV will have quite time to form. It should be emphasized that with the expansion of the nebula, that is, with an increase in its inner radius, its ability to produce energetic particles can be estimated by a semi-analytical relation (Yeghikyan 2018):

$$\eta \frac{1}{4\pi} \frac{\dot{M}_f V_f^2}{4\pi r_i^2} = \int_{E_1}^{E_{max}} J_E(E) dE \quad (14)$$

where \dot{M}_f is the rate of mass loss by the WR star (g/s), V_f is the wind velocity (cm/s), $J_E(E)$ is the differential intensity of accelerated particles ($\text{erg} \cdot \text{cm}^{-2} \cdot \text{s}^{-1} \cdot \text{sr}^{-1} \cdot \text{MeV}^{-1}$), and η is the fraction of kinetic wind energy spent on acceleration of protons by a shock wave in the energy range $E_1 \leq E \leq E_{max}$. By the way, according to the generally accepted theory of the origin of cosmic galactic rays in supernovae expanding shell, usually $\eta = 0.1 - 0.3$, but according to later observations and numerical calculations larger values are also possible, $\eta = 0.5$ (Ellison et al. 2005).

It is interesting to compare the estimate (14) for the solar wind with the measurements of the Voyager 1 probe (Yeghikyan, 2018 and references therein). Putting

$$J_E(E) = J_E(E_1) \left(\frac{E_1}{E} \right)^\gamma, \quad J_p(E) = \frac{J_E(E)}{E_1} \quad (15)$$

where $E_1=1$ MeV, $\gamma=2-4$, for the differential intensity of particles with $E = E_1=1$ MeV, (in units $\text{particles}\cdot\text{cm}^{-2}\text{s}^{-1}\text{sr}^{-1}\text{MeV}^{-1}$) we have (Yeghikyan 2018):

$$J_p(E_1) = \frac{J_E(E_1)}{E_1} = \frac{\gamma - 1}{E_1^2} \eta \frac{1}{4\pi} \frac{\dot{M}_f V_f^2}{4\pi r_i^2}. \quad (16)$$

Taking $\dot{M}_f = 2 \cdot 10^{-14} M_\odot/\text{yr}$, $V_f=400$ km/s, $r_i=100$ a.u., $\eta=0.1$, for $\gamma = 2, 3, 4$ we get, respectively, $J_p(E_1) \cong 0.8, 1.6, 2.4$ $\text{particles}\cdot\text{cm}^{-2}\text{s}^{-1}\text{sr}^{-1}\text{MeV}^{-1}$, which coincides with the Voyager-1 measurements up to a factor of 2, namely, ≈ 1.4 in the same units (Stone et al. 2005; Scherer et al. 2008). We underline again that the phenomenological estimate (14) gives the same accuracy (within a factor less than 2), if we choose $\eta = 0.1$.

We now turn to the calculation of the differential intensity of energetic protons under WR nebular conditions. Taking $\dot{M}_f = 10^{-5} M_\odot/\text{yr}$, $V_f=1500$ km/s, $r_i = 3 \cdot 10^{18}$ cm, $\eta = 0.1$, then (14) gives values where the concentration of the fast wind at the shock is determined by the relation $n_1 = \dot{M}_f / 4\pi r_i^2 V_f m_p$.

It should be emphasized that the average galactic value (for our Galaxy) $J_p(E_1) = 2 \cdot 10^{-4}$ $\text{particles}\cdot\text{cm}^{-2}\text{s}^{-1}\text{sr}^{-1}\text{MeV}^{-1}$ (Scherer et al. 2008), that is, on the inner boundary of the nebula (1 or, say, 5 pc) intensity of energetic particles which is 1000 or 40 $\text{particles}\cdot\text{cm}^{-2}\text{s}^{-1}\text{sr}^{-1}\text{MeV}^{-1}$, respectively, by more than several orders of magnitude, (7 or 5) exceeds the mean galactic one. This is not surprising, since even the heliosphere formed by a much weaker wind nevertheless causes the appearance of similar accelerated particles by 4 orders of magnitude greater than intensity of the average galactic one (Scherer et al. 2008).

Thus, WR nebulae can be a very powerful local source of energetic particles (with not very high energies) and it would be interesting to investigate their possible observational manifestations in the nebula itself.

We emphasize that the most interesting from the point of view of energy sources for chemical reactions are particles with energies of 1-10 MeV, since even with the minimal observed exponent ($\gamma \approx 2.3$), the spectral steepness is quite noticeable, and in the integrals describing, for example, the fraction of the absorbed energy, particles with energies greater than 10-20 MeV practically do not contribute. Therefore, when using formulas describing the energy spectra, one should always keep in mind the reservations with which they were obtained, especially in the case of relativistic particles.

Due to the high values of the fluxes of energetic particles in the WR nebulae, it is interesting to estimate the doses (absorbed energy) of PAHs in these nebulae. We have for the intensity of accelerated particles expression (14), in the energy range of 1-100 MeV, important in the irradiation of different species, as well as in the ionization of H_2 . Assuming $\dot{M}_f = \cdot 10^{-5} M_\odot / \text{yr}$, $V_f = 1500$ km/s, for the differential intensity of the energetic protons with $E_1 = 1$ MeV, one can write for two values of the inner radius $r_i = 1$ or 5 pc:

$$J_p(E_1) = 40 - 1000 \frac{\text{particles}}{\text{cm}^2 \cdot \text{s} \cdot \text{sr} \cdot \text{MeV}}. \quad (17)$$

Thus, at standard values of the parameters of the WR nebulae, the obtained estimates of the intensity at the inner boundary of the nebula are 5-7 orders of magnitude larger than the average galactic one (Scherer et al. 2008, their Fig.2):

$$J_p(E_1) = 1.0 \cdot 10^{-4} \frac{\text{particles}}{\text{cm}^2 \cdot \text{s} \cdot \text{sr} \cdot \text{MeV}}. \quad (18)$$

The influence of the magnetic field (if present) can be twofold: on the one hand, protons can be reflected from magnetic inhomogeneities, and, depending on the intensity and geometry of the magnetic field (1-10 μG), the flux can be decreased by 1 order (Schekinov 2005, and references therein). On the other hand, non-thermal protons of relatively low energies may possibly be accelerated to values of 1-10 MeV in the presence of magnetohydrodynamic turbulence with a specific spectrum (Fermi-2 process) (Hendrix et al. 2016; Monnier et al. 2007). Thus, in this case, the actual particle intensity at the outer edge of the nebula can decrease, at most (taking into account the geometric divergence), by 2 orders of magnitude to $J_p(E_1) = 0.1 - 10$ particles/($\text{cm}^2 \cdot \text{s} \cdot \text{sr} \cdot \text{MeV}$).

It has already been noted above that the distances to the nearest neighbor are calculated for a sphere uniformly filled with stars of the same type, using the obvious formula (13). Since all massive stars of the cluster are considered similar, we will also be interested in half of this distance, that is, $r_i = d/2$.

These values are necessary for calculating the total corpuscular radiation field from the winds of WR stars, because if the flux from one WR star at a distance r is F_0/r^2 , then from N such stars in super-association with radius R_{eff} with uniform filling will be

$$F \approx \frac{F_0}{r^2} \frac{N}{\frac{4}{3}\pi R_{eff}^3} \frac{4}{3}\pi r^3 \approx \frac{NF_0 r}{R_{eff}^3} \approx \frac{F_0 r}{d^3}, \quad (19)$$

where F_0 is the flux at a distance of 1 pc from the star. At the boundary, when $r \cong R_{eff}$, the flux will be determined by the expression

$$F \approx \frac{NF_0}{R_{eff}^2}. \quad (20)$$

By the formula (20) the lower limit of the flux is determined at any point of the cluster. The method of calculating F_0 is given above, and now we will explain the need for calculating the total flux. The fact is that the super-associations have dimensions $R_{eff} \approx 100$ pc, while the distance to the nearest neighbor is about $d \approx 10$ pc (that is $r_{1/2} = d/2 \approx 5$ pc, see Table 3). When a gas concentration is of about of several $10 - 100 \text{ cm}^{-3}$, a neutral, HI, and then molecular, H_2 layers are formed on sizes $\cong d$ protecting PAH from hard UV radiation. This can be easily verified by calculating the ionization structure of super-association regions with sizes $\cong d$ using the Cloudy computer model (Ferland et al. 2017). Everywhere, at half the distance of the nearest neighbor d , the medium is neutral, or even molecular, and can protect PAHs molecules (Yeghikyan, Martirosyan 2019).

But at densities and sizes about of R_{eff} , the medium of super-association is practically transparent for protons with energies of 1-100 MeV and higher. Such protons are formed at the shock where the stellar wind interacts with the interstellar medium (Yeghikyan 2018). The advantage of formula (20) is that despite its inaccuracy (for use at any point of super-association), it is nevertheless quite suitable for our purposes, namely, determining the lower boundary of the flux to solve the question of the survival of PAH molecules. Even more accurate relations can be used if we take into account the fact that the given star in the cluster is surrounded by 6 nearest stars at a distance d , and at the point $r_i = d/2$ the radiation comes first from two nearest stars and second from 4 stars with distances $\sqrt{5}d/2$. Thus, the lower boundary value of the flux is estimated, and the inaccuracies associated with the determination of the flux at $r_i=1$ pc are mutually compensated.

Now it is possible to calculate dD_p/dt , that is the rate of PAH irradiation by energetic protons in WR nebulae using a simple relation (Yeghikyan 2018, and references therein):

$$n_t \cdot M(n_t) \cdot \frac{dD_p}{dt} = \int_{E_1}^{E_2} F(E)S(E)dE, D_p = \frac{dD_p}{dt} \cdot t, \quad (21)$$

where $F(E) = 4\pi J_p(E)$ and $S(E) = -dE/dx$ is the particle energy loss during the passage of the path dx (in units keV/ μ) in the dust particle with the concentration n_t and molecular weight $M(n_t)$ (accordingly, $S(E)$ that is the amount of energy absorbed by the dust particle per unit length will be positive). $S(E)$ in the energy range of 1–100 MeV can be easily calculated by the Bethe-Bloch formula, using the SRIM computer program (Ziegler et al. 2003). For PAHs, for example, anthracene, $\text{C}_{14}\text{H}_{10}$, energy losses calculated by SRIM can be found in (Ziegler et al. 2003).

Further, choosing the least steep type of the spectrum, $F(E) = F(E_1) \cdot (E_1/E)^2$, we obtain $dD_p/dt = 2.263 \cdot 10^{-11} \text{ eV/s/a.m.u.}$ at a distance of $r_i = 1$ pc from the star. It is possible to calculate the total radiation dose of dust D_p for the values of distances $r_i=1$ pc and $d/2$, respectively, taking into

account the (minimal) possible number of nearby stars. In particular, for the characteristic time interval $t=500000$ years at $r_i=1$ pc, the irradiation dose is $D_p(1pc) = (dD_p/dt) \cdot t \cdot (1 + 6/(d-1)^2)$ eV/a.m.u. For larger distances comparable to distances of order d , for example, when $r_i = d/2$ pc, the irradiation dose is $D_p(d/2 pc) = D_p(1 pc) \cdot 11.2/(d-1)^2$ eV/(a.m.u.). Values D_p are given in Table 3 for the above distances. We emphasize that in the table shown are the lower limits of dose values.

According to experiments (van der Burgt et al. 2018; Dunne et al. 2017), the irradiation of anthracene with low-energy electrons (5-100 eV) leads to its fragmentation, starting from approximately 45 eV. It should also be true for protons (including higher energies), and when the corresponding dose is accumulated in the molecule, and for other PAHs (Champeaux et al. 2014; van der Burgt et al. 2018).

With a deficit of hydrogen in the stellar wind, that is, with the prevalence of helium, the resulting value should be multiplied by 10, since the energy loss of α -particles is an order of magnitude greater (Ziegler et al. 2003), and doses can reach 1000 eV/a.m.u. and higher.

WR number	$\Sigma N(L_c), s^{-1}$	N_s	R_{eff}, cm	d, pc	$D_p(1pc), eV/a.m.u.$	$D_p(d/2), eV/a.m.u.$
31	2.31+57	2.310+7	2.199+21	2.50	1307	6487
40	1.94+54	19420	3.408+20	4.11	578.8	670.7
48	1.62+54	16230	2.564+20	3.28	768.5	1653
108	9.51+53	9508	6.331+20	9.69	385.5	57.23
190	5.81+51	58	1.384+20	11.6	376.2	37.60
277	2.32+53	2321	3.268+20	8.00	400.8	91.65
288	3.03+53	3034	3.237+20	7.25	412.0	118.3
292	5.05+54	50541	4.884+20	4.28	556.1	578.5
296	3.25+51	32	3.136+20	32.0	359.3	4.183

Table 3: Dose rates and doses of PAH molecules in 500000 years

We should bear in mind the fact that these values can be at least doubled, since radiation from the previous stage O of the star, whose power is an order of magnitude less ($\dot{M}_f = 10^{-6} M_\odot/yr$), but the duration is ten times more ($t = 5$ million years). Thus, everywhere in the WR nebulae PAHs receive the dose of more than 50-100 eV and should have been destroyed. Galaxy N 296 probably is an exception, but of course with such galaxies (and of course, N 31) one should be dealt separately.

Thus, the PAH molecules should have disintegrated in a time less than the lifetime of the cluster. This leads to the conclusion that a permanent source of PAH molecules exists in a nebula associated with a cluster of young and very massive stars. Most likely, these PAH molecules are formed in supernova remnants in the same cluster.

The origin of dust, which is observed in WR nebulae, is still under discussion (Hendrix et al. 2016), it is possible that dust (and PAH) is produced under conditions of the colliding winds of massive WR pairs (Hendrix et al. 2016), but in the case of PAHs, as we found out, this is impossible due to

inevitable destruction during the star lifetime.

5. Conclusion

In this paper, we analyzed the conditions in WR galaxies, and for 9 of them the numbers of hydrogen ionizing photons were calculated based on the observed fluxes corrected for interstellar extinction. Then, the effective volume and effective radius radiation of nebulae were calculated, and assuming the number of massive stars in the cluster was equal to the number of WR stars, and, knowing also the theoretical number of hydrogen-ionizing photons from one star, the numbers of WR stars in each cluster were calculated. Further, the distance to the nearest neighbor (with a uniform distribution) turned out to be of the order of several parsecs, and besides based on the theoretical models calculated by us the gaseous medium at such a distance is already neutral, and even molecular completely protecting the nebula from UV radiation. However, the medium is exposed not only to electromagnetic, but also to corpuscular irradiation from protons with energies of 1-100 MeV, which arise in the processes of diffuse acceleration at the shock in the Fermi-1 process. The accumulated doses of radiation from these protons, calculated during the lifetime of the super-association, were everywhere in the nebula more than 50-100 eV, which should lead to the destruction of PAHs. However, PAHs are observed in WR galaxies, therefore, we came to the conclusion that PAH sources are permanently exist, most likely in supernova remnants.

References

- Ambartsumian, V. 1964, Superassociations in distant galaxies, ed. F.J.Kerr and A.W.Rodgers, IAU Symp. 20, p. 122
Brinchmann, J.; D. Kunth, D.; Durret, F. 2008, *A&A*, 485, 657
Champeaux, J.-P.; Moretto-Capelle, P.; Cafarelli, P.; Deville, C.; Sence, M.; Casta, R. 2014, *MNRAS*, 441, 1479
Conti, P. *Ap.J.*, 1991, 377, 115
Crowther, P. 2007, *ARAA*, 45, 177
Crowther, P.; Hadfield, L.; Schild, H.; Schmutz, W.; de Grijs, R.; Gonzalez, R. M.; Decourchelle, A. 2008, *Mem. S.A.It.*, 79, 44, 2008
Delgado (eds.), *Starbursts*, 2005, Springer, 21
Drury, L. 1983, *Rep. Prog. Phys.*, 46, 973
Dunne, M., Gradziel, M., van der Burgt, P., 2017, *Journal of Physics: Conf. Series* 875, 062013
Ellison, D., Decourchelle, A., Ballet, J. 2005, *A&A*, 429, 569
Ferland, G.; Chatzikos, M.; Guzman, F.; Lukins, M. et al. 2017, *RMAA*, 53, 385

- Hamann, W.-R.; Gräfener, G.; Liermann, A. 2006, *A&A* 457, 1015
 Hendrix, T., Keppens, R., van Marle, A., Camps, P., Baes, M., Zakaria, M. 2016, *MNRAS*, 460, 3975
 Martirosyan, J.; Sargsyan, L. 2012, *Astrophysics*, 55, 306
 Meynet, G.; Maeder, A.; 2005, *A&A*, 429, 581
 Monnier, J., Tuthill, P., Danchi, W., Murphy, N., Harries, T. 2007, *Astrophys. J.* 655, 1033
 Risaliti, G.; Maiolino, R.; Salvati, M. 1999, *Astrophys. J.*, 522, 157
 Shchekinov, Y. 2005, *Astron. Rep.* 49, 269, 2005
 Scherer, K., Fichtner, H., Ferreira, S., Büsching, I., Potgieter, M. 2008, *ApJ.*, 680, L105.
 Stone, E., Cummings, A., McDonald, F., Heikkila, B., La, N., Webber, W. 2005, *Science*, 309, 2017
 van der Burgt, P., Dunne, M., Gradziel, M. 2018, *The European Physical Journal D*, 72,31
 Vink1, J.; Gräfener, G.; Harries, T. 2011, *A&A*, 536, L10
 Yeghikyan, A. 2018, *Astrophys.*, 61, 469
 Yeghikyan, A.; Martirosyan, J. 2019, *Astrophysics*, to be submitted
 Ziegler, J.; Biersack, J.; Littmark, U. 2003, *The Stopping and Range of Ions in solids*, Pergamon Press, NY, 2003.

Induced Cosmological Constant in Braneworlds with Compact Dimensions

A. A. Saharian^{1*}, H. G. Sargsyan¹

¹Department of Physics, Yerevan State University, 1 Alex Manoogian Street, 0025 Yerevan,
Armenia

*E-mail: saharian@ysu.am

Abstract

We investigate the cosmological constant induced by quantum fluctuations of a bulk charged scalar field on a brane in background of locally anti-de Sitter spacetime with toroidally compact spatial dimensions. Along compact dimension quasiperiodicity conditions are imposed with general phases and, in addition, the presence of a constant gauge field is assumed. The latter gives rise to Aharonov-Bohm type effect on the characteristics of the scalar vacuum. The renormalization of the vacuum energy density on the brane is done by making use of the generalized zeta function technique. The behavior of the cosmological constant is studied as a function of the location of the brane, of the length of the compact dimensions and of the magnetic flux enclosed by the compact dimension. In particular, it is shown that the cosmological constant is a periodic function of the magnetic flux with the period equal to the flux quantum.

Keywords: *cosmological constant - braneworld scenario - anti de Sitter spacetime - Casimir effect.*

1. Introduction

The braneworld models (for reviews see Brax 2003) and Maarten (2010) provide an interesting alternative to the standard Kaluza-Klein compactification of the extra dimensions. In the corresponding constructions the standard model fields are localized on a hypersurface (brane) in a higher-dimensional spacetime. As a consequence of that, the observational restrictions on the size of extra dimensions are much weaker. The introduction of large extra spatial dimensions may provide a solution to the hierarchy problem between the gravitational and electroweak mass scales. The main idea to resolve the large hierarchy is that the small coupling of four dimensional gravity is generated by the large physical volume of extra dimensions. Braneworlds naturally appear in string/M-theory context and provide

a novel setting for discussing phenomenological and cosmological issues related to extra dimensions. The problem of the cosmological constant has been considered as the most serious mass hierarchy problem in modern particle physics (see, for instance, Martin (2012) and many attempts addressing this fine tuning issue can be found in the literature. The braneworld theories may give some alternative discussion of the cosmological constant.

The investigations of quantum effects in braneworlds are of considerable interest in particle physics and cosmology. An inherent feature is the presence of boundaries and the fields that propagate in the bulk will give Casimir-type contributions to the vacuum expectation values (VEVs) of physical observables (for reviews of the Casimir effect see Milton (2002), Bordag et al. (2009), and Casimir Physic (2011)). In particular, vacuum forces arise acting on the branes which can either stabilize or destabilize the braneworld. The Casimir energy gives a contribution to both the brane and bulk cosmological constants and, hence, has to be taken into account in the self-consistent formulation of the corresponding models. Motivated by these issues, the quantum vacuum effects induced by branes in AdS bulk have received a great deal of attention (see references cited in Bezerra de Mello et al, (2015)). The VEV of the energy-momentum tensor has been investigated in Knapman & Toms (2004).

In manifolds with boundaries the energy-momentum tensor in addition to the bulk part contains a contribution located on the boundary (see Saharian (2004) for a real scalar field). In Saharian (2004, 2006) and Saharian et al. (2018) the VEV of the surface energy-momentum tensor is evaluated for a massive scalar field subject to Robin boundary conditions on branes in AdS bulk. It has been shown that in the Randall-Sundrum models the cosmological constant induced on the visible brane by the hidden brane can serve as a model for dark energy. In the present paper we investigate the VEV of the surface energy-momentum tensor for a charged scalar field in locally AdS background spacetime with a codimension-one brane parallel to the AdS boundary and with an extra compactified dimension (generalized 1-brane Randall-Sundrum model). In addition, the presence of a constant gauge field is assumed. It is shown that the vacuum expectation value of the surface energy-momentum tensor on a brane gives rise to a cosmological constant type contribution from the point of view of an observer living on the brane.

2. Problem setup

In Poincaré coordinates, the metric tensor for a $(D+1)$ -dimensional AdS spacetime is given by the line element

$$ds^2 = g_{ik} dx^i dx^k = e^{-2y/a} \eta_{\mu\nu} dx^\mu dx^\nu - dy^2, \quad (1)$$

where $\eta_{\mu\nu} = \text{diag}(1, -1, \dots, -1)$ is the D -dimensional Minkowski metric, $\mu, \nu = 0, 1, \dots, D-1$, and the indices i, k run over 0 to D . In what follows, we use lowercase Latin letters to denote indices running from 0 to D , and lowercase Greek letters to denote indices running from 0 to $D-1$. In addition to the coordinate y , $-\infty < y < +\infty$, we introduce the coordinate z , defined as $z = ae^{y/a}$, $0 < z < \infty$. In terms of the latter the line element is written in a manifestly conformally flat form $ds^2 = (a/z)^2 (\eta_{\mu\nu} dx^\mu dx^\nu - dz^2)$. In terms of the coordinate z , the hypersurfaces $z = 0$ and $z = \infty$ correspond to the AdS boundary and horizon respectively. The Ricci scalar R and the cosmological constant Λ are related to the AdS radius a as $R = D(D+1)a^{-2}$ and $\Lambda = -D(D-1)a^{-2}/2$.

The local geometry we are going to consider here is that of AdS, given by (1), however the global properties differ. It will be assumed that the coordinate x^{D-1} is compactified on a circle S^1 with the length L , $0 \leq x^{D-1} \leq L$. For the remaining coordinates, as usual, we take $-\infty < x^i < +\infty$, $i = 1, \dots, D-2$. Note that the proper length of the compact dimension measured by an observer with fixed y is given by $L_{(p)} = aL/z = e^{-y/a}L$. The latter is decreasing with increasing y .

We are interested in quantum effects on the vacuum state for a complex scalar field $\varphi(x)$ induced by compactification of the dimension x^{D-1} . Assuming the presence of an external gauge field A_i , the corresponding equation of motion reads

$$\left(g^{ik} D_i D_k + m^2 + \xi R \right) \varphi(x) = 0, \quad (2)$$

with $D_k = \nabla_k + ieA_k$ being the gauge extended covariant derivative operator. We assume that along the compact dimension the field obeys the quasiperiodicity condition

$$\varphi(t, x^1, \dots, x^{D-1} + L, y) = e^{2\pi i \alpha} \varphi(t, x^1, \dots, x^{D-1}, y), \quad (3)$$

with a constant phase α . Here we consider a gauge field configuration with constant A_i . In this case the corresponding field strengths are zero. However due to the nontrivial spatial topology the field A_i leads to physical effects. In the geometry under consideration, in the presence of constant external gauge field the VEVs of the current densities along the compact dimensions are investigated in Bezerra de Mell et al. (2015), where it is shown that Aharonov-Bohm like effects arise due to the non-trivial topology. In the same geometry with the presence of branes the VEV of the current density is investigated in Bellucci et al. (2015, 2016).

With constant A_i , by the gauge transformation $\varphi(x) = e^{-ie\chi(x)}\varphi'(x)$, $A_i = A'_i + \partial_i\chi(x)$, with $\chi(x) = A_i x^i$, one passes to a new gauge, where $A'_i = 0$. However, the vector potential does not completely disappear from the problem: it enters into the quasiperiodicity condition for the new field

$$\varphi'(t, x^1, \dots, x^{D-1} + L, y) = e^{2\pi i \tilde{\alpha}} \varphi'(t, x^1, \dots, x^{D-1}, y), \quad (4)$$

where $\tilde{\alpha} = \alpha + eA_{D-1}L/(2\pi)$. In what follows we will work in the gauge $(\varphi'(x), A'_i)$ with $A'_i = 0$, omitting the primes for the sake of simplicity. In this gauge, the field equation takes the form (2) with $A_i = 0$. Note that the shift in the phase induced by the gauge field can be written as $eA_{D-1}L/(2\pi) = -\Phi/\Phi_0$, where Φ is the gauge field flux enclosed by compact dimension and $\Phi_0 = 2\pi/e$ is the flux quantum. In addition, we assume the presence of a brane located at $y = y_0$. On the brane the field obeys the Robin boundary condition

$$(1 + \beta^{(j)}n_{(j)}^i \nabla_i)\varphi(x) = 0, \quad (5)$$

where $\beta^{(j)}$ is a constant and $n_{(j)}^i$ is the normal to the brane. In general, the coefficients in the boundary condition can be different for the left and right surfaces of the brane. The superscript (j) differentiates between the right surface, $y = y_0 + 0$ ($j = 1$), and the left surface, $y = y_0 - 0$ ($j = 2$), of the brane.

We are interested in the VEV of the surface energy-momentum tensor $T_{ik}^{(s)}$ for the complex scalar field $\varphi(x)$, localized on the brane. The expression for the latter can be found in a way similar to that used in Saharian (2004) for a real scalar field. On the background of a $(D+1)$ -dimensional spacetime region M with timelike boundary ∂M_s the surface energy-momentum tensor has the form

$$T_{ik}^{(s)} = \delta(x; \partial M_s) \left[\xi \varphi \varphi^\dagger K_{ik} - (\xi - 1/4) h_{ik} n^l \nabla_l (\varphi \varphi^\dagger) \right], \quad (6)$$

where $h_{ik} = g_{ik} + n_i n_k$ is the induced metric, n^i is the inward pointing unit vector field normal to ∂M_s , $\delta(x; \partial M_s)$ is the one-sided delta function, and $K_{ik} = h_i^l h_k^m \nabla_l n_m$ is the extrinsic curvature tensor of the boundary.

Let us denote by $\{\varphi_\sigma^{(+)}(x), \varphi_\sigma^{(-)}(x)\}$ a complete set of positive and negative energy solutions of the field equation obeying the periodicity condition (4) and the boundary condition (5). The collective index σ specifies the set of quantum numbers specifying the solutions. For the background geometry under consideration the mode functions can be taken as

$$\varphi_\sigma^{(\pm)}(x) = z^{D/2} [C_1 J_\nu(\lambda z) + C_2 Y_\nu(\lambda z)] \exp\left[i \sum_{l=1}^{D-1} k_l x^l \mp i\omega t\right], \quad (7)$$

where $J_\nu(\lambda z)$ and $Y_\nu(\lambda z)$ are the Bessel and Neumann functions, $\omega^2 = \lambda^2 + \sum_{l=1}^{D-1} k_l^2$, and

$$\nu = \sqrt{D^2/4 - D(D+1)\xi + m^2 a^2}. \quad (8)$$

If the order ν of the cylinder functions is imaginary the corresponding vacuum state is unstable [?]. For this reason we will consider only the values

for the parameters in the problem for which $\nu \geq 0$. For the components of the momentum one has $-\infty < k_l < +\infty$, for $l = 1, \dots, D - 2$, and

$$k_{D-1} = k(n) = 2\pi \frac{n + \tilde{\alpha}}{L}, \quad n = 0, \pm 1, \pm 2, \dots \quad (9)$$

The complete set of quantum numbers σ consists of the components of momentum k_r , $r = 1, 2, \dots, D - 1$, and the "radial" quantum number λ .

The nonzero components of the induced metric on the brane $y = y_0$ and the corresponding extrinsic curvature tensor are given by $h_{\mu\nu} = g_{\mu\nu}$ and $K_{\mu\nu} = -n^{(j)} g_{\mu\nu}/a$, where $n^{(1)} = 1$ and $n^{(2)} = -1$. For Dirichlet boundary conditions, $\beta^{(j)} = 0$, the surface energy-momentum tensor vanishes and in the following discussion we will assume that $\beta^{(j)} \neq 0$. By using the boundary condition (5), for the VEV of the surface energy-momentum tensor (6) one obtains $\langle 0|T_{\mu}^{(s)\nu}|0\rangle = \delta(x; \partial M_s) \langle \tau_{\mu}^{(j)\nu} \rangle$, where

$$\langle \tau_{\mu}^{(j)\nu} \rangle = -\delta_{\mu}^{\nu} \frac{n^{(j)}}{a} \left(\xi - \frac{2\xi - 1/2}{n^{(j)}\beta^{(j)}} a \right) \langle \varphi\varphi^{\dagger} \rangle_j. \quad (10)$$

Hence, the problem is reduced to the evaluation of the VEV of the field squared on the brane $\langle \varphi\varphi^{\dagger} \rangle_{y=y_0}$. The VEV (10) is diagonal and all the non-zero components are equal. For the observer living on the brane the corresponding energy density ε_j (the energy per unit physical volume on the brane) and the stresses p_j are given by $\varepsilon_j = \langle \tau_0^{(j)0} \rangle$ and $p_j = -\varepsilon_j$. These quantities do not depend on the coordinates on the brane and correspond to a source of the cosmological constant type for the observer on the brane.

3. Regularized VEV of the field squared

The main problem in (10) is that the expression in the right-hand side diverges and some regularization procedure is required with subsequent renormalization. Here we follow the zeta function regularization technique. The consideration in the regions $y \geq y_0$ (R-region) and $y \leq y_0$ (L-region) will be presented separately.

3.1. R-region

We start with the R-region. From the boundary condition (5) for the mode functions (7) for the coefficient C_2 one gets

$$C_2 = -C_1 \bar{J}_{\nu}^{(1)}(\lambda z_0) / \bar{Y}_{\nu}^{(1)}(\lambda z_0), \quad z_0 = ae^{y_0/a}. \quad (11)$$

Here, for a given function $F(x)$ we defined the notation

$$\bar{F}^{(j)}(x) = A_j F(x) + B_j x F'(x), \quad A_j = 1 + \frac{D}{2} n^{(j)} \frac{\beta^{(j)}}{a}, \quad B_j = n^{(j)} \frac{\beta^{(j)}}{a}. \quad (12)$$

The coefficient C_1 is determined from the normalization condition in a way similar to that given in Bellucci et al. (2015).

As a result, the VEV of the field squared on the right surface of the brane, after integrating over the angular part of $\mathbf{K} = (k_1, \dots, k_{D-2})$, is presented as

$$\begin{aligned} \langle \varphi \varphi^\dagger \rangle_1 &= \frac{2^{4-D} B_1^2 z_0^D a^{1-D}}{\pi^{D/2+1} \Gamma(D/2 - 1) L} \sum_{n=-\infty}^{+\infty} \int_0^\infty dK K^{D-3} \\ &\times \int_0^\infty d\lambda \lambda \frac{[\bar{J}_\nu^{(1)2}(\lambda z_0) + \bar{Y}_\nu^{(1)2}(\lambda z_0)]^{-1}}{\sqrt{\lambda^2 + K^2 + k^2(n)}}. \end{aligned} \quad (13)$$

In this and the following sections we will omit the $y = y_0$ subscript to the VEV. The expression in the right-hand side of (13) is divergent and requires the regularization with the further renormalization.

For the regularization we define the function

$$\begin{aligned} \Phi_1(s) &= \frac{2^{4-D} a^{1-D} z_0^D B_1^2}{\pi^{D/2+1} \Gamma(D/2 - 1) \mu^{s+1} L} \sum_{n=-\infty}^{+\infty} \int_0^\infty \frac{\lambda d\lambda}{\bar{J}_\nu^{(1)2}(\lambda z_0) + \bar{Y}_\nu^{(1)2}(\lambda z_0)} \\ &\times \int_0^\infty \frac{K^{D-3} dK}{[\lambda^2 + K^2 + k^2(n)]^{-s/2}}, \end{aligned} \quad (14)$$

where μ is an arbitrary mass scale introduced to keep the dimensionality of the expression. The computation of the VEV of the field squared requires the analytic continuation of the function $\Phi(s)$ to the value $s = -1$: $\langle \varphi \varphi^\dagger \rangle_1 = \Phi_1(s)|_{s=-1}$. Evaluating the integral over K we obtain

$$\Phi_1(s) = \frac{B_1 a^{1-D} z_0^D}{(4\pi)^{\frac{D-2}{2}} L} \sum_{n=-\infty}^{+\infty} \zeta_{(1)n}(s), \quad (15)$$

where the generalized partial zeta function is defined as

$$\zeta_{(1)n}(s) = \frac{2B_1 \Gamma(-\alpha_s)}{\pi^2 \Gamma(-s/2) \mu^{s+1}} \int_0^\infty \frac{\lambda [\lambda^2 + k^2(n)]^{\alpha_s} d\lambda}{\bar{J}_\nu^{(1)2}(\lambda z_0) + \bar{Y}_\nu^{(1)2}(\lambda z_0)}, \quad (16)$$

where $\alpha_s = (D + s)/2 - 1$. Presenting the integrand in terms of the Hankel functions and rotating the integration contour in the complex plane λ , the following integral representation of the zeta function is obtained

$$\zeta_{(1)n}(s) = -\frac{\mu^{-s-1}}{\Gamma(-s/2) \Gamma(\alpha_s + 1)} \int_{k(n)}^\infty d\lambda \lambda [\lambda^2 - k^2(n)]^{\alpha_s} \frac{K_\nu(\lambda z_0)}{\bar{K}_\nu^{(1)}(\lambda z_0)}, \quad (17)$$

valid in the slice $-D < \text{Res} < 1 - D$ of complex plane s .

3.2. L-region

In the L-region, from the regularity condition on the AdS boundary $z = 0$ one gets $C_2 = 0$ and the coefficient C_1 is determined from the normalization condition. From the boundary condition at $y = y_0$ it follows that the eigenvalues of λ are the roots of the equation $\bar{J}_\nu^{(2)}(\lambda z_0) = 0$. We will denote these roots by $\lambda = \lambda_l$, $l = 1, 2, \dots$. For the corresponding regularized VEV one finds

$$\Phi_2(s) = \frac{B_2 a^{1-D} z_0^D}{(4\pi)^{\frac{D-2}{2}} L} \sum_{n=-\infty}^{+\infty} \zeta_{(2)n}(s), \quad (18)$$

where the generalized partial zeta function is defined as

$$\zeta_{(2)n}(s) = -\frac{\Gamma(-\alpha_s)}{\Gamma(-s/2)\mu^{s+1}} \sum_{l=1}^{\infty} \lambda_l \frac{[\lambda_l^2 + k^2(n)]^{\alpha_s} J_\nu(\lambda_l z_0)}{[\partial_\lambda \bar{J}_\nu^{(2)}(\lambda z_0)]_{\lambda=\lambda_l}}. \quad (19)$$

Taking into account the fact that $x = \lambda_l z_0$ is a simple zero of $\bar{J}_\nu^{(2)}(x)$ and using the residue theorem we get the representation

$$\zeta_{(2)n}(s) = -\frac{\Gamma(-\alpha_s)}{2\pi i \Gamma(-s/2)\mu^{s+1}} \int_C du u [u^2 + k^2(n)]^{\alpha_s} \frac{J_\nu(uz_0)}{\bar{J}_\nu^{(2)}(uz_0)}, \quad (20)$$

where C is a closed counterclockwise contour in the complex plane u , enclosing all the zeros λ_l . Deforming the contour C , the following integral representation

$$\zeta_{(2)n}(s) = \frac{\mu^{-s-1}}{\Gamma(\alpha_s + 1)\Gamma(-s/2)} \int_{k(n)}^{\infty} d\lambda \lambda [\lambda^2 - k^2(n)]^{\alpha_s} \frac{I_\nu(\lambda z_0)}{\bar{I}_\nu^{(2)}(\lambda z_0)}, \quad (21)$$

is obtained in the $-D < \text{Res} < 1 - D$ slice of complex plane s .

We combine the expressions (17) and (21) into a single expression

$$\zeta_{(j)n}(s) = \frac{-n^{(j)} \mu^{-s-1}}{\Gamma(\alpha_s + 1)\Gamma(-s/2)} \int_{k(n)}^{\infty} d\lambda \lambda [\lambda^2 - k^2(n)]^{\alpha_s} \frac{F_\nu(\lambda z_0)}{\bar{F}_\nu^{(j)}(\lambda z_0)}. \quad (22)$$

In this expression $F = K$ when $j = 1$ and $F = I$ when $j = 2$. Thus, for the functions $\Phi(s)$ we have

$$\Phi_j(s) = \frac{B_j a^{1-D} z_0^D}{(4\pi)^{D/2-1} L} \sum_{n=-\infty}^{+\infty} \zeta_{(j)n}(s). \quad (23)$$

This expression is valid in the slice $-D < \text{Res} < 1 - D$ and with the condition that $\bar{F}_\nu^{(j)}(u)$ does not have real zeros. To obtain the value at the physical point $s = -1$, an analytic continuation is needed.

4. Renormalization and the energy density

For non-zero B_j and for large values of u , the ratio in the integrand has the following asymptotic expansion

$$\frac{F_\nu(u)}{\bar{F}_\nu^{(j)}(u)} \sim \frac{1}{B_j} \sum_{l=1}^{\infty} \frac{v_l^{(F,j)}}{u^l}. \quad (24)$$

The coefficients for $I_\nu(u)$ and $K_\nu(u)$ are related as $v_l^{(K,j)} = (-1)^l v_l^{(I,j)}$. The first four coefficients in the series (24) are

$$\begin{aligned} v_1^{(I,j)} &= 1, & v_2^{(I,j)} &= \frac{1}{2} - \frac{A_j}{B_j}, & v_3^{(I,j)} &= \frac{3}{8} - \frac{A_j}{B_j} + \frac{A_j^2}{B_j^2} - \frac{\nu^2}{2}, \\ v_4^{(I,j)} &= \frac{3}{8} + \frac{A_j}{B_j} (\nu^2 - 1) + \frac{3 A_j^2}{2 B_j^2} - \frac{A_j^3}{B_j^3} - \nu^2. \end{aligned} \quad (25)$$

For non-zero Kaluza-Klein modes $k(n)$ we subtract and add to the fraction under integral in Eq. (22) the N leading terms of (24) and integrate the added part explicitly

$$\begin{aligned} \zeta_{(j)n}(s) &= -\frac{n^{(j)} z_0^{-2\alpha_s-2}}{\Gamma(-s/2)\mu^{s+1}} \left\{ \int_{k(n)z_0}^{\infty} du [u^2 - k^2(n)z_0^2]^{\alpha_s} \frac{u G_j(u)}{\Gamma(\alpha_s + 1)} \right. \\ &\quad \left. + \frac{1}{2B_j} \sum_{l=1}^N \frac{v_l^{(F,j)} \Gamma(l/2 - \alpha_s - 1)}{\Gamma(l/2) (k^2(n)z_0)^{l-2\alpha_s-2}} \right\}, \end{aligned} \quad (26)$$

with the notation

$$G_j(u) = \frac{F_\nu(u)}{\bar{F}_\nu^{(j)}(u)} - \frac{1}{B_j} \sum_{l=1}^N \frac{v_l^{(F,j)}}{u^l}. \quad (27)$$

If a zero mode $k(n) = 0$ exists, then we separate it from the sum in Eq. (23) and divide the corresponding integral into parts over the regions $(0, 1)$ and $(1, \infty)$ and apply the same procedure for the integral over the latter interval. As a result the following expression is obtained

$$\begin{aligned} \Phi_j(s) &= -\frac{n^{(j)} a^{1-D} B_j \mu^{-s-1} z_0^{D-2-2\alpha_s}}{(4\pi)^{D/2-1} \Gamma(-s/2) \Gamma(\alpha_s + 1) L} \\ &\quad \times \left[G_j^{(s)} + \sum_{n=-\infty}^{+\infty} \int_{u_n}^{\infty} du u [u^2 - k^2(n)z_0^2]^{\alpha_s} G_j(u) \right. \\ &\quad \left. + \frac{\Gamma(\alpha_s + 1)}{2B_j} \sum_{l=1}^N \frac{v_l^{(F,j)} \Gamma(l/2 - \alpha_s - 1) \zeta_0(l/2 - \alpha_s - 1)}{z_0^{l-2\alpha_s-2} \Gamma(l/2)} \right] \quad (28) \end{aligned}$$

where $u_n = k(n)z_0 + \delta_{0k(n)}$ and the part with

$$G_j^{(s)} = \int_0^1 du u^{2\alpha_s+1} \frac{F_\nu(u)}{\bar{F}_\nu^{(j)}(u)} - \frac{1}{B_j} \sum_{l=1}^N \frac{v_l^{(F,j)}}{2\alpha_s + 2 - l}, \quad (29)$$

comes from the zero mode and should be omitted if the problem at hand does not have a zero mode. The local zeta function $\zeta_0(x)$ in (28) is defined as $\zeta_0(x) = \sum'_{n=-\infty}^{+\infty} 1/k^{2x}(n)$, where the prime on the summation sign means that the zero mode $k(n) = 0$ is excluded from the sum.

The integral under the second sum on the right of (28) is convergent if $N > D + \text{Res} - 1$, and the sum over $k(n)$ is convergent when $N > D + \text{Res}$. Thus, if $N \geq D$ the divergencies in (28) at the point $s = -1$ come from the first term in the square brackets (a simple pole contained in the summand $l = D - 1$) and from the term with the local zeta function. In what follows we will restrict ourselves to discussing the case $\tilde{\alpha} \neq 0$. So for the phase $\tilde{\alpha}$ we assume the range $0 < \tilde{\alpha} < 1$. For the local zeta function one has $\zeta_0(x) = (L/2\pi)^{2x} \sum_{n=-\infty}^{+\infty} (n + \tilde{\alpha})^{-2x}$, and consequently

$$\zeta_0(x) = (L/2\pi)^{2x} [\zeta_H(2x, 1 - \tilde{\alpha}) + \zeta_H(2x, \tilde{\alpha})], \quad (30)$$

where $\zeta_H(x; p)$ is the Hurwitz zeta function. The local zeta function enters into the expression (28) for the VEV in the form

$$P(x, p) = \Gamma(x) [\zeta_H(2x, p) + \zeta_H(2x, 1 - p)], \quad 0 < p < 1. \quad (31)$$

It can be seen that the function $P(x, p)$ has a single simple pole located at $x = 1/2$.

For general N , we have the following expansion around the point $s = -1$:

$$\Phi_j(s) = \frac{n^{(j)}(2a)^{1-D} v_D^{(F,j)}}{\Gamma(D/2)(s+1)} + \langle \varphi \varphi^\dagger \rangle_f + \dots, \quad (32)$$

where the dots stand for the terms vanishing for $s = -1$ and for the finite part one has

$$\begin{aligned} \langle \varphi \varphi^\dagger \rangle_{j,f} = & -\frac{2(4\pi)^{\frac{1-D}{2}} n^{(j)} B_j z_0}{\Gamma\left(\frac{D-1}{2}\right) a^{D-1} L} \sum_{n=-\infty}^{\infty} \int_{k(n)z_0}^{\infty} du u [u^2 - z_0^2 k^2(n)]^{\frac{D-3}{2}} \\ & \times G_j(u) - \frac{n^{(j)} a^{1-D}}{2^D \sqrt{\pi}} \left[\frac{(2\pi)^D}{(L/z_0)^D} \sum_{l=1}^N \frac{v_l^{(F,j)} (L/z_0)^l}{(2\pi)^l \Gamma(l/2)} P\left(\frac{l-D+1}{2}, \tilde{\alpha}\right) \right. \\ & \left. - \frac{\sqrt{\pi} v_D^{(F,j)}}{\Gamma(D/2)} \left(\psi(\tilde{\alpha}) + \psi(1 - \tilde{\alpha}) + 2 \ln\left(\frac{2\pi}{L\mu}\right) \right) \right]. \quad (33) \end{aligned}$$

The prime on the summation sign over l means that the summand corresponding to $l = D$ for which the argument of the Hurwitz zeta functions

becomes 1 is omitted. The structure of the pole term in (33) allows us to absorb them into the corresponding counterterms. For the finite part of the surface energy density one gets

$$\varepsilon_{j,f} = -\frac{n^{(j)}}{a} \left(\xi - \frac{2\xi - 1/2}{n^{(j)}\beta^{(j)}} a \right) \langle \varphi \varphi^\dagger \rangle_{j,f}. \quad (34)$$

To obtain the total energy density on the brane the contributions coming from the two sides of the brane should be summed. One can see, that for odd D and boundary conditions with $n^{(1)}\beta^{(1)} = n^{(2)}\beta^{(2)} = \beta$ the pole parts in the expression of energy density coming from the two sides of the brane cancel each other and finite expression remains

$$\begin{aligned} \varepsilon = & -\frac{1}{a^D} \left(\xi - \frac{2\xi - 1/2}{\beta} a \right) \left\{ \frac{2(4\pi)^{(1-D)/2} z_0 \beta}{\Gamma((D-1)/2) L a} \sum_{n=-\infty}^{\infty} \int_{k(n)z_0}^{\infty} du u \right. \\ & \times [u^2 - z_0^2 k^2(n)]^{\frac{D-3}{2}} \left[\frac{K_\nu(u)}{\bar{K}_\nu^{(1)}(u)} + \frac{I_\nu(u)}{\bar{I}_\nu^{(2)}(u)} - \frac{a}{\beta} \sum_{l=1}^{[N/2]} \frac{2v_{2l}^{(I,2)}}{u^{2l}} \right] \\ & \left. + \frac{2\pi^{D-1/2}}{(L/z_0)^D} \sum_{l=1}^{[N/2]} \frac{v_{2l}^{(I,2)} (L/z_0)^{2l}}{\Gamma(l)(2\pi)^{2l}} P \left(\frac{2l - D + 1}{2}, \tilde{\alpha} \right) \right\}. \quad (35) \end{aligned}$$

Here $[N/2]$ means the integer part of $N/2$. Note that the expression (35) does not depend on the mass scale μ . The energy density (35) is an even periodic function of the magnetic flux Φ enclosed by compact dimension with the period equal to the flux quantum Φ_0 .

The cosmological constant measured in units of the AdS curvature scale a , $a^D \varepsilon$, depends on the ratio β/a , on the parameter $\tilde{\alpha}$, determining the magnetic flux enclosed by the compact dimension and on the ratio L/z_0 . Note that the energy density depends on the length of the compact dimension and on the location of the brane in the form of the combination L/z_0 . The latter property is a consequence of the maximal symmetry of the AdS spacetime.

5. Conclusion

We have investigated the VEV of the surface energy-momentum tensor for a charged scalar field, induced on a brane in background of a locally AdS spacetime with a compact spatial dimension. The brane is parallel to the AdS boundary and the field operator obeys Robin boundary condition on it. In general, the Robin coefficients on the left and right hand sides of the brane are different. The VEV of the surface energy-momentum tensor is expressed in terms of the VEV for the field squared. The latter is divergent and a regularization is required with the further renormalization. Here we have used the generalized zeta function regularization scheme. In this way,

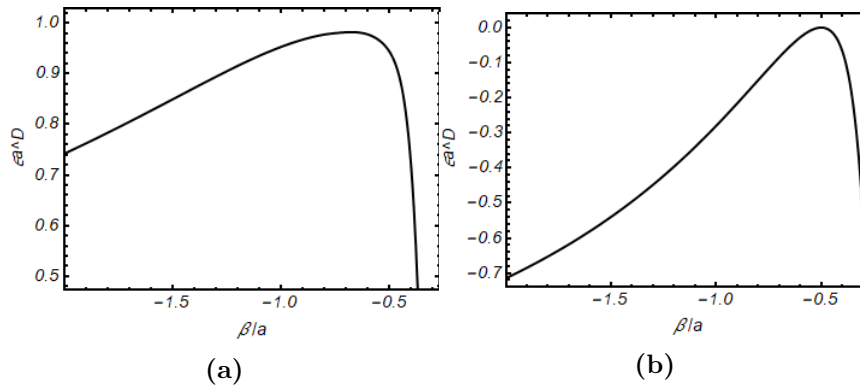


Figure 1: The dependence of $a^D \epsilon$ (determined by the eq. (35)) on the ratio β/a with fixed values of $z_0/L = 1$, $\tilde{\alpha} = 0.45$, for minimally (a) and conformally (b) coupled massless scalar fields ($m = 0$).

for both regions $y \geq y_0$ (R-region) and $y \leq y_0$ (L-region) the VEV of the field squared on the brane is decomposed into the pole and finite parts. The finite parts depend on the normalization mass scale μ . This dependence disappears in the total energy density on the brane for odd values of the spatial dimension if the Robin coefficients for the R- and L-regions are related as $\beta_1 = -\beta_2$. In this special case, the VEV of the surface energy density is given by (4.17) and for the corresponding pressures one has $p = -\epsilon$. This corresponds to a cosmological constant induced on the brane by quantum effects.

References

- Aharony, O.; Gubser, S. S.; Maldacena, J.; Ooguri, H.; Oz, Y. 2000, Phys. Rep., 323, 183
 Bellucci, S.; Saharian, A. A.; Vardanyan, V. 2015, JHEP, 11, 092
 Bellucci, S.; Saharian, A. A.; Vardanyan, V. 2016, Phys. Rev. D, 93, 084011
 Breitenlohner, P.; Freedman, D. Z. 1982, Ann. Phys. (NY) 144, 249
 Bezerra de Mello, E. R.; Saharian, A. A.; Setare, M. R. 2015, Phys. Rev. D, 92, 104005
 Bezerra de Mello, E. R.; Saharian, A. A.; Vardanyan, V. 2015, Phys. Lett. B, 741, 155
 Bordag, M.; Klimchitskaya, G. L.; Mohideen, U.; Mostepanenko, V. M. 2009, Advances in the Casimir Effect (Oxford University Press, Oxford, 2009)
 Brax, P.; Van de Bruck, C. 2003, Classical Quantum Gravity, 20, 201
 Casimir Physics 2001, edited by D. Dalvit, P. Milonni, D. Roberts,

- and F. da Rosa, Lecture Notes in Physics Vol. 834 (Springer-Verlag, Berlin, 2011)
- Elizalde, E.; Odintsov, S. D.; Saharian, A. A. 2013, Phys. Rev. D, 87, 084003
- Knapman, A.; Toms, D. J. 2004, Phys. Rev. D, 69 044023
- Maartens, R., K. Koyama, K. 2010, Living Rev. Relativity, 13, 5
- Martin, J. 2012, C. R. Physique, 13, 566
- Milton, K. A. 2002, The Casimir Effect: Physical Manifestation of Zero-Point Energy (World Scientific, Singapore, 2002)
- Saharian, A. A. 2004, Phys. Rev. D, 70, 064026
- Saharian, A. A. 2005, Nucl. Phys. B, 712, 196
- Saharian, A. A. 2006, Phys. Rev. D 73, 064019
- Saharian, A. A. 2004, Phys. Rev. D, 69, 085005
- Saharian, A. A. 2004, Phys. Rev. D, 70, 064026
- Saharian, A. A. 2006, Phys. Rev. D, 74, 124009
- Saharian, A. A.; Sargsyan, H. G. 2018, Astrophysics, 61, 375
- Shao, S.-H.; Chen, P.; Gu, J.-A. 2010, Phys. Rev. D, 81, 084036

Superdense Stellar Configurations in the Bimetric Scalar-Tensor Theory of Gravity

L. Sh. Grigorian¹, H. F. Khachatryan¹, A. A. Saharian^{1,2*}

¹*Institute of Applied Problems in Physics NAS RA, 25 Nersessian Street, 0014 Yerevan, Armenia*

²*Department of Physics, Yerevan State University, 1 Alex Manoogian Street, 0025 Yerevan, Armenia*

**E-mail: saharian@ysu.am*

Abstract

Models of static spherically-symmetric stellar configurations are discussed within the framework of the Bimetric scalar-tensor theory of gravity. The latter, in addition to the metric tensor and the scalar field, contains a background metric tensor as an absolute variable of the theory. The simplest variant of the theory with a constant coupling parameter and with a zero cosmological function is considered. The analysis includes both the white dwarfs and neutron stars. It is shown that, depending on the value of the theory parameter, the corresponding masses can be notably larger than those in general relativity.

Keywords: *scalar-tensor theories – bimetric theories – superdense stars.*

1. Introduction

The scalar-tensor theories are among the most popular alternatives of general relativity (for reviews see Will (2018), Fujii & Maeda (2009)). The gravitational sector in this theories, in addition to the metric tensor contains a scalar field, usually referred as a gravitational scalar. The recent interest to scalar-tensor theories is related to the fact that a scalar field directly interacting with curvature of the spacetime appear in a number of fundamental theories. The latter include Kaluza-Klein type theories with extra spatial dimensions, supergravity and superstring theories. The scalar fields also play an important role in recent cosmology. In particular, in a large number of inflationary models the accelerated expansion of the Universe at early stages of the evolution is driven by the stress-energy of a scalar field (inflaton). In a class of cosmological models, scalar fields are responsible for accelerated expansion of the Universe at recent epoch. The scalar-tensor theories may

also provide alternative models for dark matter and dark energy. Another class of modified gravity theories, the so-called $f(R)$ -gravities (for recent reviews in various types of modified gravity theories see Will (2018), Clifton et al. (2012), Schmidt-May & von Strauss (2016)), are presented in the form of a scalar-tensor theory with the potential for a scalar field determined by the $f(R)$ function in the gravitational Lagrangian density.

The bimetric (or tensor-tensor) theories present another class of theories alternative to general relativity. In these theories the additional field is a second rank tensor. The latter can be either dynamical or non-dynamical (absolute). Among the first examples for bimetric theories is the Rosen theory. Recent activity in considering theories of gravity with two metric tensors is partially related to non-linear extensions of Fierz-Pauli massive gravity (for a review see Hinterbichler (2012)). In these models the second tensor is required for the construction of non-linear generalizations of the Fierz-Pauli mass term.

In Grigorian & Saharian (1990a, 1990b, 1990c, 1991) we have suggested a variant of scalar-tensor theories involving a second non-dynamical metric tensor: bimetric scalar-tensor theory (BSTT). The BSTT belongs to the class of

metric theories of gravity and consequently obeys the Einstein equivalence principle (for a general review see Will (2018)). Here we consider a static, spherically symmetric configuration of gravitating masses within the framework of BSTT. In a variant of the theory with a constant coupling function and zero cosmological function the corresponding solution outside the matter distribution (external solution) has been found in Grigorian & Saharian (1990b). The results for a numerical integration of the internal equations were presented in Grigorian & Saharian (1990b) and Grigorian et al. (2018) and Avakian et al. (1991) for some special cases of the equation of state for gravitating masses.

2. BSTT action and the field equations

The BSTT belongs to the class of metric theories of gravity with a preferred geometry. In addition to the curved metric tensor g_{ik} it contains a dynamical scalar field $\varphi(x)$ and a nondynamical metric γ_{ik} . The latter is the absolute variable of the theory. We will denote by Γ_{ik}^l and $\hat{\Gamma}_{ik}^l$ the Cristoffel symbols for the metrics g_{ik} and γ_{ik} , respectively. Though these quantities are not tensors, their difference, $\bar{\Gamma}_{ik}^l = \Gamma_{ik}^l - \hat{\Gamma}_{ik}^l$, is a tensor (affine deformation tensor). It can be written as

$$\bar{\Gamma}_{ik}^l = \frac{1}{2}g^{lm} \left(\hat{\nabla}_i g_{mk} + \hat{\nabla}_k g_{mi} - \hat{\nabla}_m g_{ik} \right), \quad (1)$$

where $\hat{\nabla}_i$ stands for the covariant derivative with respect to the metric γ_{ik} . As a consequence of the latter property, in theories with two metrics it is

possible to construct a Lagrangian density for the gravitational field from the metric tensor and its first derivatives. In the bimetric formulation of general relativity, up to a coefficient, the corresponding scalar is given by

$$\Lambda_g = g^{ik} \left(\bar{\Gamma}_{in}^l \bar{\Gamma}_{kl}^n - \bar{\Gamma}_{ik}^l \bar{\Gamma}_{nl}^n \right). \quad (2)$$

This scalar differs from the Ricci scalar R for the metric g_{ik} by a total divergence, $R = \Lambda_g + \nabla_l \bar{w}^l$ with $\bar{w}^l = g^{ik} \bar{\Gamma}_{ik}^l - g^{lk} \bar{\Gamma}_{ik}^l$. As a consequence of the latter property, the field equations obtained from (2) coincide with the Einstein equations for the gravitational field in general relativity. By the standard variational procedure with respect to the background metric γ_{ik} , from (2) we can construct the energy-momentum tensor for the gravitational field (see, for example, Babak & Grishchuk (1999)).

The BSTT is constructed on the base of general relativity in bimetric formulation in a way similar to that the usual scalar-tensor theories are constructed from general relativity with the Lagrangian density proportional to the Ricci scalar. The action of the theory, in its general form, reads (here and below we use the units $c = 1$)

$$S = \int d^4x \sqrt{-g} \left[-\frac{\varphi}{2} \Lambda_g + \frac{\zeta(\varphi)}{2\varphi} g^{ik} \partial_i \varphi \partial_k \varphi - \Lambda(\varphi) + L_m(g_{ik}, q_a, \nabla_l q_a) \right], \quad (3)$$

where $\zeta(\varphi)$ is a dimensionless coupling function, $\Lambda(\varphi)$ is the cosmological function, L_m is the Lagrangian density for nongravitational fields collectively denoted by q_a , ∇_l is the covariant derivative operator with respect to the metric g_{ik} . The simplest variant of the theory corresponds to a constant coupling function $\zeta(\varphi) = \zeta = \text{const}$ and to the zero cosmological function $\Lambda(\varphi) = 0$. In the nongravitational part of the Lagrangian density the gravitational field enters through the metric tensor g_{ik} only and, hence, the theory obeys the Einstein equivalence principle. In usual scalar-tensor theories instead of Λ_g in (3) the scalar curvature R for the metric tensor g_{ik} appears. Though the difference $R - \Lambda_g$ is a total derivative, because of the spacetime dependence of φ , the field equations following from (3) differ from those for scalar-tensor theories.

The field equations for the metric tensor and the scalar field, obtained from (3), have the form

$$\begin{aligned} \varphi R_{ik} + \bar{\Gamma}_{ik}^l \partial_l \varphi - \bar{\Gamma}_{l(k}^l \partial_{i)} \varphi - \zeta(\varphi) \partial_i \varphi \partial_k \varphi / \varphi &= T_{ik} - g_{ik} T / 2 - \Lambda(\varphi) g_{ik}, \\ 2\zeta(\varphi) \nabla_l \nabla^l \varphi + [\zeta'(\varphi) - \zeta(\varphi) / \varphi] \nabla_l \varphi \nabla^l \varphi &= -\varphi [2\Lambda'(\varphi) + \Lambda_g], \end{aligned} \quad (4)$$

where $T_{ik} = (2/\sqrt{-g})\delta(\sqrt{-g}L_m)/\delta g^{ik}$ is the metric energy-momentum tensor for the nongravitational matter, $T = g^{mn}T_{mn}$, the prime means the derivative with respect to the field φ and the brackets in the index expression of the first equation mean the symmetrization with respect to the

indices included. By using the first equation in (4), the equation for the scalar field can also be written in the form

$$\nabla_l \left[2\zeta(\varphi) \nabla^l \varphi - \varphi \bar{w}^l \right] - \zeta'(\varphi) \nabla_l \varphi \nabla^l \varphi = T + 4\Lambda(\varphi) - 2\varphi \Lambda'(\varphi). \quad (5)$$

From the equation for the nongravitational matter, $\delta L_m / \delta q_a = 0$, it follows that $\nabla_k T_i^k = 0$. Note that, unlike to the usual scalar-tensor theories, in BSTT the latter equation does not follow from the field equations. This is a consequence of the presence of nondynamical metric γ_{ik} . Another consequence is that in BSTT the gravitational field is characterized by the energy-momentum tensor (Grigorian & Sahakian 1990d, 1994).

The first step to check the validity of the gravitational theory is to consider the Newtonian and post-Newtonian approximations and to compare the predictions of the theory with the observational data, in particular, for the gravitational effects in the solar system and in double pulsar systems. The gravitational effects are expressed in terms of the PPN (parametrized post-Newtonian) parameters of the theory. Under the condition $|\zeta(\varphi_0)| \gg v^2$ the PPN parameters of BSTT coincide with those for general relativity. Here $\varphi = \varphi_0 = (8\pi G)^{-1}$ is the value for the gravitational scalar at the recent stage of the Universe expansion, G is the Newtonian gravitational constant, $v^2 \sim P/\rho$ ($P/\rho \sim 10^{-5}$ in the solar system) is the velocity in a post-Newtonian system with the pressure P and the energy density ρ . In particular, in contrast to most other bimetric theories, the PPN parameters of BSTT do not depend on the cosmological connection coefficients. This is related to the fact that the background metric γ_{ik} enters in the action of the theory through its Cristoffel symbols only. Note that in the Brans-Dicke theory (the simplest variant of scalar-tensor theories with $\zeta(\varphi) = \zeta = \text{const}$ and $\Lambda(\varphi) = 0$) for the post-newtonian parameter γ one has $\gamma = (1 + \zeta)/(2 + \zeta)$ and the observational data within the framework of the solar system strongly constrain (mainly from Cassini measurements of the Shapiro time delay) the theory parameter: $\zeta > 4 \cdot 10^4$. This difference between the two scalar-tensor theories is related to that in the Brans-Dicke theory the scalar field is sourced by the scalar curvature R (in the equation for the scalar field, that is the analog of the second equation in (4), R stands instead of Λ_g) which is of the order v^2 and, hence, the same for the variations of scalar field. In BSTT, the scalar field is sourced by Λ_g which has the order v^4 and related to that the variations of scalar field in post-Newtonian systems are of the order v^4 if the theory parameter is not too small (in the variations the parameter ζ enters in the form $1/\zeta$ (see, for example, (19) below)).

The gravitational waves in BSTT have been analyzed in Saharian (1993a, 1993b). In this theory, the velocity of weak perturbations of the curved metric coincides with the speed of light in the vacuum. In a variant of the theory with zero cosmological function, the same is the case for the scalar field. Similar to general relativity, the BSTT is of class N_2 in $E(2)$ classification of

the gravitational waves polarization of metric theories of gravity. In particular, this means that in BSTT the weak perturbations for metric and scalar field propagate independently. In usual scalar-tensor theories (for example, in Brans-Dicke theory) the equation for weak perturbations of the metric tensor contain a contribution from the scalar field as well (see, for example, Will (2018)). As a consequence of that the scalar and metric perturbations are mixed and the theory belongs to the class N_3 . Related to the presence of a scalar degree of freedom, in addition to the standard quadrupole gravitational radiation, in BSTT there is also dipole gravitational radiation. The corresponding Peters-Mathews parameters for the radiation from a gravitating system with small velocities and nonrelativistic internal structure have been determined in Saharian (1993a). The corresponding formalism for a system of gravitating bodies with small velocities but with relativistic internal structure (modified Einstein-Infeld-Hoffmann formalism) has been considered in Saharian (1993b).

3. Spherically symmetric static configurations

Consider a static spherically symmetric stellar configuration described by the energy-momentum tensor

$$T_{ik} = (\rho + P) u_i u_k - P g_{ik}. \quad (6)$$

Here ρ and P are the energy density and the pressure of the matter and u_i is the corresponding four-velocity. In the coordinate system (t, r, θ, ϕ) with the background metric

$$\gamma_{ik} = \text{diag}(1, -1, -r^2, -r^2 \sin^2 \theta), \quad (7)$$

the curved metric tensor is presented as

$$g_{ik} = \text{diag}(e^\nu, -e^\lambda, -r^2 e^\mu, -r^2 e^\mu \sin^2 \theta), \quad (8)$$

where $\nu(r)$, $\lambda(r)$, $\mu(r)$ are functions of the radial coordinate tending to zero at large distances from the configuration. The scalar field depends on the radial coordinate alone: $\varphi = \varphi(r)$. We will consider the variant of the theory with $\zeta(\varphi) = \zeta = \text{const}$ and $\Lambda(\varphi) = 0$.

From the equation (4), for $0 \leq r < \infty$ we get

$$\left(1 - e^{\lambda-\mu}\right) \left[\varphi'' + \varphi' \left(\frac{2}{r} + \frac{\nu' + \lambda'}{2}\right)\right] = \varphi' (\lambda' - \mu'), \quad (9)$$

where the prime stands for the derivative with respect to r . The integration of this equation leads to the result

$$\left(e^{\mu-\lambda} - 1\right) r^2 \varphi' e^{(\nu+\lambda)/2} = \text{const}. \quad (10)$$

Assuming that $\varphi'(0)$ is finite from here we find $\mu(r) = \lambda(r)$. With this relation, the spatial part of the metric tensor (8) is conformally flat (this corresponds to isotropic coordinates in general relativity). Introducing the notation $z = (\nu + \lambda)/2$ and the functions

$$M(r) = 4\pi \int_0^r dr r^2 (\rho + 3P) e^{3z-\nu}, \quad \beta(r) = 4\pi \int_0^r dr r^2 P e^{3z-\nu}, \quad (11)$$

the remaining equations are presented in the form

$$\begin{aligned} \nu' &= \frac{M(r)e^{-z}}{4\pi r^2 \varphi}, \quad \zeta \frac{\varphi'}{\varphi} + 2z' = \frac{3\beta(r)e^{-z}}{4\pi r^2 \varphi}, \\ P' &= -\frac{\nu'}{2} (\rho + P), \quad z'^2 + \frac{2}{r} z' - \frac{\nu'^2}{4} - \frac{\zeta}{2} \left(\frac{\varphi'}{\varphi} \right)^2 = \frac{P}{\varphi} e^{2z-\nu}, \end{aligned} \quad (12)$$

In addition, the equation of state $\rho = \rho(P)$ should be given. For nongravitational sources obeying the strong energy condition one has $\rho + 3P \geq 0$ and the function $\nu(r)$ is monotonically increasing.

Let us denote by r_1 the radius of the configuration. Then, in the region $r > r_1$ one has $\rho = 0 = P$. In this region $M(r) = M(r_1) \equiv M$, $\beta(r) = \beta(r_1) \equiv \beta$ and $\varphi(r) \rightarrow \varphi_0 = 1/(8\pi G)$ for $r \rightarrow \infty$. The latter condition is required to ensure the limiting transition to the Newtonian gravity for weak fields. Note that the Tolmen formula for the mass $M = M(r_1)$ of the configuration, obtained in general relativity, is valid in BSTT as well (see Avakian et al. (1991)). In the case $\zeta \neq 2$ the corresponding solution for the function $\nu = \nu(r)$ is given by

$$e^\nu = \exp \left[\frac{1}{\sqrt{a}} \left(2 \arctan \frac{2l - \alpha/\zeta}{\sqrt{a}} - \pi \right) \right], \quad (13)$$

for $a \geq 0$ and by

$$e^\nu = \left| \frac{2l - \alpha/\zeta - \sqrt{-a}}{2l - \alpha/\zeta + \sqrt{-a}} \right|^{\frac{1}{\sqrt{-a}}}, \quad (14)$$

for $a \leq 0$. Here $l = r/r_g$, $r_g = 2GM$, and

$$\alpha = \frac{12\pi}{M} \int_0^{r_1} dr r^2 P e^{3z-\nu}, \quad a = \frac{1 - \alpha^2}{2\zeta} - \frac{1}{4}. \quad (15)$$

For the remaining metric component and the scalar field we get the expressions

$$\begin{aligned} e^\lambda &= \left| \frac{4l^2}{(2l - \alpha/\zeta)^2 + a} \right|^{\frac{2\zeta}{2-\zeta}} \exp \left[\frac{\zeta + 2(\alpha - 1)}{2 - \zeta} \nu \right], \\ \frac{\varphi}{\varphi_0} &= \left| \frac{4l^2}{(2l - \alpha/\zeta)^2 + a} \right|^{\frac{2}{\zeta-2}} \exp \left(\frac{\alpha\nu}{\zeta - 2} \right). \end{aligned} \quad (16)$$

As seen, the external solution, in addition to the mass M , is determined by the parameter α . In the special case $\zeta = 2$ the solution is specified to

$$\begin{aligned} e^\nu &= |1 - \alpha/2l|^{2/\alpha}, \quad e^\lambda = |1 - \alpha/2l|^{(1-1/\alpha)^2} \exp\left(\frac{1+1/\alpha}{2l}\right), \\ \frac{\varphi}{\varphi_0} &= |1 - \alpha/2l|^{\frac{1}{2}(1-1/\alpha)^2} \exp\left(-\frac{1+1/\alpha}{4l}\right). \end{aligned} \quad (17)$$

Under the condition $-\zeta/2 \leq \alpha^2 < 1 - \zeta/2$ the external solution is regular for all r_1 . For the values of the parameter α outside this region the external solution is singular at

$$l = l_c = \frac{1}{2} \left(\frac{\alpha}{\zeta} + \sqrt{\frac{1}{4} - \frac{1 - \alpha^2}{2\zeta}} \right),$$

if $r_1 < l_c r_g$. In the limit $\zeta \rightarrow \infty$ one has $a = -1/4$ and the solutions (14), (16) reduce to the Schwarzschild solution in general relativity in isotropic coordinates:

$$e^\nu \rightarrow \left(\frac{l - 1/4}{l + 1/4} \right)^2, \quad e^\lambda \rightarrow \left(1 + \frac{1}{4l} \right)^4, \quad \varphi \rightarrow \varphi_0. \quad (18)$$

In these coordinates the horizon corresponds to the spherical surface $r = r_g/4$.

At large distances from the spherically symmetric configuration one has

$$e^\nu \approx 1 - \frac{r_g}{r} + \frac{1 - \alpha/\zeta}{2} \left(\frac{r_g}{r} \right)^2, \quad e^\lambda \approx 1 + \frac{r_g}{r}, \quad \frac{\varphi}{\varphi_0} \approx 1 - \frac{\alpha r_g}{\zeta r}. \quad (19)$$

Similar to the post-Newtonian considerations, in the expansion for the g_{00} component of the metric tensor we have also kept the next-to-leading correction. As seen, the theory parameter enters into the corrections in the form of the ratio α/ζ . For $\alpha \ll \zeta$ (this is the case for nonrelativistic sources and for $\zeta \gtrsim 1$) the variation in the scalar field is much smaller than that for the metric tensor components. Note that in the solar system $\alpha \lesssim 5 \cdot 10^{-6}$. For this type of matter sources one has $l_c \approx (1/4) \sqrt{1 - 2/\zeta}$ and the spherical surface $l = l_c$ is inside the Schwarzschild horizon in general relativity.

4. Superdense stellar configurations

In this section we consider models of superdense configurations based on the numerical integration of the equations (12). It is convenient to use the pressure as an independent variable and to consider the equation of state of the form $\rho = \rho(P)$. For a given value of the central pressure $P(0)$, the quantities $\nu(0)$, $\lambda(0)$, $\varphi(0)$ and the mass M are determined by the matching

conditions for the external and internal solutions on the surface of the gravitating body $r = r_1$, where $P(r_1) = 0$. Figure 1 presents the dependence of the mass (in units of the solar mass M_\odot) of a superdense configuration as a function of $P(0)$ for different values of the theory parameter ζ (numbers near the curves). In the numerical integration we have used the equation of state from Sahakian (1974), Grigorian (1983), and Sahakian (1995). The curves with $\zeta = \infty$ correspond to configurations in general relativity.

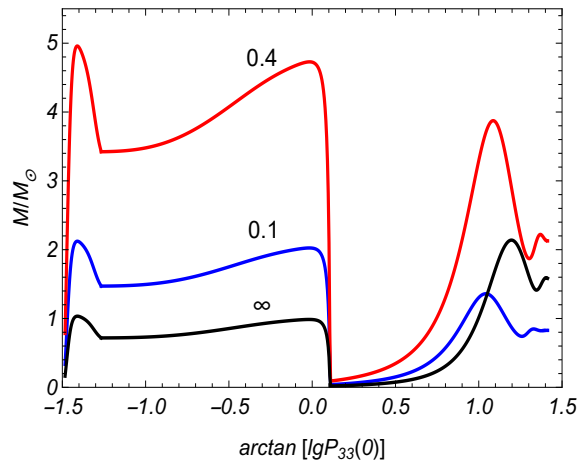


Figure 1: The mass of a superdense star as a function of the central pressure $P(0)$. The numbers near the curves correspond to the values of the BSTT parameter ζ and $P_{33} = P/10^{33} \text{erg} \cdot \text{cm}^{-3}$. The curve $\zeta = \infty$ corresponds to configurations in general relativity.

In general relativity, the configurations corresponding to the monotonically increasing segment on the left of the first local maximum correspond to white dwarfs. The monotonically increasing segment between the first and second local maxima corresponds to configurations which are unstable against radial perturbations. The monotonically increasing segment between the second and third local maxima corresponds to neutron stars. Note that in BSTT the issue of stability of the static configurations requires an additional investigation. As seen from the graphs, depending on the value of the theory parameter ζ , in BSTT the masses of the corresponding configurations for a fixed value of the pressure at the center can be essentially larger compared with the corresponding values in general relativity. For large values of the parameter, $\zeta \gg 1$, the curves in BSTT and in general relativity are practically indistinguishable. Note that the study of neutron star masses, presently has attracted a considerable interest both in the fields of theory and observations (see, for instance, Ozel & Freire (2016), Horvath et al. (2017)). This, in particular, was motivated by the observation of neutron stars with masses near $2M_\odot$.

In addition to the mass of the configuration, the external geometry is determined by $\beta \equiv \beta(r_1)$. In terms of this parameter one has $\alpha = 3\beta/M$. In figure 2 we have plotted the ratio β/M_\odot as a function of $P(0)$ for $\zeta = 0.1, 0.4, \infty$. For configurations corresponding to white dwarfs one has $\beta/M_\odot \ll 1$. The numerical analysis shows that the difference of the external solution from that in general relativity with the same value of the mass is rather small. The numerical integration shows that for $\zeta > 2$ the parameters of the configurations in BSTT are very close to those for general relativity.

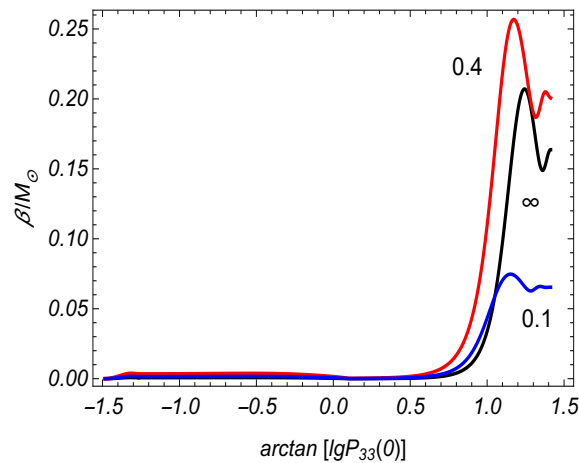


Figure 2: The dependence of the ratio β/M_\odot on the central pressure. The numbers near the curves correspond to the values of the BSTT parameter ζ .

Figure 3 presents the radius of the configuration versus the central pressure for different values of the parameter ζ (numbers near the curves). The graphs show that, depending on the value of ζ , the radii of the configurations may notably exceed the corresponding values in general relativity.

5. Conclusion

We have investigated static spherically symmetric configurations of gravitating masses in the simplest version of BSTT with a constant coupling function and with the zero cosmological function. The constraints on the coupling constant, obtained from the observations within the framework of the post-Newtonian approximation, are essentially weaker than those in usual scalar-tensor theories (Brans-Dicke theory). The corresponding external solution is given by (13), (14) and (16). In addition to the mass, the solution depends on the parameter α that is determined in terms of the integral involving the pressure of the gravitating matter. For the integration

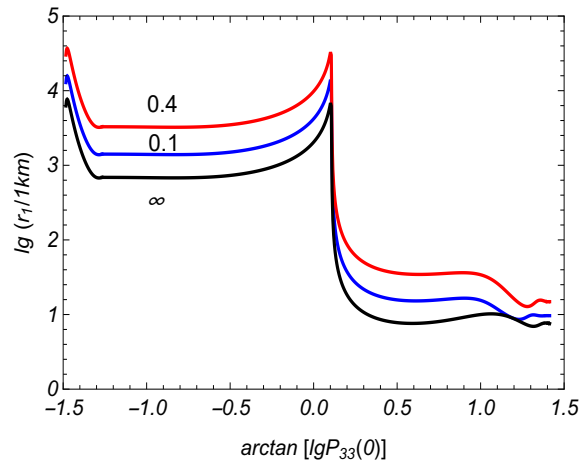


Figure 3: The radius of a superdense star versus the central pressure. The numbers near the curves correspond to the values of the parameter ζ . The curve $\zeta = \infty$ corresponds to the results in general relativity.

of the field equations inside the configuration we have used the equation of state from Sahakian (1974, 1995) and Grigorian & Sahakian (1983). The corresponding numerical data are presented in figures 1-3. These results show that, for strong gravitational fields, depending on the value of the BSTT parameter ζ the characteristics of the superdense configurations may essentially differ from those in general relativity. Note that we have considered spherically symmetric solutions with variable gravitational scalar.

References

- Avakian, M.R.; Grigorian, L.Sh.; Saharian, A.A. 1990, *Astrophysics*, 35, 121
- Avakian, M.R.; Grigorian, L.Sh.; Saharian, A.A. 1991, *Astrophysics*, 34, 265
- Babak, S.V.; Grishchuk, L.P. 1999, *Phys. Rev. D*, 61, 024038
- Clifton, T.; Ferreira, P.G.; Padilla, A.; Skordis, C. 2012, *Modified gravity and cosmology. Phys. Rep.*, 513, 1-189
- Fujii, Y.; Maeda, K. 2009 *The Scalar-Tensor Theory of Gravitation*, Cambridge University Press, England
- Grigorian, L.Sh.; Khachatryan, H.F.; Saharian, A.A. 2018, *Models of compact stars in the Bimetric scalar-tensor theory of gravitation. Particles*, 1, 203
- Grigorian, L.Sh.; Sahakian, G.S. 1983, *Astrophys. Space Sci.*, 95, 305
- Grigorian, L.Sh.; Saharian, A.A. 1990a, *Astrophysics*, 31, 359

- Grigorian, L.Sh.; Saharian, A.A. 1990b, *Astrophys. Space Sci.*, 167, 271
- Grigorian, L.Sh.; Saharian, A.A. 1990c, *Astrophysics*, 32, 491
- Grigorian, L.Sh.; Saharian, A.A. 1991, *Astrophys. Space Sci.*, 180, 39
- Grigorian, L.Sh.; Saharian, A.A. 1990d, *Astrophysics*, 33, 107
- Grigorian, L.Sh.; Saharian, A.A. 1994, *Astrophysics*, 37, 167
- Hinterbichler, K. 2012, *Theoretical aspects of massive gravity*, *Rev. Mod. Phys.*, 84, 671
- Horvath, J.E.; Valentim, R. The Masses of Neutron Stars. In: Alsabti A.; Murdin P. (eds) *Handbook of Supernovae*; Springer: Cham, 2017.
- Özel, F.; Freire, P. 2016, *Annu. Rev. Astron. Astrophys.*, 54, 401
- Sahakian, G.S. 1974, *Equilibrium Configurations of Degenerate Gaseous Masses*; Halsted (Wiley): New York, Israel Program for Scientific Translations, Jerusalem, 1974.
- Sahakian, G.S. *Physics of Neutron Stars*; JINR Publishing Department: Dubna, Russia, 1995.
- Saharian, A.A. 1993a, *Astrophysics*, 36, 423
- Saharian, A.A. 1993b, *Astrophysics*, 36, 603
- Schmidt-May, A.; von Strauss, M. 2016, *Recent developments in bimetric theory*. *J. Phys. A: Math. Theor.*, 49, 183001
- Will, C.M. 2018 *Theory and Experiment in Gravitational Physics*, Cambridge University Press, England

On the importance of resistivity and Hall effect in MHD simulations of binary neutron star mergers

A. S. Harutyunyan

*NAS RA V. Ambartsumian Byurakan Astrophysical Observatory (BAO), Armenia
Yerevan State University (YSU), Armenia
E-mail: arus@bao.sci.am*

Abstract

We examine the range of rest-mass densities, temperatures and magnetic fields involved in simulations of binary neutron star mergers (BNSM) and identify the conditions under which the ideal magneto-hydrodynamics (MHD) breaks down using recently computed conductivities of warm, magnetized plasma created in such systems. While previous dissipative MHD studies of BNSMs assumed that dissipation sets in due to low conduction at low rest-mass densities, we show that this paradigm must be shifted: the ideal MHD is applicable up to the regime where the hydrodynamic description of matter breaks down. We also find that the Hall effect can be important at low densities and low temperatures, where it can induce a non-dissipative rearrangement of the magnetic field. Finally, we mark the region in temperature-density plane where the hydrodynamic description breaks down.

Keywords: *binary neutron star mergers - magnetohydrodynamic simulations - magnetic-field decay - electrical conductivity - Hall effect*

1. Introduction

The recent detections of gravitational waves by the LIGO and Virgo detectors have opened a new chapter in multimessenger astronomy. The observations of GW170817 and GRB170817A provided the first direct evidence that a class of short gamma-ray bursts (GRB) can be associated with the inspiral and merger of binary compact stars. As the magnetic field plays a central role in the generation of the GRBs, the physics of inspiral and merger of magnetized neutron stars can now be constrained directly by observations. The general-relativistic MHD simulations of these processes have advanced steadily over the recent years (Faber 2012, Paschalidis 2016, Baiotti 2016) and can be carried out either in the case of ideal (Rezzolla

2011, Kiuchi 2014, Palenzuela 2015, Kawamura 2016, Ruiz 2016, Kiuchi 2017, Ruiz 2018) or resistive MHD (Dionysopoulou 2012, Palenzuela 2013b, Palenzuela 2013a, Dionysopoulou 2015).

The aim of this work is to investigate the conditions under which the non-ideal MHD effects can be important in the contexts of BNSMs and the evolution of the post-merger object. For doing so, we first discuss briefly the relevant time- and lengthscales over which the physical parameters evolve in the simulations of magnetized BNSMs. Characteristic timescales of simulations set the upper bound τ_0 over which the relevant quantities need to change to be relevant dynamically. The current highest resolution simulations of the merger process (Siegel 2013, Kiuchi 2015, Kiuchi 2017) are limited in time after merger due to numerical costs. Lower-resolution simulations can be carried out up to the point of the collapse to a black hole or the formation of a differentially rotating and unstable neutron star, and last typically tens of milliseconds (Dionysopoulou 2012, Dionysopoulou 2015).

To extract the relevant lengthscales we use an ideal MHD simulation of the merger of an equal-mass magnetized binary system with a total ADM mass of $M_{\text{ADM}} = 3.25M_{\odot}$ and initial orbital separation of 45 km. The finest resolution of the simulation is $l_0 \approx 227$ m, and the merger takes place at $t_{\text{mg}} \simeq 3.5$ ms after the start of the simulation (see ref. Harutyunyan 2018 for details).

The main features of the ideal-MHD simulations which are important for our estimates are: (a) the characteristic lengthscales over which the magnetic-field variations can be significant are $\lambda_B \simeq 1$ km or less, with the lower limit obviously given by the resolution of the simulation; (b) the characteristic lengthscales over which the rest-mass density variations can be significant are $\lambda_{\rho} \simeq 10$ km, *i.e.*, the density of matter is approximately constant over the lengthscales of variation of magnetic field; (c) the characteristic timescales relevant for the simulations are of the order of $\tau_0 \simeq 10$ ms.

We start this review by collecting the relevant formulae for the characteristic timescales which describe the evolution of the magnetic field in Sec. 2. In Sec. 3 we present our numerical results and identify the density-temperature regimes where the ideal MHD approximation as well as MHD description of plasma are justified. Our results are summarized in Sec. 4.

2. Ohmic diffusion and Hall timescales

As is well-known, the MHD description of low-frequency phenomena in neutron stars is based on the following Maxwell equations

$$\nabla \times \mathbf{E} = -\frac{1}{c} \frac{\partial \mathbf{B}}{\partial t}, \quad \nabla \times \mathbf{B} = \frac{4\pi}{c} \hat{\sigma} \mathbf{E}, \quad (1)$$

where $\hat{\sigma}$ is the electrical conductivity tensor. Eliminating the electric field \mathbf{E} , we obtain an evolution equation for the magnetic-field

$$\frac{\partial \mathbf{B}}{\partial t} = -\nabla \times (\hat{\varrho} \nabla \times \mathbf{B}), \quad (2)$$

where $\hat{\varrho}$ is the electrical resistivity tensor defined as $\hat{\varrho} = (c^2/4\pi)\hat{\sigma}^{-1}$.

In the case of isotropic conduction $\hat{\sigma}_{ij} = \delta_{ij}\sigma$, and Eq. (2) reduces to

$$\frac{4\pi\sigma}{c^2} \frac{\partial \mathbf{B}}{\partial t} = \Delta \mathbf{B}. \quad (3)$$

For qualitative estimates we approximate $|\Delta \mathbf{B}| \simeq B/\lambda_B^2$ and $|\partial \mathbf{B}/\partial t| \simeq B/\tau_d$, from where we find an estimate for the magnetic field decay (Ohmic diffusion) timescale τ_d

$$\tau_d = \frac{4\pi\sigma\lambda_B^2}{c^2}. \quad (4)$$

In the presence of strong magnetic fields the electrical conductivity and resistivity tensors can be decomposed as ($b_k = B_k/B$)

$$\sigma_{kj} = \delta_{kj}\sigma_0 - \epsilon_{kjm}b_m\sigma_1 + b_kb_j\sigma_2, \quad (5)$$

$$\varrho_{ik} = \delta_{ik}\varrho_0 + \epsilon_{ikm}b_m\varrho_1 + b_ib_k\varrho_2. \quad (6)$$

The components of the resistivity tensor $\hat{\varrho}$ are related to those of $\hat{\sigma}$ by

$$\varrho_0 = \frac{c^2}{4\pi} \frac{\sigma_0}{\sigma_0^2 + \sigma_1^2}, \quad \varrho_1 = \frac{c^2}{4\pi} \frac{\sigma_1}{\sigma_0^2 + \sigma_1^2}, \quad \varrho_2 = \frac{c^2}{4\pi\sigma} \frac{\sigma_1^2 - \sigma_0\sigma_2}{\sigma_0^2 + \sigma_1^2}, \quad (7)$$

where $\sigma = \sigma_0 + \sigma_2$ is the longitudinal conductivity, *i.e.*, the electrical conductivity in the absence of magnetic field. The three components of the conductivity tensor are given by the following Drude-type formulas (Harutyunyan 2016)

$$\sigma = \frac{n_e e^2 c^2 \tau}{\varepsilon}, \quad \sigma_0 = \frac{\sigma}{1 + (\omega_c \tau)^2}, \quad \sigma_1 = \frac{(\omega_c \tau) \sigma}{1 + (\omega_c \tau)^2} = (\omega_c \tau) \sigma_0. \quad (8)$$

Here n_e is the electron number density, e is the elementary charge, c is the speed of light, τ is the electron mean collision time, $\omega_c := ecB\varepsilon^{-1}$ is the cyclotron frequency, and ε is the characteristic energy-scale of electrons.

From Eqs. (7) and (8) we obtain the following estimates for the components of the resistivity tensor

$$\varrho_0 \simeq \frac{c^2}{4\pi\sigma}, \quad \varrho_1 \simeq (\omega_c \tau) \varrho_0, \quad \varrho_2 \simeq 0. \quad (9)$$

Now, upon using Eqs. (6) and (9) and approximating again $\partial_i B \simeq B/\lambda_B$, we estimate the right-hand side of Eq. (2)

$$|\hat{\varrho} \nabla \times \mathbf{B}| \simeq \max(1, \omega_c \tau) \varrho_0 \frac{B}{\lambda_B}. \quad (10)$$

In the case of small magnetic fields $\omega_c\tau \ll 1$ we recover the isotropic case from Eqs. (2) and (10). The evolution of magnetic field is then determined by the Ohmic diffusion timescale τ_d given by Eq. (4). Conversely, in the strongly anisotropic regime, where $\omega_c\tau \gg 1$, the magnetic field evolution is determined by the characteristic timescale τ_B given by

$$\tau_B = \frac{\tau_d}{\omega_c\tau} = \frac{4\pi n_e e \lambda_B^2}{cB} = \frac{4\pi e \rho \lambda_B^2}{cB} \frac{Z}{Am_n}. \quad (11)$$

In the last step we used the condition of the charge neutrality, which implies $n_e = Z\rho/(Am_n)$, where Z and A are the charge and the mass number of nuclei, respectively, and m_n is the atomic mass unit.

Thus, in the strongly anisotropic regime which is realized for sufficiently high magnetic fields and low rest-mass densities the characteristic timescale over which the magnetic field evolves is reduced by a factor of $\omega_c\tau$ due to the Hall effect. We see from Eq. (11) that the timescale τ_B decreases with an increase of the magnetic field and, in contrast to the Ohmic diffusion timescale τ_d , is independent of the electrical conductivity σ . The physical reason for this difference lies in the fact that the Hall effect *per-se* is not dissipative. Note however that it can act to facilitate Ohmic dissipation. For instance, the Hall effect may cause the fragmentation of magnetic field into smaller structures through the Hall instability, which can then accelerate the decay of the field via standard Ohmic dissipation (Gourgouliatos 2016, Kitchatinov 2017).

3. Results

In order to estimate the Ohmic diffusion timescale given by Eq. (4) we use the following fit formula for the electrical conductivity σ (Harutyunyan 2016, Harutyunyan 2017)

$$\sigma = \frac{1.5 \times 10^{22}}{Z} \left(\frac{T_F}{1 \text{ MeV}} \right)^a \left(\frac{T}{T_F} \right)^{-b} \left(\frac{T}{T_F} + d \right)^c \text{ s}^{-1}, \quad (12)$$

where T and $T_F = 0.511[\sqrt{1 + (Z\rho_6/A)^{2/3}} - 1]$ MeV are the temperature of stellar matter and the Fermi temperature of electrons, respectively, $\rho_6 := \rho/(10^6 \text{ g cm}^{-3})$, and the fitting parameters a, b, c, d are functions of Z .

At low-density ($\rho_6 \lesssim 1$) and high-temperature ($T \gtrsim 1 \text{ MeV}$) regime of stellar matter where we are mainly interested, the matter consists mainly of hydrogen nuclei. In this case $a = 0.924$, $b = 0.507$, $c = 1.295$, $d = 0.279$ (Harutyunyan 2017), and, approximating also $T_F \simeq 0.25 \rho_6^{2/3} \text{ MeV} \ll T$ in Eq. (12), we find the following estimate for Eq. (4)

$$\tau_d \simeq 5 \times 10^{11} \left(\frac{\rho}{1 \text{ g cm}^{-3}} \right)^{0.1} \left(\frac{T}{1 \text{ MeV}} \right)^{0.8} \left(\frac{\lambda_B}{1 \text{ km}} \right)^2 \text{ s}. \quad (13)$$

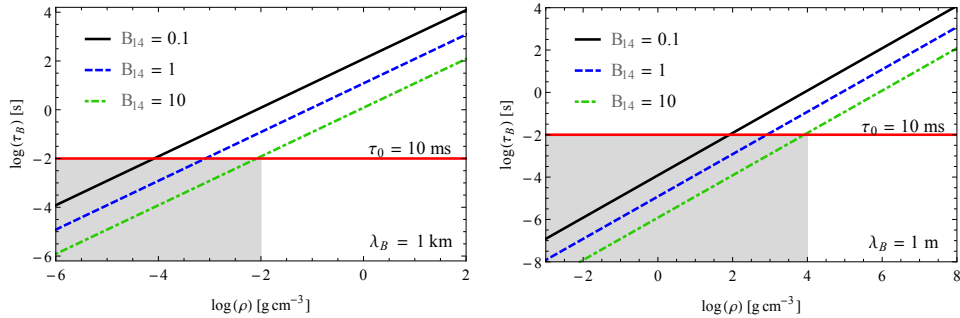


Figure 1: Dependence of the Hall timescale τ_B on the rest-mass density for two values of the magnetic-field scale-height $\lambda_B = 1$ km (*left panel*), and $\lambda_B = 1$ m (*right panel*). The solid horizontal lines correspond to the typical timescale of $\tau_0 = 10$ ms. The shaded areas where $\tau_B \leq \tau_0$ are the regions where the Hall effect becomes important.

This timescale is clearly much larger than the typical timescales $\tau_0 \simeq 10$ ms involved in a merger. Given the current limitations on the resolution to the order of a meter and choosing the most favorable temperature and density values we can obtain an effective lower limit on τ_d by substituting in Eq. (13) $\lambda_B = 1$ m, $\rho \simeq 10^{-3}$ g cm $^{-3}$, and $T = 0.1$ MeV, in which case $\tau_d \sim 10^4$ s, which is still much larger than τ_0 (although smaller rest-mass densities can be reached in BNSMs, for $\lambda_B = 1$ m and $T = 0.1$ MeV the MHD approach breaks down already at $\rho \lesssim 10^{-3}$ g cm $^{-3}$; see the discussion in Sec. 3.1). Thus, our analysis suggests that resistive effects do not play an important role in the MHD phenomenology of BNSMs and the ideal-MHD approximation in BNSM simulations is always justified as long as the MHD description itself is valid. Our conclusion is in contrast with the previous paradigm of onset of dissipative MHD in low-density regime (Dionysopoulou 2012, Dionysopoulou 2015) where the nearly zero-conductivity of matter would have implied $\tau_d \rightarrow 0$.

In a similar way we express the Hall timescale τ_B given by Eq. (11) as

$$\tau_B \simeq 12 \times B_{14}^{-1} \left(\frac{\rho}{1 \text{ g cm}^{-3}} \right) \left(\frac{\lambda_B}{1 \text{ km}} \right)^2 \text{ s}, \quad (14)$$

where $B_{14} := B/(10^{14} \text{ G})$. Clearly, the timescale τ_B is much shorter than the diffusion timescale and it can be in the relevant range of milliseconds for sufficiently low densities and large magnetic fields.

The dependence of τ_B on the rest-mass density is shown in Fig. 1 for $\lambda_B = 1$ km and $\lambda_B = 1$ m for several values of the magnetic field. At low densities (the shaded areas in the figure) we have $\tau_B < \tau_0$, therefore in these regions the magnetic field can be subject to the Hall effect, which will change its distribution on a timescale τ_B . It is seen from Fig. 1 that, *e.g.*, for

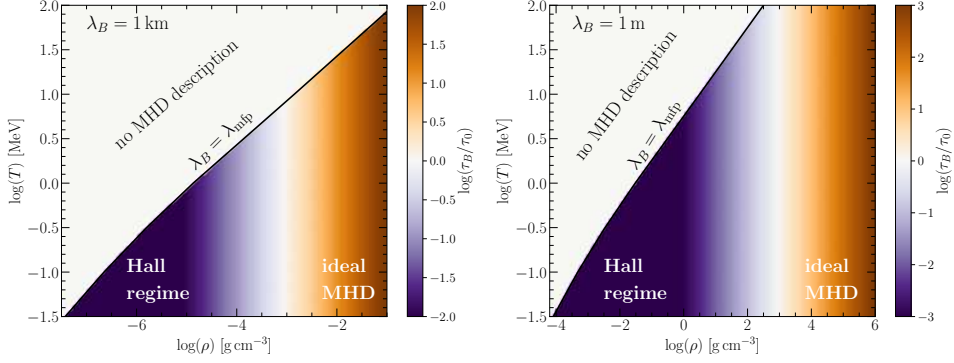


Figure 2: Regions of the validity of MHD and ideal MHD on the temperature-density plane for $\lambda_B = 1$ km (*left panel*), and $\lambda_B = 1$ m (*right panel*). The value of the magnetic field is fixed at $B_{14} = 1$, and the typical timescale is taken $\tau_0 = 10$ ms. Areas shaded in dark-orange are the regions where the ideal-MHD approximation holds; areas shaded in dark-violet are the regions where the Hall effect becomes important. Above the solid black line $\lambda_B = \lambda_{\text{mfp}}$ the MHD description of matter breaks down.

$B_{14} = 1$, τ_B reaches the value $\tau_0 = 10$ ms for $\lambda_B = 1$ km at very low densities $\rho \leq 10^{-3} \text{ g cm}^{-3}$, while for $\lambda_B = 1$ m the value $\tau_B = 10$ ms is reached already at the densities $\rho \leq 10^3 \text{ g cm}^{-3}$, in agreement with the scaling $\tau_B \propto \rho \lambda_B^2$.

3.1. Validity of the MHD approach

After having assessed the ranges of validity of ideal MHD, we can now turn to the next natural question: what limits the applicability of the MHD approach in the present context? Clearly, at very low rest-mass densities the mean free path of electrons $\lambda_{\text{mfp}} = \tau v$ becomes large and the validity of the MHD description of matter itself can break down. We recall that hydrodynamic description of matter breaks down whenever $\lambda_{\text{mfp}} \geq \lambda_B$.

At low densities and high temperatures we can obtain a simple estimate for λ_{mfp} [the arguments are similar to those leading to Eq. (13)]

$$\lambda_{\text{mfp}} \simeq 4.2 \left(\frac{\rho}{1 \text{ g cm}^{-3}} \right)^{-0.9} \left(\frac{T}{1 \text{ MeV}} \right)^{1.8} \text{ cm}. \quad (15)$$

Now the condition of applicability of MHD description, *i.e.*, $\lambda_{\text{mfp}} \leq \lambda_B$, can be written as

$$\rho \gtrsim 1.4 \times 10^{-5} \left(\frac{T}{1 \text{ MeV}} \right)^2 \left(\frac{\lambda_B}{1 \text{ km}} \right)^{-1.1} \text{ g cm}^{-3}. \quad (16)$$

It follows from Eq. (16) that the higher the temperature or the smaller the typical lengthscale λ_B , the higher the rest-mass density below which the

MHD description breaks down. Figure 2 shows the regions of validity of the MHD description in the temperature-density plane for $\lambda_B = 1$ km and $\lambda_B = 1$ m. The low-temperature and high-density region corresponds to the regime where ideal MHD conditions are fulfilled. Adjacent to this, a lower density region emerges where the MHD is applicable, but the Hall effect should be taken into account; the exact location of this region depends on the strength of the magnetic field. It moves to lower rest-mass densities for the weaker magnetic field. Above the separation line $\lambda_B = \lambda_{\text{mfp}}$ the low-density and high-temperature region features matter in the non-hydrodynamic regime, *i.e.*, in a regime where the MHD approximation breaks down and a kinetic approach based on the Boltzmann equation is needed.

4. Summary

Motivated by recent developments of multimessenger astronomy started with the observations of GW170817 in electromagnetic and gravitational waves, we addressed in this work the role of dissipative processes in the MHD description of BNSMs. Using recently obtained conductivities of warm plasma in strongly magnetized matter we analysed the timescales for the evolution of the magnetic field under the conditions which are relevant for BNSMs. We found that the magnetic-field decay time is much larger than the relevant timescales for the merger process in the entire density-temperature range characteristic for these processes. In other words, the ideal MHD approximation is applicable throughout the entire processes of the merger. This conclusion holds for lengthscales down to a meter, which is at least an order of magnitude smaller than currently feasible computational grids. Our finding implies a paradigm shift in resistive MHD treatment of BNSMs, as these were based on the modeling of conductivities which vanish in the low-density limit (Dionysopoulou 2015). We have demonstrated that the ideal MHD description does not break down due to the onset of dissipation, rather it becomes inapplicable when the MHD description of matter becomes invalid.

We have demonstrated that the Hall effect plays an important role in the low-density and low-temperature regime. Thus, the ideal MHD description must be supplemented by an approach which takes into account the anisotropy of the fluid via the Hall effect. As is well-known, the Hall effect can act as a mechanism of rearrangement of the magnetic field resulting in resistive instabilities (Gourgouliatos 2016, Kitchatinov 2017). We hope that our study will stimulate MHD simulations which will include these effects.

Acknowledgements

I would like to thank Prof. Armen Sedrakian, Prof. Lucciano Rezzolla and Dr. Antonios Nathanail for scientific collaboration and fruitful discussions. I also acknowledge support from the

HGS-HIRE graduate program at Goethe University, Frankfurt. The simulations were performed on the LOEWE cluster in CSC in Frankfurt by A. Nathanail.

References

- Baiotti, L.; Rezzolla, L. 2017, Rept. Prog. Phys. 80, 096901
Dionysopoulou, K.; Alic, D.; Palenzuela, C.; Rezzolla, L.; Giacomazzo, B., 2013, Phys. Rev. D 88, 044020
Dionysopoulou, K.; Alic, D.; Rezzolla, L. 2015, Phys. Rev. D 92, 084064
Gourgouliatos, K. N.; Hollerbach, R. 2016, MNRAS, 463, 3381
Harutyunyan, A. 2017, Relativistic hydrodynamics and transport in strongly correlated systems. PhD thesis, Goethe University, Frankfurt am Main, Germany
Harutyunyan, A.; Nathanail, A.; Rezzolla, L.; Sedrakian, A. 2018, EPJ A 54, 191
Harutyunyan, A.; Sedrakian, A. 2016, Phys. Rev. C 94, 025805
Faber, J. A. 2012, Living Rev. Relativity, 15, 8
Kawamura, T.; Giacomazzo, B.; Kastaun, W.; Ciolfi, R.; Endrizzi, A.; Baiotti, L. et al. 2016, Phys. Rev. D 94, 064012
Kitchatinov, L. L. 2017, Astronomy Letters, 43, 624
Kiuchi, K.; Kyutoku, K.; Sekiguchi, Y.; Shibata, M. 2018, Phys. Rev. D 97, 124039
Kiuchi, K., Kyutoku, K., Sekiguchi, Y.; Shibata, M.; Wada, T. 2014, Phys. Rev. D 90, 041502
Kiuchi, K.; Sekiguchi, Y.; Kyutoku, K.; Shibata, M.; Taniguchi, K.; Wada, T. 2015, Phys. Rev. D 92, 064034
Palenzuela, C.; Lehner, L.; Liebling, S. L.; Ponce, M.; Anderson, M.; Neilsen, D. et al. 2013, Phys. Rev. D 88, 043011
Palenzuela, C.; Lehner, L.; Ponce, M.; Liebling, S. L.; Anderson, M.; Neilsen, D. et al. 2013, Phys. Rev. Lett. 111, 061105
Palenzuela, C.; Liebling, S. L., Neilsen, D.; Lehner, L.; Caballero, O. L.; O'Connor, E. et al. 2015, Phys. Rev. D 92, 044045
Paschalidis, V. 2017, Classical and Quantum Gravity, 34, 084002
Rezzolla, L.; Giacomazzo, B.; Baiotti, L.; Granot, J.; Kouveliotou, C.; Aloy, M. A. 2011, ApJ. 732, L6
Ruiz, M.; Lang, R. N.; Paschalidis, V.; Shapiro, S. L. 2016, ApJ, 824, L6
Ruiz, M.; Shapiro, S. L.; Tsokaros, A., 2018, GW170817, general relativistic magnetohydrodynamic simulations, and the neutron star maximum mass, 97, 021501
Siegel, D. M.; Ciolfi, R.; Harte, A. I., Rezzolla, L. 2013, Phys. Rev. D R 87, 121302

Galaxy dynamo in inhomogeneous interstellar medium

E. A. Mikhailov¹ *, D. A. Grachev¹

¹*M.V.Lomonosov Moscow State University, Russia*

**E-mail: ea.mikhajlov@physics.msu.ru*

Abstract

In some galaxies there are magnetic fields of several microgauss. Their evolution is connected with dynamo mechanism which is based on joint action of alpha-effect and differential rotation. The equations of the dynamo theory usually include some averaged kinematic characteristics of the interstellar turbulence. This approach is quite suitable for galaxies with "calm" interstellar medium. As for the galaxies with intensive star formation or supernovae explosions it will not give proper results. For this case the HII regions are quite small, exist for small-time and their localization can be assumed random. So it is useful to take the dynamo equations with random coefficients, which take one of two values (the first one is connected with HI regions, and the second one – with HII). We have studied the magnetic field evolution in the stochastic dynamo model for some typical cases. From the mathematical point of view, the results show some special effects. Firstly, the magnetic field evolution demonstrates the intermittency effect: higher statistical moments of the field grow faster than the lower ones. Moreover, the magnetic field in this model can have large fluctuations, so we have also described the correlation function of the field.

Keywords: *galaxies - magnetic fields - dynamo - intermittency - correlation function.*

1. Introduction

Nowadays it is no doubt that some of the galaxies have large-scale magnetic fields of order of microgauss (Beck et al. 1996). From the observational point of view, they are studied by the measurements of Faraday rotation of polarization plane of radiowaves on modern radio telescopes, such as VLA, LOFAR and SKA (in future). Also their existence is proved by synchrotron emission spectra. It is thought that the magnetic field has two different components: the first one (small-scale) is fully random and it has the typical

lengthscale of 50–100 pc, and the second one has the lengthscale comparable with the whole galaxy. It can be obtained as a result of averaging the full magnetic field, and it is called regular, or large-scale magnetic field.

As for theoretical description, the galactic magnetic fields evolution is usually connected with the dynamo theory (Arshakian et al. 2009). As for the large-scale field, the dynamo mechanism is based on joint action of alpha-effect and differential rotation. Alpha-effect is connected with vorticity of the interstellar turbulent motions (it makes the radial component of the magnetic field from the angular one). The second effect characterizes non-solid rotation of the galaxy, and it transforms the radial magnetic field to the angular one. They compete with the turbulent diffusion, which makes the field decay. If the joint intensity of the alpha-effect and differential rotation is higher than the dissipative processes, the magnetic field grows, else it decays. So the dynamo mechanism is threshold: the field evolution is characterized by so-called dynamo number, and the field enlarges only for some of its values.

The evolution of the regular magnetic field is described by the Steenbeck – Krause – Rädler equation, which is quite difficult to be solved both analytically and numerically. So the equations are usually solved using different simplified models for the field. One of the most important approaches is connected with so-called no- z approximation. It takes into account that the galaxy disc is quite thin, so some of the derivatives can be changed by the algebraic expressions. The equations of the no- z approximation include coefficients constructed of averaged characteristics of the interstellar turbulence (Moss 1995; Phillips 2001).

This method is quite well for modelling the magnetic field in "calm" galaxies, where the parameters of the interstellar motions are well described by averaged one. However, there are a lot of galaxies where there are such intensive processes as star formation, supernovae explosions, outflows from stars etc. The interstellar turbulence can differ very much from the effective characteristics. There are two different ways of modelling the magnetic fields in such objects. On the one hand, we can parameterize the velocity of the interstellar motions, typical lengthscale of turbulence and another values (Mikhailov et al. 2012). On the other hand, the star formation (and other active processes) are quite rapid and they are localized in some small regions. Roughly it can be said that the localization of these regions is random. So it would be useful to describe the magnetic field evolution taking the model with random coefficients. The estimates of the magnetic field evolution have been made in some previous works (Mikhailov & Modyaev 2015; Mikhailov & Pushkarev 2018). It is also interesting to study the correlation function for the magnetic field, which can connect the values of the field at different times. In this work we give the results for the magnetic field evolution for the model with random coefficients and for the correlation function.

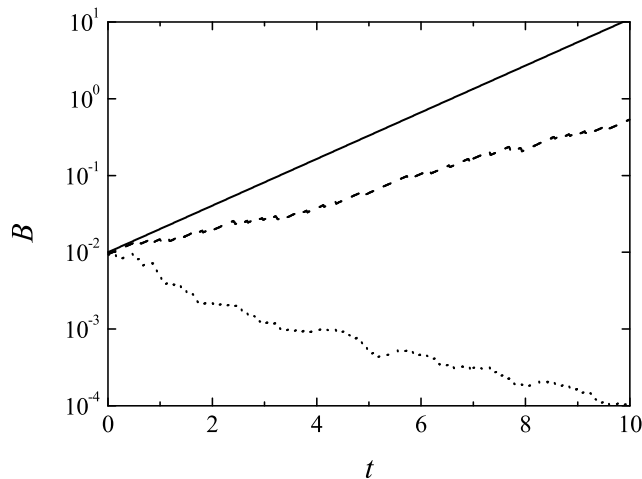


Figure 1: Evolution of the magnetic field. Solid line shows $p = 0.00$, dashed line – $p = 0.05$, dotted line – $p = 0.20$.

2. Basic equations

The galactic magnetic field \mathbf{H} contain two main parts:

$$\mathbf{H} = \mathbf{B} + \mathbf{b},$$

where \mathbf{b} is the small scale magnetic field, which has the same lengthscale as the turbulent motions, and \mathbf{B} is the large-scale component of the field. The evolution of this component is described by Steenbeck – Krause – Rädler equation (Steenbeck et al. 1966):

$$\frac{\partial \mathbf{B}}{\partial t} = \text{curl}[\mathbf{V}, \mathbf{B}] + \text{curl}(\alpha \mathbf{B}) + \eta \Delta \mathbf{B};$$

where \mathbf{V} is the large-scale velocity of the interstellar medium (usually it is connected with rotation of the galaxy), α characterizes the vorticity of the turbulent motions, η is the turbulent diffusivity.

In the no- z approximation it is assumed that the magnetic field nearly lies in the equatorial plane, and for the field components we have:

$$B_{r,\varphi}(r, \varphi, z, t) = B_{r,\varphi}(r, \varphi, 0, t) \cos\left(\frac{\pi z}{2h}\right),$$

where h is the half-thickness of the galaxy disc. So the z -derivatives of the field will be the following:

$$\frac{\partial^2 B_{r,\varphi}}{\partial z^2} = -\frac{\pi^2 B_{r,\varphi}}{4h^2}.$$

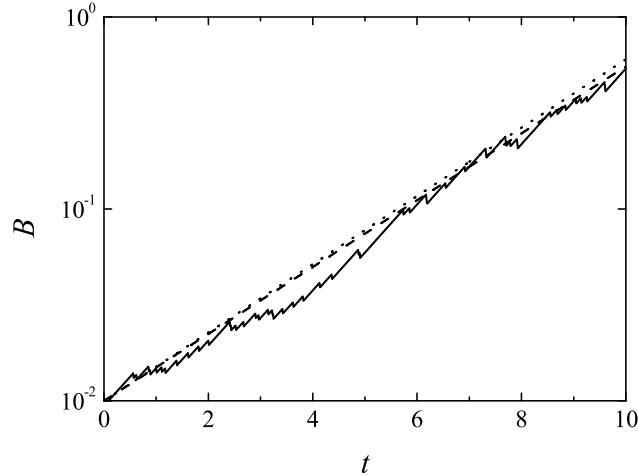


Figure 2: Momentums of the magnetic field. Solid line shows the typical field, dashed line – mean field, dotted line – mean square field.

As for the alpha-effect, it is often used that $\alpha = \alpha_0 \frac{z}{h}$, where $\alpha_0 = \frac{\Omega l^2}{h}$. Usually it is convenient to use the dimensionless time measured in units of h^2/η . If we neglect the dissipation in the disc plane, for the magnetic field we have the equations (Moss 1995; Phillips 2001; Mikhailov & Modyaev 2015):

$$\begin{aligned} \frac{\partial B_r}{\partial t} &= -R_\alpha B_\varphi - \frac{\pi^2 k B_r}{4}; \\ \frac{\partial B_\varphi}{\partial t} &= -R_\omega B_r - \frac{\pi^2 k B_\varphi}{4}, \end{aligned}$$

where R_α characterizes alpha-effect, R_ω – differential rotation. The coefficient k depends on the velocity of the turbulent motions. The values of $k = 1$ can characterize "calm" galaxies, and $k \approx 3$ is connected with regions of star formation.

3. Model with random coefficients

If we solve the eigenvalue problem for no- z approximation equations, we obtain that the field can grow with velocity of

$$\gamma = -\frac{\pi^2 k}{4} + \sqrt{D},$$

where $D = R_\alpha R_\omega$ is the dynamo-number which described the possibility of the field generation. Usually for such galaxies as Milky Way or M31 $D \approx 10$,

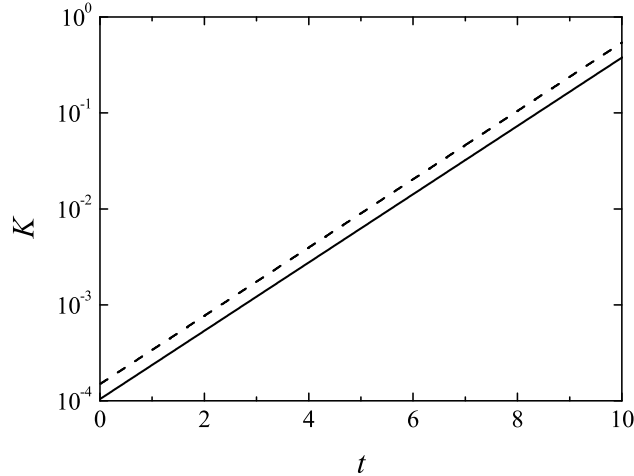


Figure 3: Correlation function for the field. Solid line shows $T = 0.1$, dashed line – $T = 1.0$.

so if the star formation is weak ($k = 1$), the field can grow. If we have more intensive turbulent diffusivity, the field will decay.

To model the magnetic field, we use the equations with random coefficient k . It is constant during time intervals $[0, \Delta t)$, $[\Delta t, 2\Delta t)$, ..., $[(n - 1)\Delta t, n\Delta t)$, ... and it takes random values:

$$k = \begin{cases} k_1 & \text{with probability } p; \\ k_2 & \text{with probability } (1 - p) \end{cases}$$

We take $k_1 = 3.5$ (for HII regions) and $k_2 = 1.0$ (for HI). The probability p can be connected with star formation rate Σ (Mikhailov 2014):

$$p \approx 12\Sigma,$$

where Σ is measured in $M_\odot \text{kpc}^{-2} \text{yr}^{-1}$. The field evolution is shown on Figure 1. We can see that the magnetic field can grow if $p < 0.12$, else large-scale structures decay. It is connected with intensive turbulent dissipation processes, which destroy regular structures of the field.

It is also interesting to study the statistical momentums of the solution, which characterize the field evolution (Figure 2). We can see the intermittency effect: mean square field grows faster than the mean one. This is connected with rare, but very large solutions of the equations (Zeldovich et al. 1987).

Such effects can be studied better using the correlation function of the field, which connects its values for different time momentums:

$$K(t, T) = \langle B(t), B(t + T) \rangle .$$

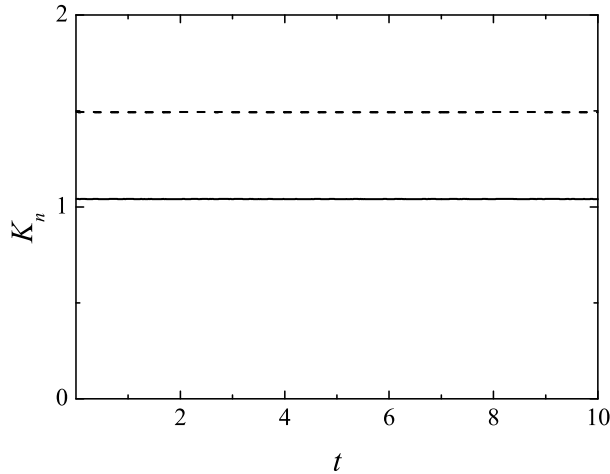


Figure 4: Normalized correlation function for the field. Solid line shows $T = 0.1$, dashed line – $T = 1.0$.

The typical results are shown on Figure 3. The main part of the correlation function is connected with the exponential growth. To study the connection between the field for different times, it is much better to use the normalized correlation function:

$$K_n(t, T) = \frac{K(t, T)}{K(t, 0)}.$$

It is shown on Figure 4.

4. Conclusions

We have studied the magnetic field evolution in the galaxies with inhomogeneous interstellar medium, using the model with random coefficients. We have shown that for intensive star formation the large-scale structures of the field can be destroyed. This effect can be supported by the observations of the magnetic field in NGC 6946: the field in this galaxy is concentrated *between* the spiral arms, where there is quite intensive star formation (Beck & Hoernes 1996).

The magnetic field also demonstrates the intermittency effect in this model: the higher momentums grow faster than lower ones. We have studied the correlation function for the field, too. It shows that in our model the values of the field for different momentums are quite close.

It would be interesting to study another random effects in the dynamo model. For example, we can study the fluctuations of another governing parameters, or injections of the magnetic field (Moss et al. 2014).

Acknowledgements

This work was supported by Russian Foundation for Basic Research under grant 18-32-00124. Authors thank the organizers of the International Conference Dedicated to Victor Ambartsumian's 110th Anniversary "Instability Phenomena and Evolution of the Universe" for the opportunity to present this work.

References

- Arshakian, T.; Beck, R.; Krause, M.; Sokoloff, D. 2009, *A&A* 494, 21
Beck, R.; Brandenburg, A.; Moss, D. et al. 1996, *ARA&A* 34, 155
Beck, R.; Hoernes, P. 1996, *Nature*, 379, 47
Mikhailov, E. 2014, *Ast. Lett.*, 40, 398
Mikhailov, E.; Modyaev I. 2015, *Balt. Astron.* 24, 194
Mikhailov, E.; Pushkarev, V. 2018, *A&AT*, 30, 343
Mikhailov, E.; Sokoloff, D.; Yefremov Yu.N. 2012, *Astron. Lett.* 38, 543
Moss, D. 1995, *MNRAS* 275, 191
Moss, D.; Sokoloff, D.; Beck, R.; Krause, M. 2014, *A&A*, 566, A40
Phillips, A. 2001, *Geophys. Astrophys. Fluid Dyn.* 94, 135
Steenbeck, M.; Krause, F.; Rädler K.-H. 1966, *Z. Naturforsch.*, 369 (in German)
Zeldovich, Ya.B.; Molchanov, S.A.; Ruzmaikin, A.A; Sokoloff, D.D. 1987, *Sov.Phys.*, 30, 353

On the Magnetic Field Inside the Solar Circle of the Galaxy: on the Possibility of Investigation of Some of Characteristics of the Interstellar Medium Using Pulsars with Large Faraday Rotation Values

R. R. Andriasyan^{1*}, H. R. Andriasyan¹, G. M. Paronyan¹

¹NAS RA V. Ambartsumian Byurakan Astrophysical Observatory (BAO), Armenia

*E-mail: randrasy@bao.sci.am

Abstract

To study some characteristics of the interstellar medium, observational data of pulsars with large Faraday rotation values ($|RM| > 300$ rad / m²) were used. It was suggested and justified that large $|RM|$ values can be due to the contribution of the regions with increased electron concentration, projected on the pulsar. Most likely these are the HII regions, dark nebulae and molecular clouds. In these objects the magnetic field can be oriented in the direction of a large-scale field of the Galaxy, or simply is a deformed extension of the galactic field. It was shown that the Galactic distribution of rotation measures of pulsars with $|RM| > 300 \frac{\text{rad}}{\text{m}^2}$ corresponds to the circular model of the magnetic field of the Galaxy, with the counter-clockwise direction of the magnetic field in the galactocentric circle $5 \text{ kpc} < R < 7 \text{ kpc}$.

Keywords: *Faraday rotation, distribution of pulsars, radio pulsars, circular model of the magnetic field, magnetic field*

1. Introduction

The study of the magnetic fields of galaxies and, in particular, of our Galaxy has a great importance for explaining many dynamical and active processes taking place in these objects (see, for example, Pacholczyk 1973; Andriasyan 2011; Van Loo Sven 2015). The presence of the magnetic field of the Galaxy can explain the transportation of cosmic rays through the interstellar medium, as well as synchrotron background radiation in the Galaxy (Fermi E. 1949; Kiepenheuer 1950). The magnetic field of the Galaxy was studied using observational data of various types, such as interstellar polarization of starlight, Zeeman splitting of spectral lines of HI

and different molecules in the radio range, data on Faraday rotation of extragalactic radio sources and pulsars (see, for example, Andreev 1989; Vlemmings 2008; Manchester R. 1980). It is known that pulsars, for which numerous and diverse observational data were obtained, can be considered probes for studying the interstellar medium. In particular, data on dispersion measures (DM), which practically are known for all known pulsars, and about measures of Faraday rotation (RM) (of the order of 1150 pulsars) are very important for studying the magnetic field of the Galaxy. These data are directly derived from observations of pulsars. Theoretically they are expressed by the electron density n_e in the interstellar medium through which the polarized radio emission of the pulsar passes and the projection of the magnetic field B_L (in Gauss) in this medium, using the following formulas:

$$DM = \int n_e dL \quad (1),$$

$$RM = \alpha \int n_e B_L dL, \quad (\alpha = 8.1 \cdot 10^5) \quad (2).$$

In these formulas, integration is carried out over the entire traversed path of radiation (L in parsecs) from the pulsar to the observer. Formula 1 makes it possible to determine the distance of a pulsar with the known electron density distribution in the Galaxy, and formula 2 together with formula 1 makes possible to determine the average component of the tension of interstellar magnetic field $[B_L]$ on the line of sight in micro gauss (μG).

$$[B_L] = \frac{1}{\alpha} \frac{RM}{DM} = 1.23 \frac{RM}{DM}. \quad (3)$$

RM and DM data were used to study the structure and magnitude of the magnetic field of the Galaxy, since 1970s, when the rotation measures were known for only 3-4 tens of pulsars (Manchester 1972; Ruzmaikin 1977). As the amount of RM data increases, more detailed studies have been carried out and various models have been proposed for the plane component of the Galactic magnetic field (Rand 1989; Rand 1994; Han 1994; Vallée 2005), as well as for the magnetic field in the Halo of the Galaxy (see, for example, Andreev 1988; Han 1997; Han 2006). In particular, in the work of Andreev and Makarov 1988, where the model of the two-component magnetic field of our Galaxy was proposed, for the first time it was shown that the data on the rotation measures of pulsars and extragalactic radio sources are in good agreement with the model when the magnetic field of the plane component of the spiral arms is embedded in the magnetic field of the galactic halo with the dipole configuration, which is deformed due to the differential rotation of the Galaxy. In [2], using the data of RM, DM and the distance of pulsars, we constructed a two-color map of the plane component of the magnetic field of the Galaxy, on which large-scale regions with regular magnetic fields, approximately corresponding to the spiral structure of the Galaxy, were clearly distinguished.

It should be noted that in all the works mentioned above, three models of the plane component of the magnetic field of the Galaxy are mainly discussed: 1) a bisymmetric spiral (BSS), in which the magnetic field in neighbor spiral arms has opposite directions; 2) an axially symmetric (ASS) structure with two changes in the direction of the field inside the solar circle; 3) concentric circular model. In particular, it was shown in [14] that in the general galactocentric magnetic field, which is directed clockwise, the magnetic field in the ring with a galactocentric distance of 5-7 kpc directed counterclockwise is mainly emitted. There were also proposed models in which the spiral structure of the magnetic field roughly coincides with the inter arm regions of the Galaxy. There are also works (see, for example, Men H. 2008) in which it is shown that none of these models correspond to observational data better than the other. It should be noted, that in addition to the spiral arms inside the solar circle, magnetic fields outside this circle were also discussed, for example, in the Perseus spiral arm and in the local Orion arm, which is probably a branch from the Perseus arm. The magnetic fields in these arms (see, for example, Andriasyan R. R. 1989) have a direction opposite to the inner spiral arm of Sagittarius, in which a fairly regular magnetic field is directed toward the observer.

Note that inside the solar circle, in addition to the spiral arm of Sagittarius, there are two other spiral arms (see, for example, Han 2006; Cordes 2002; Hou 2014), whose magnetic fields are also studied using the data of RM of pulsars located inside or further of these arms see Fig. 1).

Figure 1 shows the distribution of the electron density n_e in the Galactic plane, taken from Cordes 2002. As follows from Fig. 1, the polarized radiation of distant pulsars observed by us passes through several spiral arms and carries total information on the magnetic field of these arms. These data are used to construct the above-mentioned models of the plane component of the Galactic magnetic field. If we take into account the fact that the error in determining the distances of distant pulsars in directions closer to the center of the Galaxy due to this model of electron concentration can reach tens of percents Cordes 2002, as well as the presence of small-scale fluctuations of the magnetic field, the intensity of which reaches (or even exceeds) the same values as in regular fields, it becomes clear that the task of choosing a more plausible model of the magnetic field from the above is very difficult or even impossible at the present time.

In this paper, to study the magnetic field in regions inside the solar circle, we will use pulsars with large rotation measures $|RM| > 300 \frac{\text{rad}}{\text{m}^2}$, closer to the center of the Galaxy. It is clear that: firstly, distant pulsars basically have large rotation measures, and, second, the numerous data of pulsars with small values $|RM|$ and with significant errors in the distances, can clutter the graphs very much, from which important details of the distribution of the magnetic field can be lost. The limitation $|RM| > 300 \frac{\text{rad}}{\text{m}^2}$ is also due to the fact that, as will be seen later, these pulsars are mainly concentrated

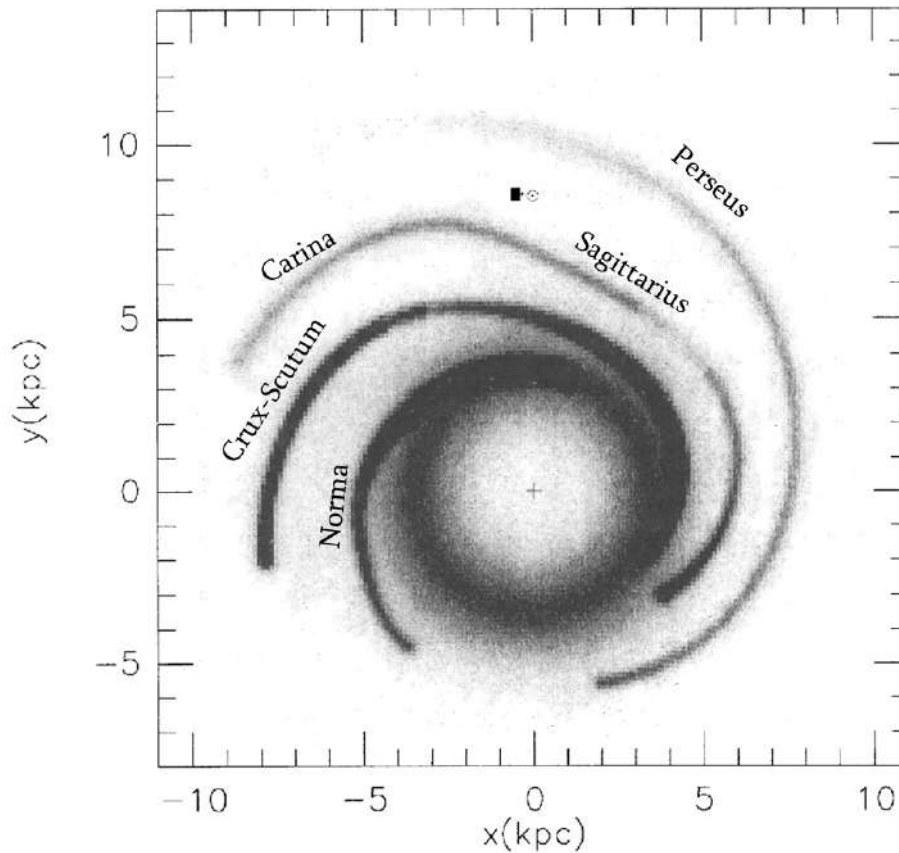


Figure 1: Distribution of electron concentration n_e in the Galactic plane. In the vicinity of the Sun $n_e \approx 0.019 \text{ cm}^{-3}$. The largest electron concentration corresponds to the darkest part in the figure.

in the region around the galactic center in Galactic longitudes $0^\circ < l < 90^\circ$, and $270^\circ < l < 360^\circ$ (in directions to the anti-center of the Galaxy we have only 6 this kind of pulsars), and, consequently, they can be used to study the magnetic field in regions inside the solar circle of the Galaxy.

2. Distribution of pulsars along galactic longitude

The data from the ATNF pulsar catalog are used in the work Manchester R. N. 2005. In this paper we use data from 199 pulsars with $|RM| > 300 \frac{\text{rad}}{\text{m}^2}$, selected from 1133 pulsars with known rotation measures. It turns out that pulsars with large values of $|RM|$ basically (with the exception of 10 pulsars) are concentrated near the plane of the Galaxy in a layer of ± 500 parsecs. Figure 2 shows the distribution of Faraday rotation measures over galactic longitude l . In constructing the plot, almost all pulsars with

$|RM| > 300 \frac{\text{rad}}{\text{m}^2}$ were used. For the compactness of the figure, 6 pulsars with $|RM| > 2000 \frac{\text{rad}}{\text{m}^2}$, as well as 6 pulsars that are in the directions of the galactic longitude $90^\circ < l < 270^\circ$ (in the direction of the anticenter) were excluded from consideration. In the figure, the galactic longitudes $-90^\circ < l < 0^\circ$ correspond to the coordinates $-(360^\circ - l)$.

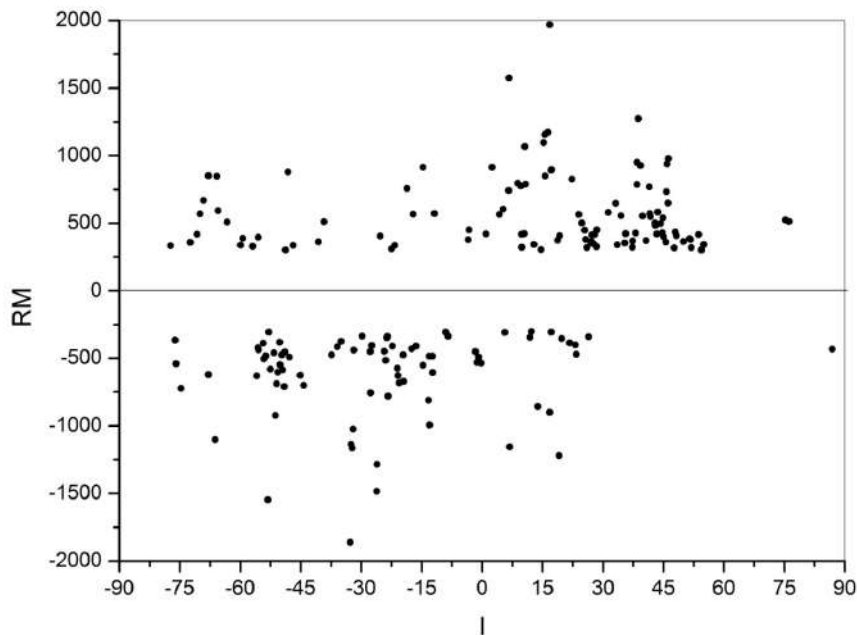


Figure 2: Distribution of Faraday rotation measures $|RM| > 300 \frac{\text{rad}}{\text{m}^2}$ over galactic longitude l .

It can be seen from Fig. 2 that the magnitudes of the rotation measures with respect to the galactic coordinate's l are distributed rather chaotically. Sometimes pulsars with angular distances less than one or two degrees have rotation measures that differ even in sign. There are more than twenty such examples in the list of used pulsars and on the graph. Therefore, we can assume that the characteristic size of the chaotic distribution of the rotation measures corresponds to angular distances in the order of 1-2 degrees. In many spatially close pulsars, even if the Faraday rotation signs coincide, their magnitudes sometimes differ by several times. This can mean that such rotation measures can not be formed in the large-scale magnetic field of the Galaxy.

We note that when analyzing the map of the magnetic field of our Galaxy (Andreasyan 2003), we showed that one of the largest formations with a fairly regular magnetic field in the Galaxy is the spiral arm of Sagittarius. But even in this direction the magnetic field does not reach such large values. A regular magnetic field in the direction of Sagittarius's spiral arm is also

seen in Fig. 2 in galactic longitudes 30° - 70° .

From the foregoing, it can be assumed that a very large rotation measure of pulsar is probably due to the influence of one nearby object (relative to the pulsar), which has large electron concentrations n_e , and perhaps also a large value of the average magnetic field strength B_L . Such objects are projected on pulsars, and the polarized radiation of pulsars passing through them acquires a large Faraday rotation. In this connection we note that in our early work (Andreasyan 1982) it was shown that large rotation measures $|RM|$ unidentified extragalactic radio sources located in directions close to the plane of our Galaxy can also be explained by the passage of polarized radio emission of these radio sources through the HII regions located in the Galactic plane. The conclusion that pulsar radiation can pass through nearby objects with large electron concentrations n_e can also be based on certain features of the distribution of pulsars with large rotation measures. For example, the majority of pulsars with large rotation measures are mainly located near or inside a 4 kpc ring with a large electron concentration (Cordes 2002). It can be assumed that this ring is patchy and consists of numerous condensations with dimensions of about 100 parsecs or less. At distances of the majority of the used pulsars, such dimensions correspond to one or two angular degrees, that is, of the order of the characteristic distance of the chaotic distribution of the rotation measures (see Fig. 2). Passing through such condensations, the polarized radiation of pulsars can undergo additional Faraday rotation of different signs and different magnitudes, depending on the magnetic field in these objects. However, in most cases it is most likely that this additional Faraday rotation is due to the effect of only one condensation. Such an assumption can be justified by the following arguments: from the analysis of rotation measures (RM) and dispersion measures (DM) of pulsars with large Faraday rotation values, it turns out that the magnetic field averaged over the entire path is 1-3 micro gauss, as in other sections in the interstellar medium (see formulas 1, 2 and 3, and also Fig. 3).

From formula 2 it follows that the dispersion measure is additive, and increases when the pulsar radiation passes through each new condensation. However, the rotation measure does not have such an additive property (see formula 1), because, in addition to the electron concentration, it also depends on the direction and magnitude of the magnetic field. Assuming that both the rotation measure and the dispersion measure are formed due to passage of the pulsar radiation through several condensations, the dispersion measure DM would increase after each passage in a linear manner, while the rotation measure RM would decrease due to compensation of the Faraday rotation by separate condensations with different directions of the magnetic field, or even increased, it will be more slowly. This is due to the fact that it is difficult to imagine that several clouds with the same direction of the magnetic field are located on the line of sight, while a few clouds are

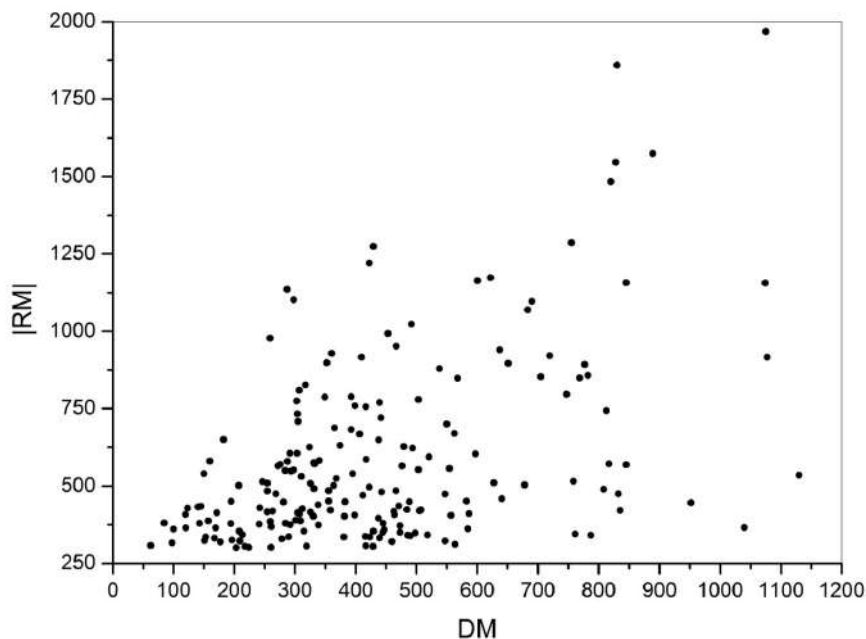


Figure 3: The dependence $|RM|$ from DM for pulsars with $|RM| > 300 \frac{\text{rad}}{\text{m}^2}$

also located in the very close direction, but with the opposite direction of the magnetic field. It follows from the above that when a polarized radio emission of a pulsar passes through several clouds, there should not be a noticeable positive correlation between $|RM|$ and DM, while in Figure 4 there is a noticeable correlation between them. Although this correlation is weak (the correlation coefficient is in the order of 0.5), this too can be considered as indirect evidence in favor of the assumption that in most cases the additional Faraday rotation is due to the influence of one condensation.

3. Distribution of pulsars with large RMs in the Galactic plane

In the previous section it was suggested that the large Faraday rotations of pulsars are in most cases due to the contribution of one cloud (presumably HII regions, molecular clouds or dark nebulae) located between the pulsar and the observer. The magnetic field in this cloud can be oriented along the direction of a large-scale field of the Galaxy, or simply a deformed continuation of the galactic field. Consequently, data on pulsars with large $|RM|$ can contain information about the galactic magnetic field and can be useful for studying the large-scale magnetic field of the Galaxy. Figure 4 shows the distribution of pulsars with $|RM| > 300 \frac{\text{rad}}{\text{m}^2}$ on the plane of the Galaxy. The coordinate axes pass through the center of the Galaxy. The coordinates

of the Sun, indicated by an asterisk - (0 kpc; 8.5 kpc). Pulsars are indicated by circles. The black circles correspond to pulsars with positive values of RM (the projection of the magnetic field is directed toward the observer), and the white circles correspond to pulsars with negative values of RM. The figure clearly identifies the ring located between galactocentric circles with radii R about 5 and 7 kilo parsec. In this ring, almost all pulsars on the right side (with the exception of 3 pulsars) have Faraday rotations with a positive sign, and on the left side, except for 4 pulsars, all the others have a RM with a negative sign. This distribution of the signs of the pulsars RM in an excellent manner corresponds to the direction of the magnetic field counterclockwise in the ring with $5\text{kpc} < R < 7\text{kpc}$ (case of 7 pulsars, which are an exception to this scheme, can be investigated separately). In the remaining areas, it is difficult to highlight a sufficiently large-scale region with such a clearly marked direction of the magnetic field. This probably can be a consequence of the fact that in the direction of the center of the Galaxy, where the line of sight passes through several galactic arms, the error in determining the distances of pulsars is larger.

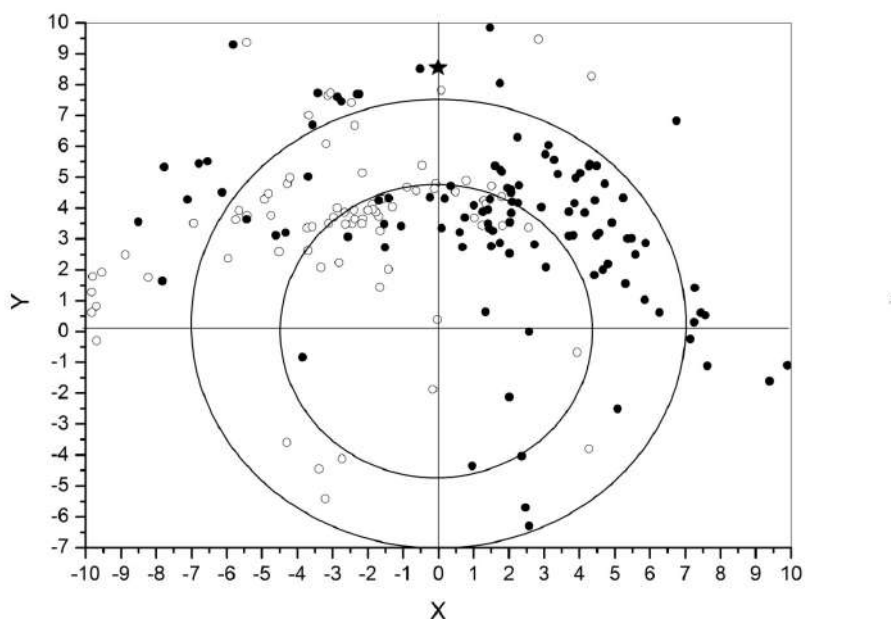


Figure 4: Distribution of rotation measures of pulsars in the plane of the Galaxy. Black circles denote pulsars in $RM > 300 \frac{\text{rad}}{\text{m}^2}$ (the projection of the magnetic field on the line of sight is directed toward the observer), white circles - in which $RM < -300 \frac{\text{rad}}{\text{m}^2}$ (the projection of the magnetic field is directed from the observer).

Thus, the analysis of pulsar data with $|RM| > 300 \frac{\text{rad}}{\text{m}^2}$ partially corresponds to the model of the magnetic field of the Galaxy proposed in (Vallée

2005), which proposes a circular model of the magnetic field of the Galaxy, directed clockwise, with a unique change in the direction of the field in the galactocentric ring with $5 \text{ kpc} < R < 7 \text{ kpc}$, where the magnetic field is directed counter-clockwise. Once again, we recall that we were supposed that large $|RM|$ are due to the contribution of regions projected on the pulsar with an increased electron concentration in which the magnetic field is oriented along the direction of the large-scale field of the Galaxy, or simply is a deformed extension of the Galactic field.

4. Identification of pulsars with large RM

As was suggested in the previous sections, large rotation measures of pulsars can be caused by clouds with an increased concentration of free electrons through which the polarized radio emission of pulsars passes. To determine what these clouds represent, we searched for interesting objects in the region of 5 angular minutes around pulsars with large RM-s. To search for objects, we used the database "SIMBAD". At distances of the considered pulsars, the 5-minute region is a circle with a diameter of the order of 10-15 parsecs. So, if these objects are closer to us than the pulsar and fall into this region, then they probably have dimensions of the order of 10-15 parsecs, or less. Thus, searches were carried out around 199 pulsars with the $|RM| > 300 \frac{\text{rad}}{\text{m}^2}$. As a result, around 70 pulsars, nebular objects were found, mainly: HII regions $\sim 35 \%$, dark nebulae $\sim 45 \%$, and molecular clouds $\sim 20 \%$.

It is known that the characteristic sizes of HII regions and dark nebulae are larger or of the order of 10-15 parsecs, and since the electron density n_e is much larger in them than in the interstellar medium (on average 0.03 cm^{-3}) and the magnetic field strength is greater or in the order of the mean field of interstellar medium (2-3 micro gauss), then indeed part of the large rotational measures of the mentioned 70 pulsars can be explained by the passage of polarized radio emission of pulsars through HII regions and dark nebulae. Simple estimates show that the contribution to the RM of the HII region or the Stromgren zones around young O-B stars which radius can reach about 100 parsecs, the electron concentration n_e is in the order of 1 cm^{-3} , and the magnetic field, as in the interstellar medium, is in the order of 2-3 micro gauss, can be in the order of 320-480 $\frac{\text{rad}}{\text{m}^2}$. Similar estimates can be obtained for dark nebulae whose dimensions are smaller than the size of the HII regions, but the electron concentration is probably much larger than in the HII regions. This means that the contribution of HII regions, molecular clouds and dark nebulae to the large value of the Faraday rotation of the pulsar can be decisive.

5. Conclusion

In conclusion, we note that using the observational data of pulsars with large Faraday rotation values, several results have been obtained in this paper. First, it was shown that the galactic distribution of the pulsars with rotation measures $|RM| > 300 \frac{\text{rad}}{\text{m}^2}$ better corresponds to the circular model of the magnetic field of the Galaxy (Vallée 2005), with the counterclockwise direction of the magnetic field in the galactocentric circle $5 \text{ kpc} < R < 7 \text{ kpc}$. It was also suggested and justified that large $|RM|$ may be due to the contribution of regions with an increased electron concentration (probably HII regions, dark nebulae and molecular clouds), projected on the pulsar. In these objects, the magnetic field can be oriented along the direction of a large-scale field of the Galaxy, or simply be a deformed extension of the galactic field.

Note that in order to study the large-scale magnetic field of the Galaxy, data from more than 150 HII regions and molecular clouds in which the magnetic fields were estimated by different methods (mainly by the Zeeman splitting of spectral radio lines) were also used in (Han 2007). It was also suggested that the magnetic fields in these objects can be a relic of the magnetic field of the Galaxy. We made an attempt to identify these objects with ours, but the direction of none of them coincided with the coordinates of the pulsars in this paper.

It should also be noted that from the conclusions of this paper a new possibility arises for estimating magnetic fields and some other characteristics of those HII regions, molecular clouds and dark nebulae that are closer than the pulsar, but are projected on it. This can be done by estimating the contribution of these nebular objects in the Faraday rotation of this pulsar.

Acknowledgements

The authors are grateful to the authors of the pulsar catalog (ATNF Pulsar Catalog), <http://www.atnf.csiro.au/research/pulsar/psrcat/>; Manchester, R. N., Hobbs, G.B., Teoh, A., Hobbs, M., AJ, 129, 1993-2006 (2005).

References

- Andreasyan, R. R.; Balayan, S. K.; Movsesyan, V. H., 2011, *Astrophysics*, Volume 54, Issue 2, pp. 177-183
- Andreasyan, R. R.; Makarov, A. N., 1989, *Astrophysics*, Volume 31, Issue 2, pp. 560-567
- Andreasyan, R. R.; Makarov, A. N., 1988, *Astrophysics*, Vol.28, No. 2, p. 247
- Andreasyan, R. R.; Makarov, A. N., 1989, *Astrophysics*, Vol.30, No. 1/July, p. 101, 1989
- Andreasyan, R. R.; Hovhannisyan, M. A.; Andreasyan, M. R., 2003, *Astrophysics (English translation of Astrofizika)*, v. 46, Issue 3, p. 341-349
- Andreasyan, R. R., 1982, *Astrophysics*, vol. 18, no. 2, Oct. 1982, p. 156-160. Translation. *Astrofizika*, vol. 18, Apr.-June 1982, p. 255-262.
- Cordes, J.; Lazio, T.; Chatterjee, S.; Arzoumanian, Z.; Chernoff, D., 2002, 34th COSPAR Scientific Assembly, The Second World Space Congress, held 10-19 October, 2002 in Houston, TX, USA., meeting abstract, id.2305
- Fermi, E., 1949, *Physical Review*, vol. 75, Issue 8, pp. 1169-1174

- Han, J. L.; Zhang, J. S., 2007, *Astronomy and Astrophysics*, Volume 464, Issue 2, March III 2007, pp. 609-614
- Han, J. L.; Qiao, G. J., 1994, *Astronomy and Astrophysics*, Vol. 288, pp. 759-772
- Han, J. L.; Manchester, R. N.; Berkhuijsen, E. M.; Beck, R., 1997, *Astronomy and Astrophysics*, v.322, pp. 98-102
- Han, J. L.; Manchester, R. N.; Lyne, A. G.; Qiao, G. J.; van Straten, W., 2006, *the Astrophysical Journal*, Volume 642, Issue 2, pp. 868-881.
- Hou, L. G.; Han, J. L., 2014, *Astronomy & Astrophysics*, Volume 569, id.A125, 21 p.
- Kiepenheuer, K. O., 1950, *Physical Review*, vol. 79, Issue 4, pp. 738-739
- Men, H.; Ferrière, K.; Han, J. L., 2008, *Astronomy and Astrophysics*, Vol. 486, Issue 3, 2008, pp. 819-828
- Manchester, R.; Taylor, J., 1980, *Pulsars.*, by Manchester, R.; Taylor, J.. Translated from the English edition. Moskva: Mir, 292 p.
- Manchester, R. N., 1972, *Astrophysical Journal*, Vol. 172, p. 43
- Manchester, R. N.; Hobbs, G. B.; Teoh, A.; Hobbs, M., 2005, *the Astronomical Journal*, Volume 129, Issue 4, pp. 1993-2006
- Pacholczyk, A. G. , 1973, *Non thermal processes in galactic and extragalactic sources*, Translated from the English edition Moskva: Mir, p. 252
- Rand, Richard J.; Kulkarni, Shrinivas R., 1989, *strophysical Journal*, Part 1 (ISSN 0004-637X), vol. 343, Aug. 15, 1989, pp. 760-772
- Rand, R. J.; Lyne, A. G., 1994, *onthly Notices of the Royal Astronomical Society*, Vol. 268, NO. 2/MAY15, p. 497
- Ruzmaikin, A. A.; Sokoloff, D. D., 1977, *Astrophysics and Space Science*, Vol. 52, p. 375
- Vallée, Jacques P., 2005, *The Astrophysical Journal*, Volume 619, Issue 1, pp. 297-305
- Van Loo, Sven; Tan, Jonathan C.; Falle, Sam A. E. G., 2015, *The Astrophysical Journal Letters*, Volume 800, Issue 1, article id. L11, 7 p.
- Vlemmings, W. H. T., 2008, *Astronomy and Astrophysics*, Volume 484, Issue 3, pp. 773-781

Analytical solution of the simple nonlinear radiative transfer problem

H. V. Pikichyan^{1*}

¹*NAS RA V. Ambartsumian Byurakan Astrophysical Observatory (BAO), Armenia*

**E-mail: hovpik@gmail.com, hovpik@bao.sci.am*

Abstract

Exploring the “Principle of invariance” and the method of “Linear images”, the simple nonlinear conservative problem of radiative transfer is analyzed. The solutions of nonlinear reflection-transmission and internal field problems of one dimensional scattering-absorbing medium of finite optical thickness are obtained, whereas both boundaries of medium illuminated by powerful radiation beams. Using two different approaches – a direct and inverse problem, the analytical solution of the internal field problem is derived.

1. Introduction

The properties of the scattering-absorbing medium in the linear theory of radiation transfer are assumed to be known in advance. While by solving the radiative transfer equation, the random walk properties of radiation can be determined from the analysis of the multiple interactions between the radiation and matter. But in nonlinear theory of radiative transfer, due to multiple interactions between the radiation and matter (Ambartsumian 1964a), the initial optical properties of both the radiation and absorbing-scattering medium are mutually affecting each other, in self-consistent manner. Indeed, if the intensity of an exciting radiation is higher, then some statistically measured fraction of atoms in medium is permanently resided in excited state, i.e. they do not absorb photons. This consequently decreases the value of absorption coefficient of each elementary volume of the medium, until the latter becomes more transparent (Ambartsumian 1964b). In nonlinear case, therefore, it is necessary to take into account the dependence of optical parameters of medium from the intensity of external exciting radiation. The Fig. 1 schematically plots the photon diffusion processes in linear (right) and nonlinear (left) cases. The unshaded circles denote the atoms being in the excited state, which are already eliminated from the multiple absorbing-scattering processes of the medium.

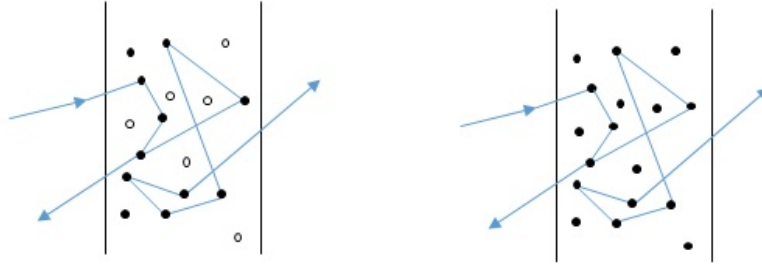


Figure 1: The photon diffusion processes in linear (right) and nonlinear (left) cases.

A goal of this report is to show on the example of simple one-dimensional conservative and isotropically scattering medium of two-level atoms: a) the affection of the mentioned above a non-linearity feature (including also the induced radiation) on properties of the solution of reflection-transmission problem, and on the internal field intensity in medium of a finite optical thickness; b) an efficiency of the implications previously introduced concept of “Linear Images (LI)” (Pikichyan 2016, 2014) together with Ambartsumian’s principle of invariance (Ambartsumian 1964a, Pikichyan 2010) for analyzing nonlinear problems of radiative transfer theory.

2. Two properties of “inverse” and “direct” formulation of the same internal field problem

Let us to consider the one-dimensional, conservatively and isotropically absorbing-scattering medium of a finite optical thickness, consisted of two-level atoms (Fig. 2). The medium is continuously illuminated from its both boundaries by powerful beams of exciting radiation of the given intensities x (left) and y (right). It is required to find internal I^\pm and outgoing u, v intensities of diffuse radiation field.

We may invoke the Boltzmann kinetic equation, written for the “photon gas” (the radiative transfer equation), usually formulating the “two-point” boundary value problem for determining the radiation intensity $I^\pm \equiv I^\pm(\tau, x, y, \tau_0)$, at the optical depth τ , for the medium of finite optical thickness τ_0 ($\tau \in [0, \tau_0]$) :

$$\begin{cases} \frac{dI^\pm}{d\tau} = \pm\alpha^\pm(I^+, I^-) \\ I^+|_{\tau=0} = x, \quad I^-|_{\tau=\tau_0} = y, \end{cases} \quad (1)$$

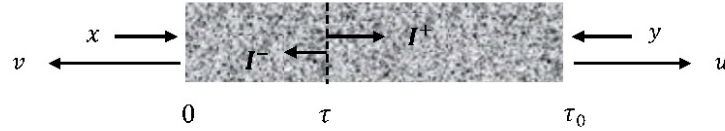


Figure 2: The one-dimensional isotropic, conservatively and isotropically absorbing-scattering medium of finite optical thickness.

where

$$\alpha^\pm(I^+, I^-) = \mp \frac{I^+ - I^-}{2[1 + b \cdot (I^+ + I^-)]} \quad (2)$$

is the known specified form of “integral of collisions” and

$$d\tau = k_0(l)dl, \quad l \in [0, l_0], \quad k_0(l) = n(l) \frac{h \cdot \nu}{2} B_{12}, \quad (3)$$

$$b \equiv \frac{B_{12} + B_{21}}{2A_{21}} = \frac{c^2}{4h\nu^3} \left(1 + \frac{g_2}{g_1}\right).$$

The l and l_0 are geometrical parameters of one-dimensional medium, respectively, depth and thickness. Also, the micro quantities are given in conventional notations (Ivanov 1969).

The Cauchy problem for the same radiative transfer equation can be formulated as an “inverse” one:

$$\begin{cases} \frac{dI^\pm}{d\tau} = \pm \alpha^\pm(I^+, I^-) \\ I^+|_{\tau=0} = x, \quad I^-|_{\tau=0} = v, \quad \text{or} \quad I^+|_{\tau=\tau_0} = u, \quad I^-|_{\tau=\tau_0} = y. \end{cases} \quad (4)$$

Here the $v \equiv v(x, y) \equiv v(x, y, \tau_0)$ and $u \equiv u(x, y) \equiv u(x, y, \tau_0)$ are “known” solution of reflection-transmission problem for the same medium (Fig.3). That is, we have an inverse problem of a restoration of internal field intensity by means of known external radiation, given only at the one boundary (left or right) of medium.



Figure 3: The “known” solution of reflection-transmission problem for the medium $[0, \tau_0]$

Direct problem formulation of obtaining the same internal field intensities I^+ and I^- can be readily constructed by exploring the nonlinear version of the Ambartsumian's "layers addition method" (Ambartsumian 1964a).

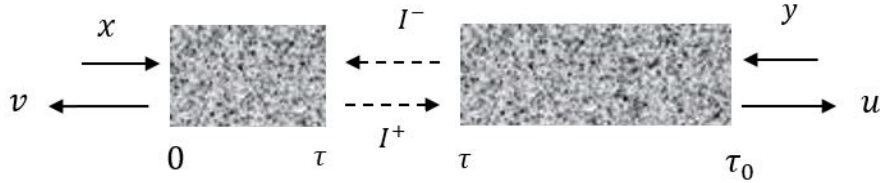


Figure 4: Addition of layers $[0, \tau]$ and $[\tau, \tau_0]$.

If the reflection-transmission properties of two separate layers $[0, \tau]$ and $[\tau, \tau_0]$, respectively, of the finite optical thicknesses τ and $(\tau_0 - \tau)$ are known (Fig.4), then the solution for the composite medium $[0, \tau_0]$ problem can be recast (Pikichyan 2014) in the form:

$$\begin{cases} I^+ = u(x, I^-, \tau) \\ I^- = v(I^+, y, \tau_0 - \tau) \end{cases} \quad (5)$$

Hence, it is obvious that for a determination of the internal field I^\pm of radiation in quest, by means of both inverse or direct methods, we need to obtain in advance a solution of reflection-transmission problem u (or/and v).

3. Solution of reflection-transmission problem

Non-linear form of Ambartsumian's principle of invariance (Ambartsumian 1964a) (see e.g. . Bellman, Kalaba, Wing 1960) give us two differential equations of invariant imbedding for the function $u(y, x)$ (Pikichyan 2010):

$$\frac{\partial u}{\partial \tau_0} = \alpha(u, y) \frac{\partial u}{\partial y} + \alpha(y, u), \quad (6)$$

$$\frac{\partial u}{\partial \tau_0} = \alpha(v, x) \frac{\partial u}{\partial x}, \quad v(x, y) \equiv u(y, x). \quad (7)$$

Eliminating the terms which include differentiation over the layer thickness, we obtain the functional equation of Ambartsumian's complete invariance:

$$\alpha(v, x) \frac{\partial u}{\partial x} - \alpha(u, y) \frac{\partial u}{\partial y} = \alpha(y, u). \quad (8)$$

In the linear case,

$$\alpha(x, y) = \frac{\lambda}{2}x - \left(1 - \frac{\lambda}{2}\right)y,$$

and the equation (8) becomes the Ambartsumian's known relation for coefficients of reflection and transmission of finite medium (Ambartsumian 1944):

$$R^2 - 2\frac{2-\lambda}{\lambda}R + 1 = T^2.$$

To solve the equation (8), we may use the method of, so-called, "linear images" (Pikichyan 2016, 2014). The solution $u(x, y, \tau_0)$ is found as a linear combination of the two auxiliary functions - $T \equiv T(x, y) \equiv T(x, y, \tau_0)$ and $R \equiv R(x, y) \equiv R(x, y, \tau_0)$. They are called the "linear images" of required solution $u(x, y, \tau_0)$:

$$u = T \cdot x + R \cdot y. \quad (9)$$

In the linear case, the quantities T and R are constants, and they are identical to real reflection and transmission coefficients of medium, illuminated only from one side. In a conservative case, we have $\lambda = 1$ and $R + T = 1$. We can easily derive, from relations (8) and (9), a symmetrical functional equation for determining the linear image T in quest:

$$\left[k(x+v) \frac{\partial}{\partial x} + k(y+u) \frac{\partial}{\partial y} \right] T = -T \cdot \frac{k(x+v) - k(y+u)}{x-y}, \quad (10)$$

where $k(\xi) = \frac{k_0(l)}{1+b\xi}$. Integration of (10) shows that, in the case at hand, the linear image T depends only on the sum of its arguments $T(x, y) \equiv T(x+y) = T(\xi)$. It can be written explicitly as

$$T(\xi) = q \frac{1+b\xi}{1+qb\xi} = \frac{2(1+b\xi)}{\tau_0 + 2(1+b\xi)}. \quad (11)$$

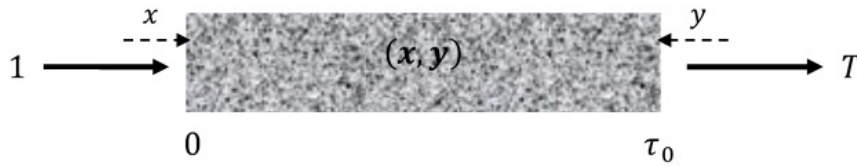


Figure 5: Physical meaning of Linear Image $T(x, y, \tau_0)$

The linear image $T(\xi, \tau_0)$ has a clear physical meaning (Fig.5), namely it is the light transmission probability of the layer which has the "limiting" optical depth τ_0 (be relative to linear case, i.e. non-excited medium), whereas a single photon or unit beam of radiation falls on to one boundary of medium, but layer is continuously under the bilateral influence of external incident intensities (x, y) , respectively. Solution of nonlinear reflection-transmission problem can be written in terms of the linear image as

$$u(x, y) = y + (x - y) \cdot T(x + y), \quad (12)$$

note that $v(x, y) = u(y, x)$. So we see that the function $u(x, y)$ (or $v(x, y)$), which depends on two energy variables, can be expressed through the new axillary function $T(\xi)$ of only one variable $\xi \equiv x + y$.

4. Internal field solution as an inverse problem

Using the forms (11) and (12), we see that the solutions of both Cauchy problems (4) give us the same result (see also Pikichyan 2018)

$$I^+ = I^- + (x - y) \cdot T(x + y), \quad A \cdot (I^-)^2 + B \cdot I^- - C = 0, \quad (13)$$

where the coefficients and free member of the quadratic equation set forms ($\xi^\pm \equiv x \pm y$):

$$\begin{aligned} A &= b [\tau_0 + 2(1 + b\xi^+)], \quad B = \tau_0 + 2(1 + b\xi^+)(1 + b\xi^-), \\ C &= \tau_0(1 + bx)x - \tau(1 + b\xi^+)\xi^- + 2y(1 + bx)(1 + b\xi^+). \end{aligned} \quad (14)$$

Physical solution of the quadratic equation corresponds to a positive sign of the discriminant of the quadratic Trinomial in (13), because it satisfies the linear limit of the problem. Linear task formally corresponds to $b \equiv 0$.

Thus, the functional equation of ‘‘Ambartsumian’s complete invariance’’ (8) was derived from principle of invariance for determination of outgoing radiation $u(x, y, \tau_0)$. The last one is then transformed to (10) for LI $T(\xi, \tau_0)$, which is solved analytically (11). Solution of ‘‘reflection-transmission’’ problem in explicit elementary form (12) was obtained through the LI. Presence of this solution is now a sufficient condition to formulate the Cauchy problem (4), which can be solved analytically in order to ‘‘restore’’ a radiation field inside the medium (13). Thus, the sequence for final determination of unknown quantities is ($\xi \equiv x + y$)

$$T(\xi, \tau_0) \rightarrow u(x, y, \tau_0) \rightarrow I^\pm(\tau, x, y, \tau_0). \quad (15)$$

5. Internal field solution as a direct problem

Implications of the concept of LI and formulas (11), (12) in the system (5) for the solution of direct problem give the form

$$\begin{cases} (1 + q_\tau bx)(I^+ - I^-) + (I^- \cdot I^+)q_\tau b = -q_\tau I^- + (1 + bx)q_\tau x \\ (1 + q_{\tau_0 - \tau} by)(I^+ - I^-) - (I^+ \cdot I^-)q_{\tau_0 - \tau} b = q_{\tau_0 - \tau} I^+ - (1 + by)q_{\tau_0 - \tau} y \end{cases}, \quad (16)$$

where the value $q_\beta = 2/(\beta + 2)$ is the solution of the linear transmission problem for the layer $[0, \beta]$. Solution of this algebraic system leads to the same expressions (13), which we have already obtained in the inverse problem.

6. Plot illustrations

Below we bring three diagrams of diffuse radiation field intensity dependence of increase of intensity of external radiation (in all calculations conventionally $b \equiv 1$). Fig. 6 shows the change of the unit beam intensity which is passing through the medium of given optical thickness, while the total exciting power of external radiation increases. Here the initial value ($\xi=0$) of transmitted radiation corresponds to the linear

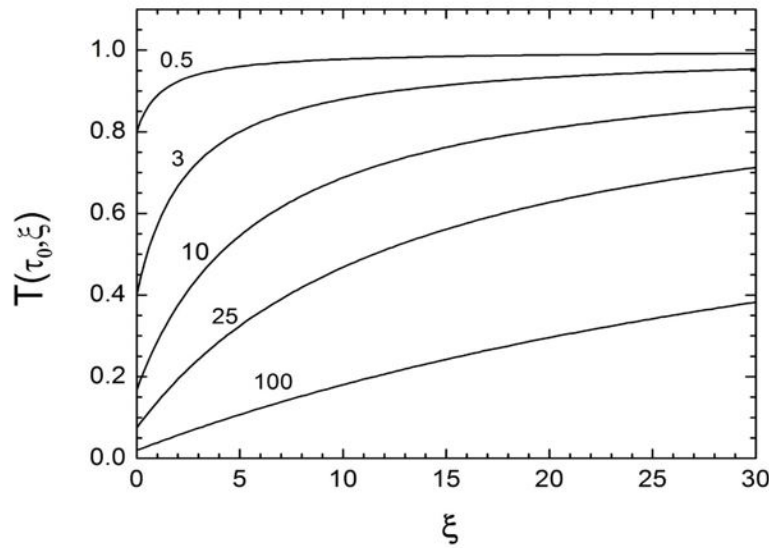


Figure 6: Evolution of medium transmittance $T(\xi, \tau_0)$.

case, i. e. it refers to an unexcited medium. During growth of excitation level ($\xi \rightarrow \infty$), the transmittance of medium increases (Ambartsumian 1964b) and it becomes more enlightened up to achieve the level of full transparency

$$\lim_{\xi \rightarrow \infty} T(\xi, \tau_0) \rightarrow 1 \quad (17)$$

Fig.7 shows the dependence of the transmitted radiation $u(x, y, \tau_0)$ of growth of right-hand external irradiation y , while $x = 2$, $\tau_0 = 1$ and $\tau_0 = 10$.

The solid curves correspond to nonlinear case, and the dotted curves represent the solutions of linear problem. In comparison with linear case, an increase of radiation field in nonlinear theory is more slowly, because of medium enlightenment phenomena (Ambartsumian 1964b). The deviation between the curves of linear and non-linear tasks continuously increases.

The same, but on a larger scale we see on curves of internal field problem. The Fig.8 shows the progress of the internal field intensity $I^\pm(\tau, x, y, \tau_0)$ in dependence on growth of external radiation, with $\tau = 0.5$ and $\tau_0 = 1$, while

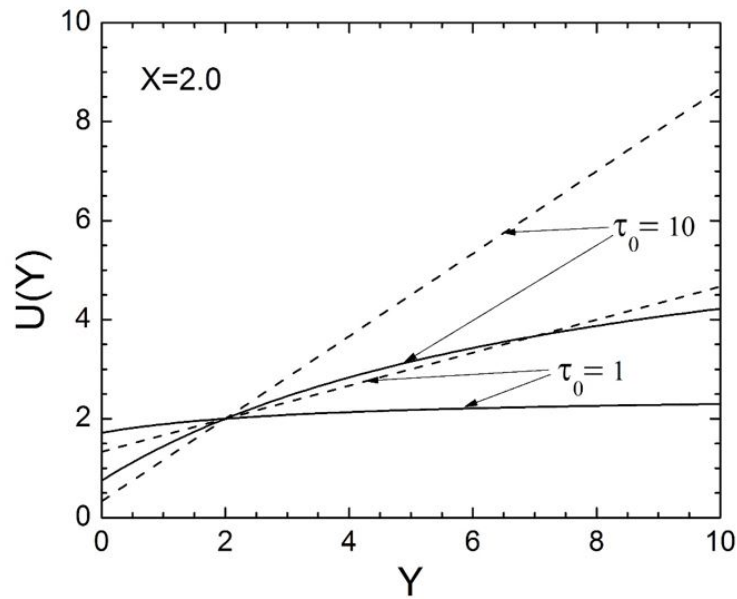


Figure 7: The progress of transmitted radiation $u(x,y,\tau_0)$

$x = y$ (i.e. in the middle of medium of unit optical thickness), when both external boundaries of the slab irradiated with the same value of beams.

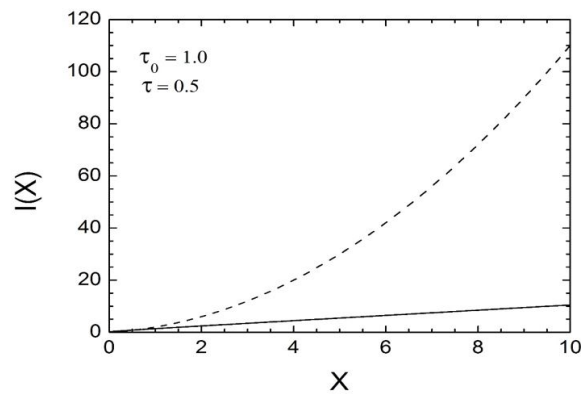


Figure 8: Behavior of internal radiation field $I^\pm(\tau, x, y, \tau_0)$.

7. Concluding remarks

In this report, we further expose on the simple example the assertions made in non-linear problem:

- 1) A definition of linear structures in the solution of nonlinear problem

of radiative transfer by means of a concept of “linear images” presents a good opportunity for simplification of the solutions of the problems of inverse or direct formulations. In some simple cases, the solution may be brought up to an explicit analytic form.

- 2) When analyzing the fields of diffuse radiation only by means of linear problems of multiple scattering, there is a deficiency of over-estimate of values of real fields of the diffuse radiation, as well as the optical parameters of the medium, even in case of relatively small values of external excitation fields.

References

- Ambartsumian V. A. 1944, *Trans. Armenian Acad. Sci. (Izv. Acad. Nauk Arm. SSR, estestv. nauki)*, №1-2, 31-36, (in Russian).
- Ambartsumian V.A. 1964a, *Proc. Armenian Acad. Sci. (Dokl. Acad. Nauk Arm. SSR)*, 38, №4, 225-230, (in Russian).
- Ambartsumian V. A. 1964b, *Proc. Armenian Acad. Sci. (Dokl. Acad. Nauk Arm. SSR)*, 39, №3, 159-165, (in Russian).
- Bellman R., Kalaba R., Wing M. 1960, *Proc. Nat. Acad. Sci. USA*, 46, 1646-1649.
- Ivanov V. V. 1969, *Radiative Transfer and Spectra of Celestial Bodies*, Science, M., 472 p. (in Russian).
- Pikichyan H. V. 2010, *Astrofizika*, 53, 285-299, 2010 (in Russian); English edition: *Astrophysics*, 53, 251-267.
- Pikichyan H. V. 2014, pp. 48-49, in: *Book of abstracts “5-th Russian-Armenian Conference on mathematical physics, complex analysis and related issues”* (Sept.28- Oct.3, 2014, Yerevan, Armenia), Publ. NAN RA, Yerevan, 56 p. (in Russian).
- Pikichyan H. V. 2016, *JQSRT*, 183, pp.113-127.
- Pikichyan H. V. 2018, pp. 64-67, in.: *Thesis book of “7-th Russian-Armenian Conference on mathematical physics, complex analysis and related issues”* (9-15 Sept. 2018, Yerevan, Armenia), Publ. house “Githyun” of NAS RA, Yerevan, 84 p. (in Russian).

Hybrid modeling of diffusive shock acceleration in collisionless shocks in multispecies plasma.

J. A. Kropotina^{1,2*}, A. M. Bykov^{1,2}, V. E. Ermolina¹, S. M. Osipov²,
V. I. Romansky²

¹ *Peter the Great St. Petersburg Polytechnic University (SPbPU), Russia*

² *Ioffe Institute, Russia*

* *E-mail: juliett.k@gmail.com*

Abstract

Diffusive shock acceleration (DSA) is a very efficient mechanism of high energy particle acceleration in heliosphere, supernova remnants, stellar winds and gamma-ray bursts. We present microscopic simulation of particle injection and diffusive shock acceleration which is performed with 3D divergence-conserving second-order accurate hybrid code “Maximus”. Hydrogen plasma with admixture of various heavy ions is considered. The injection process is found to start through shock reflection for both hydrogen and heavier ions. However, the reflection process depends on charge-to-mass ratio. While hydrogen ions reflection appears at shock ramp and is governed by the cross-shock potential, the reflection of ions with greater A/Z proceeds deeper downstream via gyration in perpendicular magnetic field component. The heavy ions appear to inject into the DSA preferentially, but this chemical enhancement saturates with growing A/Z . The protons injection efficiency is estimated within various approaches, and it is shown that about 20% of initial flow energy goes into accelerated particles.

Keywords: *Cosmic Rays - Diffusive Shock Acceleration - injection.*

1. Introduction

The Cosmic Rays (CR) – extremely energetic space particles – are observed both directly in the vicinity of the Earth and via X-ray and gamma-ray observations in distant sources (See, e.g., Aharonian et al. 2012). The latter observations confirm that the Supernova Remnant (SNR) shocks are effective CR accelerators and can be considered as the major Galactic CR sources. The other astrophysical collisionless shocks can effectively accelerate particles as well. The main mechanism proposed for this process is DSA

(first order Fermi mechanism), which consists of particles multiple reflection upstream and downstream of the shock. This process leads to constant energy gain of particles and the formation of the power law spectrum with depending on shock compression (Bell 1978).

The details of the DSA process are extensively studied in the last decades (see, e.g., Caprioli & Spitkovsky 2014, Sundberg et al. 2015), mostly by means of numerical modeling. Particularly, the special attention is paid to the investigation of injection and acceleration of ions heavier than protons (see, e.g., Caprioli et al. 2017). The detailed investigation of this topic can help to resolve the kinetics of heavy ions in collisionless shocks, estimate the fluxes of accelerated heavy ions from supernova shocks and, therefore, better understand the observed anomalies in cosmic rays composition. The existing works (Caprioli et al. 2017, Hanush et al. 2017, 2018) confirm the preferential injection of ions with high mass-to-charge ratio, but do not show consistency in dependency of the injection enhancement on A/Z . Also the individual heavy ions trajectories and kinetics were not addressed yet. So in the current paper the results of (Caprioli et al. 2017) are extended to the heavy weakly charged elements, and the saturation of the injection enhancement with growing A/Z , in consistency with (Hanush et al 2017, 2018), is shown.

Also the analyses of individual particles trajectories are performed, revealing a slightly different injection mechanism for the ions with high A/Z . The multispecies collisionless shock is simulated by means of the 3d second order accurate divergence-conserving hybrid code “Maximus” (Kropotina et al. 2018). Such type of codes is well suited for kinetic simulations of ion-governed processes (see, e.g., Winske 1985).

The overall cosmic rays acceleration efficiency, defined as the fraction of bulk kinetic energy going into accelerated particles, is also of special interest. This parameter plays a crucial role, e.g., in simulations of stars and galaxies formation and evolution. So the new technique of CR acceleration efficiency is proposed, revealing nearly 20% efficiency of bulk kinetic energy conversion to energetic particles.

2. Simulation

Collisionless shock simulation was performed with the three-dimensional second-order accurate divergence-conserving hybrid code “Maximus” (Kropotina et al. 2018). The dimensionless quantities, measured in units of the far upstream proton inertial length (l_i), gyrofrequency (Ω_i), alfvénic velocity (V_a) and plasma density, were introduced. Shock was initialized via the wall reflection of the super-alfvénic flow moving in negative x direction (the so-called rigid piston method). The initially uniform magnetic field was inclined by $\theta = 10^\circ$ to the shock normal (the quasi-parallel configuration is

believed to be optimal for the effective DSA process (Caprioli & Spitkovsky 2014)). Shock parameters, characteristic for the supernova remnant forward shocks, were chosen: the initial flow afvenic Mach number $Ma=10$ (in the downstream frame), the upstream ratio of thermal to magnetic pressure $\beta = 1.0$. The hydrogen plasma with negligible admixture of various heavy ions (namely He(+2), He(+1), C(+3), C(+2), C(+1), O(+1)) was considered. Simulation was performed in 2d rectangular box of size $40000 \times 1 \times 100$ proton inertial lengths until time $T = 2800\Omega_i^{-1}$. So long time ensured that the DSA spectrum completely formed for most ions.

3. Heavy ions injection enhancement

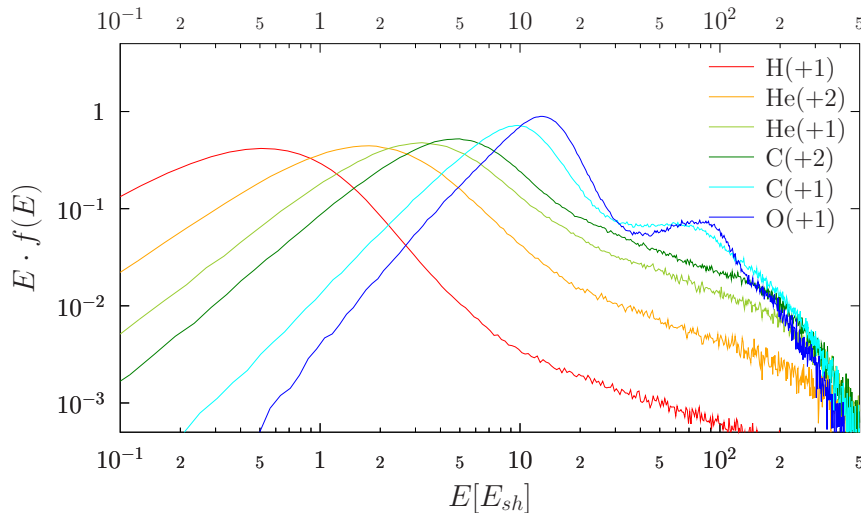


Figure 1: Various ions energy spectra far downstream of the shock with $M_a = 10$, $\theta = 10^\circ$, $\beta = 1$

The resulting far downstream ions spectra are shown in fig. 1. The distribution functions of various sorts are normalized by unit to compare injection efficiency. The maxwellian core and nonthermal power law parts of the spectrum are clearly distinguishable for all sorts. However, it should be noted that the most heavy and weakly charged ions (C(+1) and O(+1)) still show prominent deviations from both maxwellian distribution in the low-energy part and simple power-law at high energies. This behaviour just reflects the fact that all processes with such ions are much slower than those for the protons, and they have not relaxed to the steady distributions yet. Some ions with smaller A/Z (C(+3), C(+2)) showed similar features at ear-

lier times, so C(+1) and O(+1) are expected to relax later.

The chemical enhancement (growth of the power law normalization with A/Z) can be seen. This effect was first shown by Caprioli et al. 2017, where authors considered sorts with A/Z up to 8 and proposed linear growth of the enhancement with A/Z . At the same time the 1d simulations in Hanush et al. 2018 showed the saturation and further decrease of the chemical enhancement for $A/Z > 8$. The latter results are confirmed by our two dimensional model.

4. Ions injection process

In previous works (Caprioli & Spitkovsky 2014, Caprioli et al. 2015) the protons injection process was studied by means of individual particle trajectories analyses. The general conclusion was that the injection into the DSA process proceeds via reflection of a fraction of bulk particles during the first shock encounter. After that the reflected ions enter the shock drift acceleration (SDA) process, when they move along the electric field in the shock surface and gain sufficient energy to eventually escape upstream and enter the DSA. In current work the trajectories of accelerated heavy ions were analysed as well, showing that the principal injection mechanism remains the same for all sorts. At the same time, the injection details differ for ions with high A/Z .

Fig. 2 shows the phase space trajectories of accelerated particles at times

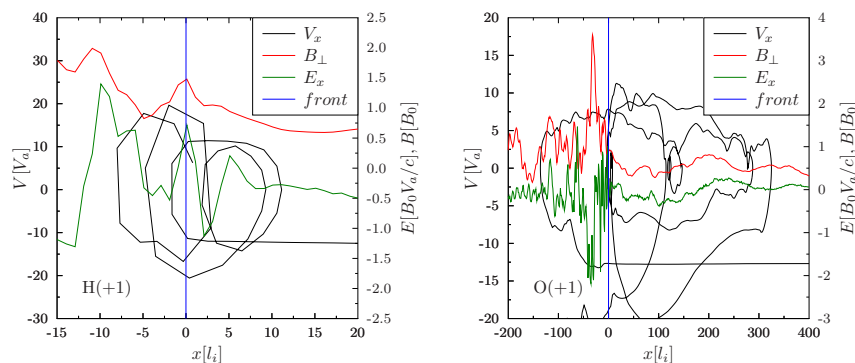


Figure 2: Trajectories of the accelerated protons and O(+1) ions in the same shock (the corresponding electromagnetic fields are shown for clarity).

close to their first front reflection. The corresponding perpendicular magnetic field and parallel electric field are shown in the same figure (right

axes). From the left panel it is clear that the reflection point of hydrogen ions coincides with both B_{\perp} and E_x maxima. This means that the shock transition is governed by the protons reflection and in turn tuned for it. It is actually hard to distinguish the which reason leads to the protons reflection – locally perpendicular magnetic field or cross-shock potential, as they operate together.

5. Injection efficiency

The ion injection efficiency can be estimated in various ways. The first one considers just the normalization of the power law tail (Caprioli et al. 2017, Hanush et al. 2017, 2018). However, it does not illustrate the percent of bulk energy going into the accelerated particles. The second way suggests to simply take a ratio of the downstream energy density (or pressure) in the non-thermal part of the spectrum to the total one. This means just an integration of $E \cdot f(E)$ (see fig. 1) from some arbitrary chosen threshold to the maximum energy. However, the downstream distribution function evolves with time, and the power-law tail grows, which means that the estimated injection efficiency grows as well and is limited only by the system size. Moreover, this method does not take into account those accelerated particles which currently reside in the upstream region. In the current paper we suggest a self-consistent way of estimating the injection efficiency from the hybrid simulations. To do it the time evolution of the energy in particles with $E > E_0 = 10E_{sh}$ and of the total kinetic energy is calculated at each time step. Both appear to grow up nearly linearly after $t \approx 100\Omega_i^{-1}$. This means that their averaged slopes ratio is constant in time and can be treated as the ions injection efficiency. For the considered shock its value corresponded to about 20%. The same value can be obtained from the approximate downstream temperature, which appears to be about 75-80% of that expected from the Hugonio relations. This means that the rest of the energy came into magnetic field amplification (which usually takes about a few percent) and CR acceleration.

6. Summary

The hybrid code “Maximus” was used to simulate collisionless shocks in hydrogen plasma with the admixture of various heavy ions. The injection process was found to start through the shock reflection for both hydrogen and heavier ions. However, while hydrogen ions reflection appears at shock ramp and is governed by the cross-shock potential, the reflection of ions with greater A/Z proceeds deeper downstream via gyration in perpendicular magnetic field component. The heavy ions appear to inject into the DSA preferentially, but this chemical enhancement saturates with growing A/Z .

The protons injection efficiency is estimated within various approaches, and it is shown that about 20% of initial flow energy goes into accelerated particles.

Acknowledgements

The reported study was funded by RFBR according to the research project 18-32-00158

References

- Aharonian F., Bykov A., Etienne P. et al. 2012, SSR 166, 97
Bell, A. R. 1978, MNRAS 182, 147
Caprioli D., Pop A.-R., Spitkovsky, A. 2015, ApJL 798, L28R
Caprioli D., Spitkovsky A. 2014, ApJ 783, 2, 783:91
Caprioli D., Yi D.T., Spitkovsky A. 2017, Physical Review Letters 119, 171101
Hanusch A., Liseykina T., Malkov M. 2017, 35th International Cosmic Ray Conference, 10-20 July, Bexco, Busan, Korea
Hanusch A., Liseykina T., Malkov M. 2018, ArXiv:1803.00428v1
Kropotina J. A., Bykov A.M., Krassiltchikov A.M., Levenfish K.P. 2018, Communications in Computer and Information Science, in press Winske D. 1985, SSR 42, 53
Caprioli D., Pop A.-R., Spitkovsky, A. 2015, ApJL 798, L28R
Sundberg T., Haynes C.T., Burgess D., Mazelle C. X. 2015, ApJ 820, 1, 21

The impact of spiral density waves on the star formation distribution: a view from core-collapse supernovae

A. G. Karapetyan^{1*}, A. A. Hakobyan^{1*}, L. V. Barkhudaryan¹,
G. A. Maion², D. Kunth², V. Adibekyan³, M. Turatto⁴

¹*Byurakan Astrophysical Observatory, Armenia*

²*Institut d'Astrophysique de Paris, France*

³*Instituto de Astrofísica e Ciência do Espaço, Universidade do Porto, Portugal*

⁴*Osservatorio Astronomico di Padova, Italy*

**E-mail: karapetyan@bao.sci.am (AGK); hakobyan@bao.sci.am (AAH)*

Abstract

We present an analysis of the impact of spiral density waves (DWs) on the radial and surface density distributions of core-collapse (CC) supernovae (SNe) in host galaxies with different arm classes. For the first time, we show that the corotation radius normalized surface density distribution of CC SNe (tracers of massive star formation) indicates a dip at corotation in long-armed grand-design (LGD) galaxies. The high SNe surface density just inside and outside corotation may be the sign of triggered massive star formation by the DWs. Our results may support the large-scale shock scenario induced by spiral DWs in LGD galaxies, which predicts a higher star formation efficiency around the shock fronts, avoiding the corotation region.

Keywords: *supernovae: general - galaxies: kinematics and dynamics - galaxies: spiral - galaxies: star formation - galaxies: structure.*

1. Introduction

According to the pioneering work of Lin & Shu (1964), semi-permanent spiral patterns especially in grand-design (GD) galaxies, i.e. spiral galaxies with prominent and well-defined spiral arms, are created by long-lived quasi-stationary density waves (DWs). The results of many observational studies are consistent with the picture where the DWs generate large-scale shocks and trigger star formation, as originally proposed by Roberts (1969), causing massive star formation to occur by compressing gas clouds as they pass

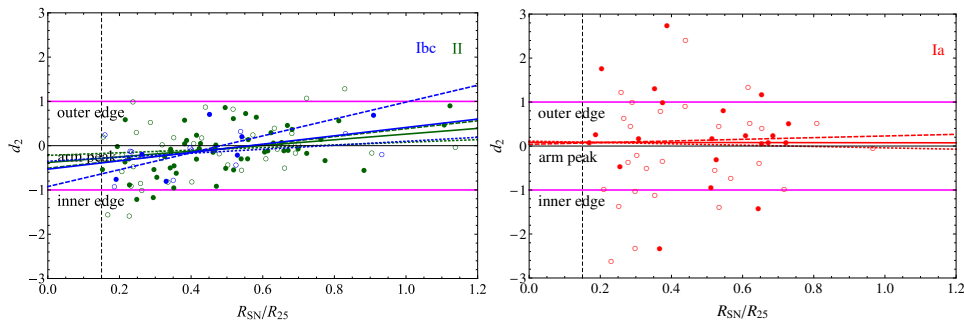


Figure 1: Distributions of the d_2 distances of Types Ibc (blue), II (green) and Ia (red) SNe relative to the peaks of spiral arms (normalized to the arm semi-width) versus the deprojected and normalized galactocentric distance (R_{SN}/R_{25}). Filled and open circles respectively show SNe in GD and NGD galaxies. In all figures, the linear fits are given for the full (solid), GD (dashed), and NGD (dotted) samples. The inner and outer edges, as well the peaks of spiral arms are shown with parallel lines. Because of the selection effect near the center of host galaxies, the region to radius $R_{\text{SN}}/R_{25} = 0.15$ (dashed vertical line) is excluded. This figure is from Aramyan et al (2016), the reader is referred to the original paper for more details.

through the spiral arms of GD galaxies (e.g. Cepa & Beckman 1990; Knapen et al. 1996; Seigar & James 2002; Grosbøl & Dottori 2009; Martínez-García et al. 2009; Cedrés et al. 2013; Pour-Imani et al. 2016; Shabani et al. 2018).

In this contribution to the international conference “*Instability Phenomena and Evolution of the Universe*” dedicated to V. Ambartsumian’s 110th anniversary (Yerevan-Byurakan, Armenia, 17-21 Sep, 2018), we briefly present the results of Karapetyan et al. (2018) on the possible impact of spiral DWs (triggering effect) on the distribution of supernovae (SNe) in discs of host galaxies, when viewing in the light of different nature of Type Ia and core-collapse (CC; Types Ibc and II) SNe progenitors, i.e. less-massive/longer-lived and massive/short-lived stars, respectively.

Although based on small number statistics, the early attempts to study the distribution of CC SNe within the framework of DW theory were performed by Moore (1973); McMillan & Ciardullo (1996) and Mikhailova et al. (2007). In our recent paper (Aramyan et al. 2016), we studied the distribution of 215 SNe relative to the spiral arms of their GD and non-GD (NGD)¹ host galaxies, using the Sloan Digital Sky Survey (SDSS) images. We found that the distribution of CC SNe (i.e. tracers of recent star formation) is affected by the spiral DWs in their host GD galaxies, being distributed closer to the corresponding edges of spiral arms where large-scale shocks, thus star formation triggering, are expected (Fig. 1). Such an effect was not observed

¹These galaxies with flocculent arms appear to lack global DWs, instead their spirals may be sheared self-propagating star formation regions (see review by Buta 2013, and references therein).

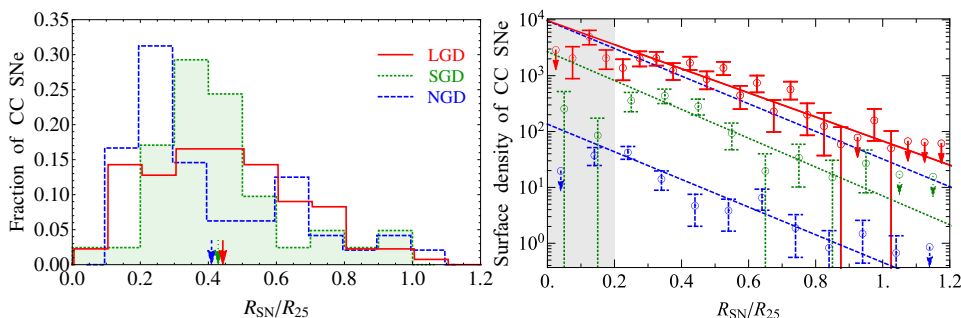


Figure 2: *Left panel:* distributions of deprojected and normalized galactocentric radii (R_{SN}/R_{25}) of CC SNe in LGD (red solid), SGD (green dotted), and NGD (blue dashed) host galaxies. The mean values of the distributions are shown by arrows. *Right panel:* surface density distributions of CC SNe in the mentioned hosts. The fitted exponential surface density profiles are estimated for the inner-truncated discs (outside the shaded area). For better visibility, the distributions and profiles are shifted vertically sorted by increasing the mean R_{SN}/R_{25} as one moves upwards, and also slightly shifted horizontally. To visually compare the distribution of CC SNe in LGD hosts with the fitted profile in NGD galaxies, the latter is also positioned with the central surface density matched with that in LGD hosts. This figure is from Karapetyan et al. (2018), the reader is referred to the original paper for more details.

for Type Ia SNe (less-massive and longer-lived progenitors) in GD galaxies, as well as for both types of SNe in NGD hosts (Fig. 1).

In Karapetyan et al. (2018), we expanded our previous work, and for the first time checked the triggering effect at different galactocentric radii and studied the consistency of the surface density distribution of SNe (normalized to the optical radii $[R_{25}]^2$, and for a smaller sample also to corotation radii $[R_C]$ of hosts) with an exponential profile in unbarred GD and NGD galaxies.

2. The sample

From the coverage of SDSS Data Release 13 (Albaret et al. 2017), we used a well-defined and homogeneous sample of SN host galaxies (Hakobyan et al. 2012, 2014, 2016) with different spiral arm classes according to the classification scheme by Elmegreen & Elmegreen (1987). The sample consists of 269 relatively nearby (≤ 150 Mpc), low-inclination ($i \leq 60^\circ$), morphologically non-disturbed and unbarred Sa–Sc galaxies, hosting 333 SNe in total. In addition, we performed an extensive literature search for corotation radii, collecting data for 30 host galaxies with 56 SNe. For more details of sample selection and reduction, the reader is referred to Karapetyan et al. (2018).

²The R_{25} is the SDSS g -band 25th magnitude isophotal semimajor axis of galaxy.

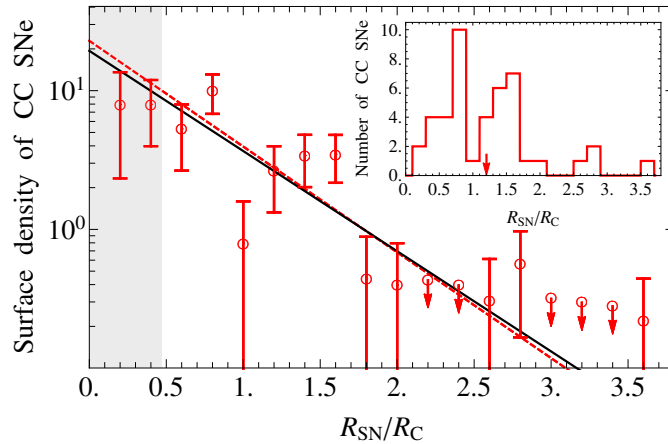


Figure 3: R_C -normalized surface density profile of CC SNe in LGD host galaxies. The black solid and red dashed lines are the best maximum-likelihood fits of global and inner-truncated (from 0.48 corotation radii outwards to avoid the obscured inner region [grey shaded]) exponential surface density models, respectively. The inset presents the histogram of SN radii (the mean value is shown by arrow). This figure is from Karapetyan et al. (2018), the reader is referred to the original paper for more details.

3. Summary of the results and conclusions

The main results and conclusions concerning the deprojected and inner-truncated ($R_{\text{SN}}/R_{25} \geq 0.2$) distributions of SNe in host galactic discs are the following:

- 1) We found no statistical differences between the pairs of the R_{25} -normalized radial distributions of Type Ia and CC SNe in discs of host galaxies with different spiral arm classes, with only one significant exception: CC SNe in long-armed GD (LGD)³ and NGD galaxies have significantly different radius distributions. The radial distribution of CC SNe in NGDs is concentrated to the centre of galaxies with relatively narrow peak and fast exponential decline at the outer region, while the distribution of CC SNe in LGD galaxies has a broader peak, shifted to the outer region of the discs (left panel of Fig. 2). The distribution of SNe in short-armed GD (SGD)⁴ hosts appears to be intermediate between those in NGD and LGD galaxies.
- 2) The surface density distributions of Type Ia and CC SNe in most of the

³The underlying mechanism that explains the lengths of arms and their global symmetry in these galaxies is most probably a DW, dominating the entire optical disc (e.g. Elmegreen et al. 1992).

⁴The short inner symmetric arms in these galaxies might be explained by the DW mechanism, dominating only in the inner part of the optical disc (e.g. Elmegreen et al. 1992).

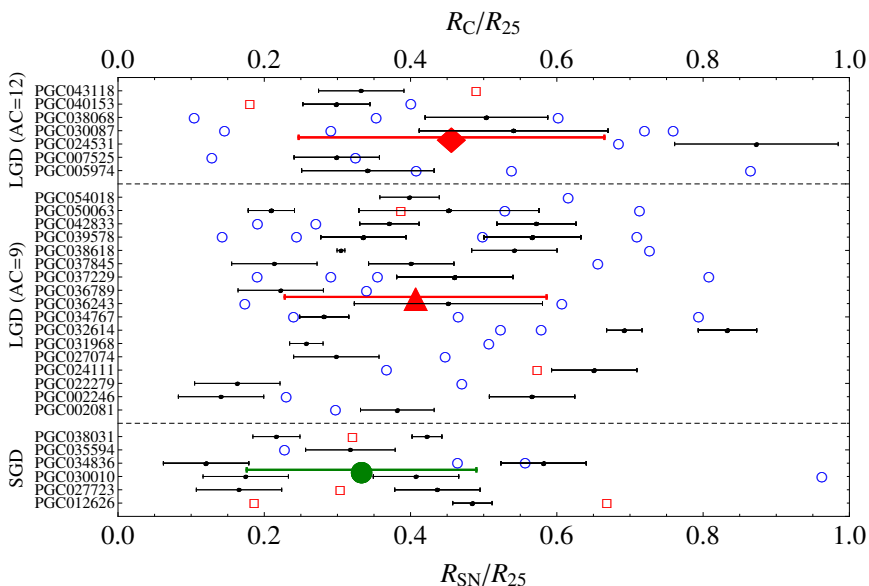


Figure 4: Galactocentric positions of normalized corotation radii (black points) with their errors for SNe host galaxies. SGD and LGD galaxies are separated by horizontal dashed lines. The spiral arm classes (ACs) of host galaxies correspond to the classification by Elmegreen & Elmegreen (1987). The filled diamond, triangle, and circle are the corresponding mean values of the corotation radii (with their standard deviations). For each host galaxy, galactocentric positions of Type Ia (red empty squares) and CC (blue empty circles) SNe are also presented. This figure is from Karapetyan et al. (2018), the reader is referred to the original paper for more details.

subsamples are consistent with the exponential profiles (e.g. van den Bergh 1997; Wang et al. 2010; Hakobyan et al. 2009, 2016). Only the distribution of CC SNe in LGD galaxies appears to be inconsistent with an exponential profile, being marginally higher at $0.4 \lesssim R_{\text{SN}}/R_{25} \lesssim 0.7$ (right panel of Fig. 2). The inconsistency becomes more evident when comparing the same distribution with the scaled exponential profile of CC SNe in NGD galaxies (upper blue dashed line in the right panel of Fig. 2).

- 3) Using a smaller sample of LGD galaxies with estimated corotation radii, we showed, for the first time, that the surface density distribution of CC SNe shows a dip at corotation, and enhancements at ${}^{+0.5}_{-0.2}$ corotation radii around it (Fig. 3). However, these features are not statistically significant. The CC SNe enhancements around corotation may, if confirmed with larger samples, indicate that massive star formation is triggered by the DWs in LGD host galaxies. Considering that the different LGD host galaxies have various corotation radii (Fig. 4) distributed around the mean value of $\langle R_{\text{C}}/R_{25} \rangle = 0.42 \pm 0.18$,

the radii of triggered star formation by DWs are most probably blurred within a radial region including ~ 0.4 to ~ 0.7 range in units of R_{25} , without a prominent drop in the mean corotation region (right panel of Fig. 2).

These results for CC SNe in LGD galaxies may, if confirmed with larger samples and better corotation estimates, support the large-scale shock scenario (e.g. Moore 1973), originally proposed by Roberts (1969), which predicts a higher star formation efficiency, avoiding the corotation region (e.g. Cepa & Beckman 1990; Seigar & James 2002; Cedrés et al. 2013; Aramyan et al. 2016).

When more information will become available on corotation radii of SN host galaxies, it would be worthwhile to extend our study, by comparing the R_C -normalized radial and surface density distributions of Type Ia and CC SNe in LGD galaxies. This will also allow to check the impact of spiral DWs on the distribution of less-massive and longer-lived progenitors of Type Ia SNe. Moreover, similar analysis of SNe in SGD galaxies can help to understand the role of DWs in star formation triggering, if any.

Acknowledgements

This work was supported by the RA MES State Committee of Science, in the frames of the research project number 15T-1C129. This work was made possible in part by a research grant from the Armenian National Science and Education Fund (ANSEF) based in New York, USA.

References

- Albaret, F. D., Allende Prieto, C., Almeida, A., et al. 2017, *ApJS*, 233, 25
Aramyan, L. S., Hakobyan, A. A., Petrosian, A. R., et al. 2016, *MNRAS*, 459, 3130
Buta, R. J. 2013, in Oswalt T. D., Keel W. C., eds, *Planets, Stars and Stellar Systems*, 6, 1
Cedrés, B., Cepa, J., Bongiovanni, A., et al. 2013, *A&A*, 560, A59
Cepa, J., & Beckman, J. E. 1990, *ApJ*, 349, 497
Elmegreen, B. G., Elmegreen, D. M., & Montenegro, L. 1992, *ApJS*, 79, 37
Elmegreen, D. M., & Elmegreen, B. G. 1987, *ApJ*, 314, 3
Grosbøl, P., & Dottori, H. 2009, *A&A*, 499, L21
Hakobyan, A. A., Adibekyan, V. Z., Aramyan, L. S., et al. 2012, *A&A*, 544, A81
Hakobyan, A. A., Karapetyan, A. G., Barkhudaryan, L. V., et al. 2016, *MNRAS*, 456, 2848
Hakobyan, A. A., Mamon, G. A., Petrosian, A. R., et al. 2009, *A&A*, 508, 1259
Hakobyan, A. A., Nazaryan, T. A., Adibekyan, V. Z., et al. 2014, *MNRAS*, 444, 2428
Karapetyan, A. G., Hakobyan, A. A., Barkhudaryan, L. V., et al. 2018, *MNRAS*, 481, 566
Knapen, J. H., Beckman, J. E., Cepa, J., & Nakai, N. 1996, *A&A*, 308, 27
Lin, C. C., & Shu, F. H. 1964, *ApJ*, 140, 646
Martínez-García, E. E., González-Lópezlira, R. A., & Bruzual-A, G. 2009, *ApJ*, 694, 512
McMillan, R. J., & Ciardullo, R. 1996, *ApJ*, 473, 707
Mikhailova, G. A., Bartunov, O. S., & Tsvetkov, D. Y. 2007, *Astronomy Letters*, 33, 715
Moore, E. 1973, *PASP*, 85, 564
Pour-Imani, H., Kenefick, D., Kenefick, J., et al. 2016, *ApJL*, 827, L2
Roberts, W. W. 1969, *ApJ*, 158, 123
Seigar, M. S., & James, P. A. 2002, *MNRAS*, 337, 1113
Shabani, F., Grebel, E. K., Pasquali, A., et al. 2018, *MNRAS*, 478, 3590
van den Bergh, S. 1997, *AJ*, 113, 197
Wang, J., Deng, J. S., & Wei, J. Y. 2010, *MNRAS*, 405, 2529

Number Count of MRS Galaxies in the J, H, K Bands

S. Arbabi Bidgoli^{1*}, M. Rah^{2†}, A. Yousefi-Sostani^{3‡}

¹*Department of Physics, Faculty of Science, Qom University of Technology(QUT), Qom, Iran*

²*Research Institute for Astronomy & Astrophysics of Maragha (RIAAM)-Maragha, IRAN,
P.O.Box: 55134-441*

³*Shahid Department of Physics(SBU), Shahid Beheshti University, G.C., Evin, Tehran 19839,
Iran*

**E-mail: arbabi@qut.ac.ir*

†E-mail: mariarah.astro@gmail.com

‡E-mail: a.yousefisostani@mail.sbu.ac.ir

Abstract

The Copernican principle has been the motivation for the present study on the number density of galaxies. In this work we have carried out a number count of galaxies in the 2MRS catalog in the K, H and J bands. The results presented here have obtained on volume-limited samples with equal widths or redshift bins. The main result of this study is the number count of galaxies which have been plotted in concentric spherical shells with the observer at the center. The obtained result in the three bands show a similar behavior up to a distance of 1.7×10^2 Mpc and behave differently from there on.

Keywords: *Number Count - J, H, K Band - 2Mass Redshift Survey - Copernicious Principal.*

1 Introduction

The Copernican principle states that the Earth is not at a preferred position in the universe, thus one might study if observational data are consistent with this assumption? The importance of the principle is closely connected to the Cosmological principle, stating that the universe must be homogeneous and isotropic. In recent years many authors have discussed the question if the principle holds, cf. (Labini 2010; Jia et al. 2008; Uzan 2009; Uzan et al. 2008; Caldwell et al. 2008; February et al. 2013) .However they have not explicitly studied whether the Copernican principle stands up to observational tests.

2 The Database

We chose the 2MRS (2Mass Redshift Survey) for the purpose of our study. This catalog is currently one of the most comprehensive surveys of the galaxies, which has been compiled in the near infrared. For the completion of this survey, the spectra of some of the around a million galaxies of the original 2Mass (2 Micron All Sky Survey) have been taken, and the recession velocity has been measured at three wavelengths, (J $1.24 \mu m$), (H $1.66 \mu m$), (K_s $2.16 \mu m$). The resulting catalog, at which our study was aimed, comprises a number of 43533 galaxies, for each 25 parameters have been reported in the data. For our analysis the following parameters are relevant: Identity code, right ascension and declination, galactic coordinates, the photometric magnitude in the J, K, H bands together with their errors, galaxy type, redshift (or recession velocity) and its error. Other parameters such as distance, apparent magnitude, distance modulus, . . . for each galaxy have been calculated in the analysis, as detailed in the next section. (cf. Huchra et al. 2011; Tekhanovich et al. 2016)

3 Data analysis and calculations

In order to obtain the number counts and the corresponding number densities, we have assumed concentric circles with the Milky Way at the center. The spaces between two such spheres are consecutive spherical shells, defining the examination volumes. After applying the selection criteria, we have counted the galaxies in each spherical shell, determining the number density of the galaxy types at each distance. Thus in this section we describe how the calculations are made and the selection criteria are applied. Part 1 deals with the calculation of the distance, part 2 the volume, the volume-limiting schemes, and accordingly the denominator of the number counts. Part 3 describes the way the magnitude limits have been applied to calculate the numerator of the number counts and in part 4 the results and the diagrams are presented. (cf. Shafieloo et al. 2010; Stefanon et al. 2013)

3.1 Distances

Given the redshifts of each galaxy z , we require a relation to convert the redshifts to a distance, which we take from eq. 10 in Riess et al. 2004 and Bassett et al. 2015 as:

$$d_l(z) = \frac{cz}{H_0} \left[1 + \frac{1}{2}(1 - q_0)z - \frac{1}{6}(1 - q_0 - 3q_0^2 + j_0)z^2 + \mathcal{O}(z^3) \right] \quad (1)$$

Here H_0 and j_0 are the Hubble and the jerk parameters, respectively. Here the values $H_0 = 70.8 \text{ km.Mpc}^{-1}.s^{-1}$. and $j_0 = 1$ have been assumed according to Pop Lawski 2006. $\mathcal{O}(z^3)$ denotes terms of third and higher orders

in the Taylor expansion. q_0 is the deceleration parameter, determined by $\frac{1}{2}\Omega_m - \Omega_\Lambda$. The values which we have entered here are 0.6911 and 0.3089 (cf. Springel et al. 2006; Riess et al. 2004) and thus added two columns to the original catalog.

3.2 Volume

For the calculation of the number density as a fraction of number divided by volume, we need to subdivide the total volume according to distance of the farthest galaxy in the catalog. If we draw concentric spheres with the milky way at the center, each with a radius of ca. 12.7 *Mpc* larger than the previous one, there will be around 40 spheres up the furthest point. Then we take the volume between two consecutive spheres as a shell.

The shell volumes are calculated as:

$$V(spher) = V_s|_{d_2} - V_s|_{d_1} = \frac{4}{3}\pi d_1^3 - \frac{4}{3}\pi d_2^3. \quad (2)$$

The conic volumes which have to be excluded are:

$$V(roll) = \frac{(S|_{d_2} - S|_{d_1})}{2} \times (d_2 - d_1), \quad (3)$$

With $S_d = 2\pi d \times D$ and $D = \frac{d \times \theta''}{206205}$ finally giving:

$$V(\text{each } l) = V(spher)|_l - V(roll)|_l. \quad (4)$$

Taking into account the part of the sky obscured by dust in the Milky Way, the conic volume representing the zone of avoidance, and consequently, a conic section must be subtracted from each spherical shell. The subtracted conic sections and the distribution of the galaxies in declination and right ascension are shown in Figures 1 and 2 respectively. The volumes of the spherical shells takes into account the distances and the corresponding position angles of the galaxies.

3.3 Magnitudes

The number of galaxies in each shell represents the numerator of the number density fraction. Thus the number of the galaxies in each shell has to be normalized. The normalization is carried out by taking into account the magnitude limit as the criterion. For the determination of the critical magnitude limit in each shell, we take the galaxy with highest absolute magnitude and calculate the corresponding apparent magnitude by the relation:

$$m_k = M_k + 5 \log_{10}(d_l) + 25 + e_k \quad (5)$$

where e_k is error.

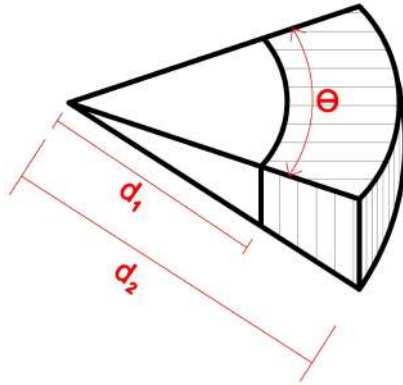


Figure 1: Volume determination

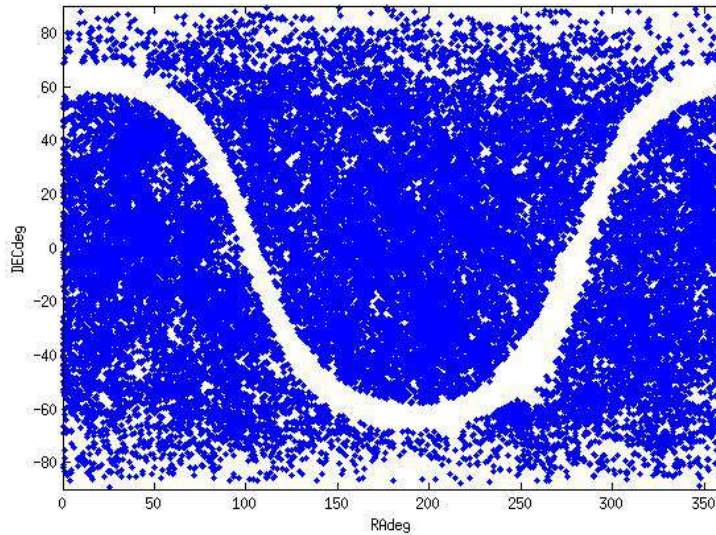


Figure 2: Angular distribution of galaxies

We take m_k as the as the critical magnitude limit of that shell Riess et al. 2004 . If a galaxy fulfills the condition $m_k < m_g$ the galaxy with the magnitude is kept and otherwise excluded. This procedure ensures that galaxies in each shell are selected with the same limit in absolute magnitude, in other words each shell is a volume-limited subsample. This procedure is repeated for all three wavelengths.

3.4 Results

We have obtained the number of galaxies in each shell according to the above described procedure separately. This procedure is repeated for all three wavelengths J, H, K. The number densities of each shell have been

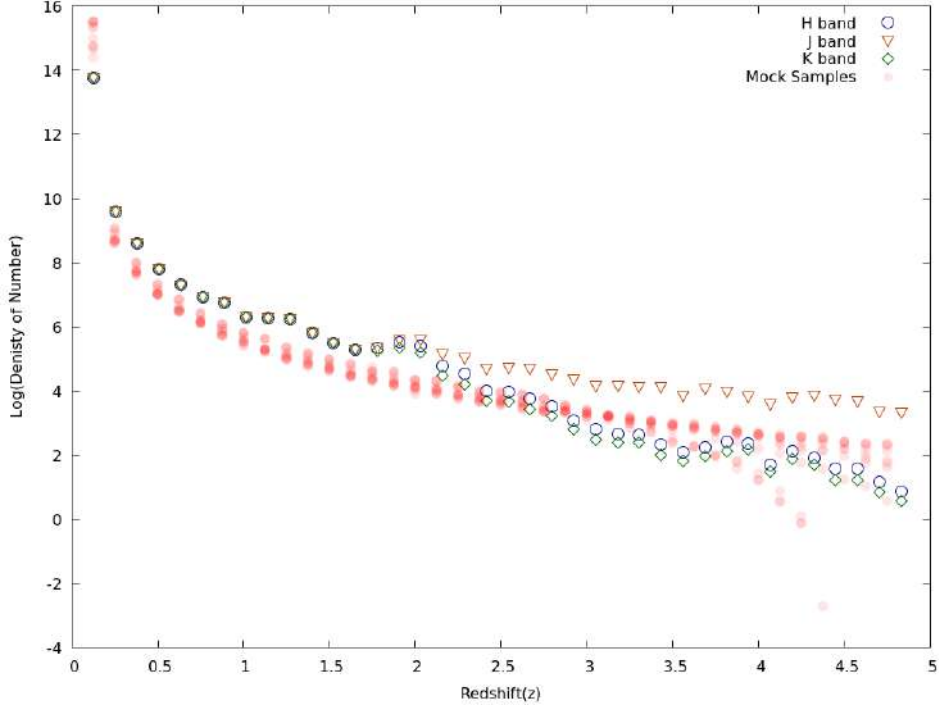


Figure 3: Density of Numeber in J, K, H Band and Mock Sapmples

plotted against the mean redshift of each shell in figure 3, and has been compared to corresponding mock distributions. The first step in the generation of mock samples is a 3 dimensional distribution of points with x, y, z coordinates between 0 and 1, which are created with a random number generator. On this basis we create a 3 dimensional map of mock galaxies, each with a right ascension, a declination and a luminosity. Different from the positions, the luminosities are generated with a distribution to comply with the Schechter function(cf. Singh et al 2016):

$$\Phi(M)dM = 0.4 \log(10) \Phi_* 10^{0.4(M_* - M)(\alpha - 1)} e^{-10^{0.4(M_* - M)}} dM \quad (6)$$

The normalization is:

$$\Phi_* = 0.002(h_{0.5})^3 Mpc^{-3} \pm 10\%$$

With the magnitude is:

$$M_* = -21.0 + 5 \log_{10}(h_{0.5}) \pm 0.25$$

And the slope parameter is:

$$\alpha = 1.20 \pm 0.1.$$

4 Conclusions and discussion

According to the results obtained in the three wavelengths as shown in figure 3 we conclude that this data may be used for the study of the Copernican principle. Such a study requires a comparison of real data from the 2MRS with repeatedly generated mock catalogs, with the same selection criteria as the observations. Mock catalogs can be designed conforming to the Copernican principle or to violate it in some certain predefined way. This study is currently underway.

Acknowledgement

The second author of this work, M.R. would like to thank RIAAM, because this work has been supported financially by Research Institute for Astronomy & Astrophysics of Maragha (RIAAM) under research project No. 1/4717-172.

References

- Barrow, J. D.; Levin, J. 2003, arXiv:gr-qc/0304038v1
Bassett, B.A.; Fantaye, Y.; Hlozek, R.; Sabiu, C.; Smith M. 2013 arXiv:1312.2593v2 [astro-ph.CO]
Bell, E. F.; Mcintosh, D.H.; Katz, N.; Weinberg, M.D. 2003, arXiv:astro-ph/0302543v2
Bilicki, M.; Jarrett, T.H.; Peacock, J. A.; Cluver, M.E.; Steward, L. 2014, ApJ.Suppl.210, 9
Bolejko, K.; Stuart, J.; Wyithe, B. 2008, arXiv:0807.2891v2 [astro-ph].
Clarkson, C.; Bassett, T. Hui-Ching Lu, T. 2007, arXiv:0712.3457v2 [astro-ph]
Caldwell, R. R.; Stebbins, A. 2007, arXiv:0711.3459v1 [astro-ph]
Clifton, T.; Ferreira, P. G.; Land L. 2008, arXiv:0807.1443v2 [astro-ph]
February S.; Clarkson, C.; Maartens R. 2013, JCAP 1303, 023.
Gilmore, G. 2008 arXiv:0808.3188v1 [astro-ph]
Huchra J. P.; et al. 2011, arXiv:1108.066p
Jia, J.; H. Zhang, H. 2008, arXiv:0809.2597v2 [astro-ph]
Labini, F.S.; Baryshev, F.S. 2010, arXiv:1006.0801v1 [astro-ph.CO]
Pietronero, L.; Labini, F. S. 1995, arXiv:astro-ph/9504013v1
Pop lawski, N.J. 2006, arXiv:gr-qc/0607021v2
Riess, A.G.; et al. 2004, arXiv:astro-ph/0402512v2
ShaRiess, A.G.; Riess, A.G.; Fieloo, A.; Clarkson, C. 2010, Phys. Rev. D 81, 083537
Singh, S. A.; et al. 2016, IJAA, Vol.06, No.03

- Springel, V.; Frenk, C. S.; White, S. D. M. 2006, arXiv:astro-ph/0604561v1.
- Stefanon, C.; Marchesini D. 2013, MNRAS. 429, 881 (2013)
- Tekhanovich, D.I.; Baryshev, Yu. V. 2016, Astrophysical Bulletin, vol. 71, Iss. 2, pp. 155 – 164
- Valkenburg, W.; Marra, V.; Clarkson C. 2014, MNRAS, 438, L6-L10
- Uzan, J. P. 2009, arXiv:0907.3081v1 [gr-qc]
- Uzan, J. P.; Clarkson, C.; Ellis, G.F.R. 2008, arXiv:0801.0068v2 [astro-ph]
- Zhang P., Stebbins, A. 2011, Phys.Rev.Lett. 107, 041301

Abundance and Star Formation Determinations in MARK galaxies from SDSS Spectra

M. V. Gyulzadyan^{1*}, A. M. Mickaelian¹, H. V. Abrahamyan¹, G. A. Mikayelyan¹, G. M. Paronyan¹

¹*NAS RA V. Ambartsumian Byurakan Astrophysical Observatory (BAO), Armenia*

**E-mail: mgyulz@yahoo.com*

Abstract

We analyse the oxygen and nitrogen abundance and specific star formation rates (sSFR) in Markarian galaxies from Sloan Digital Sky Survey (SDSS) spectra. The Data Release 7 (DR7) of SDSS contains photometric data for more than 1000 and spectral information for more than 700 Markarian objects. The Mrk sample has played a central role in the task of distinguishing between the astrophysical different types of phenomena that occur in AGNs. In the course of the Markarian survey, more than 200 Seyfert galaxies, and hundreds of starburst, blue compact, and H II galaxies were discovered. The Markarian survey remains perhaps the best-known source of such objects in the local universe. We have measured their line fluxes and derived the O and N abundances using recent calibrations. We have compared the oxygen and nitrogen abundances derived from global emission-line Sloan Digital Sky Survey (SDSS) spectra of galaxies using (1) the Te method and (2) two recent strong-line calibrations: the ON and NS calibrations. The behavior of the [N/H] ratio in under abundant regions gives strong support to a partially primary origin of nitrogen. The star formation rate (SFR) is one of the main parameters used to analyse the evolution of galaxies through time. In the local Universe, the H α luminosity derived from IFS observations can be used to measure SFR, at least in statistically significant, optically-selected galaxy samples, once stellar continuum absorption and dust attenuation effects are accounted for.

Keywords: *galaxies, Markarian galaxies, spectra.*

1. Mark galaxies

The First Byurakan Spectral Sky Survey (FBS), also commonly known as Markarian Survey, was initiated in 1965. It was the first systematic objective-prism search for galaxies with strong ultraviolet (UV) continuum

emission. The observations were carried out with Byurakan Astrophysical Observatory (BAO, Armenia) 1m Schmidt telescope equipped with a low-dispersion (2500μ at H_β and 1800μ at H_β) 1.5° objective prism. It was mostly used with Kodak IIA-F plates to detect galaxies with excess UV radiation (UVX, UV-excess). The survey consisted of 1133 fields (each having $4^\circ \times 4^\circ$ size) and covered $17,056 \text{ deg}^2$ north of -15° declination, excluding some regions within 15° - 20° of the Galactic plane. It was completed in 1978 and published in a series of 15 papers including 1500 UVX objects (Markarian et al. 1981 and references therein).

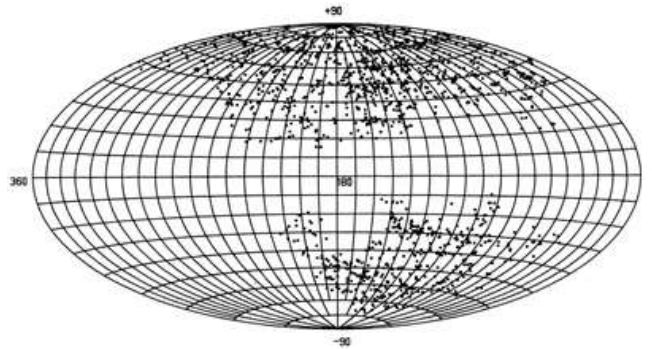


Figure 1: An all sky Hamer-Aitof projection of the 1500 Mark galaxies in Galactic coordinates (l, b)

The Mrk sample has played a central role in the task of distinguishing between the astrophysical different types of phenomena that occur in AGNs. For example, the original stratification of **Seyfert galaxies** into two types by Khachikian and Weedman (1971) was based largely on measurements of emission-line widths in spectra of a small number of galaxies discovered very early in Mrk survey. Later among MRK galaxies were discovered **LINERS** (Heckman 1980), galaxies with spectra that resemble HII regions (French 1980) (HII galaxies). Active galactic nuclei which appear to be the result of a short-lived outburst of star formation have become known as **starburst galaxies** (Weedman et al. 1981).

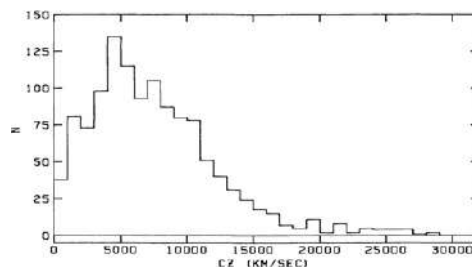


Figure 2: Velocity distribution of Mark galaxies.

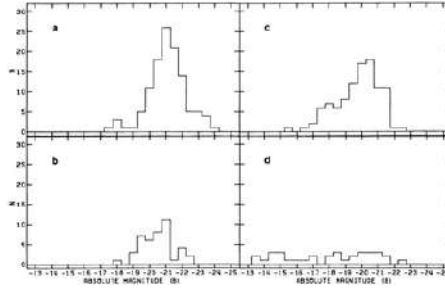


Figure 3: a) distribution of Sy1 & intermediate galaxies, b) distribution of Sy2 galaxies, c) distribution of SB galaxies, c) distribution of HII galaxies

The 70% region of the sky covered by the FBS is represented in the SDSS catalog (Sloan Digital Sky Survey; <http://www.sdss.org>). The Data Release 7 (DR7) of SDSS contains photometric data for more than 1000 and spectral information for more than 700 Markarian objects. The following emission lines are observed in the spectra of these galaxies: H_{α} , H_{β} , $[\text{OIII}]\lambda\lambda 4959\text{\AA}$, 5007\AA , $[\text{NII}]\lambda\lambda 6548\text{\AA}$, 6584\AA , $[\text{OII}]\lambda\lambda 3726\text{\AA}$, 3729\AA , $[\text{OI}]\lambda 6300\text{\AA}$, $[\text{SII}]\lambda\lambda 6717\text{\AA}$, 6731\AA , etc. The majority of starburst nuclei have $[\text{OIII}]\lambda\lambda 4959$, 5007 emission-line widths less than 250 km/s full width at half-maximum (FWHM), with a median FWHM of 140 km/s. This is to be compared with the median FWHM of Sy $[\text{OIII}]$ emission lines, 375 km/s for Sy 1 galaxies and 510 km/s for Sy 2 galaxies.

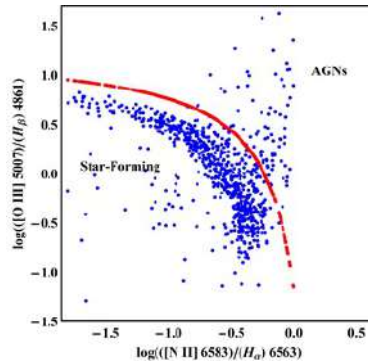


Figure 4: AGN selection in the Lee diagram (2008) for Mark galaxies from SDSS DR7

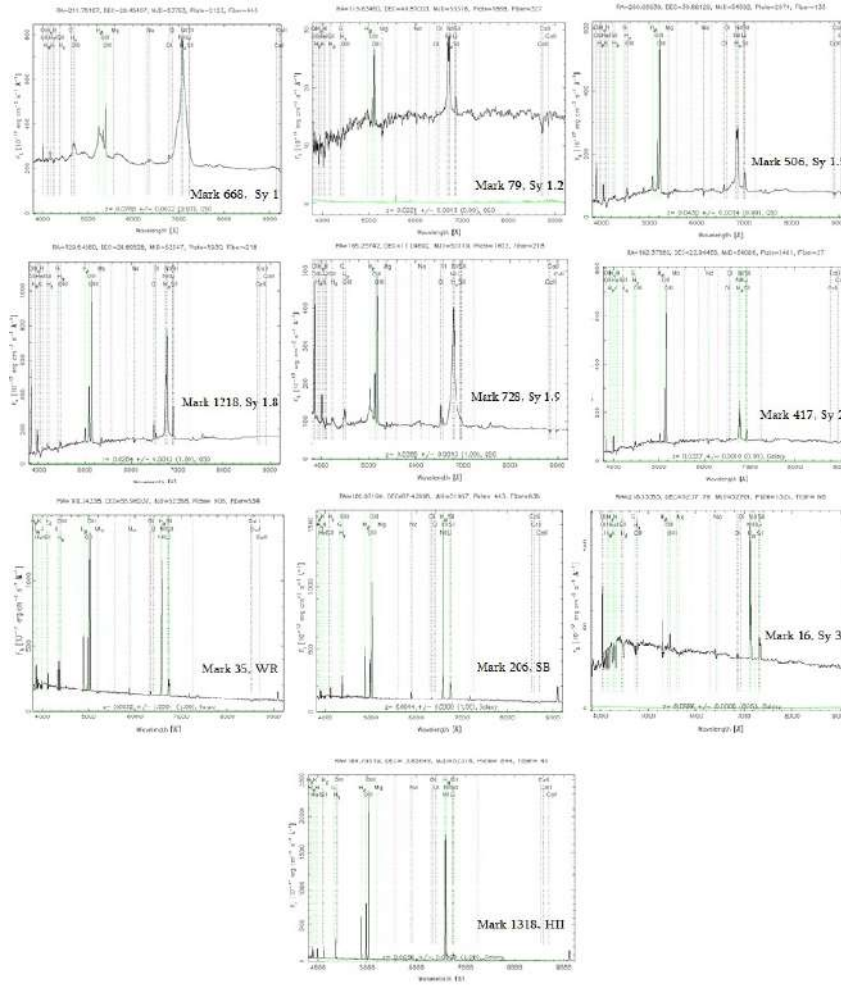


Figure 5: Examples of SDSS spectra of different subsystem type of Mark galaxies

2. The determination of electron temperatures and oxygen and nitrogen abundances in Mark Galaxies

Accurate metallicity play a key role in many investigations of galaxies. Gas-phase oxygen and nitrogen abundances are broadly used to measure these metallicity. It is believed (e.g., Stasinska 2006) that emission lines due to photoionization by massive stars are the most powerful indicator of the chemical composition of galaxies, both in the low- and intermediate redshift universe. Accurate oxygen and nitrogen abundances in H II regions can be derived via the classic T_e method, often referred to as the direct method. This method is base on the measurement of the electron temperature t_3

within the [O III] zone and/or the electron temperature t_2 within the [O II] zone. The ratio of the nebular to auroral oxygen line intensities $[\text{O III}](\lambda 4959 + \lambda 5007)/[\text{O III}]\lambda 4363$ is usually used for the t_3 determination, while the ratios of the nebular to auroral nitrogen line intensities $[\text{N II}](\lambda 6548 + \lambda 6584)/[\text{N II}]\lambda 5755$ or $[\text{O II}](\lambda 3727 + \lambda 3729)/[\text{O II}](\lambda 7320 + \lambda 7330)$ are used for the t_2 determination. In high-metallicity Hii regions, however, the auroral lines become too faint to be detected.

To select accurate measurements of HII regions in spiral galaxies, we require that the deviation of the oxygen abundance of the HII region from the general linear relation that describes the radial oxygen abundance gradient in the disk to be less than ~ 0.1 dex. works. As a result, the abundances from different works are not homogeneous and cannot be directly compared to each other. Therefore, the abundances from different works can be compared and analysed only after those abundances are homogenised, i. e., all the abundances are redetermined in a uniform way. Spectroscopic measurements of H II regions in nearby galaxies were carried out in many.

Spectroscopic measurements of H II regions in nearby galaxies were carried out in many works. The H II regions in one or several galaxies are usually measured and the element abundances are estimated. The different methods for abundance determinations are used in different works.

3. Star Formation Rate

Studies of the star formation rate (SFR) in galaxies are important for understanding their formation and evolution. Many indicators for determining the SFR in various parts of the electromagnetic spectrum are currently known. The SFR is widely determined using ultraviolet (UV) continuum emission (Bell & Kennicutt, 2001), far infrared (FIR) emission (E. F. Bell, 2003) and emission in the radio frequency range (E. F. Bell, 2003), as well as the emission of recombination and forbidden lines in the visible (Moustakas et. al. 2006). One of the most widely used indicators for determining the star formation rate is the H_α line, which is formed in the gaseous medium, after absorption and reprocessing of the emission from young stars beyond the Lyman series limit. It is known that in most galaxies with an ultraviolet excess, the strong UV emission originates mainly in the thermal radiation from young OB-stars. Thus, studies of star formation activity in the nuclei of these galaxies are important.

The results of detailed investigation of physical conditions and chemical abundances about 759 Mark galaxies from SDSS DR7 - DR9 will be published in our extended article.

References

- French, H. B. 1980, ApJ 240, 41
Goodrich, R. W.; Osterbrock, D. E. 1983, ApJ 269, 416
Heckman, T. M. 1980, Astr. Ap. 87, 152
Huchra, J. P. 1977, ApJS 35, 171
Khachikian, E. E.; Weedman, D. W. 1971, ApJ 7, 389
Markarian, B. E. 1967, Ap 3, 24
Markarian, B. E. 1969, Ap 5, 443
Markarian, B. E.; Lipovetskii, V. A.; Stepanian, J. A, 1981, Ap 17, 321
Osterbrock, D. E. 1976, ApJ 203, 329
Osterbrock, D. E. 1977, ApJ 215, 733
Osterbrock, D. E. 1981, ApJ 249, 462
Osterbrock, D. E.; Dahari, O. 1983, ApJ 273, 478
Weedman, D. W. 1973, ApJ 183, 29
Weedman, D. W.; et al. 1981, ApJ 248, 105
Lee, J., H. ; et al., 2007, Ap. J., 663, 69
Pilygin, L., S., 2010, A&A, 720, 1738
Ho, L., C.; et al., 1997, Ap. J., 487, 579

Investigations of the extended radio galaxy NGC 6251 and the galaxies in the environment

M. A. Hovhannisyan^{1*}, R. R. Andriasyan², G. M. Paronyan²

¹*NAS RA Institute of Applied Problems of Physics, Armenia*

²*NAS RA V. Ambartsumian Byurakan Astrophysical Observatory (BAO), Armenia*

**E-mail: martin@bao.sci.am*

Abstract

The environment of one of the most extended radio galaxies, NGC 6251, has been studied. The surface density of the environment galaxies in the region with the radius 300 arcmin around a radio galaxy NGC 6251 is 0.0315 in one arcmin². In the distances less than 180 arcmin, the density of galaxies decreases, which is most likely due to the strong radio loudness and the interaction of radio galaxy with its surroundings.

Keywords: *radio galaxies – NGC6251 – density of galaxies.*

1. Introduction

There is a strong interaction between extended radio galaxies and galaxies in the neighborhood. In the vicinity of extended radio galaxies, there is a great number of objects that probably are connected together. The neighborhood of 35 investigated extended radio galaxies differs from the common field, as well as from each other. But the difference of behavior of each other mainly is not so strong. Around 4 objects from the 35 extended radio galaxies there is a deficiency of galaxies in a such large scale that we can think about the existence of large scale voids in the space. For the detailed study of these regions will be dedicated a separate work. In the vicinity of some other extended radio galaxies, there is great number of abundance of objects comparing with the field. The results of investigation of these regions are also very interesting, but it needs a study of another character.

2. The environment of the radio galaxy NGC 6251

This work is dedicated to the investigation of one of the most extended radio galaxies, NGC 6251. Around the extended radio galaxy NGC 6251,

the density of neighboring galaxies is similar to majority of radio galaxies. 28 of the above-mentioned 35 extended radio galaxies exhibit similar behavior. NGC 6251 is the largest radio galaxy in the Northern sky. Its sizes reach up to 1.2 degrees (Waggett 1977). This radio galaxy is one of the most active ones in the region of all electromagnetic waves and has also large morphological varieties (Cohen 1977; Mingo 2014; Aswathy 2018; Croston 2018; Tseng 2016; Hovatta 2014; Babyk 2018).

We have investigated the environment objects of NGC 6251 (double galaxies, triples, groups, clusters, quasars), the density of these objects depending of the distances from the radio galaxy.

In the Table 1 there are galaxies and the densities of galaxies in the region of 300 arcmin around NGC 6251.

Region	Galaxies	Density
90-120	225	0.0114
120-180	613	0.0108
180-240	1303	0.0218
240-300	5981	0.0588

Table 1: Galaxies and the densities of galaxies in the region of 300 arc.min. around NGC6251

The distance of NGC 6251 is about 100 Mpc and its linear dimension is about 2 Mpc. We discuss the existence of galaxies in the region 20-25 Mpc around the radio galaxy. As we have not all distances of galaxies in this region, so we use the angular distances for the environment galaxies. The galaxies of this region have a large influence on the radio galaxy, and the radio galaxy in turn has a strong influence on the galaxies around. This influence is large on the activity as well as on the morphology of galaxies. We suppose that in spite of the fact that these influences are significant, but most of the properties of galaxies are initial and exist from the beginning of formation of these objects.

The surface density of galaxies in the region with the radius 300 arcmin around the radio galaxy NGC 6251 is 0.0315 in one arcmin². In the distances less than 180 arcmin, the density of galaxies decreases, which is most likely due to the large proportion of radio loudness and the interaction of radio galaxy with its surroundings.

References

- Aswathy, S.; Ravikumar, C. D. 2018, MNRAS, 477, 2399
 Babyk, Iu. V.; McNamara, B. R.; Nulsen, P. E. J.; Hogan, M. T.;

- Vantygghem, A. N.; Russell, H. R.; Pulido, F. A.; Edge, A. et al. 2018, ApJ., 857, 32
- Cohen, M.; Readhead, A. 1977, ApJ, 233, L101
- Croston, J. H.; Ineson, J.; Hardcastle, M. J. 2018, MNRAS, 476, 1614
- Hovatta, T.; Pavlidou, V.; King, O. G.; Mahabal, A.; Sesar, B.; Dancikova, R.; Djorgovski, S. G.; Drake, A.; Laher, R.; Levitan, D.; Max-Moerbeck, W.; Ofek, E. O.; Pearson, T. J.; Prince, T. A.; Readhead, A. C. S.; Richards, J. L.; Surace, J. 2014, MNRAS 439, 690
- Mingo, B.; Hardcastle, M. J.; Croston J.H. Dicken D.; Evans D. A., Morganti R., Tadhunter C. A 2014, MNRAS, 440, 269
- Tseng, C.-Y.; Asada, K. i; Nakamura, M.; Pu, H.-Yi; Algaba, J.-C.; Lo, W.-P. 2016, ApJ, 833, 288
- Waggett, P. C., Warner, P. J., Baldwin, J. E. 1977, MNRAS, 181, 465

Dependences between the magnitude gap of groups and the morphology of two brightest galaxies

A. P. Mahtessian*, V. H. Movsisyan, L. A. Mahtessian,
G. S. Karapetian

NAS RA V. Ambartsumian Byurakan Astrophysical Observatory (BAO), Armenia

**E-mail: amahtes@bao.sci.am*

Abstract

In the present study, the dependencies of the morphological types of the first and second ranked group galaxies on the magnitude gap were studied.

It is shown that there is no increase in the relative number of elliptical galaxies among the first and second ranked group galaxies with large magnitude gaps (in comparison with the expectation, by assuming that the morphological type of these galaxies does not depend on the magnitude gap). This result contradicts the merger hypothesis. The hypothesis proposed by Ambartsumian does not contradict this result.

1. Introduction

Works relating to groups of galaxies are inclined to prove that in these groups the main mechanism of evolution of galaxies is associated with the merging of galaxies.

It should be noted that there is another hypothesis proposed by V. Ambartsumian in the Byurakan Observatory, in which the evolution of galaxies is interpreted in a diametrically opposite way (V. A. Ambartsumian 1956; 1964).

Many observational facts can be explained by both mechanisms, but the dependences of the characteristics of galaxies from the magnitude gap of the groups might enable us to understand which of these two opposite mechanisms, in fact, makes a big contribution to the evolution of galaxies.

As the first characteristic, we can take the observed morphological type of galaxies. According to the merging scenario, the mass (or luminosity) of the central galaxy of the group must grow with the time, and the central galaxy must take an elliptical form. According to Ambartsumian's version

of the evolution of galaxies, no assumption is made about the morphology of the central galaxy.

Thus, from the point of view of the adherents of the merging hypothesis, a large magnitude gap of group means a long dynamical evolution. From the point of view of the formation of galaxies from protogroup matter through disintegration, this gap is either not related to the dynamical evolution of the groups or there must be an inverse relationship, i. e., a large gap m_{12} means a short dynamic age.

In this paper we consider the dependence between magnitude gap and the morphological types of the first and second ranked galaxies of groups.

2. Sample

We have used the list of groups of galaxies suggested by Mahtessian & Movsessian (2010). The study area is limited to the following: $1000 km/s \leq V \leq 15000 km/s$, $|bII| \geq 20^\circ$.

2.1. Completeness of the sample

The CfA2 survey is complete up to $m = 15.5$ (Mahtessian 2011). In this paper, the completeness of the samples of galaxies with measured morphological types has also been studied and it is shown that the completeness does not depend on the morphological types. The identification of the groups was carried out independently of the morphological types of galaxies (see Mahtessian & Movsessian 2010). On the other hand, initially, the definition of morphological types of galaxies is completely independent of their belonging to groups or from the magnitude gap m_{12} . Therefore, our sample can be considered as representative for studying this problem.

3. Results

Let us estimate the dependence of the morphological type of a first ranked galaxy on the magnitude gap m_{12} . The results are shown in Table 1. In the table, the galaxies are grouped according to the morphological types of the first ranked galaxies, as follows:

- E,L ($T = -7 \div -1$) – elliptical and lenticular galaxies,
- S,I ($T = 0 \div 20$) – spiral and irregular galaxies.

In the table, for a given subsample of galaxies, the observed number and the expected number (in parentheses, based on the assumption that there is no correlation between the morphological type of the first ranked galaxy and the magnitude gap) are given, and the frequency of appearance of m_{12}

is given below. In the last row, regardless of the morphological type, the distributions of the number and the relative number of gaps m_{12} are given.

In the case of elliptical and lenticular galaxies, the statistical significance of the difference between the distributions of the observed and expected numbers is 0.15 by the χ^2 method. In the case of spiral and irregular galaxies, this is ~ 0.4 . This means that between these distributions there is no significant statistical difference.

Thus, we can state that the relative number of brightest elliptical galaxy in groups does not increase with increasing magnitude gap m_{12} .

The continuation of Table 1 shows that this applies to extremely larger gaps also.

This casts doubt on the mechanism of merging.

Table 2 shows the distribution of the magnitude gap m_{12} in groups, depending on the morphological type of the second ranked galaxy. It can be seen from the table that in the transition from groups with small gap to groups with large gap, the number of elliptical and lenticular galaxies decreases with respect to the expected number. The statistical significance of the above, based on the χ^2 criterion, is higher (< 0.01).

This applies to extremely larger gaps also (see continuation of Table 2).

This fact cannot be explained by the mechanism of merging.

Let us consider the same question by dividing the sample by m_{12} into two parts. Table 3 gives the corresponding data for the brightest galaxy for $m_{12} < 2.0$ and $m_{12} \geq 2.0$.

Table 3 shows that the relative number of elliptical and lenticular galaxies among a first ranked galaxy groups with $m_{12} \geq 2.0$ is even smaller than the expected number (but its statistical significance is small, ≈ 0.3 , estimated by a method χ^2 , as well as with using a normal approximation).

Table 4 gives the corresponding data for second ranked galaxies for the cases $m_{12} < 2.0$ and $m_{12} \geq 2.0$. From the table, it can be seen that in the groups with the magnitude gaps $m_{12} \geq 2.0$ among the second ranked galaxies there is no observed large relative number of elliptical and lenticular galaxies in comparison with the expected one. It seems that the opposite phenomenon is observed, but its statistical significance is small ($\alpha \approx 0.2$).

A similar result was obtained when in Tables 1-4 instead of $S, I(T = 0 \div 20)$ galaxies only spiral galaxies $S(T = 0 \div 9)$ were considered.

Thus, it can be confidently asserted that the relative number of elliptical and lenticular galaxies among the first and second ranked galaxies does not increase with respect to the expected when the gap m_{12} increases (when it is assumed that there is no connection between the morphological types the first and second ranked galaxies and the magnitude gap m_{12}). This contradicts the merger hypothesis. As concerning the hypothesis proposed by Ambartsumian about the origin of galaxies due to the division of superdense proto-stellar matter, there is no contradiction here. However, more research is needed. The followings are possible topics for further investiga-

Table 1. Distributions of magnitude gap in groups, depending on the first ranked galaxy morphology type

m_{12}	$0 \div 0.5$	$0.5 \div 1.0$	$1.0 \div 1.5$	≥ 1.5	All_{gap}
E, L	217(230.9)	146(125.7)	71(69.1)	41(49.3)	475
	0.45	0.31	0.15	0.09	
S, I	472(458.0)	229(249.3)	135(136.9)	106(97.7)	942
	0.50	0.24	0.14	0.11	
All_{Type}	689	375	206	147	1417
	0.49	0.26	0.15	0.10	
continued					
m_{12}	≥ 2.0	≥ 2.5	≥ 3.0		
E, L	17(21.5)	10(10.7)	4(5.0)		
	0.036	0.021	0.008		
S, I	47(42.5)	22(21.3)	11(10.0)		
	0.050	0.023	0.012		
All_{Type}	64	32	15		
	0.045	0.023	0.011		

tion: a detailed morphological study of the first and second ranked galaxies, the study of dynamical conditions in groups, the study of X-ray, infrared, radio emission of groups and these galaxies, star formation, etc. We will carry out this research in the future.

Table 2. Distributions of magnitude gap in groups, depending on the second ranked galaxy morphology type.

m_{12}	$0 \div 0.5$	$0.5 \div 1.0$	$1.0 \div 1.5$	≥ 1.5	All_{gap}
E, L	173(149.9)	66(67.7)	25(34.1)	12(24.3)	276
	0.63	0.24	0.09	0.04	
S, I	420(443.1)	202(200.3)	110(100.9)	84(71.7)	816
	0.51	0.25	0.13	0.10	
All_{Type}	593	268	135	96	1092
	0.54	0.25	0.12	0.09	
continued					
m_{12}	≥ 2.0	≥ 2.5	≥ 3.0		
E, L	7(11.1)	2(5.6)	1(2.5)		
	0.025	0.007	0.004		
S, I	37(32.9)	20(16.4)	9(7.5)		
	0.045	0.025	0.011		
All_{Type}	44	22	10		
	0.040	0.020	0.009		

Table 3. The same as table 1 for $m_{12} < 2.0$ and $m_{12} \geq 2.0$

m_{12}	$0 \div 2.0$	≥ 2.0	All_{gap}
E, L	458(453.5)	17(21.5)	475
	0.964	0.036	
S, I	895(899.5)	47(42.5)	942
	0.950	0.050	
All_{Type}	1353	64	1417
	0.955	0.045	

Table 4. The same as table 2 for $m_{12} < 2.0$ and $m_{12} \geq 2.0$

m_{12}	$0 \div 2.0$	≥ 2.0	All_{gap}
E, L	269(264.9)	7(11.1)	276
	0.975	0.025	
S, I	779(783.1)	37(32.9)	816
	0.955	0.045	
All_{Type}	1048	44	1092
	0.960	0.040	

References

- Ambartsumian, V. 1956, *Izv. Akad. Nauk Arm. SSR, Ser. Fiz.-Mat. Nauk*, 9, 23
Ambartsumian, V. 1962, *Trans. Int. Astron. Union*, 12, 145
Mahtessian, A.; Movsessian V. 2010, *Afz*, 53, 83
Mahtessian, A. 2011, *Afz*, 54, 189

Search for Galaxies Clusters around Radio Galaxies with Different Linear Sizes

G. A. Ohanian

NAS RA V. Ambartsumian Byurakan Astrophysical Observatory (BAO), Armenia

E-mail: gohanian@bao.sci.am

Abstract

In order to understand how galaxies have formed and evolved in dense environments, and how these environments themselves evolve, we use the method of optical photometric survey of the field around radio galaxies. For this purpose, a statistical significant sample of radio galaxies consisting of 3 size radio source subclasses – GPS, CSS and FRI/II is selected for observations at the 1m Schmidt telescope of the Byurakan Astrophysical Observatory. This method will allow us not only to detect distant clusters of galaxies, but also watch the sequence of development of these clusters – how changes their compactness, richness, and so on.

Keywords: *Radio Galaxies – Galaxies Clusters – Galaxies Formation – Galaxies Evolution – AGN.*

1. Introduction

One of the main problems of extragalactic astronomy is the understanding how galaxies have formed and evolved. There are two basic approaches to solve this problem. One of which, that is widely accepted in the literature is so called standard scenario (e. g. Benson, 2010), and the other, which is less disseminated in the scientific literature, is Ambartsumian's concept (Ambartsumian 1958).

It is a fact that yet more than 60 years ago Ambartsumian (Ambartsumian 1958) stressed the role of AGN in galaxies formation and evolution. In recent years many works appear where importance of the role of AGN in galaxy formation and evolution have been revealed (e. g. Morganti et al. 2009). But the role of AGN in the above mentioned approaches is essentially different.

In the standard scenarios, it is believed that injection of matter and others types of activity are secondary phenomena, and a primarily phenomenon

is the gravitationally binding energy released from accretion of diffuse matter onto galaxies nuclei, which contain super massive black holes (SMBHs), and is discussed the efficiency with which AGN can transfer energy to the surrounding gas.

According to Ambartsumian's concept, the source of energy is effect of interior property of nuclei of galaxies, and a mechanism by which it can be transferred is still open.

Essentially, a key question, which arises when clear up a problem of formation and evolution of galaxies, irrespective of approaches, is the question of energy: what is the source of energy of AGN and its budget owing to formed galaxies and provide its subsequent development?

The main aim of our project is clear up this question. Our research is based not on preconceived opinion, but mainly on the observational data. When analyzing observational data, one bears in mind the following circumstance: the state of a galaxy is to be explained in terms of the entire activity of the nucleus over the preceding period that is the whole history of the nucleus. This means that the state of the galaxy should correlate with the present state of the nucleus (Ambartsumian 1965). These data, particularly collected during the last 10-15 years are the following:

- determination of the correlation of the integral parameters of the nuclei with those of the galaxies (e. g. Ferrarese & Merritt 2000),
- collected data about stellar populations of galaxies galaxies (e. g. Hicks et al. 2010),
- growing evidence for the AGN intermittent activity (e. g. Saikia & Jamrozy 2010,
- evolution of radio sources (e. g. O'Dea and Baum 1997).

Research should be made, including a thorough analysis of the above-mentioned factual material and by correctly summarizing the results obtained. It will allow us to discover the patterns of galaxies development and approach the problem of their origin (even with one step). In addition to the mentioned research, bellow is presented an observational program that can be implementing with medium and large telescopes.

2. Search for Galaxies Clusters Around Radio Galaxies with Different Linear Sizes. Objectives and sample selection

Clusters represent the largest gravitationally bound and densest structures in the universe. As such, they provide a unique context for studying the formation of both galaxies and large scale structure. In order to understand how galaxies form and evolve in dense environments, and how these environments themselves evolve, it is important to trace the origins of galaxy clusters.

Many studies show that radio quiet AGN, which are usually associated with less massive spiral galaxies, are less clustered than radio loud AGN, which are associated with more massive elliptical galaxies (e. g. Falder et al. 2010). So, the method of detecting cluster of galaxies around radio galaxies is very effective (e. g. Miley & De Breuck 2008).

The sizes of the most powerful radio emitters in the Universe vary from less than 1 pc to more than 1 Mpc. This large range of sizes has been interpreted as evidence for the evolution of the linear sizes of radio structure (e. g. O’Dea & Baum 1997). A crucial element in the study of their evolution is the identification of the young compact counterparts of “old” FRI/FRII (B. L. Fanaroff & J. M. Riley 1974) extended objects. Good candidates for young radio sources are those with peaked spectra (Gigahertz Peaked Spectrum – GPS, linear sizes < 1 kpc and Compact Steep Spectrum – CSS, linear sizes between 1 kpc and 20 kpc. In the general scenario of the evolution of powerful radio loud AGNs, GPS sources evolve into CSS sources and these into super galactic-size FR I or FR II objects. The dynamic evolution of the double-lobed radio sources, characterized by the total extent of the source, advance speed of the hotspots and the dependence of the density distribution of the interstellar and intergalactic medium along the way of the propagating jets and lobes, predicts the increase of the radio power with the linear size of the source in the GPS and CSS phase until they reach the 1-3 kpc size. Then the larger CSS objects should start to slowly decrease their luminosity but the sharp radio power decrease is visible only in the FR I and FR II phase of evolution (K. R. Kaiser & P. N. Best, 2007). Finally, after the cut off of the material supply to the central engine of the galaxy, the sources begin their fading phase. They can come back on the main evolutionary sequence after the re-ignition of the radio activity (C. Konar et al. 2012).

If it is true that GPS and CSS sources are young version of the large radio sources, it means that large scale radio sources host galaxies must live GPS-CSS phase. Therefore, the method of detecting the cluster of galaxies around radio galaxies with different linear sizes will enable not only discover clusters of galaxies, but also watch the sequence of development of these clusters – how changes their compactness, richness, and so on.

For this purpose, we selected from literature four type of radio galaxies:

- GPS radio sources, linear sizes are within the range of galactic nuclei,
- CSS radio sources, linear sizes are within the optical dimensions of the galaxies,
- FR II and FR I radio sources, linear sizes are larger in optical dimensions of the galaxy and can reach up to several Mpc.

3. Research Methods

An efficient technique for finding clusters of galaxies is an optical narrow-band survey of the field around radio galaxies. This observational program can be realized with modernized 1m Schmidt telescope of the Byurakan Astrophysical Observatory of the National Academy of Sciences of Armenia (Movsesian et al. 2018). The $4k \times 4k$ Apogee (USA) liquid-cooled CCD with RON 11.1e-, a pixel size of 0.868 arcsec, and field of view of about 1 degree was mounted in the focus of the telescope. The detector is equipped with a turret bearing 20 intermediate-band filters (FWHM = 250 Å) uniformly covering the 4000-9000 Å wavelength range, five broadband filters (SDSS u, g, r, i, z) and three narrow-band filters (5000 Å, 6560 Å and 6760 Å, FWHM = 100 Å).

4. Expected Results and Summary

The method of detecting the cluster of galaxies around radio galaxies with different linear sizes will enable us not only discover clusters of galaxies, but also watch the sequence of development of these clusters. Averaging richness, compactness of clusters of galaxies over the size subclasses enables us to investigate correlations between mean properties of clusters of galaxies and radio sources sizes.

To specify in more concrete terms, we expect to obtain in the course of this project the following results – photometry of galaxies, obtaining their photometric redshifts, estimating richness and compactness of clusters of galaxies. So, this data will enable not only discover clusters of galaxies, but also watch the sequence of development of these clusters – how changes their compactness, richness, and so on.

This project is open for collaboration.

References

- Ambartsumian, V. A., 1958, *La Structure et l'Evolution de l'Univers*, Editions Stoops, Bruxelles, 241
- Ambartsumian, V. A., 1965, *The Structure and Evolution of Galaxies*, Interscience Publishers, 1
- Benson, A. J., arXiv: astro-ph/10065394
- Best et al., 2007, *MNRAS*, 379, 894
- Burns, J. O., 1990, *AJ*, 99, 14
- Falder, J. T., Stevens, J. A. et al., 2010, *MNRAS*, 405, 347
- Fanaroff, B. L., Riley, J. M., 1974, *MNRAS*, 167P, 31
- Ferrarese, L., Merritt, D. 2000, *ApJ*, 539, 9
- Hicks, A. K., Mushotzky, R., Donahue, M., 2010, *ApJ*, 719, 1844
- Kaiser, K. R., Best, P. N., 2007, *MNRAS*, 381, 1548
- Konar, C., et. al., 2012, *MNRAS*, 424, 1061
- Miley G. K. and De Breuck, C., 2008, *AARv*,15, 67, 2008
- Movsessian, T. A., Dodonov, S. N., Gabrielyan, V. V., Kotov, S. S., Gevorgyan, M., 2017, *ComBAO*, V. 1, 92-101
- O'Dea, C. P., 1998, *PASP*, 110, 493, 1998
- Overzier, R. A. et al., 2009, *ApJ*, 704, 548
- Saikia J. A., Jamrozy M., arXiv:astro-ph/1004.0640.

Activity types of galaxies selected from HRC/BHRC sample

G. M. Paronyan^{1*}, A. M. Mickaelian¹, H. V. Abrahamyan¹,
G. A. Mikayelyan¹

¹*NAS RA V. Ambartsumian Byurakan Astrophysical Observatory (BAO), Armenia*

**E-mail: paronyan.gurgen@yahoo.com*

Abstract

In this study we carry out detailed spectral classification of 123 AGN candidates from the Joint HRC/BHRC sample, which is a combination of HRC (Hamburg-ROSAT Catalogue) and BHRC (Byurakan-Hamburg-ROSAT Catalogue). These objects were revealed as optical counterparts for ROSAT X-ray sources, however spectra for 123 of them are given in SDSS-III, IV without definite spectral classification. We studied these 123 objects using the SDSS spectra and revealed the detailed activity types for them. Three diagnostic diagrams and direct examination of the spectra were used to have more confident classification. We also made identification of these sources in other wavelength ranges and calculated some of their parameters.

Keywords: *X-ray; AGN candidates; spectral classification; activity types*

1. Introduction

ROSAT data are mainly listed in two catalogs: ROSAT Bright Source Catalogue (BSC) (Voges 1999) and ROSAT Faint Source Catalogue (FSC) (Voges 2000). They are clearly distinguished from each other by X-ray flux expressed in count-rate (CR; the number of particles registered by the receiver per unit time, namely per 1 sec).

Among the identification works, the ROSAT Bright Sources (RBS, Schwobe 2000) is well-known. 2012 BSC sources with $CR \geq 0.20$ and $|b| > 30^\circ$ have been optically identified. However, most of the identified sources come from the Hamburg Quasar Survey (HQS, Hagen 1995), which was used as a basis for optical identifications.

Two main projects have been carried out: Hamburg-ROSAT Catalogue (HRC, Zickgraf 2003) and Byurakan-Hamburg-ROSAT Catalogue (BHRC, Mickaelian 2006). HRC is based on ROSAT-BSC and BHRC is based on

ROSAT-FSC fainter sources (down to CR=0.04 to have confident X-ray sources) at $|b| > 20^\circ$ and $\delta > 0^\circ$ area.

In both catalogues, the selection of optical sources was made due to the following advantages of HQS:

1. The survey covers the entire extragalactic northern sky with $\delta > 0^\circ$ and $|b| > 20^\circ$.
2. Spectra were received with the help of an objective prism with a dispersion $1390 \text{ \AA} / \text{mm}$ allowing follow spectral energy distribution (SED) and notice some broad emission and absorption lines.
3. All plates of the survey are digitized with high quality and are accessible for studies.
4. HQS allows a quick identification of objects and finding their data in other catalogues.

We combined these two Catalogues and created a new homogeneous and complete catalogue of X-ray selected AGN, which covers all the northern sky limited by high galactic latitudes ($\delta > 0^\circ$, $|b| > 20^\circ$), and with CR > 0.04 . After some checks from various available catalogs, we have excluded a number of objects and included some missed AGN and finally it contained 4253 AGN or their candidates.

Out of the 4253 HRC-BHRC objects, 3369 sources were confirmed as AGN by means of optical spectral classifications; the main criteria in VCV-13 and BZCAT (Veron-Cetty 2010, Massaro 2012), 173 in Paronyan (2019) and the rest 711 are left as AGN candidates.

Out of these 711, for 123 AGN candidates in our sample there are spectra from SDSS-III and IV; we are carrying out a detailed spectral classification thus introducing new AGN or rejecting some objects.

2. Observing material

As observing material we had 123 spectra of HRC-BHRC objects from SDSS DR10-14 (Ahn 2014, Alam 2015, Albaretti 2017, Abolfathi 2018). Spectroscopic redshifts, intensities (assigned as “heights”) and equivalent widths of spectral lines for 123 of them from SDSS DR10-DR14 are available.

Very often SDSS measurements from their spectra are based on very low-quality lines at the level of noise. These automatic measurements give some artificial numbers that indicate non-real data. So, one needs to carefully check the spectra along all wavelengths and decide which measurements should be used for further studies. Especially important are those, which

are being used in the diagnostic diagrams ($H\beta$, $[OIII] 5007\text{\AA}$, $[OI] 6300\text{\AA}$, $H\alpha$, $[NII] 6583\text{\AA}$, and $[SII] 6716+6731\text{\AA}$) (Veilleux and 1987).

3. Classification Principles

We have used several methods for classification of our spectra

- By eye examination (taking into account all features and effects).
- By diagnostic diagram using $[OIII]/H\beta$ and $[OI]/H\alpha$ ratios.
- By diagnostic diagram using $[OIII]/H\beta$ and $[NII]/H\alpha$ ratios.
- By diagnostic diagram using $[OIII]/H\beta$ and $[SII]/H\alpha$ ratios.

Classification by eye has been done to compare with the classification by diagnostic diagrams and because not all objects appeared on them. Besides, the broad emission line component is not taken into account on the diagnostic diagrams, and this may be crucial for the classification of Seyfert 1.2-1.9 subclasses. Roughly, we distinguish Seyferts from LINERs by the criteria: $[OIII]/H\beta > 4$, and AGN from HII by $[NII]/H\alpha > 2/3$, $[OI]/H\alpha > 0.1$ criteria.

4. Results of Study of Spectra and Classification

We started studying spectra with identifications of spectral lines. We have used only lines having intensities 3σ over the noise level. $H\beta$ also appears in absorption on most of these spectra. We studied the influence of $H\beta$ absorption component on the emission one, which is important for using of the numerical data given in SDSS tables. After identifications of the emission lines we decided which of them should be used to build diagnostic diagrams (Veilleux and 1987).

On diagnostic diagrams the narrow-line AGN are separated into 3 main groups (HII, Sy, LINER). In addition, there are objects in intermediate areas, which have been classified as Composites (Veilleux and 1987) having both AGN and HII features.

5. Summary and Conclusion

We have created sample of X-ray selected AGN candidates and carried out spectroscopic investigation for those objects having SDSS spectra. 123 objects appear in this list and we have classified them by activity types using three diagnostic diagrams and eye examination of the spectra (to be

complete in classification of broad line AGN). Many Seyferts, LINERs, Composites and Starburst have been revealed. We have applied all possible parameters for fine classification to distinguish between narrow and classical broad line Seyferts, and to identify all details related to Seyfert subtypes depending on the strength of their broad components. We have introduced subtypes of NLS1, namely NLS1.0, NLS1.2, NLS1.5 and NLS1.8, giving more importance to these details (Osterbrock 1980, Winkler1992, Osterbrock 1985, Heckman 1980, Ho 1997, Weedman 1977, Veron 1997). Further accumulation of statistics may provide possibilities to understand the physical differences.

These 123 objects have been cross-correlated with GALEX (Bianchi 2011), SDSS, 2MASS (Skrutskie 2006) NIR, All WISE (Cutri 2013) , IRAS PSC (Beichman 1988), aFSC (Moshir 1992), NVSS (Condon 1988), and FIRST (Becker 1997) catalogues.

We have calculated all possible physical parameters of the studied objects: radial velocities, distances, absolute magnitudes, luminosity, etc.

One of the most intriguing class of objects among the X-ray sources are absorption line galaxies. The brightest ones may just appear in this sample due to their integral high luminosity, however we find that many such objects have low luminosity and still appear to be strong X-ray sources. We consider these objects as possible hidden AGN. The optical spectra do not show any signatures of emission.

References

- Abazajian, K. et al. 2009, ApJS 182, 543
 Abolfathi, B. et al., arXiv:1707.09322v3, (2018)
 Ahn, C. P.; Alexandroff, R.; Allende Prieto, C.; Anders, F.; Anderson, S. F.; Anderton, T.; Andrews, B. H.; Aubourg, E.; et al. 2014, ApJS 211, 17
 Alam, S. ; Albareti, F. D. ; Allende Prieto, C. et al., Astrophysical Journal Supplement 219 (2015) 12
 Albaretti, S. D. et al., arXiv:1608.02013v2 , (2017)
 Beichman, C. A.; Neugebauer, G.; Habing, H. J.; Clegg, P. E.; Chester, Thomas J. 1988, Infrared astronomical satellite (IRAS) catalogs and atlases
 Becker, R. H.; Helfand, D. J.; White, R. L.; Gregg, M. D.; Laurent-Muehleisen, S. A. 1997, ApJ 475, 479
 Bianchi, L.; Herald, J.; Efremova, B.; Girardi, L.; Zobot, A.; Marigo, P.; Conti, A.; Shiao, B. 2011, ApSS 335, 161
 Condon, J. J.; Cotton, W. D.; Greisen, E. W.; Yin, Q. F.; Perley, R. A.; Taylor, G. B.; Broderick, J. J. 1998, AJ 115, 1693
 Cutri, R. M., et al. 2013, IPAC/Caltech

- Hagen, H.-J.; Grootte, D.; Engels, D.; Reimers, D. 1995, *A&AS* 111, 195
- Heckman, T.M. 1980, *A&Ap* 87, 152
- Ho, L. C. ; Filippenko, A. V. ; Sargent, W. L. W., 1997, Proceedings of IAU Colloquium No. 159
- Massaro, E.; Giommi, P.; Leto, C.; Marchegiani, P.; Maselli, A.; Perri, M.; Piranomonte, S.; Sclavi, S. 2012, *A&A* 495, 691 (2009), online version 2012
- Mickaelian, A. M.; Hovhannisyan, L. R.; Engels, D.; Hagen, H.-J.; Voges, W. 2006, *A&A* 449, 425
- Moshir, M.; Kopan, G.; Conrow, T.; Hacking, P.; Gregorich, D.; Rohrbach, G.; Melnyk, M.; et al. 1992, IRAS Faint Source Survey, Version 2, JPL D-10015 8/92, (IPAC)
- Osterbrock, D. E.; Pogge, R. W., 1985, *ApJvol.* 297, p. 166-176
- Osterbrock, D.E., 1980, Proc. Texas Symposium on Relativistic Astrophysics, 9th, Munich, West Germany, Dec 14-19, 1978, New York, New York Academy of Sciences, p. 22
- Paronyan, G. M. et al. 2019, in press
- Schwope, A.; Hasinger, G.; Lehmann, I.; et al. 2000, *AN* 321, 1
- Skrutskie, M. F.; Cutri, R. M.; Stiening, R.; Weinberg, M. D.; Schneider, S.; Carpenter, J. M.; Beichman, C.; et al. 2006, *AJ* 131, 1163
- Veilleux, S. and Osterbrock, D. E. 1987, *ApJS* 63, 295
- Veron, P.; Goncalves, A. C.; Veron-Cetty-P., M., 1997, *A&Ap* 319, 52
- Veron-Cetty, M. P.; Veron, P. 2010, *A&A* 518, A10
- Voges, W.; Aschenbach, B.; Boller, Th.; Brauning, H.; Briel, U.; Burkert, W.; Dennerl, K.; et al. 2000, *IAU Circ.* 7432R
- Voges, W.; Aschenbach, B.; Boller, Th.; Brauning, H.; Briel, U.; Burkert, W.; Dennerl, K.; et al. 1999, *A&A* 349, 389
- Weedman, D.W. 1977, *VistasinAstronomy* 21, 55
- Winkler, H., 1992, *MNRAS*, vol. 257, no. 4, p. 677-688
- Zickgraf, F.-J.; Engels, D.; Hagen, H.-J.; Reimers, D.; Voges, W. 2003, *A&A* 406, 535

On the Connection Between Galaxies with Ultraviolet Excess

A. A. Yeghiazaryan

NAS RA V. Ambartsumian Byurakan Astrophysical Observatory (BAO)

Byurakan 0213, Aragatzotn Province, Armenia

E-mail: anahit@bao.sci.am

Abstract

A possible correlation between the characteristic parameters of physically coupled galaxies with ultraviolet excess is discussed. It is known that for mutually independent combinations the observed number of galactic pairs with Markarian components is greater than expected. It is shown, that the most of nearby Kazarian galaxies with ultraviolet excess form physical systems.

Keywords: *galaxies – ultraviolet excess – physical connection – spectra.*

The observational data indicate that characteristics of this galaxy largely depend on the characteristics of the surrounding galaxies, that is to say the correlation exists between characteristic of the shown galaxy and the characteristics of the members of the system in which this galaxy is included (Smirnov 1980, Giuricin 1985, Mahtesyan 1985). In the groups with relatively high density the galaxies are redder in the systems with relatively high number of elliptical galaxies, and elliptical galaxies are bluer in the systems where increased quantity of spiral galaxies is observed. There are also differences observed between isolated galaxies and galaxies that are members of multiple systems of galaxies. There are more emission galaxies in the galactic pairs and groups, and normal galaxies dominate among the isolated galaxies (Shuder 1981, Markarian 1882) whereas majority of galaxies belonging to pairs are peculiar (Sahakian 1975, Stoke 1978). There is an observed excess of galaxies with ultraviolet excess among the components of the galactic pairs, and with mutually independent combinations the observed number of pairs with Markarian components is distinctly larger than expected (Karachentsev 1981; 1984).

The above-mentioned suggests a possibility of correlation between characteristic parameters of physically coupled galaxies with ultraviolet excess.

The subject of a possible physical link between nearby galaxies with ultraviolet excess from the Kazarian list was considered (Kazarian 1979a,b, 1980, 1982). Taking into consideration only those pairs, which simultaneously are galaxies from the Kazarian list, the distribution of the angular distances on the celestial sphere of the first three near-neighbors for all Kazarian galaxies were considered. The observed and the Poisson distributions of the first, second and third near-neighbors of the Kazarian galaxies did not coincide. It was seen from the distribution that in 25% of the galaxies the angular distances of the first near-neighbors are less than $10'$. It was assumed that the majority of nearby galaxies with the ultraviolet excess from the Kazarian lists with angular distance less than $10'$ compose physically related systems (Yeghiazaryan 1987). The first research data of the spectroscopic study of the first near-neighbors for 27 Kazarian galaxies demonstrated that 12 out of 14 binary systems which angular distances between components are less than $10'$ form the physically related systems, which is consistent with the expected results (Kazarian 1987; Yeghiazaryan 1986a; 1986b; Yeghiazaryan & Khachikian 1988a; 1988b).

The catalog of Kazarian galaxies with ultraviolet excess, published in 2010, consists of 706 galaxies, of which the values of redshifts for 502, and the activity classes for 150 galaxies are given (Kazarian et al. 2010). Among them there are 28 pairs and 2 triplets of physically connected galaxies. Further studies of the Kazarian galaxies have shown that notable groups of the Kazarian galaxies are indeed observed (Yeghiazaryan 1995; 2016; 2018).

Figure 1 shows the spectrogram of the galaxy Kaz 195, and the figure 2 shows the spectrogram of the galaxy Kaz 197, obtained in 2017 with the 2.6m telescope of the Byurakan Astrophysical Observatory.

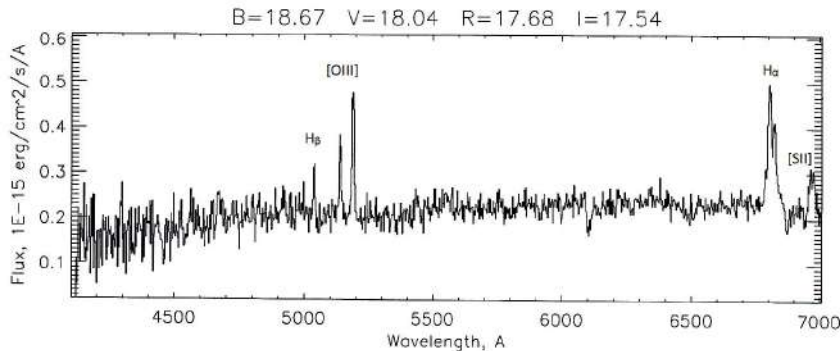
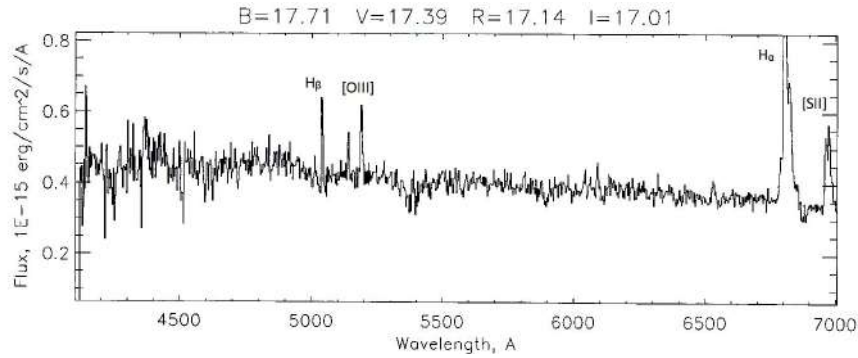


Figure 1: Spectrum of the galaxy Kaz 195


Figure 2: Spectrum of the galaxy Kaz 197

Kaz	α	δ	SMC	m	R	V
195	18 ^h 14 ^m 01 ^m	70° 18' 05"	s3	17.1	146.4	10980
197	18 ^h 14 ^m 07 ^m	70° 17' 38"	s2	17.2	146.1	10950

Table 1: Parameters of galaxies Kaz 195 and Kaz 197

Table 1 shows the parameters of galaxies Kaz 195 and Kaz 197 (Kaz number, equatorial coordinates α and δ , activity class, apparent isophotal magnitude, distance in Mpc, radial velocity in km/sec).

If classified, the studied galaxies with UV excess by their spectral features, among them there are many double systems with similar spectral characteristics of their components. Conducting a comprehensive study of closely spaced galaxies with ultraviolet excess would be beneficial in order to find out the correlation between individual physical characteristics and morphological features of the components of physically connected active galaxies.

References

- Giuricin G.; Mardirossian F.; Mezzetti M.; *Astron. Astrophys. Suppl.*, 1985, 62, 157
 Karachentsev I. D.; Karachensteva V. E.; *AZh*, 1974, 51, 724
 Karachentsev I. D.; *PAZh*, 1981, 7, 3
 Kazarian M. A.; *Astrofizika*, 1979a, 15, 5
 Kazarian M. A.; *Astrofizika*, 1979b, 15, 193
 Kazarian M. A.; Adibekyan V. Zh.; McLean B.; Allen R. J.; Petrosian A. R.; *Astrofizika*, 2010, 53, 1
 Kazarian M. A.; Kazarian E.S.; *Astrofizika*, 1980, 16, 17
 Kazarian M. A.; Kazarian E.S.; *Astrofizika*, 1982, 18, 512

- Kazarian M. A.; Kazarian E.S.; *Astrofizika*, 1983, 19, 213
Kazarian M. A.; Khachikian E. Ye.; Yeghiazaryan A. A.; *Astrophys. Space Sci.*; 1982, 82, 105
Mahtesyan A. P.; *So. Byu.* 1985, 57, 13
Markarian B. E.; *Astrofizika*, 1972, 8, 165
Sahakian K. A.; Khachikian E. Ye.; *Astrofizika*, 1975, 11, 207
Shuder S. H.; Osterbroch D. E.; *Astrophys. J.*, 1981, 250, 55
Smirnov M. A.; Comberg B. V.; *Astrofizika*, 1980, 16, 431
Stoke J. T.; *Astron. J.*, 1978, 83, 348
Yeghiazaryan A. A.; *So. Byu.* 1986a, 58, 68
Yeghiazaryan A. A.; *Astrofizika*, 1986b, 25, 425
Yeghiazaryan A. A.; *Astrofizika*, 1995, 38, 690, 1995
Yeghiazaryan A. A.; *Astrofizika*, 2018, 61, 455
Yeghiazaryan A. A.; Khachikian E. Ye.; *So. Byu.* 1988a, 60, 1
Yeghiazaryan A. A.; Khachikian E. Ye.; *So. Byu.*; 1988b, 60,13
Yeghiazaryan A. A.; Nazaryan T. A.; Hakobyan A. A.; *J. Astrophys. Ast.*, 2016, 37, 1
Yeghiazaryan A. A.; Zaratsian S. V.; Mahtesian A. P.; *So. Byu.*; 1987, 59, 53